University of Liege
Faculty of Applied Science
Department of Chemical Engineering
Products, Environment and Processes

Characterization and modeling of a photobioreactor for the culture of encapsulated microalgae

A thesis submitted in partial fulfillment of the requirements
for the degree of Doctor of Philosophy (PhD) in Engineering Science

by **Klara Weck**

under the supervision of Pr. Dominique Toye

DOCTORAL COLLEGE IN CHEMICAL ENGINEERING

May 2022

Thesis Jury

President

Angélique Léonard, University of Liege

Supervisor

Dominique Toye, University of Liege

Members

Jérôme Morchain, INSA, Toulouse

Diane Thomas, University of Mons

Fabrice Franck, University of Liege

Angélique Delafosse, University of Liege

Acknowledgments

Je souhaite remercier en premier lieu la Professeure Dominique Toye, promotrice de ce doctorat, de m'avoir donné l'opportunité de réaliser ce projet, ses conseils toujours pertinents et ses corrections.

Je suis très reconnaissante envers les Docteurs Sébastien Calvo et Angélique Delafosse pour leur encadrement, leur expertise, leur aide et leurs corrections.

J'aimerais remercier les personnes qui ont travaillées directement avec moi sur ce projet. Les deux stagiaires que j'ai eu le plaisir d'encadrer et qui ont fait un très bon travail : Raphaël Crépin et Joséphine Van den Bossche, ainsi que Nicolas Graindorge qui m'a brillamment aidé sur le développement du modèle biologique.

Je tiens à remercier Thierry Salmon et Christian Szykula pour leur aide et leur expertise au laboratoire.

Je remercie le Docteur Fabrice Franck, Directeur de recherche FNRS, qui m'a permis d'utiliser son laboratoire de Bioénergétique sans quoi je n'aurais pas pu cultiver de microalgues. J'aimerais remercier toute l'équipe du laboratoire pour leur accueil chaleureux et, en particulier, la Docteur Stéphanie Gérin de m'avoir partagé avec patience son expertise biologique et expérimentale.

Je remercie les membres du jury de prendre le temps de lire et commenter ce manuscrit. Je souhaite remercier chaleureusement le Docteur Jérôme Morchain, Maître de Conférences, d'avoir accepté de faire partie de ce jury. Merci au Docteur Fabrice Franck et à la Professeure Diane Thomas qui, faisant partis de mon comité de thèse, ont donné leur avis sur mon travail tout au long de mon doctorat. Merci à la Professeure Angélique Léonard d'avoir accepté de présider ce jury.

Je suis très reconnaissante envers la Région Wallonne et le FEDER d'avoir financé ce projet de recherche. Merci aussi à toutes les personnes qui ont travaillé sur ce projet avec lesquelles nous avons eu des échanges fructueux: la Professeure Anne-Lise Hantson et Robin Ronneau de l'Université de Mons; le Professeur Bao Lian Su, les Docteurs Li Wang et Cyrille Delneuville de l'Université de Namur ainsi que la Professeure Claire Remacle de l'Université de Liège.

J'aimerais remercier Frédéric Lox et Martin Gerday pour leur travaux sur la conception du photobioréacteur, qui m'ont beaucoup servis. Je souhaite remercier le Docteur Kyle Lauersen pour ses travaux d'ingénierie génétique sur la souche utilisée dans cette thèse.

J'aimerais remercier toutes les personnes faisant (ou ayant fait) parties du département de Chemical Engineering de l'Université de Liège. En particulier, les personnes que j'ai côtoyées au quotidien tout au long de ce doctorat et qui ont égayé mes journées en plus de me procurer une aide bienvenue: Anne, David, Chiara, Florence, Amir, Céline, Zaheer, Coralie, François, Jean-Luc, Marc, Hajer et Mohamad.

Un grand merci à Martine Lovato, Marlène Goffin et Cécile Prégaldien pour leur disponibilité et leur aide administrative.

Pour finir, j'aimerais adresser des remerciements plus personnels. A mes amis, que j'ai rencontrés à Liège et ont fait de ces quelques années une expérience géniale: Etienne, Margaux, Tommaso, Ana, Marine, Romain, Valentin, Kévin, Andrea, Guillaume, Fabien, Cédric, Julien. Un grand merci à tous mes amis français qui m'ont encouragée à distance ou qui ont fait le déplacement jusqu'à Liège.

Merci à ma famille: mes parents, mes sœurs et mes beaux-frères, qui m'ont toujours supportée dans mon parcours scolaire et étudiant, et qui étaient toujours présents même à distance. J'ai une pensée pour mes neveux, nés pendant cette période, qui ont ébloui mes journées par leurs sourires.

Merci à Brian de m'avoir suivie jusqu'à Liège, et pour son soutien inconditionnel et quotidien, toutes ces années.

Abstract

This thesis aims to model and scale-up the culture of encapsulated microalgae. A strain of *Chlamydomonas reinhardtii* is encapsulated in alginate beads by cross linking with $CaCl_2$. As often observed in literature, the growth rate of the encapsulated algae measured in flasks is lower than the free (suspended) culture. The studied photobioreactor is a rectangular liquid-solid fluidized bed reactor of 5 L. It enables to cultivate the strain almost 20 days without cell leakage. It allows to efficiently cultivate it as it leads to higher growth rates than in flasks (conditions are similar).

A global model to predict biomass growth in the photobioreactor is developed considering hydrodynamics, light and biological kinetics. Hydrodynamics is studied using CFD (Computational Fluid Dynamics). The liquid phase is first modeled. CFD is validated experimentally by PIV (Particle Image Velocimetry) on five vertical planes. Mean and fluctuating vertical velocities are compared. CFD correctly models the unusual flow of the reactor: laminar and unsteady. CFD and PIV are in fairly good agreement which allows to quantitatively validate the model.

The liquid-solid model is then validated using a light attenuation method which gives access to local solid distribution through the reactor depth. CFD allows to highlight a high influence of bead density (which is close to water) and of the lift force on the flow. Moreover, CFD gives access to liquid and solid velocities. This allows to quantify the influence of solid on liquid flow.

Relying on these simulations, a CFD-based compartment model is adapted to the studied reactor. This allows to describe hydrodynamics with less computation time. On the compartment model, a stochastic model is used which predicts the solid movement in the reactor thus the bead displacement in the light field. Light attenuation is modeled using Beer-Lambert law. Hence, the light intensity received by algae during the culture is known. As light is the most limiting growth parameter, it is possible to link biomass growth and "light history" of cells. Besides, light attenuation due to growth is considered. A three-states type PSF (PhotoSynthetic Factory) model is used to calculate the growth in the reactor and parameters are fitted on experimental results. The model allows to reach a final dry weight close to the experimental one. This global model predicts a high influence of hydrodynamics on biomass growth in this photobioreactor.

Résumé

Cette thèse a pour objectif la modélisation et la montée en échelle de la culture de microalgues encapsulées. Une souche de *Chlamydomonas reinhardtii* est encapsulée dans des billes d'alginate formées par réticulation dans une solution de $CaCl_2$. Comme observé la plupart du temps dans la littérature, le taux de croissance de l'algue encapsulée mesuré en erlenmeyer est plus faible que celui de l'algue cultivée de manière suspendue. Le photobioréacteur étudié est un lit fluidisé liquide-solide rectangulaire de 5 L. Il permet de cultiver efficacement la souche pendant près de 20 jours sans fuites dans le milieu de culture, en obtenant un taux de croissance plus important qu'en erlenmeyer (les conditions sont similaires).

Un modèle global pour prédire la croissance de la biomasse dans le réacteur est développé, prenant en compte l'hydrodynamique, la lumière et les cinétiques biologiques. L'hydrodynamique est étudié à l'aide de la CFD (mécanique des fluides numérique). Dans un premier temps, seule la phase liquide est modélisée. Le modèle CFD est validé expérimentalement par PIV (vélocimétrie par images de particules) sur 5 plans verticaux. Les vitesses moyennes et fluctuantes de la composante verticale sont comparées. Le modèle CFD permet de rendre compte de l'écoulement inhabituel du réacteur: laminaire et instationnaire. Une concordance satisfaisante entre les résultats CFD et PIV permet de valider quantitativement le modèle.

Le modèle liquide-solide est ensuite validé par une méthode d'atténuation de la lumière qui donne accès à la distribution locale de solide à travers l'épaisseur du réacteur. Le modèle CFD permet de mettre en évidence la forte influence de la densité des billes (qui est proche de l'eau) et de la force de portance sur l'écoulement. De plus, la CFD donne accès aux vitesses liquides et solides. Cela permet de quantifier l'influence du solide sur l'écoulement liquide.

Se fondant sur ces simulations, un modèle compartimenté basé sur la CFD est adapté au réacteur étudié. Cela permet de décrire l'hydrodynamique avec un temps de calcul réduit. Sur le modèle compartimenté, un modèle stochastique est utilisé pour prédire le mouvement du solide dans le réacteur et ainsi le déplacement des billes dans le champ de lumière. L'atténuation de la lumière est modélisée par une loi de type Beer-Lambert. Par conséquent, l'intensité lumineuse reçue par les algues lors de la culture est connue. Comme la lumière est le paramètre principal limitant la culture, il est possible de relier la croissance de la biomasse et « l'histoire lumineuse » des cellules. En outre, l'atténuation de la lumière due à la croissance est prise en compte. Un modèle à trois états de type PSF (PhotoSynthetic Factory) est utilisé pour calculer la croissance au sein du réacteur et les paramètres sont ajustés aux résultats expérimentaux. Le modèle permet d'atteindre une masse sèche finale proche de celle mesurée expérimentalement. Ce modèle global prévoit une forte influence de l'hydrodynamique sur la croissance de la biomasse dans ce photobioréacteur.

List of communications

Publications

Weck, K., Calvo, S., Delafosse, A., & Toye, D. (2021). Hydrodynamic Characterization of a Non-conventional Photobioreactor. Chemical Engineering and Technology, 44(10), 1803–1813. https://doi.org/10.1002/ceat.202100076

International communications

"Experimental study and modelling of hydrodynamics and light distribution in a photobioreactor for the culture of encapsulated microalgae (ValoAlgue project)". 12th European Symposium on Biochemical Engineering Science. K. Weck, S. Calvo, S. Gerin, F. Franck, D. Toye. Lisbon, Portugal. (September 2018).

"Caractérisation hydrodynamique d'un photobioréacteur pour la culture de microalgues encapsulées". K. Weck, S. Calvo, A. Delafosse, D. Toye. 17ème édition du congrès de la Société Française en Génie des Procédés. Nantes, France. (October 2019).

"Photobioreactor scale-up for the culture of encapsulated microalgae". K. Weck, S. Calvo, A. Delafosse, D. Toye. AlgaEurope 2020. Online. (December 2020).

International communications submitted

"Développement d'un modèle couplant hydrodynamique/lumière/croissance pour les procédés de culture de microalgues". K. Weck, A. Delafosse, S. Calvo, D. Toye. 18ème édition du congrès de la Société Française en Génie des Procédés. Toulouse, France. (Novembre 2020).

National communications

"Photobioreactor characterization for the culture of encapsulated microalgae". K. Weck, S. Calvo, D. Toye. GEPROC Scientific Day 2018. Liège, Belgique. (October 2018).

"Caractérisation hydrodynamique d'un photobioréacteur pour la culture de microalgues encapsulées". K. Weck, S. Calvo, A. Delafosse, D. Toye. GEPROC. Mons, Belgique. (November 2019).

Contents

1 Introduction

1.1 Thesis context

This thesis is part of ValoAlgue project which is included in the portfolio Algae Factory (FEDER grant 469780-671950). The project aims to study and scale-up the culture of encapsulated microalgae to produce high-added value metabolites. Different teams are involved in the project. The laboratory of Bioenergetics of the University of Liege provides the strain and studies the conditions of culture. The CMI laboratory of the University of Namur develops the encapsulation material. The Chemical and Biochemical Process group of the University of Mons studies the behavior of the encapsulation material and develops analytical methods. This thesis, performed in the PEP's laboratory (Chemical Engineering department) of the University of Liege, is focused on the photobioreactor development.

This thesis focuses on high-added value metabolites to consider a potentially profitable process. It is chosen to study a strain of *Chlamydomonas reinhardtii* which is able to secrete extracellularly *Gaussia* luciferase, a recombinant protein of high-added value.

The ValoAlgue project aims to scale-up the culture of encapsulated algae. A photobioreactor (liquid-solid fluidized bed) is developed especially for the culture of encapsulated algae. To understand and enhance the culture of encapsulated algae, the reactor is characterized and modeled in this thesis. A global model which considered hydrodynamics, light and predict growth is developed.

1.2 Microalgae

1.2.1 Microalgae definition

1.2.1.1 Phylogeny

Microalgae are microscopic organisms which most often contain chlorophyll a (and potentially other pigments that can color the cell) and are able to perform oxygenic photosynthesis, i.e., converting light energy into chemical energy by consuming carbon dioxide that produces back oxygen (European Algae Biomass Association, 2021). It must be noticed that some microalgae (heterotrophic cells) do not perform photosynthesis and grow in the dark transforming an organic carbon source (glucose, acetate, …) into energy (Krebs cycle). Microalgae are unicellular although they can form colonies or filaments.

There are around 40 000 species of microalgae identified around the world, but phycologists estimate the total number of species to be up to some millions (Metting, 1996; Norton et al., 1996). Thus the term "microalga" brings together a considerable diversity of species. It refers to eukaryote and, most of the time, also includes prokaryote (cyanobacteria) cells. It designates thus species that are not taxonomically related. Historically, species were morphologically regrouped but more recently, new groups have been formed using molecular biology (J. Singh & Saxena, 2015). However, there is no consensus on taxonomic classification of microalgae. The European Algae Biomass Association proposes a classification based on Tree of Life project (*Tree of Life Web Project*, n.d.) and John & Whitton, 2011. It suggests four main kingdoms to classify microalgae: *Eubacteria* (which contains cyanobacteria), *Archaeplastida, Chromalveolata* and *Excavata*. Figure 1.1 represents the classification proposed by Pierre et al., 2019; Not et al., 2012. It shows that *Chromalveolata* are divided into *Rhizaria, Alveolata* and *Heterokontophyta*.

As microalgae are represented in a lot of different evolutionary lines, they have a huge morphological and molecular diversity. Microalgae can be of different colors (green, red, brown), shapes (circular, elongated, spiral form, …) and sizes (0.2 µm – 2 mm (Not et al., 2012)). They can grow in various environments: most of the time in fresh or marine water, but they can also develop on glaciers, rocks or desert (Cardon et al., 2008; Williamson et al., 2019). Some species can live in extreme conditions in terms of temperature or pH (Pierre et al., 2019).

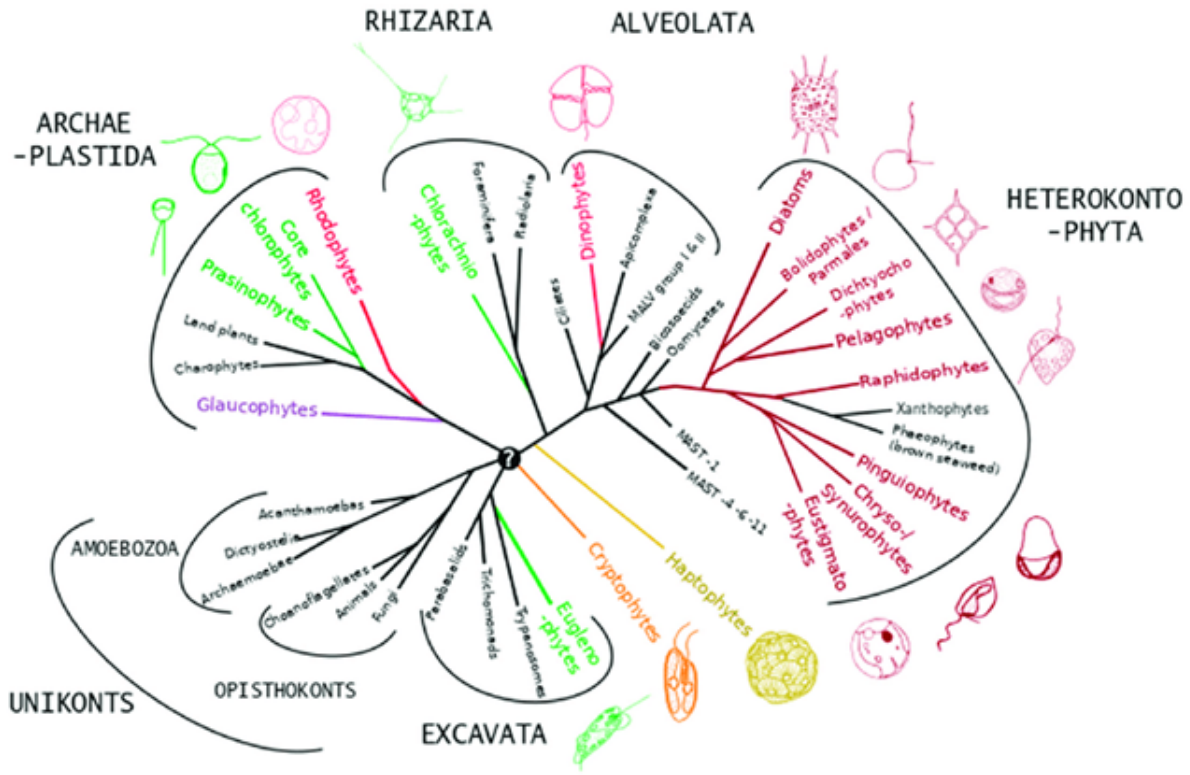

Figure 1.1 – Microalgae phylogenic tree representing eukaryotic species. Reproduced from (Pierre et al., 2019) *with authorization.*

1.2.1.2 Chlamydomonas reinhardtii

Chlamydomonas reinhardtii is a green microalga belonging to the phylum Chlorophyta. It measures between 6 and 11 µm of diameter (Gallaher et al., 2015). As all algae from *Chlamydomonas* genus, it is characterized by two flagella, a cell wall and a single chloroplast containing one or more pyrenoids (Figure 1.2) (Harris et al., 2009). Flagella allow *Chlamydomonas* to move in the culture medium (Silflow-2001). This alga can grow autotrophically (performing photosynthesis) or heterotrophically (F. Chen & Johns, 1996). It grows on the soil or in fresh water.

Chlamydomonas reinhardtii is a model organism used to study biological processes. It grows rapidly and can be easily modified genetically. Strains used in laboratory come from an original strain isolated by G.M. Smith in 1945 (Harris et al., 2009). Numerous advances on genetics, biochemistry and cell biology have been made studying it, mainly on cell cycle, pyrenoid structure, photosynthesis, sexual reproduction or cell light acclimation (Sasso et al., 2018). In 2007, the entire genome of *Chlamydomonas reinhardtii* has been published in the literature (Merchant et al., 2007).

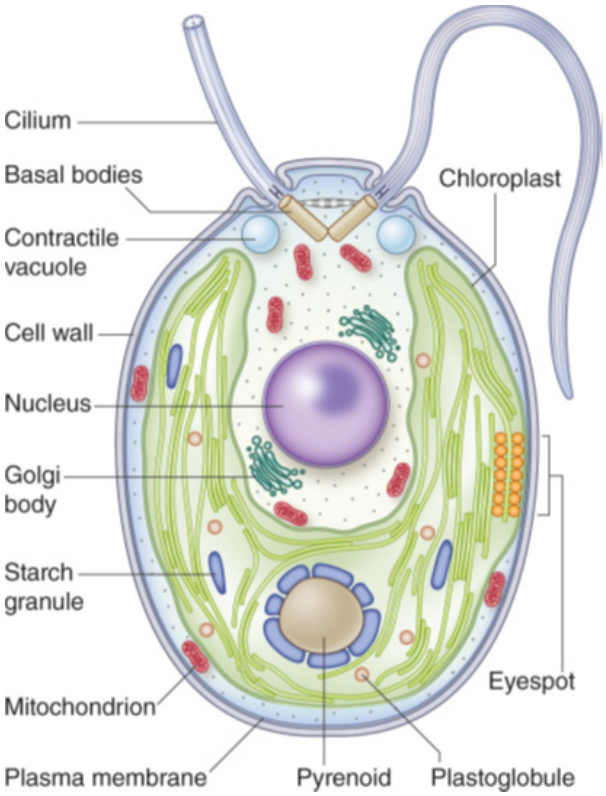

Figure 1.2 – Schematic representation of a Chlamydomonas reinhardtii cell. Reproduced from (Sasso et al., 2018) *published under the Creative Commons Attribution 4.0 International Public License (https://creativecommons.org/licenses/by/4.0/). No changes were made.*

1.2.2 Production of microalgae biomass and metabolites

1.2.2.1 Production steps

The production of microalgae requires generally four main steps (Figure 1.3). The first one is the inoculation which is the addition of a small number of algae cells in the bioreactor to allow the cells multiplication. Then there is a step of microalgal culture, strictly speaking, when the algae are in growing phase. This step can take place in open or close bioreactors as explained in section 1.2.2.2. This step is the one that will be studied in the present thesis as it deals with photobioreactor characterization and performance optimization. The third step is the harvesting step and consists in the separation of algae from their culture medium. Different methods exist and are detailed in section 1.2.2.3. Finally, algae are usually dried and transformed depending on their purpose. As metabolites of interest are, most of the time, situated inside the cell, a step of cell disruption (high-pressure homogenization for example) can be necessary (Halim et al., 2012). Algae can also be dried and milled in powder before extraction. Extraction is thus performed using organic solvent or supercritical fluid. Avoiding this step by using algae which extracellularly secrete metabolites, allows to save energy or solvent costs.

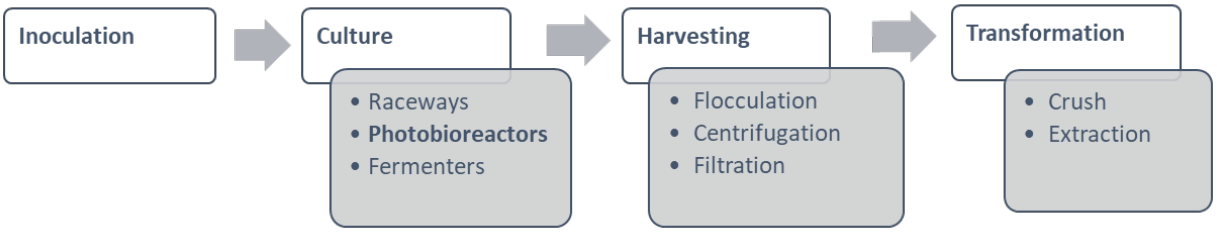

Figure 1.3 – Four main production steps from microalgae.

1.2.2.2 Culture of microalgae

1.2.2.2.1 Cultivation modes

1.2.2.2.1.1 Choice of trophic mode

Autotrophic cultivation mode which uses the ability of microalgae for photosynthesis enables to consume carbon dioxide and produce oxygen. Heterotrophic cultivation mode (in the dark using organic carbon source) enables to obtain high biomass productivities, but bacterial or fungal contaminations are more common (W. Zhou et al., 2020). Furthermore, this causes undesirable CO_2 emissions. Mixotrophic cells, which are using both metabolic schemes previously described, can grow with the help of an organic carbon source or light. This leads generally to a two-step culture beginning with a fast growth when cells are consuming organic carbon (W. Zhou et al., 2020). Autotrophic and mixotrophic (flask scale) modes are discussed in this thesis. Heterotrophic mode, which requires the use of fermenters, is not studied.

1.2.2.2.1.2 Operating modes

The culture of microalgae can be performed in continuous, semi-continuous or discontinuous modes. The discontinuous or batch mode is the most used mode in industry because of its technical simplicity (Takache, 2010). No fresh culture medium is added in the system after inoculation. Hence, the entire culture is harvest when the algae concentration has reached its maximum value.

The continuous mode consists in pumping fresh culture medium into the system while withdrawing the same amount of culture (Ramos Tercero et al., 2014). Two methods exist, the chemostat and the turbidostat. Chemostat method uses a fixed dilution flow rate that is equal to the growth rate. In turbidostat method, the dilution depends on biomass concentration which is continuously measured and kept constant. Even if the continuous mode gives better biomass productivity than batch mode in theory, it is difficult to scale-up as the biomass is harvested at any time.

In semi-continuous systems, a certain amount of culture (1/3 of the total volume for example) is punctually withdrawn and the equivalent volume of fresh culture medium is added (Benvenuti et al., 2016). For practical reasons, it is easier to scale-up than continuous mode.

Finally, fed-batch mode refers to punctual addition of nutrients. It is employed to avoid a potential inhibition at the beginning of culture due to high concentration of a nutrient (Ferreira et al., 2010).

1.2.2.2.2 Open systems

Open systems exist from the beginning of microalgal culture, in the 1950's (Chisti, 2013; Sompech et al., 2012). They can be lagoons (stagnant water near seacoasts), but raceway ponds are mostly used. These last consist in a closed-loop recirculation channel, taking its name from racetrack (Figure 1.4). A paddlewheel ensures the liquid circulation through the loop and therefore the mixing. Generally, only one eight bladed paddlewheel is used for energy saving reasons. The flow velocity is generally around 0.3 m/s to prevent cells from sedimentation (Chisti, 2013). Raceways are generally 0.25-0.30 m deep. They require a high surface of land (which can be non-arable land). Depending on the location (illumination, temperature, …), they can be used only in some periods of the year.

While raceway ponds are the most adopted systems to cultivate microalgae because of their low cost, they suffer from several drawbacks (Mendoza et al., 2013). Indeed, due to their geometrical conception they do not allow the control and regulation of some main culture parameters such as temperature or pH. In addition, light penetration within culture medium decreases rapidly thus limits global growth inside the system: more than 80 % of the culture is considered to be in dark zone (Chisti, 2013). Another limitation is the fact that the mixing induced by the paddlewheel is not sufficient to ensure a proper renewal of cells near the free surface (Sompech et al., 2012). The poor mixing also results in low gas mass transfer between culture medium and atmosphere or injected gas (CO_2 can be bubbled directly at the bottom of the reactor). This leads to insufficient intake of carbon to cells and insufficient stripping of accumulated oxygen, which both have a negative effect on growth (Mendoza et al., 2013). Moreover, some CO_2 not transferred to the culture medium is released in the atmosphere.

Finally, open systems are subject to contaminations as they exchange directly with the environment. It can be viruses, bacteria, fungi or other species of microalgae (Chisti, 2013). Therefore, only fast-growth and extremophile algae, which grow in high pH or high salinity medium that prevents other micro-organisms development, are cultivated in open ponds nowadays. They can be placed under greenhouses to limit contaminations (R. N. Singh & Sharma, 2012). This also enables a better temperature control. Raceways are also subject to evaporation (Chisti, 2013). Hence raceways are commonly used to cultivate microalgae due to their low cost but do not allow to obtain a high biomass concentration which increases harvesting step costs.

Figure 1.4 – Photography of a raceway pond for the culture of microalgae. Reproduced from (Chowdury et al., 2020).

1.2.2.2.3 Closed systems

Closed systems or photobioreactors are transparent bioreactors made in glass or plastic to allow light penetration. As closed systems, they allow to control the different parameters which have an impact on growth. Temperature can be regulated using a heat exchanger or spraying water on the surface of the reactor (R. N. Singh & Sharma, 2012). pH is generally measured by probes and regulated with enriched air/CO_2 injections. Thanks to their low depth, light path through the culture is enhanced compared to raceway ponds, leading to thinner dark zones. Furthermore, they are designed to favor mixing. This enables an adequate light access for cells and enhance gas-liquid mass transfer. For all these reasons, photobioreactors allow to obtain high cell concentration. Moreover, as they have no direct exchange with the environment, they enable to axenically cultivate strains which cannot be grown in raceways (R. N. Singh & Sharma, 2012).

A lot of different photobioreactors exist. Several geometries and mixing types have been designed (Figure 1.5). The most frequently used types are tubular reactors (Miyamoto et al., 1988; Molina et al., 2001; Travieso et al., 2001). They can be vertical, helical, or horizontal (Figure 1.5 a (A), (B), (C) respectively). Horizontal reactors require more land than vertical but optimize access to natural light while vertical reactors can be inclined to optimize natural light inflow (Tredici & Zittelli, 1998). They are equipped with a degassing system used to collect residual gas. Tubular reactors require a high energy consumption as a low shear pump is needed to drive the flow (R. N. Singh & Sharma, 2012).

Other geometries as rectangular columns are used to grow microalgae. They are, most of the time, in the form of flat panels (Figure 1.5 a (D)). Due to their low thickness, they maximize light inflow that leads to high biomass concentration. They used gas sparger at the bottom of the reactor which provides an efficient mixing and gas-liquid mass transfer. No pump is needed thus these reactors need less energy than tubular reactors. To enhance mixing and transfers, airlift technology can be used (Degen et al., 2001). Geometry of this type uses baffles to extend the way of the gas going up to enhance gas-liquid transfer (Figure 1.5 a (E)).

Some cylindrical vessels also exist although they do not allow light to easily penetrate. Bubble columns are one of them (Figure 1.5 a (H)). Other cylindrical vessels which can be used are stirred tank reactors (using also gas sparger) (Figure 1.5 a (G)) (Muñoz et al., 2004) but they provide high shear stress in the impeller region which can damage cells (Aslanbay Guler et al., 2020).

More recently, innovative designs have been investigated. Hybrid photobioreactors, which used several geometries to take different advantages of the reactors previously cited, have been designed. For example, tubular and air-lift reactors have been successfully combined (Acien Fernandez et al., 2001). New photobioreactors such as floating reactors for offshore production have been studied (Kim et al., 2016; Wiley, 2013). They facilitate temperature control and mixing is driven by waves. Rotating biofilm reactors have been designed to increase biomass concentration and reduce harvesting costs but biofilm attachment must be sufficient (Blanken et al., 2014). Biofilm culture is one of immobilization methods discussed in section 1.2.3.1.

As they allow to better control culture conditions, photobioreactors enable to get a significantly higher biomass productivity than raceway ponds. However, they require higher investment and production costs. At present, photobioreactors can only be used to produce high added value products to be profitable (see section 1.3.5) (Souliès, 2014), while raceway ponds are considered as more cost-efficient for large-scale culture of microalgae (Kang et al., 2015). To extend the range of applications of PBR, the associated costs must be drastically reduced or their performances must be further increased, so more research on photobioreactors: design, optimization, ... is needed.

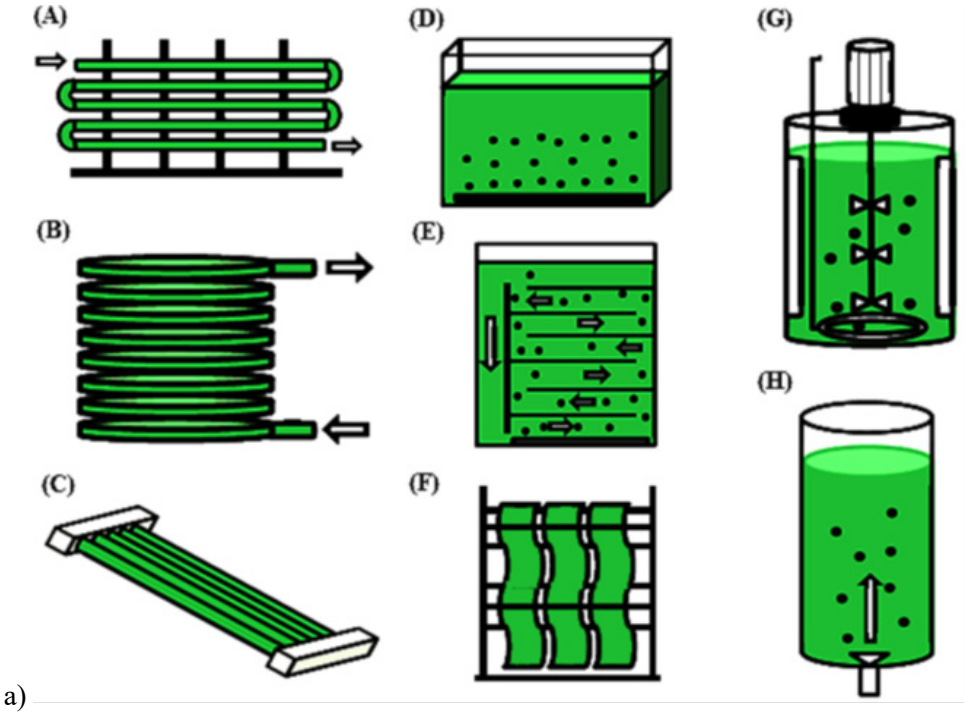

Figure 1.5 – Schematic representation of different types of photobioreactors (a): (A): vertical tubular, (B): helical tubular, (C): horizontal tubular, (D): flat panel, (E): airlift, (F): accordion type, (G): stirred tank, (H): bubble column. Reproduced from (Khetkorn et al., 2017) with authorization. *Photography of industrial tubular reactors (b). A Varicon Aqua Phyco-Flow serpentine photobioreactor growing Haematococcus pluvialis in Kona, Hawaii. Image courtesy of Varicon Aqua Solutions Ltd. UK (2018)* (Varicon Aqua Solutions, n.d.).

1.2.2.3 Microalgae harvesting

Microalgal culture are very dilute, reaching between 0.05-0.3 % of dry matter at the end of the culture. Hence, a step of harvesting is needed to increase the biomass concentration before its valorization. Several methods exist to harvest microalgae: chemical, mechanical and biological methods. The selection of the method is based on different criteria: biomass quantity, processing time, cost, biomass quality, species characteristic and toxicity (G. Singh & Patidar, 2018).

Natural sedimentation can be used but is very slow and inefficient. However, as microalgae are negatively charged, flocculation can be used to aggregate cells before sedimentation. Different types of flocculation/coagulation exist according to the flocculating agent. Chemical flocculation refers to addition of cationic polymers (Danquah et al., 2009), pH increase (Vandamme et al., 2012) or electrolyte

addition (Granados et al., 2012). Bio-flocculation can also be used: addition of bacteria to form microalgal-bacterial flocs thanks to polymers produced by bacteria (Lee et al., 2009). Electrical methods are studied as well. Electrical power enables to recover algae on electrodes or by sedimentation (S. Gao et al., 2010). Finally, flotation uses gas bubbles to carry algae on top of liquid, often after a flocculation step (Garg et al., 2015). It is efficient for low density algae.

In industry, centrifugation (gravity sedimentation using centrifugal force) is mostly used (Person, 2011). It can be used in continuous or batch mode. Centrifuges are efficient (more than 90 % of separation) but requires a high consumption of energy and can damage cells due to high shear stress (G. Singh & Patidar, 2018).

Filtration through a membrane (nano, ultra or microfiltration) using a pressure drop can be used to efficiently separate microalgae from their culture medium (Sun et al., 2014). However, membranes are expensive and subject to fouling: cells accumulation which block the flow through the membrane (Liang et al., 2008). Tangential and dead-end membranes are the most appropriates to reduce fouling (Babel & Takizawa, 2010; Danquah et al., 2009).

It is often profitable to combine two methods (Barros et al., 2015). The aim of the first step is culture medium thickening. It is done by flocculation/coagulation, flotation … which allows to obtain a biomass concentration between 2 and 7 % of total volume. Then a dewatering step (centrifugation, filtration) is used to concentrates the biomass up to 15-20 % of total volume.

Due to high energy consumption, the cost of harvesting is considered to represent 20-30 % of the total cost process of microalgae culture (Barros et al., 2015; G. Singh & Patidar, 2018). More recently, Fasaei et al., 2018 calculated that the actual harvesting costs represent 3-15 % of total cost. It is worth noting that the harvesting cost is highly dependent on labor cost, energy cost and dry matter content. In all cases, this step of the process must thus be studied and optimized to lower the total cost of microalgae production which is not always profitable (Barros et al., 2015).

1.2.3 Encapsulation of microalgae

Immobilization hinders cell mobility by the attachment or entrapment of microorganisms on or inside a carrier. It thus differs from the leading method of microalgae cultivation which consists in performing suspended cells cultures. If bacteria or enzyme immobilization are common, microalgae immobilization have been developed more recently. Microalgae immobilization allows to locally densify cultures and thus facilitates the harvesting step. It must be noticed that microalgae have the tendency to form biofilm or aggregates in nature (Karsten et al., 2007). These configurations protect microorganisms from biological or physical stresses such as extreme temperatures, UV radiations or contaminants (Costerton et al., 1995; Vasilieva et al., 2016). This shows that some microalgae easily tolerate and are able to grow when immobilized.

1.2.3.1 Immobilization

1.2.3.1.1 Methods

Different methods of artificial immobilization exist (Figure 1.6). They can be divided into passive and active techniques. Passive techniques refer to natural attachment (adsorption) while active force the attachment between cells and the carrier (covalent bonding, membranes, entrapment).

Natural attachment (adsorption) on a support is enabled by weak forces as van der Waals forces, hydrogen, ionic or hydrophobic bonds (Bayat et al., 2015). This method is easy, not costly and allows a

direct contact between cells and nutrients. But the weakness of the binding force leads to cell leakage. The link depends on several factors: the hydrophobicity and surface charge of the carrier and the microorganism, pH, temperature, culture medium flow... (Costa et al., 2005).

To favorize a better attachment on a carrier, active techniques have been developed as covalent bonding. It consists in using chemicals as glutaraldehyde to form a covalent bond between cells and the carrier (Pan et al., 2009; Yigitoglu & Temoçin, 2010). This irreversible covalent bonding method enables to obtain a strong attachment. However, bonding agents can be toxic, which causes cell losses (Bouabidi et al., 2019). Therefore, this method is sometimes employed on non-living cells. Dead cells can be used for metal removal (Mallick, 2002).

Finally, entrapment, in which cells are captured in a polymeric porous matrix, is the most used immobilization method (Moreno-Garrido, 2008). This method protects cells but reduces nutrients accessibility. Entrapment can be performed in different shapes such as layer or beads. This one is called "encapsulation" and corresponds to the method used in this thesis. It is described in more details in section 1.2.3.2.

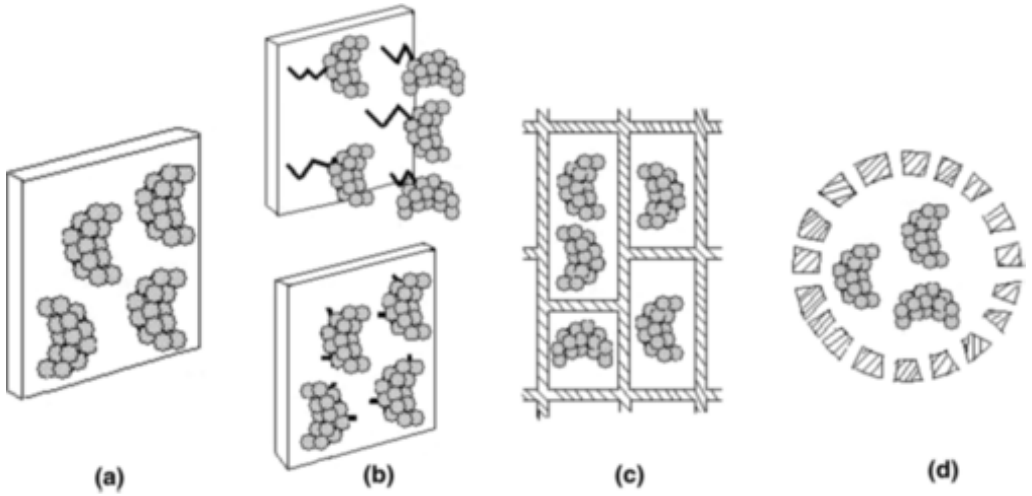

Figure 1.6 – Schematic representations of main immobilization methods: adsorption (a), covalent bonding (b), entrapment (c) and encapsulation (d). Reproduced from (Costa et al., 2005) *with authorization.*

1.2.3.1.2 Carrier choice

Several carriers can be used for microalgae immobilization depending on the method, strain and applications (Figure 1.7). The carrier must also be mechanically, chemically and biologically stable, i.e., it must not be degraded by shear/collisions, dissolved by the medium (pH, …) or bio-degraded by the biomass (Vasilieva et al., 2016). It must be hydrophilic to allow a good transfer with aqueous media, but insoluble (Bouabidi et al., 2019). Carriers can be organic or inorganic, natural or synthetic. Natural carriers are highly biocompatible, hydrophilic and achieve high diffusivity but are less resistant and more expansive than synthetic carriers (Bouabidi et al., 2019; de-Bashan & Bashan, 2010; Vasilieva et al., 2016). In passive immobilization, cucurbits type loofa is commonly used as it is biodegradable, biocompatible and relatively inexpensive (Vasilieva et al., 2016). Polyurethane foam cubes can be used in the same way. Carriers made from activated charcoal, glass, wood, zeolite, mineral or plastic can also be used (Bouabidi et al., 2019; Vasilieva et al., 2016). Other supports which can be used are membranes (hollow fiber for example) (Hyde et al., 1991; Naessens et al., 2000). There are some drawbacks: membranes are expansive and growth within it can lead to its breakage when high concentration of biomass is reached (Mallick, 2002).

For entrapment, more constraints are imposed as the material must be transparent (for light transmission) and permeable (for nutrients and gases) in addition of being biocompatible and resistant (Lebeau & Robert, 2006). Natural polymers as agar, carrageenan, agarose, chitin or alginate are used (Moreno-Garrido, 2008). Synthetic carriers used can be acrylamide, polyurethane, polyvinyl or resins (de-Bashan & Bashan, 2010; Vasilieva et al., 2016). To entrap cells in these materials, physical (temperature change) or chemical (cross-linking with multivalent cations) methods of polymerization exist (de-Bashan & Bashan, 2010). They must give as less stress as possible to cells in terms of toxicity, pH and temperature (Lebeau & Robert, 2006). Alginate, which is widespread for encapsulation processes, is used in the present thesis as described in section 1.2.3.2.2.

In order to gain benefits on both characteristics, composite carriers made from organic and inorganic materials can also be developed. They can exploit mechanical strength of inorganic material and biocompatibility and diffusivity of organic carrier (Desmet et al., 2014), which can lead to a better growth inside the material than with an organic carrier only (L. Zhou et al., 2010). However, the material preparation and encapsulation process are more complex which make them more difficult to scale-up or mass produce.

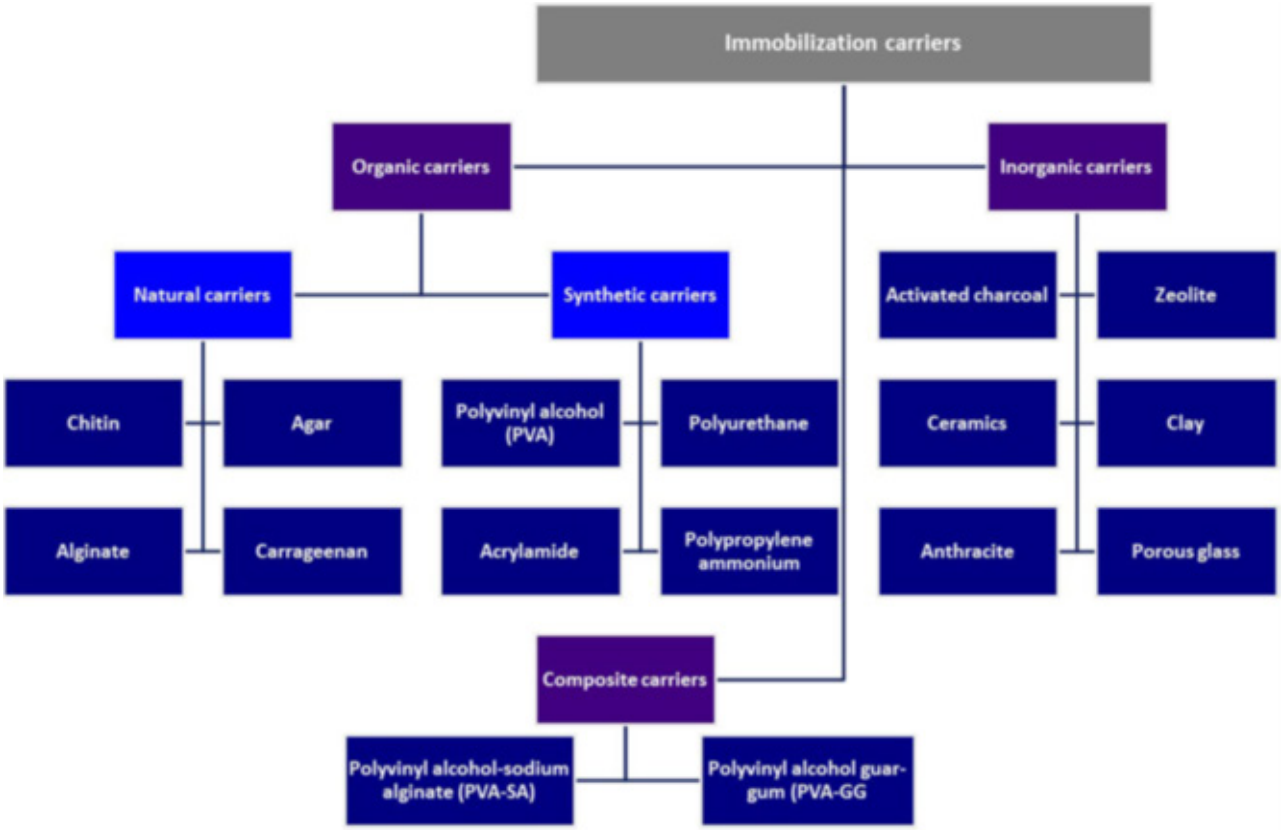

Figure 1.7 – Description of different carriers which can be used for microalgae immobilization. Reproduced from (Bouabidi et al., 2019) *with authorization.*

1.2.3.2 Encapsulation

1.2.3.2.1 Benefits and bottlenecks

Encapsulation of microalgae presents several advantages. As all immobilization methods, encapsulation enables to increase local biomass concentration and facilitates harvesting step of the microalgae

production (de-Bashan & Bashan, 2010; Vasilieva et al., 2016). Indeed, only a coarse filter is needed to separate algae from the culture medium while costly and energy consuming methods are needed for suspended free cell cultures (section 1.2.2.3). Recovered biomass can then be valorized as usual. An easier manipulation of the biomass is possible as well, as microscopic cells are not easy to manipulate compared to beads of a few millimeters. Encapsulation also enables to cultivate genetically modified strain without a risk of spreading in the environment. In case of vessel breakage, beads can be safely collected.

Encapsulation also enables to work more easily with a continuous process (Bayat et al., 2015). The culture medium can be replaced without algae renewal. Encapsulation enables to reuse cells without any cell wash-out (Lebeau & Robert, 2006). It allows to recover high-added value metabolites in the culture medium as well, if they are secreted extracellularly by the cells (Figure 1.8). In the latter case, metabolites have thus to pass through two barriers: cell and encapsulation matrix. The extracellular secretion allows to prevent extraction of the metabolite from the cell while encapsulation enables to avoid the harvesting step. The product can then be recovered in the culture medium using an adequate separation technique (a membrane for example). In the case of luciferase, ultrafiltration cassettes have been successfully used to concentrate the metabolite.

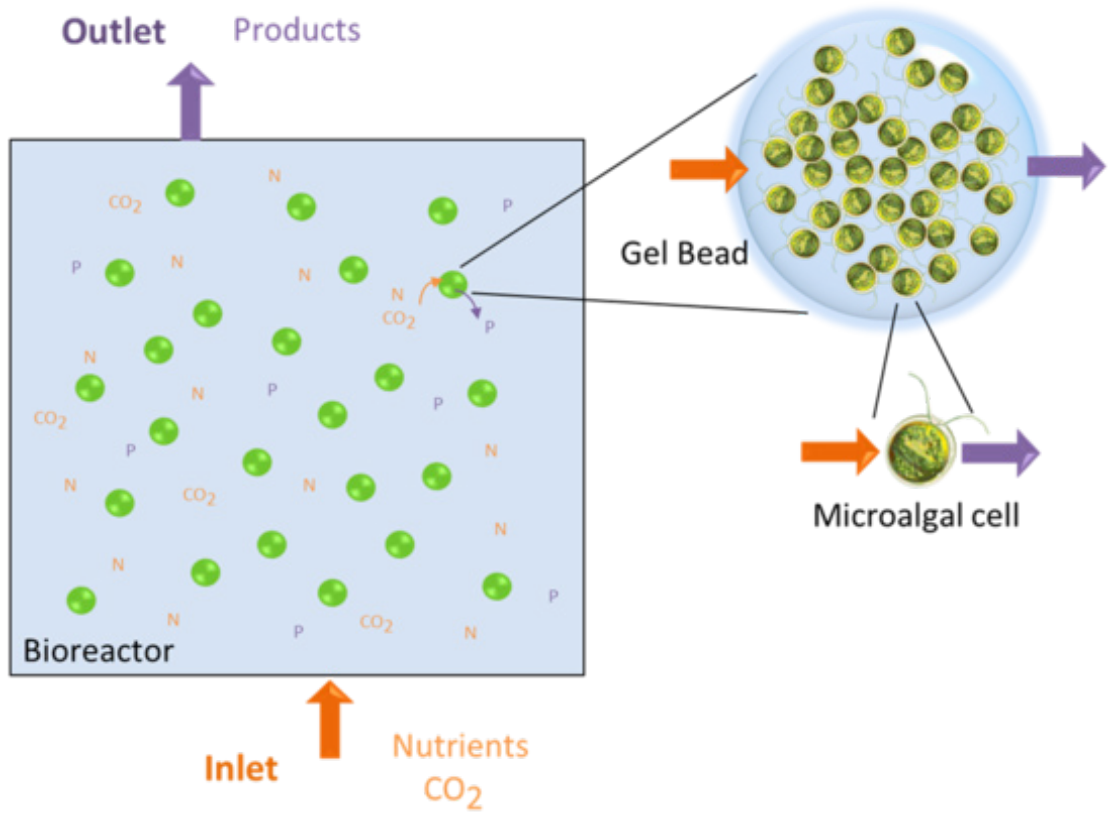

Figure 1.8 – Schematic representation of continuous process involving encapsulated microalgae to produce high-added value metabolite, secreted extracellularly by the cell.

Besides, encapsulation matrix preserves cells from different external unfavorable conditions. It attenuates sudden changes of temperature and pH (Vasilieva et al., 2016). It protects cells from shear stress which allows to cultivate fragile strains (Bayat et al., 2015). Moreover, the encapsulation shell decreases the risk of contamination, especially in the bead, in the direct vicinity of algae, even if the culture medium is contaminated (Vílchez et al., 1997).

Encapsulation enables to co-immobilize several species which have symbiotic relationship. It can be bacteria which favorize directly microalgae growth or enhance oxygen supply through the encapsulation material (Chevalier & de la Noüe, 1988; Gonzalez & Bashan, 2000).

In the context of the ValoAlgue project, encapsulation has several advantages using *Chlamydomonas reinhardtii* strain modified to secrete *Gaussia* luciferase. It allows to protect the fragile strain (which lacks a cell wall (Lauersen, Berger, et al., 2013) and to prevent the spread in the environment of this genetically modified strain. Moreover, luciferase secreted extracellularly by the cells can be recovered in the culture medium.

The positive and negative impacts of encapsulation on growth and metabolites secretion is described in chapter 2. They mostly depend on the strain and secretion strategy thus no systematic advantage or drawback can be highlighted.

One drawback of encapsulation is the high cost of the polymer (Vasilieva et al., 2016). Even if alginate is considered as less expensive than other polymers (de-Bashan & Bashan, 2010), the economic feasibility of the process must be calculated. Moreover, a fast and reliable method of encapsulation at large scale must still be developed. The method must be reproducible and able to produce at large scale under sterile conditions. Research on encapsulation material is needed to improve diffusion rates and mechanical strength. Moreover, the material must be optimized depending on the strain and application.

These reasons lead to poor knowledge on encapsulation at large scale. There are few existing systems as described in section 1.2.3.3. They are mostly focused on a rather small scale (1 L).

1.2.3.2.2 Method

In many applications, sodium alginate is used to encapsulate the algal strain. Alginate is a polysaccharide made from brown macroalgae formed with mannuronate and guluronate monomers. It has several advantages: transparent, permeable, biocompatible, easy to handle, safe for human and an abundant feedstock (de-Bashan & Bashan, 2010; Moreno-Garrido, 2008). The immobilization process does not require extreme conditions for cells as high temperature or pH (Lebeau & Robert, 2006; Moreno-Garrido, 2008). On the other hand, alginate composition is dependent on the algae origin, which can lead to reproducibility issues. Furthermore, it can be degraded by some contaminants or sea water (de-Bashan & Bashan, 2010; Vasilieva et al., 2016).

To form beads, the most common method is to cross-link alginate in bivalent cation solution to solidify the shell (Figure 1.9). The mixture of alginate and microalgae is dropped through a needle to form beads. Beads must stay in the reticulation solution a certain period of time before being rinsed and placed in culture medium.

The bead diameter must be low enough to allow a good light access and nutrient transfer. But smaller beads are more fragile. Hence a compromise must be made for the size of the beads. Beads size and shape depends on a lot of parameters: needle diameter, needle height, flow speed through the needle, alginate concentration, duration of reticulation, reticulation solution concentration, …. Operating parameters are usually set to obtained beads from 2 mm to 3 mm. The mechanical strength of beads increases with the reticulation time and solution concentration, but bead porosity decreases leading to lower mass transfer with the culture medium (de-Bashan & Bashan, 2010). This last step must then be optimized depending on the alginate and the application.

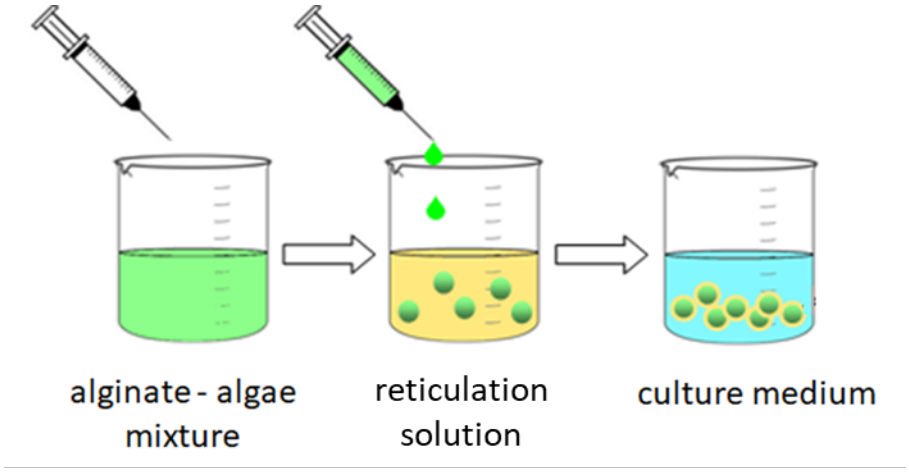

Figure 1.9 – General description of bead formation by cross-linking: alginate is dropped in reticulation solution.

To scale-up the production of alginate beads, as manual production is time consuming, several automatic methods can be used to produce several beads at a time. A multinozzle system based on laminar jet break-up caused by vibration, has been designed by (Brandenberger & Widmer, 1998). The production occurs under sterile conditions and can produce up to 5 $L.h^{-1}$. Another system was developed using a showerhead box containing several apertures (de-Bashan & Bashan, 2010). Beads are formed when passing apertures using gravity and the system produces 6 $L.h^{-1}$. A last method was used to produce microbeads (100-200 µm) by low pressure spraying through a nozzle (Bashan et al., 2002).

1.2.3.3 Photobioreactors for encapsulated algae culture

Few studies are dealing with the culture of encapsulated microalgae at a pilot scale. Different reactor types can be used: fluidized bed, packed bed, parallel-plate bioreactors and air-lift bioreactors (Mallick, 2002). A fluidized bed reactor enhances carbon dioxide diffusion within solids and thus is particularly appropriate for the culture of immobilized microalgae (Jaycor, 1985). Light supply is better in a fluidized bed reactor than in a packed bed. However, it must be considered that the flow rate monitoring of fluidized bed is difficult because of bead density evolution due to microalgae growth (Jaycor, 1985).

Most study obtained better results using a fluidized bed reactor than in other types of reactors. Regarding growth, Cheirsilp et al., 2017 obtained similar growth rate for encapsulated *Nannochloropsis sp.* cultivated in fluidized bed and free culture. Fluidized bed reactors gave higher metabolites production as well. A better marennine (pigment of interest) production yield has been obtained using a fluidized bed than a tubular reactor from the strain *Haslea ostrearia* (Lebeau et al., 2002). Ross & Pott, 2021 shows a higher production of hydrogen, secreted by Rhodopseudomonas palustris, using a fluidized bed than using a packed bed or free culture. Finally, from a bioremediation point a view, Travieso et al., 1992 shows a better COD removal and nutrient uptake using a fluidized bed reactor of 1 L than a packed bed. In both previous references, the same beads are used in the fluidized than in the packed bed reactor. As fluidized bed reactors have given better results in several cases, a fluidized bed reactor has been chosen in this thesis to cultivate encapsulated microalgae in the form of beads as this type of reactor seems to enhance light supply and nutrients transfer. Most designs use gas to fluidize beads of encapsulated algae (Figure 1.10 a b). In this thesis, it has been chosen to use a solid-liquid photobioreactor. The gas-liquid exchanges take place in a column installed outside the reactor, in the external loop. Ross & Pott, 2021 cultivated encapsulated algae in this kind of reactors as well (Figure

1.10 c). Concerning the shape of the photobioreactor itself, its design is unusual: a rectangular column divided by a central panel, which improves bead recirculation and their renewal near walls (chapter 2).

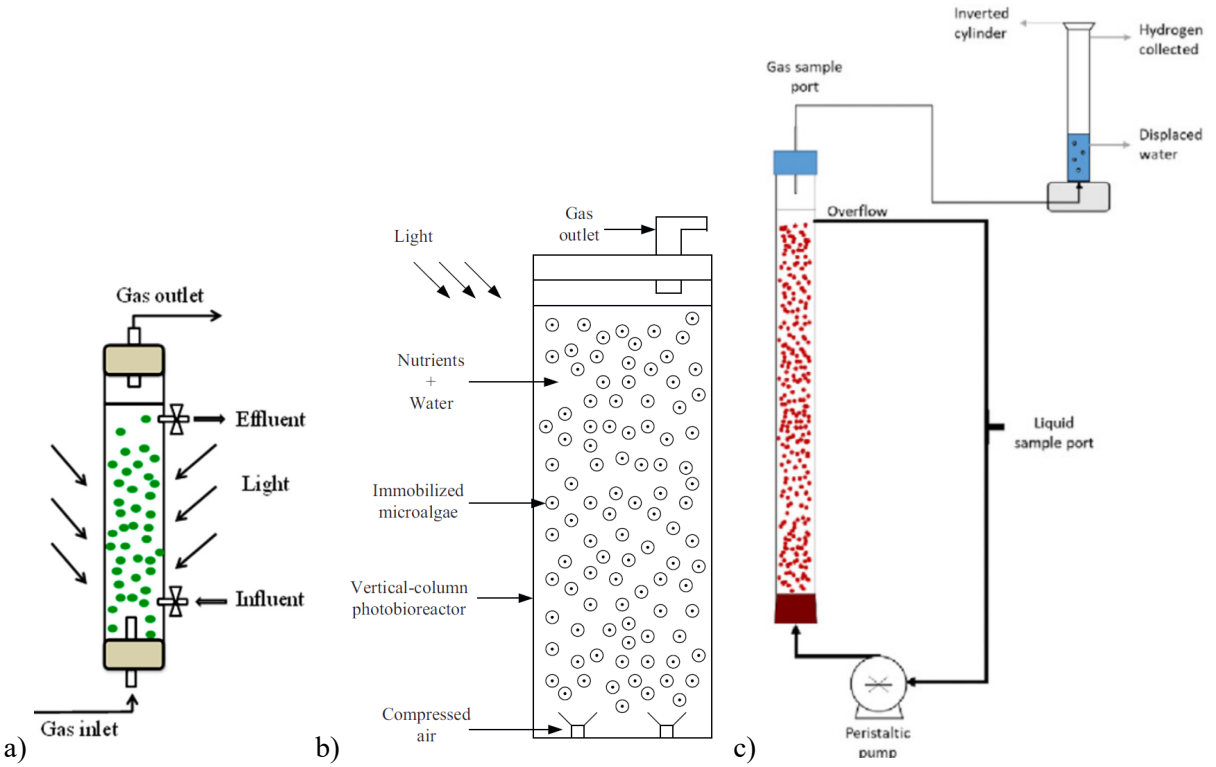

Figure 1.10 – Examples of fluidized bed reactors used for the culture of encapsulated microalgae in the literature. Reproduced from a) (Cheirsilp et al., 2017)*, b)* (Lam & Lee, 2012)*, c)* (Ross & Pott, 2021) *with authorizations.*

1.3 Commercial applications of microalgae

Microalgal culture for commercial purposes began in the 1960s. The market grows over the years to become a significant industry mostly in Asia, USA and Australia (Spolaore et al., 2006). In 2004, between 7 000 and 10 000 tons of dry matter were produced each year, which represents more than 4.5 billion US dollars (Person, 2011). In 2010, 10 000 tons of dry matter were produced (Person, 2011).

Nowadays, *Arthrospira* (*Spirulina*), *Chlorella* and *Dunaliella* are the most cultivated species (Milledge, 2011). They grow rapidly and in extreme conditions (high pH, nutrient-rich media or high salinity) which avoid contaminations even in open systems (Milledge, 2011). They are mostly marketed for human and animal nutrition and cosmetics (Table 1.1). However, the huge diversity of microalgae and the development of closed systems open opportunities for microalgae in a wide range of commercial applications.

Table 1.1– Microalgal production in 2004. Reproduced from (Spolaore et al., 2006) *with authorization.*

Alga	Annual production	Commercial applications
Arthrospira	3000 tons/year	Human and animal nutrition, cosmetics, phycobiliproteins
Chlorella	2000 tons/year	Human nutrition, aquaculture, cosmetics
Dunaliella salina	1200 tons/year	Human nutrition, cosmetics, β-carotene (pigment)
Aphanizomenon flos-aquae	500 tons/year	Human nutrition
Haematococcus pluvialis	300 tons/year	Aquaculture, astaxanthin (pigment)

1.3.1 Nutrition

Some microalgae (*Arthrospira* (*Spirulina*), *Chlorella, Dunaliella,* …) are used as human food due to their very high protein and nutritive value content (vitamins, enzymes, fibers, …) (Priyadarshani & Rath, 2012). They can be consumed as fresh paste but, most of the time, are sold as powders, tablets or capsules. Microalgae can be considered as nutraceutical or functional food source. It refers to food which have positive effects on the body (Borowitzka, 2013).

Furthermore, due to their high contents in pigments (as carotenoids), algae are used as food colorants, boosted by the increasing demand for natural colorants (Priyadarshani & Rath, 2012).

Microalgae may also be used to feed animals. They are particularly used in aquaculture as live feed for larvae, young fish or zooplankton used to feed bigger fish. They also have a role as natural orange pigment for prawns and salmons (Priyadarshani & Rath, 2012). They can be used to feed farming animals (cow, poultry, …) or pets (dog, cats, ...) (Bahadur et al., 2015).

1.3.2 Energy

Due to their high lipids and polysaccharides content, microalgae can be used to produce biofuels (Bahadar & Bilal Khan, 2013). Biofuels produced from algae are referred to as third generation biofuels. Unlike first generation biofuels, they do not compete with arable lands. Moreover, particularly using vertical bioreactors, they require less land than plant crops to produce the same amount of fuel (Mata et al., 2010).
Different biofuels can be synthetized from microalgae (Bahadar & Bilal Khan, 2013). High lipids content (50 - 70 %) of some microalgae (*Chlorella*, *Botryococcus braunii, Schizochytrium, …*) dedicate them to produce biodiesel by transesterification. Besides, carbohydrates contained in algae (*Chlorella protothecoides, Chlorococcum, Spirogyra, …*) can be used to produce bioethanol by fermentation. *Chlamydomonas reinhardtii* and some cyanobacteria can produce biohydrogen by biophotolysis: photolyzing water using solar energy and enzymes. Algae can also be used to produce methane by anaerobic digestion.

1.3.3 Environmental applications

Microalgae (*Platymonas subcordiformis, Caulerpa, Dunaliella salina, Oscillatoria*, …) can be used for bioremediation of polluted soils. Their high capacity to absorb heavy metals such as lead, cadmium or mercury allows to treat soils polluted by industries (plastic manufacturing, battery production, or smelting industries) (Bahadur et al., 2015). They can also be used to capture CO_2 released from fossil fuel power plant gas effluents (Klinthong et al., 2015).

Moreover, it is possible to treat wastewater using microalgae (*Chlorella, Ankistrodesmus*, *Scenedesmus*, …). They consume nitrates, phosphates and biotransforme xenobiotics contained in wastewater (Bahadur et al., 2015). Microalgae also remove coliform bacteria and reduce Chemical or Biochemical Oxygen Demand in autotrophic, as well as mixotrophic or heterotrophic mode (Abdel-Raouf et al., 2012). The biomass produced treating wastewater can be valorized in almost all sectors (energy, high-added compounds, …) except nutrition.

1.3.4 High-added value compounds

Some microalgae (*Dunaliella, Haematococcus, Spirulina, Porphyridium, Rhodella*, *Crypthecodinium,* …) produce secondary metabolites which can be high-added value compounds used in cosmetical or pharmaceutical industries. They can secrete pigments: carotenoids (β-carotene, astaxanthin, …), phycobiliproteins (phycocyanin, phycoerythrin), or polyunsaturated fatty acids (omega 3) which can be valued in cosmetical or pharmaceutical industries for their properties (Bahadur et al., 2015; Borowitzka, 2013; Milledge, 2011). Their properties: antioxidant, antiaging, anti-irritant, regenerant… are attractive in skin or hair care products. Some amino acids produced by algae (*Ankistrodesmus spiralis, Chlorella, Dunaliella tertiolecta*, …) to protect themselves from UV are also used in sunscreens (Priyadarshani & Rath, 2012). Others diverse properties interest pharmaceutical industry: antibacterial, antifungal and antiviral activity; anti-inflammatory, anti-hypotensive and prevent cardiovascular disorders, cancer, type 2 diabetes, depression or schizophrenia (Priyadarshani & Rath, 2012). However, further studies must confirm these properties (Bahadur et al., 2015). Proteins secreted by algae can be valuable as therapeutic cells (1.3.7).

Cyanobacteria, green algae or diatoms can also synthetize gold or silver nanoparticles from these metal salts by bioreduction (Lengke et al., 2006). This synthesis is less expansive and decreases environmental impact of current processes used to synthetize metallic nanoparticles (Bahadur et al., 2015).

1.3.5 Microalgal culture profitability

Microalgae are thus a promising raw material for numerous applications. Several have been discussed but microalgae can also be employed as biofertilizer or biostimulant (Dineshkumar et al., 2018; Garcia-Gonzalez & Sommerfeld, 2016) and to produce biomaterials (Cinar et al., 2020). However, as a new feedstock mainly under research stage, the profitability of microalgae industrialization is discussed.

It must be noticed that profitability depends on several factors: location of the plant which have an impact on temperature, light supply and employing labor costs; cultivation process; cost of the existing method of production (Borowitzka, 2013; Ruiz et al., 2016). Nowadays, high-added value metabolites or food market can be profitable (Ruiz et al., 2016) but biomaterials or biofuels market are not yet competitive (Bahadar & Bilal Khan, 2013; Mata et al., 2014; Milledge, 2011). However, as larger markets, economies of scale will help to make them profitable. It must be noticed that biofuels market is highly dependent on crude oil price (Bahadar & Bilal Khan, 2013; Borowitzka, 2013) and thus on its availability. The biorefinery concept, which consists in exploiting all marketable fractions of

microalgae, will play a role to make microalgae culture profitable (Bravo-Fritz et al., 2016). The microalgae market will thus change as production costs will decrease with the help of research (Figure 1.11). Biofuels and green chemistry could be profitable in several years but in the short term, high-added value compounds are a more realistic market for microalgae. Progresses in cell engineering will allow to enhance secretion of metabolites by strains. Besides, improvements on cultivation processes (photobioreactor and raceways) are needed as well to decrease the processes costs.

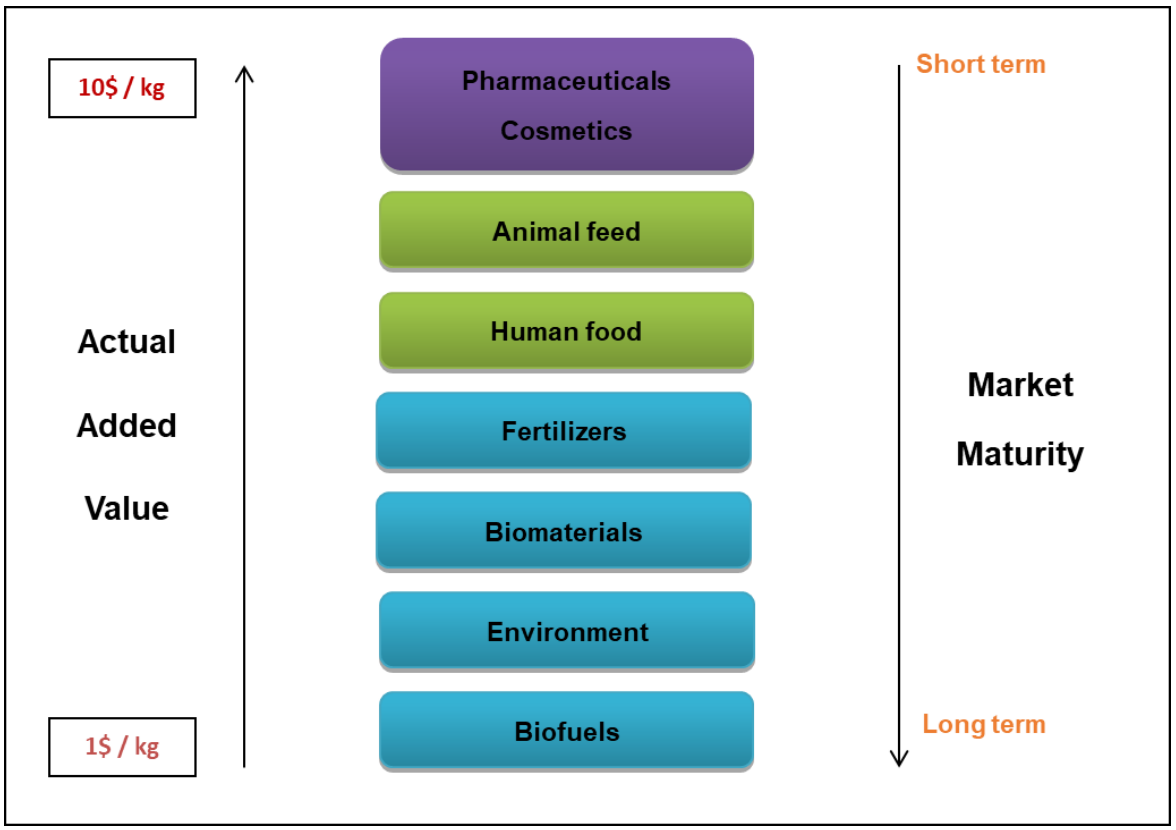

Figure 1.11 - Microalgae profitability according to commercial application. Adapted from (Person, 2011).

1.3.6 Commercial applications of encapsulated microalgae

Among all commercial applications (1.3), the most common one for immobilized algae is wastewater treatment (Praveen & Loh, 2015; Ruiz-Marin et al., 2010; Whitton et al., 2019; Zamani et al., 2012). Encapsulated microalgae are used to biocapture nutrients as well as heavy metals. Different encapsulation advantages are favorable for wastewater treatment: higher resistance to contaminants, easy separation, higher mechanical resistance, possibility to use continuous process without problem of cell washout and co-immobilization (de-Bashan & Bashan, 2010; Mallick, 2002; Vasilieva et al., 2016).

The production of high-added value metabolites is also widespread. It can be intracellularly or extracellularly secreted metabolites to enables continuous recovery of metabolites. This is the targeted application of this thesis therefore a literature review is available in chapter 2.

Encapsulated microalgae are used to produce energy as well, mainly hydrogen (Brouers & Hall, 1986; Homburg, Venkanna, et al., 2019; Stojkovic et al., 2015). Immobilization enables to increase hydrogen production of cells. Cell reuse and continuous process facilitated by encapsulation are advantageous for biohydrogen production by microalgae.

Finally, encapsulation is used for culture handling of microalgae. It allows to store microalgae for a longer time than free cells. Different studies reported high cell viability after storage in darkness and at low temperature, even after several years (Benson et al., 2018; Y.-C. Chen, 2001; Romo & Perez-Martinez, 1997). This enables to save time and costs for culture collection handling (Lebeau & Robert, 2006; Moreno-Garrido, 2008)

The long conservation of immobilized microalgae allows to use it as biosensor or bioassay to detect low dose of molecule and its toxicity (Naessens et al., 1999; Shitanda et al., 2005; Védrine et al., 2003). It is usually based on photosynthetic activity, measuring fluorescence of chlorophyl or oxygen. It is particularly interesting to use immobilized cell to transport it or to perform a continuous test.

1.3.7 Context of the project: recombinant proteins

Recombinant proteins are proteins produced by genetically modified cells. They result from the expression of recombinant DNA. Genome of microalgae can be easily manipulated to produce proteins, particularly in chloroplasts of green algae (Gimpel et al., 2015). *Chlamydomonas reinhardtii* has been used most of the times, as its genome is entirely known and several molecular toolkits exist (Gong et al., 2011).

Recombinant proteins are used as industrial enzymes and therapeutic cells: antibodies or vaccines (Barrera & Mayfield, 2013). The market of recombinant proteins represents 100 billion dollars every year (Barrera & Mayfield, 2013). They are nowadays produced by mammalian cells or bacteria. There are several benefits of using microalgae to produce these kinds of proteins. They grow fast and at low-cost compared to the cells currently used (Gimpel et al., 2015). They can grow autotrophically or heterotrophically, in close systems which avoid spread in the environment (Gong et al., 2011). Finally, microalgae are generally edible which facilitates the ingestion of therapeutic cells by humans (Gong et al., 2011). However, some bottlenecks on recombinant protein commercialization remain. The most commercialized microalgal strains, which easily grow and are well characterized, have not been used to produce recombinant proteins. Expression levels of protein by algae can be low, and proteins must be stable once secreted (de Grahl et al., 2020; Gong et al., 2011). Besides, more studies on recombinant proteins secreted by algae are needed before they are allowed for human consumption.

Although microalgae are not yet commercially cultivated to produce recombinant proteins, they are a promising source of these high-added value metabolites. This is the reason why the ValoAlgue project is dedicated to this subject, with a *Chlamydomonas reinhardtii* strain able to secrete extracellularly *Gaussia* luciferase (chapter 2) (Lauersen, Berger, et al., 2013). Moreover, recombinant proteins production is particularly indicated to be produced by encapsulated cells as explained in section 1.2.3.2.1.

1.4 Characterization and modeling of photobioreactors

Microalgal growth and metabolite production depend on numerous parameters: light, pH, temperature, nutrients... In photobioreactor, most of them can be controlled: pH is often regulated by air-CO_2 injection, a system of temperature regulation is implemented, and an excess of nutrients is provided. Among all growth factors, light is the most difficult to control due to shelf-shading of microalgae. This is the reason why photobioreactor models focus mainly on light modeling. Nutrient consumption is sometimes modeled as well but is not considered in this thesis as a large excess of nutrients was used.

As growth depends on light received by algae, the model must consider the light input truly experienced by cells. This is possible by modeling hydrodynamics which governs bead circulation in the

photobioreactor and coupling it with an attenuation light law, which describes light distribution in the photobioreactor (as a function of biomass concentration). Hence, a global photobioreactor model can be built using a hydrodynamic, light attenuation and biological model to predict microalgal growth (Figure 1.12).

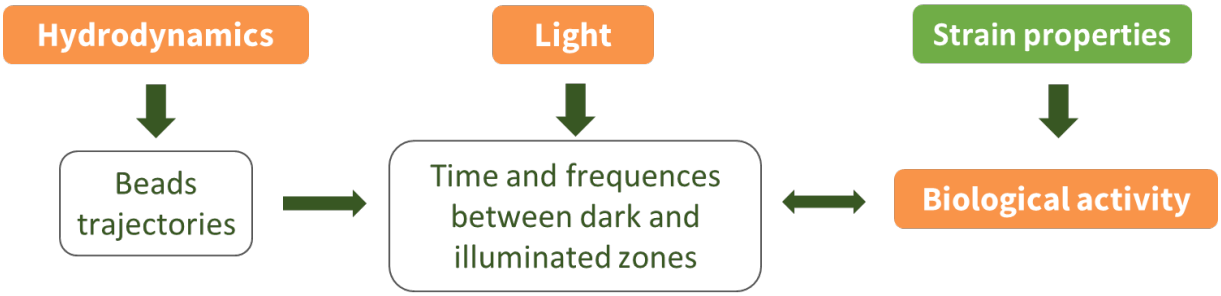

Figure 1.12 – Interactions between hydrodynamics, light and biological activity of microalgae in photobioreactors.

1.4.1 Light

1.4.1.1 Light characterization

1.4.1.1.1 Definitions

Light can be described with photometry or radiometry. Photometry, using lumen or candela as units, has been created to adapt to human eye with a non-linear response to light wavelength. This is the reason why radiometric units (as watt) are more adapted for microalgae (Legrand, 2016). Irradiance ($W.m^{-2}$), which is light power per unit area, is often used to describe light input on photobioreactors.

Microalgae absorb photons in a spectral range called Photosynthetically Active Radiation (PAR) between 400 and 700 nm. To describe the light used by microorganisms, mole of photons (corresponding to Einsteins) unit is more often used than watt (1 J approximately equals to 4.6 μmol_{ph}). Hence the photon flux density (PFD) in $\mu mol_{ph}.m^{-2}.s^{-1}$ or in $\mu E.m^{-2}.s^{-1}$ (used in this thesis) is employed to describe light intensity at the reactor surface. PAR probes are dedicated to measure the light intensity in the PAR range and directly gives results in $\mu E.m^{-2}.s^{-1}$. Another parameter used to quantify light utilization by microalgae is the photosynthetic efficiency which describes the percent of energy stored as biomass produced per unit of light energy absorbed.

1.4.1.1.2 Light transmission in a photobioreactor

The energy at the reactor surface (PFD) is different from the available energy inside the reactor (Souliès, 2014). Indeed, the light passing through a microalgae culture will be absorbed, refracted and reflected (Figure 1.13). The sum of refracted and reflected beams, which is called scattering, is transmitted to the other cells (Legrand, 2016). Absorption is described by a specific light absorption coefficient which depends on the cell's pigmentation. However, microalgae can change their pigmentation according to light by a process called photoacclimation. Therefore, microalgae which are low-light acclimated will have a higher specific light absorption coefficient than high-light acclimated cells (Legrand, 2016).

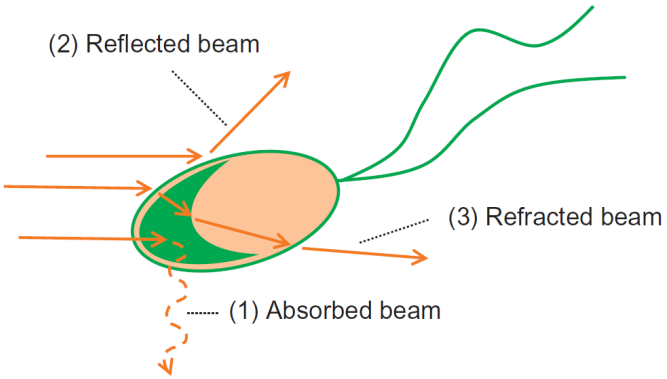

Figure 1.13 - Light deflection by a microalgal cell. Reproduced from (Legrand, 2016) *with authorization.*

There is thus a light gradient inside a photobioreactor due to microalgae absorption and scattering. There is a zone close to the reactor surface which is highly illuminated and potentially a dark zone where the light cannot penetrate. The boundary between illuminated and dark zones is fixed arbitrarily. Janssen et al., 2003 defines the illuminated zone as "the depth at which 90 % of the incoming photon flux is absorbed" while Souliès, 2014 defines it as the zone where photosynthetic reactions are predominant compared with respiration. The system must be optimized, providing enough light without losing energy if light input is increased and some light is not used by cells.

Moreover, light input can only be increased to a certain point because microalgae cells can also be damaged by a strong light. This phenomenon is called photoinhibition. It describes the excess of light which affects reaction center proteins situated in the photosystem units (Legrand, 2016). This is why in case of excessive light input in the photobioreactor, microalgal growth can decrease or this can cause cells death in worth cases. Hence there is a balance to obtain the fastest growth as possible without damaging the cells and optimizing energy input. In any case, the most economical and sustainable solution is to use sunlight but this leads to highly unpredictable and potentially inadequate light input.

1.4.1.2 Light distribution modeling

Some models describe outdoor photobioreactors thus characterize natural sunlight depending on time of the day and geographical position. This is not discussed in this thesis as an artificial source of light (LED) is used. Moreover, the alternation of day and night (which should not be confused with light/dark cycles inside the reactor that are discussed afterwards) is not taken into account as a permanent illumination is used to facilitate modeling.

1.4.1.2.1 Beer-Lambert law

Beer-Lambert law may be used to model light attenuation in the PBR. It predicts an exponential decrease of light with depth in the culture depending on the biomass concentration and the specific light absorption coefficient (Figure 1.14). It is based on three assumptions: the light beams are unidirectional, the light is monochromatic, and scattering is negligible compared to absorption (Acién Fernández et al., 1997).

$$I(x) = I_0 . e^{-(\varepsilon_b . C_x + \varepsilon_w) . y} \qquad \textit{(Equation 1.1)}$$

with I the light intensity, I_0 the light intensity at the reactor surface, y the distance to the reactor surface, C_x the biomass concentration (dry weight), ε_b the absorption coefficient of the biomass, ε_w the absorption coefficient of the water.

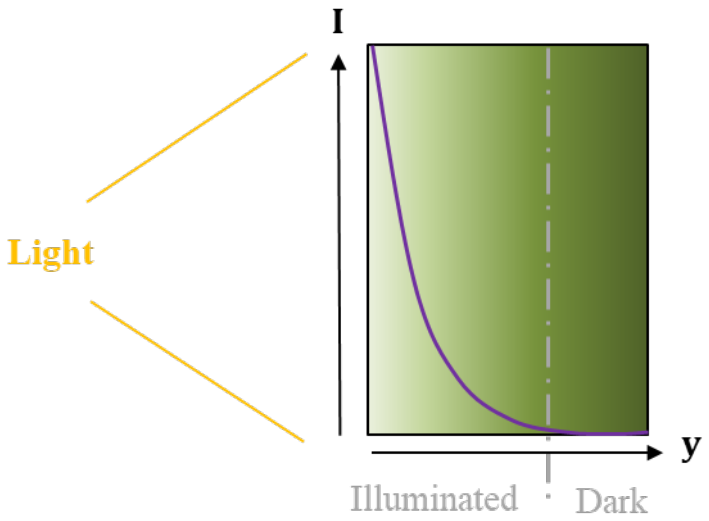

Figure 1.14 - Schematic light attenuation in a depth of a photobioreactor.

Due to its simplicity, Beer-Lambert law (Equation 1.1) is often used to describe the light attenuation in photobioreactors (Souliès, 2014). However, because the scattering effect in dense culture is not always negligible compared to absorption, enhanced models have been developed.

1.4.1.2.2 Extensive models

A widely used model which takes absorption and scattering into account is the Radiative Transfer Equation (RTE) which is a simplification of the Boltzmann transport equation (Legrand, 2016). This equation can be solved by Monte Carlo method (stochastic method) which is time consuming (Souliès, 2014). In RTE basic equation, absorption is considered uniform in the culture while it depends on cells pigmentation (Souliès, 2014). A model has also been developed to take cells pigmentation into account (Murphy & Berberoğlu, 2011).

While RTE uses a mesoscopic point of view, attenuation models have been developed in a macroscopic point of view. The first method integrates RTE in all propagation directions to get a diffusion equation. This is possible using an approximation on luminance angular distribution which is called P1 approximation. Nevertheless, this model does not fit well with a collimated source.

A simple macroscopic model (called two-flux model) has been developed which proposed that light absorption and scattering are described with two independent coefficients in Beer-Lambert law (Figure 1.15) (Cornet et al., 1995). It is based on unidirectional light attenuation and is a good compromise between accurate results and a short calculation time (Takache, 2010).

Any of these models is used in this thesis as explained in section 1.4.1.2.3.

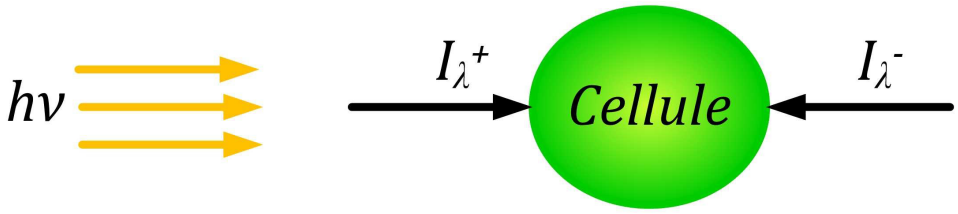

Figure 1.15 – Schematic representation of two-flux model. Reproduced from (Takache, 2010).

1.4.1.2.3 Light transmission through encapsulated microalgae

The absorption and scattering effects in encapsulated microalgae culture are different than in free microalgae culture. Indeed the model should take into account the absorption and scattering due to the encapsulation matrix in addition to the algae absorption and scattering (Figure 1.16). Moreover, the spatial distribution of encapsulated algae compared to free algae is different. Due to the complexity of the system, only absorption is considered and Beer-Lambert law, with adapted attenuation coefficient (5.2.2.2), is used in this thesis.

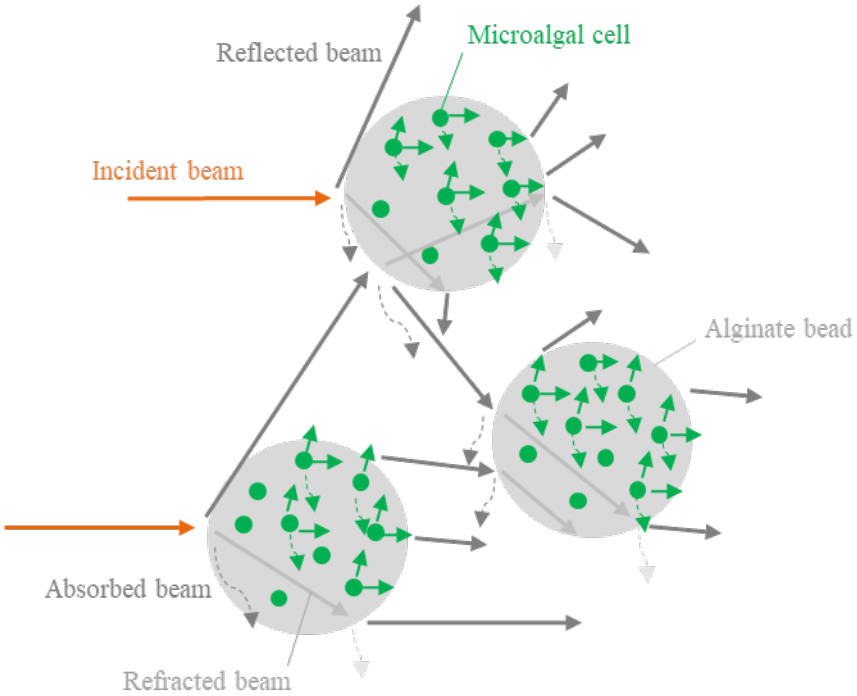

Figure 1.16 - Schematic representation of light attenuation through microalgae encapsulated in alginate beads.

1.4.1.3 Light/dark cycles

According to Molina Grima et al., 1999, the time algae cells spend in illuminated and dark zones is not sufficient to quantify a photobioreactor productivity, but the frequencies at which the cells go from an illuminated to a dark zone must be taken into account. These are called light/dark cycles (L/D cycles). As L/D cycles are due to renewal of cells in the reactor walls, the L/D cycle depends on superficial liquid velocities in the reactor.

A positive effect (called “flashing light effect”) of L/D cycle on photosynthetic efficiency has been found over the years on different species. Different strategies have been elaborated to experimentally study the flashing light effect. Average frequencies of L/D cycles have been estimated based on liquid flow in different geometries (Janssen et al., 2003). Another way of studying L/D cycles is to induce frequencies by different methods: using flashing LEDs (Matthijs et al., 1996) or by periodically shading parts of the reactor (Liao et al., 2014). The best results were found for the shorter L/D cycles in any case (frequencies higher than 1 Hz). A biological explanation of the positive impact of flashing light effect could be that photons utilization by cells is not instantaneous (Takache, 2010). During a short period, more photons are absorbed but cannot be used by the cells. As a consequence, under continuous illumination, some photons are lost. L/D cycles can thus enable to reduce the energy consumption. Flashing light effect can also have a positive impact on secretion of metabolites such as proteins, fatty acids or pigments (Lima et al., 2021). One should notice that some studies did not find any positive influence of flashing light effect on growth for some species (Schulze et al., 2020). Moreover, frequencies truly experienced by the cells are complex to measure and a favorable impact of increasing velocities can also be due to better transport processes (Takache, 2010).

However, frequencies of L/D cycles experienced by cells in photobioreactor are lower than 1 Hz most of the time. The influence of medium-duration L/D cycles on growth has been studied experimentally on *Chlamydomonas reinhardtii*. Janssen et al., 2000 measured a lower photosynthetic activity under L/D cycles between 6 and 25 s than with continuous illumination. Takache et al., 2015 measured a positive impact of L/D cycles under 12 s (they suggest L/D cycles influence pigment content which influences growth). The influence of medium-duration L/D cycles on growth thus remains unclear.

The influence of L/D cycles on growth has also been studied using models. Under intermittent light, growth rate can be calculated by two asymptotic approaches. On the one hand, the full integration approach suggests cells does not take into account fluctuating light and growth rate can be calculated with a mean light intensity. On the other hand, the approach without integration considers cells instantaneously detect and adapt to light variations. The approach depends on the light intensity and the frequencies of cycles. Takache, 2010 suggests *Chlamydomonas reinhardtii* follows an instantaneous adaptation approach for cycles higher than 40 s. However, for L/D cycles under 12 s, they measured an algae response following a partial integration, i.e. between the two asymptotic approaches. Hence the global growth rate cannot be directly predicted. Gernigon et al., 2019 introduced a Damköhler number (Equation 1.2) which is the ratio of the characteristic times of biological response (τ_{bio}) and light fluctuations (τ_I).

$$Da = \frac{\tau_{bio}}{\tau_I} \qquad \textit{(Equation 1.2)}$$

If Da << 1, the approach without integration must be used, while if Da >>1, the full integration method is used to describe growth. Photobioreactors in which cells experience cycles of a few minutes lead to Da ≈ 1, which suggest a partial integration. As the characteristic time of light fluctuations depends on light distribution and hydrodynamics, the coupling between flow and light must be studied in this case.

1.4.2 Hydrodynamics

Studying hydrodynamics is particularly important in bioreactors as it influences the microenvironment experienced by cells. Especially, hydrodynamics of a photobioreactor plays a leading role as it has an impact on growth through several factors. It influences mixing and may thus prevent or not the development of temperature or nutrients gradients. These can have a negative impact on cells. Mixing also has a direct impact on mass transfer as mass transfer coefficients depend, among others, on agitation rate (Bitog et al., 2011). Finally, hydrodynamics has a direct impact on light access for cells. The time

a cell spends in an illuminated zone is directly correlated to velocity fields within the reactor. Moreover, flow motion determines the frequencies cells pass through illuminated and dark zones, i.e. L/D cycles (as mentioned in section 1.4.1.3). Hence, mixing must be sufficient to allow a good mass transfer and a high enough cell turnover in the light zone. But it must be optimized to reduce energy input and keep low shear stress.

Computational Fluid Dynamics (CFD) is widely used to model hydrodynamics in photobioreactors (Bitog et al., 2011; Pires et al., 2017). The method consists in dividing the reactor in a high number of elements called cells, according to its geometry. It calculates then fluid flow motions based on the resolution of Navier Stokes equations inside each cell. A mesh optimization must be performed to balance calculation time and accuracy of the results. In any case, this numerical tool enables to save costs and time needed for experimental work. It is advised though to perform an experimental validation of a base case, especially for unusual geometries, to verify the abilities of CFD model to reflect reality. To this end, several experimental methods exist as Particle Image Velocimetry (PIV) used in this thesis (chapter 3). CFD may be used to improve and optimize reactors design. One of the best examples is that it can be used to detect dead zones in a reactor. In the case of photobioreactors, it has enabled to optimize gas bubbling (Huang et al., 2010) or mixing (Pruvost et al., 2006).

Standard photobioreactors (to cultivate free algae cultures), as air lift or tubular reactors, imply most of the time gas-liquid simulations (X. Gao et al., 2018). This requires studying gas bubbles size and light transfer through the bubbles. In this thesis, which involves encapsulated microalgae, a solid-liquid system is studied which does not raise the same issues (chapter 0).

Indeed, the gas injection occurs in an absorption column outside the reactor and is not modeled. In standard photobioreactors, most of the time, the liquid flow regime is turbulent and can be studied with a k-ε model (X. Gao et al., 2018) while the flow in the photobioreactor involved in this study is laminar (chapter 3).

However, CFD is time consuming, especially for multiphase flows. To overcome this bottleneck, compartment models have been developed (Delafosse et al., 2014; Nauha & Alopaeus, 2013; Weber et al., 2019). They contain a lower number of meshes (compartments) which are considered ideally mixed, to decrease the calculation time. Moreover, one can easily integrate biological equations in the hydrodynamic model, which make them attractive to model PBR performance (chapter 5).

is time consuming, especially for multiphase flows. To overcome this bottleneck, compartment models have been developed (Delafosse et al., 2014; Nauha & Alopaeus, 2013; Weber et al., 2019). They contain a lower number of meshes (compartments) which are considered ideally mixed, to decrease the calculation time. Moreover, one can easily integrate biological equations in the hydrodynamic model, which make them attractive to model PBR performance (chapter 5).

1.4.3 Biological models

Several models have been developed to characterize the influence of parameters on microalgae growth. For example, Monod, 1949 developed a useful model to predict nutrient consumption by microalgae. The attention is focused here on light as a preponderant limiting parameter as explained in (equation 1.4). There are numerous correlations between growth and light intensity depending on the strain. For example, Fouchard et al., 2009 used growth kinetics developed by Andrews, 1968 for *Chlamydomonas reinhardtii* (Equation 1.3).

$$\mu = \mu_{max} \frac{I}{K_1 + I + \left(\frac{I^2}{K_H}\right)} \qquad \textit{(Equation 1.3)}$$

with K_1 the half-saturation constant and K_H the inhibition constant.

This type of equations is highly dependent on the system and on the quantities which are considered. For example, the light intensity used can be the incident light at the photobioreactor surface or the mean light intensity inside the reactor (Béchet et al., 2013).

Other models have been developed which combine a light attenuation law (as Beer-Lambert law) with a growth equation depending on light. The reactor is divided into several parts and both equations are calculated in these parts and summed. However, these models do not consider the "light history" of cells, i.e. L/D cycles.

To overcome this, PhotoSynthetic Unit (PSU) models, also known as Photosynthetic Factory (PSF), have been developed. It sets that biomass is divided in three states: active, resting and inhibited (Figure 1.17). The state of biomass depends on light input. Biomass is first considered in the resting state (x_1). By receiving a certain number of photons, it reaches the active state (x_2). Two possibilities occur then. It can either go back to the resting state and the energy provided by photons is used to produce biomass. Otherwise, if receiving additional photons, biomass goes to the inhibited state (x_3). Once in this state, it is recovered in the resting state after a certain time. Thus, equations used to describe the models require constants ($\propto$, β, γ and δ) for each transition between states. Theses constants depend on the strain and on the system (Equation 1.4), (Equation 1.5), (Equation 1.6). As γ and δ constants depend on time, this model is able to account for L/D cycles.

The model was first developed by Eilers & Peeters, 1988. Different modifications have been suggested. Wu & Merchuk, 2001 added two parameters in the equations (k, M_e) to consider negative growth in dark (Equation 1.7).

The equations associated to this model are simple ordinary differential equations, which can be easily implemented in a global performance model.

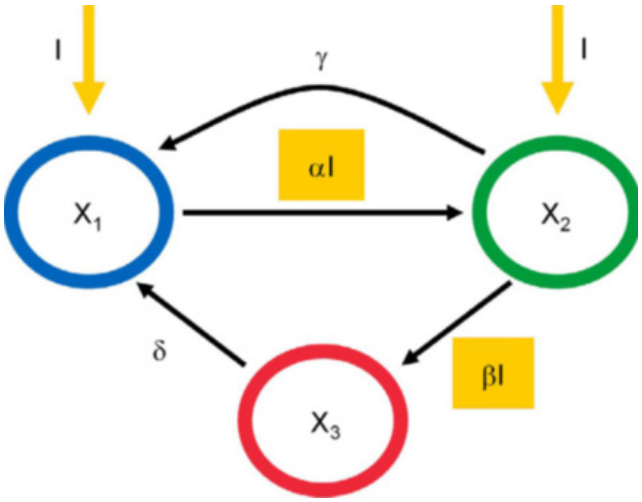

Figure 1.17 – Structure of PhotoSynthetic Unit (PSU) model. x1, x2 and x3 represent the resting, activated and inhibited state respectively. Reproduced from (Nauha & Alopaeus, 2013) with authorization.

$$\frac{dx_1}{dt} = -\propto Ix_1 + \gamma x_2 + \delta x_3 \qquad \textit{(Equation 1.4)}$$

$$\frac{dx_2}{dt} = \propto Ix_1 - \gamma x_2 - \beta x_2 \qquad \textit{(Equation 1.5)}$$

$$\frac{dx_3}{dt} = \beta Ix_2 - \delta x_3 \qquad \textit{(Equation 1.6)}$$

$$\mu = k\gamma x_2 - M_e \qquad \textit{(Equation 1.7)}$$

1.5 Thesis strategy

1.5.1 Objectives and methodology

Two main objectives of the thesis can be defined: the scale-up of the culture of encapsulated microalgae and the modeling of the photobioreactor. They are linked as the reactor modeling allows a better knowledge of the culture of encapsulated microalgae which can improve ultimately the scale-up.

The first aim of the thesis, as part of ValoAlgue project, is to scale-up the culture of encapsulated microalgae. Encapsulation method is still under research stage. Really few studies deal with the culture of encapsulated microalgae at pilot scale. First, measurements are realized in flasks. This enables to compare encapsulated and free (suspended) cultures of algae. This allows to study mechanisms of secretion of luciferase as well. Then, cultures in 1 L photobioreactor are realized. Results are not described in this thesis as they are more of practical/technological than scientific interest. This enables to test the encapsulation material and the UV disinfection system. Finally, a fluidized bed photobioreactor of 5 L is used to cultivate encapsulated algae and results are analyzed and compared to cultures in flasks. Results are used in the global model as well.

The second aim of the thesis is to develop a global model of the reactor. The model includes hydrodynamics, light and biological equations. Hydrodynamics is modeled using CFD. One main innovative contribution of the thesis is to model a photobioreactor dedicated to the culture of encapsulated algae. While traditional photobioreactor models deal with liquid or gas-liquid processes, the studied reactor involves solid and liquid. This leads to a different strategy, especially regarding hydrodynamics. Flows of liquid and then solid are studied and modeled. Models are experimentally validated at each step. Liquid CFD model is validated using PIV and the two-phase model is then validated using a light attenuation method which gives access to solid distribution. Light is modeled using Beer-Lambert law. The biomass absorption coefficient is calculated based on light attenuation measurements through the reactor during the culture.

Another particularity of this thesis is to use a CFD-based compartment model as a base for the global performance model. Compartment models have already been used to model photobioreactors but it is still unusual (Nauha & Alopaeus, 2013; S. Papacek et al., 2007).

1.5.2 Outlines

Even if the thesis is built to lead to the global model of the photobioreactor, each chapter is a step of the model and is written to be read independently. As methods used in every chapter are very different, they are detailed before the corresponding results.

Chapter 2 is focused on the culture of encapsulated microalgae in flasks and in the 5 L photobioreactor. The chapter describes thus biological measurements. Growth of encapsulated algae in flasks is compared to the growth of free algae in the studied conditions. The extracellular secretion of luciferase by algae and its diffusion through the beads are studied. The culture inside the 5 L photobioreactor is finally discussed. The growth and main parameters which have an influence on growth are followed.

Chapter 3 and 0 are dedicated to the hydrodynamics characterization of the photobioreactor. Two phases are present in the reactor: a solid phase constituted of beads containing microalgae and a liquid phase which is the culture medium.

As a first step in the analysis of hydrodynamics, only the liquid phase is studied in chapter 3. An experimental method, PIV (Particle Image Velocimetry) is used to measure velocity fields in the reactor in 5 different vertical planes. In parallel, a CFD (Computational Fluid Dynamics) model is developed to be used in the development of the photobioreactor global model. PIV results are used to validate the CFD model.

Chapter 0 is dedicated to the study of both phases in the reactor (liquid and solid) and their interactions. A two-phase CFD model is developed. The specificities of solid (density close to water and low diameter) have a high impact on the liquid – solid suspension behavior and are studied. An experimental method based on light attenuation and giving access to the solid distribution in the reactor is used to validate the CFD model. The influence of the presence of solid on the liquid phase flow is studied as well.

The last chapter, Chapter 5, presents the building of the global model from its constitutive “blocks”. It groups together the biological results obtained in chapter 2 and the hydrodynamics knowledge brought by chapter 3 and 0. First, a compartment model is built based on CFD results of two-phase simulations of chapter 0. A stochastic model is then added to the compartment model, to describe the movement of solid (beads) in the reactor. On the other hand, light distribution in the reactor is modeled using Beer-Lambert law, considering the influence of algae growth on light attenuation. Trajectories of beads from the stochastic model are then coupled with light distribution fields to get a light history of biomass contained in beads. The growth of biomass is calculated using a biological PSF (PhotoSynthetic Factory) type model. Model parameters are fitted and simulation results are validated by comparison to experimental results obtained in chapter 2. The global model is finally used to numerically study the impact of different parameters (light, liquid flow rate) on the algae culture performance.

At the end of the thesis, a general conclusion summarizes the main results on characterizing a photobioreactor for the culture of encapsulated algae. Furthermore, it suggests outlooks for future studies on culture of encapsulated algae and photobioreactor modeling.

2 Culture of encapsulated algae

2.1 Introduction

In the present study, the impact of immobilizing by encapsulation *Chlamydomonas reinhardtii* microalgae in a spherical alginate matrix is studied. Microorganism immobilization is a well-known process that finds an increasing number of applications for 30 years. Nevertheless, if processes involving encapsulation of microorganism such as enzyme or heterotrophic cells are well controlled, it is not the case for microalgae (Hameed & Ebrahim, 2007; Katarzyna et al., 2015).

There is no general rule on the influence of encapsulation on growth and physiology of algae cells, especially because of the diversity of microalgae strains. Growth of encapsulated microalgae has proved to be generally lower than free microalgae (Faafeng et al., 1994; Ferro et al., 2012; Homburg, Venkanna, et al., 2019; Pane et al., 1998). I. Moreno-Garrido et al., 2005 have shown that some microalgae species do not grow when encapsulated (Heterocapsa sp. and S. costatum). Some studies found a similar growth rate for free and encapsulated strains (Lau et al., 1997). A higher growth rate of encapsulated algae compared to free one has also been observed (Guolan et al., 2000; Hertzberg & Jensen, 1989). Hence, the influence of encapsulation on growth highly depends on the strain and on encapsulation conditions (bead diameter, material concentration...). Moreover, the encapsulated cell concentration at the beginning of the culture has an impact on the viability of the culture (Ignacio Moreno-Garrido, 2008). In some cases, a longer lag period at the beginning of the culture has been observed for encapsulated cells (Chevalier & de la Noüe, 1985; Lau et al., 1997). Besides, encapsulation can have an impact on cell morphology. Encapsulation can lead to larger cells (De-Bashan et al., 2002; Lukavsky et al., 1986). Formation of colonies have also been noticed (Bailliez et al., 1985).

Table 2.1 – Influence of encapsulation on growth for different microalgae. ≈ sign indicates growth rates have been calculated by the author based on growth curves.

Algae	Encapsulated compared to free growth	Reference
Chlamydomonas reinhardtii	- 13 %	Ferro et al., 2012
Chlamydomonas reinhardtii	- 36 %	Homburg, Venkanna, et al., 2019
S. capricomutum	- 80 % (10 °C) - 60 % (20 °C)	Faafeng et al., 1994
Tetraselmis suecica	- 29 %	Pane et al., 1998
Chlorella vulgaris	- 1 %	Lau et al., 1997
Chlorella	≈ + 6 %	Guolan et al., 2000
Phaeodactylum tricornutum	≈ + 60 %	Hertzberg & Jensen, 1989

Most published studies on encapsulated microalgae are in the fields of wastewater treatment or heavy metals removal (de-Bashan & Bashan, 2010; Mallick, 2002; Ruiz-Marin et al., 2010; Zamani et al., 2012). Production of energy (mainly hydrogen) from encapsulated microalgae is also studied (Homburg, Kruse, et al., 2019; Seibert & Torzillo, 2018). However, the secretion of high added value metabolites by encapsulated microalgae is less studied. Studies are compiled in Table 2.2. Different species have been immobilized and cultivated to secrete various metabolites (Cheirsilp et al., 2017; Choix et al., 2012;

Hatanaka et al., 1999; Lam & Lee, 2012; Santos-Rosa et al., 1989; Sicard et al., 2010; Thakur & Kumar, 1999).

Most papers deal with a metabolite secretion intracellularly thus a recovery inside the encapsulation matrix is possible. Using a strain able to secrete extracellularly a metabolite of interest which can be recovered in the culture medium is a real advantage for continuous processes. Few strains have this ability but some studies on the secretion of metabolites in the culture medium by encapsulated microalgae have been found. Some immobilized cells may produce more metabolite than free cells (León & Galván, 1994; Tripathi et al., 2002; Vílchez et al., 1991). Secretion can also be enhanced by changing the $\frac{O_2}{CO_2}$ ratio every 12 h (Vílchez et al., 1991) or as a response to an osmotic shock (León & Galván, 1994).

In this chapter, a strain of *Chlamydomonas reinhardtii* genetically modified to secrete extracellularly *Gaussia* luciferase is encapsulated. This fluorescent recombinant protein is used in biotechnology or in microscopy as a marker. It does not require a source of light but a substrate to produce bioluminescence. A very low amount of luciferase is needed to catalyze the reaction, but the cost of this protein is high. Lyophilized luciferase protein powder is sold 1250 $/mg in 2021 (Nanolight, ref. 321-100) for luminometer control.

Table 2.2 – Metabolite production from encapsulated microalgae.

Algae	Metabolite	Extra cellular	Quantity	Comparison with free cells	Reference
Dunaliella parva	propanediol	No	50 $mmol.L^{-1}$ after 160 h	=	(Hatanaka et al., 1999)
Dunaliella salina	glycerol	No	8.4 $\mu mol.L^{-1}$. mg chl a^{-1}	+	(Thakur & Kumar, 1999)
Chlorella	total carbohydrates	No	150 $mg.100mL^{-1}.day^{-1}$	NA	(Choix et al., 2012)
Chlorella	lipids	No	12% of total biomass	NA	(Lam & Lee, 2012)
Nannochloropsis	lipids	No	0.362 $g.L^{-1}$	=	(Cheirsilp et al., 2017)
Klebsormidium flaccidum	gold nanoparticles	No	NA	NA	(Sicard et al., 2010)
Haematococcus pluvialis	vanillin	Yes	10.6 $mg.L^{-1}$	+	(Tripathi et al., 2002)
Chlamydomonas reinhardtii	ammonium	No	2700 $\mu mol.h^{-1}$	NA	(Santos-Rosa et al., 1989)
Chlamydomonas reinhardtii	glycolate	Yes	23 $\mu mol.(mg\ chl)^{-1}.h^{-1}$	+	(Vílchez et al., 1991)
Chlamydomonas reinhardtii	glycerol	Yes	4 $g.L^{-1}$ after 120 h	+	(León & Galván, 1994)
Haslea ostrearia	marennine	Yes	0.39 $mg.(10^8\ cells)^{-1}.day^{-1}$	-	(Lebeau et al., 2002; Rossignol et al., 2000)

Most studies focus on the culture of encapsulated microalgae in flasks. Very few of them are dealing with the culture of encapsulated microalgae at a pilot scale in photobioreactors. Regarding the culture of encapsulated algae in form of beads, some photobioreactors have been developed for a 2 L working volume scale (Cheirsilp et al., 2017; Kitcha & Cheirsilp, 2014; Serp et al., 2000). Only one study was found in the available literature on a 5 L bioreactor (Lam & Lee, 2012).
This study focuses on the encapsulation of *Chlamydomonas reinhardtii* genetically modified to secrete extracellularly *Gaussia* luciferase. The growths of free and encapsulated microalgae are compared. The influence of encapsulation on the secretion of luciferase is studied as well. Bioluminescence of the secreted protein makes it easy to dose. The impacts of growth rate and of culture medium composition on secretion are considered. The influence of adding a polycation (PDADMAC - poly(diallyldimethylammonium chloride)) to the reticulation solution used for encapsulation is also studied. All these experiments are performed in flasks. Furthermore, an innovative liquid-solid fluidized bed photobioreactor of 5 L is used for the culture of encapsulated microalgae, to analyze the scalability of the process.

2.2 Materials and methods

2.2.1 Strain

The strain used is a *Chlamydomonas reinhardtii* strain genetically modified by K. Lauersen (Bielefeld University) to secrete *Gaussia princeps* luciferase (Lauersen et al., 2015; Lauersen, Berger, et al., 2013). The nuclear DNA of the UVM4 mutant of *Chlamydomonas reinhardtii* has been modified. The secretion signal for the extracellular carbonic anhydrase 1 of the native strain has been replaced with a *Gaussia* luciferase marker. The strain is referred to as “algae” or “microalgae” in the following.

2.2.2 Culture medium

Tris-Acetate-Phosphate (TAP) NH_4 medium ($C_2H_3NaO_2$ 17 mM, NH_4Cl 7.5 mM, TRIS-HCl 20 mM, pH 7.2) and Tris-Minimal-Phosphate (TMP) NH_4 medium (which corresponds to the TAP medium without acetate) are widely used to cultivate *Chlamydomonas reinhardtii* (Adam et al., 1993; Ermilova et al., 2003; Kumar et al., 2004). Mixotrophic conditions (TAP NH_4) are not easily controlled in photobioreactor due to bacterial proliferation, TMP NH_4 is then used for cultures in photobioreactor. As TMP NH_4 medium has a low concentration in nutrients, especially for culture under CO_2, it is concentrated 2 or 4 times, except for the TRIS component. TAP NH_4 and TMP NH_4 are named TAP and TMP in the following. TMP concentrated 2 or 4 times are named TMP 2x and TMP 4x, respectively. For cultures in photobioreactor, no TRIS (buffer) is added in the culture medium as pH regulation is made by CO_2 addition. Chemical buffers are not usually used at large scale due to their high costs.

2.2.3 Cultivation methods and algae encapsulation

2.2.3.1 Flasks

Free and encapsulated *Chlamydomonas* is cultivated in 500 ml flasks filled with 200 mL of culture medium and fixed on an orbital shaker. The orbital shaker (110 rpm) is placed in a room where the temperature is between 20 °C and 25 °C. Fluorescent lamps (Philips Master TL5 HO 54W/827) that provide up to 70 $\mu E.m^{-2}.s^{-1}$ (on the orbital shaker) are used to enlighten the flasks from the top.

2.2.3.2 Encapsulation

Chlamydomonas is encapsulated in an alginate matrix. A 3.75 %wt sodium alginate solution (Sigma-Aldrich, ref. 71238) is considered as optimal for encapsulation by our partner from the CMI laboratory (University of Namur). The solution is sterilized by autoclave at 120 °C for 20 minutes. As alginate properties are changing with temperature, the viscosity of alginate is measured by a falling ball viscometer before and after autoclaving. The dynamic viscosity of the non-sterile solution of 3.75 %wt is 5730 mPa.s. After testing different concentrations, a 5.50 %wt alginate solution sterilized by autoclave is chosen as its viscosity, equal to 5480 mPa.s, is very close to the viscosity of the optimal non-sterilized 3.75 %wt solution (4 % relative difference).
Algae are first grown in flasks as free cultures in TMP medium for one week. 50 mL of free culture is then centrifuged (2000 g, 2 min) and suspended in 1 mL of fresh culture medium. They are mixed with alginate to get an algae/alginate volume ratio of 1:4.
The mix of alginate solution and microalgae is dropped in a reticulation solution (aqueous solution of $CaCl_2$, 100 mM, sterilized by 0.22 µm filtration) to form beads. Due to its influence on material porosity, PDADMAC (0.4 %) can be added in the reticulation solution (containing $CaCl_2$). PDADMAC is a cationic polymer. It is used to form a cationic layer around the anionic sodium alginate to increase the bead resistance (Desmet et al., 2014). Its impact on the secretion of luciferase is studied in 2.3.1.1.2.
To ensure sterile conditions and minimize bacteria proliferation inside the photobioreactor, all the encapsulation process is carried under a laminar flow hood.

Bead making is time consuming thus requires semi-automatic methods. A simple method, which have been used in the present case, is to use a peristaltic pump, a tubing and a needle (Figure 2.1). The method still takes time as beads are made one by one but enables a reliable bead formation and reproducibility.

a)

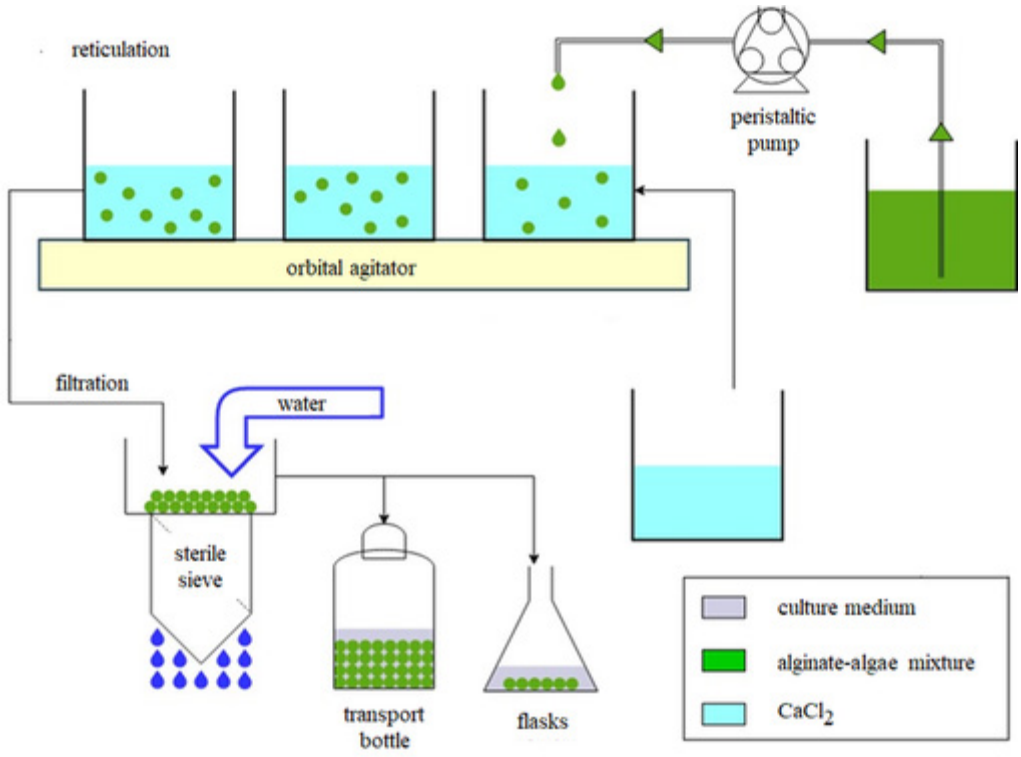

b)

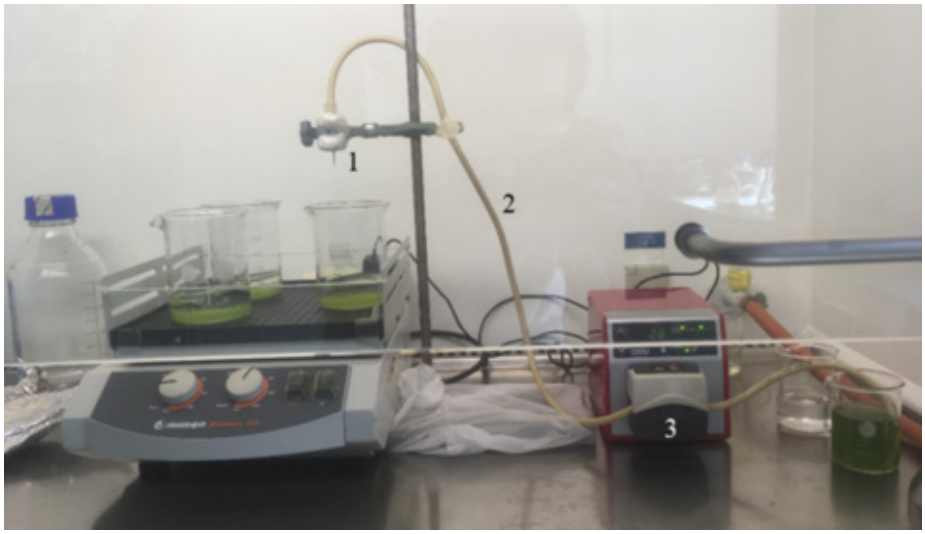

Figure 2.1 – Automatic method to produce Ca-alginate beads. Schematic representation of the method (a). Photography of the set-up (b) using a peristaltic pump (3), tubing (2) and a needle (1).

2.2.3.3 Photobioreactor

The photobioreactor is specifically designed for the culture of encapsulated microalgae. It is a two-phase flow fluidized bed reactor in which beads of encapsulated microalgae are the dispersed solid particles and culture medium is the liquid continuous phase. It is a flat, rectangular reactor of 38.05 cm height, 35.10 cm width and 4.25 cm depth (Figure 2.3). Walls are made of 8 mm thick transparent Plexiglas sheets to allow light transmission. The working volume of the reactor, where microalgae beads are circulating, is around 5 L. Fluidization of the solid is ensured by a liquid injection at the bottom of the reactor through an off-centered slit of 1 mm thick disposed over the whole width of the photobioreactor. The liquid outlet is situated at the top of the photobioreactor whereas a grid is disposed to keep the solid

particles within the working volume. The liquid is recirculated from the top to the bottom of the photobioreactor by the means of an external loop. A 5.5 mm thick internal wall enables to control the circulation inside the reactor and to homogeneously distribute the beads. As a consequence of the internal wall and of the off-centered liquid inlet, the flow is ascending on one side of the internal wall and descending on the other side. A prism is set at the bottom of the reactor to force the circulation of the liquid and the beads over the slit at the reactor bottom, avoiding a dead zone.
In this study, a solid volume fraction of 4 %v is chosen. To keep sterile conditions, the solid is introduced in the photobioreactor using a lateral valve which is disinfected with ethanol before use. A liquid flow rate of 0.1444 $kg.s^{-1}$ (520 $L.h^{-1}$) is chosen, which corresponds to the flow rate required to fluidize a bed of beads with specific characteristics (diameter: 3.3 ± 0.1 mm, density unknown) for the solid volume fraction involved. The liquid flow rate is highly dependent on beads characteristics (chapter 0). For a solid volume fraction of 4 %v, the flow rate varies from 0.1138 $kg.s^{-1}$ to 0.1444 $kg.s^{-1}$ for a bead diameter of 2.8 and 3.3 ± 0.1 mm and a density around 1018 $kg.m^{-3}$ at 20 °C.
A LED light system is used to enlighten the reactor on the descending zone side (Figure 2.3 b c). The mean light intensity equals 60 $\mu E.m^{-2}.s^{-1}$. Detailed information on light attenuation in the reactor is given in chapter 5.
The photobioreactor external loop is used to implement all the probes and equipment required to control the culture conditions. The temperature is kept at 25 °C using a heat exchanger and a water bath. An electronic controller (Consort, multi-parameter controller, R3620) regulates the pH under 7.2 by means of a pH probe and an air-CO_2 injection through absorption column disposed in the external loop. The absorption column allows enhancing gas-liquid transfers between culture medium and atmosphere. It improves CO_2 transfer to the liquid phase and stripes the excess of dissolved oxygen in the culture medium due to photosynthesis which can be harmful for algae. Oxygen concentration of 30 $mg.L^{-1}$ can be harmful for microalgae (Kazbar et al., 2019). A concentration of 10 $mg.L^{-1}$ is reached using an air-lift reactor (Sánchez Mirón et al., 2002) while a higher concentration (33 $mg.L^{-1}$) is obtained with a tubular reactor (Molina et al., 2001). The global amount of CO_2 added during the culture, is monitored by weighing the CO_2 cylinder (scale: Sartorius Entris 2). Dissolved oxygen concentration is measured using a probe (Hach, LDO101) and a controller (Hach, HQ40d).

A UV system (Philips, PL-S Module 25W) is also set on the external loop to limit the bacterial proliferation within the culture medium. As a matter of fact, the separation of the algae and the medium allow the continuous sterilization of the culture medium by UV as long as it does not have a negative impact on the metabolites of interest that are secreted in the medium.
Before each culture, the photobioreactor is chemically sterilized using sodium hypochlorite and washed with distilled water. Culture medium is then introduced through a 0.22 µm filter. 0.22 µm gas filters are also used to sterilized injected air and CO_2, as well as for gas exhausting from the photobioreactor during culture.

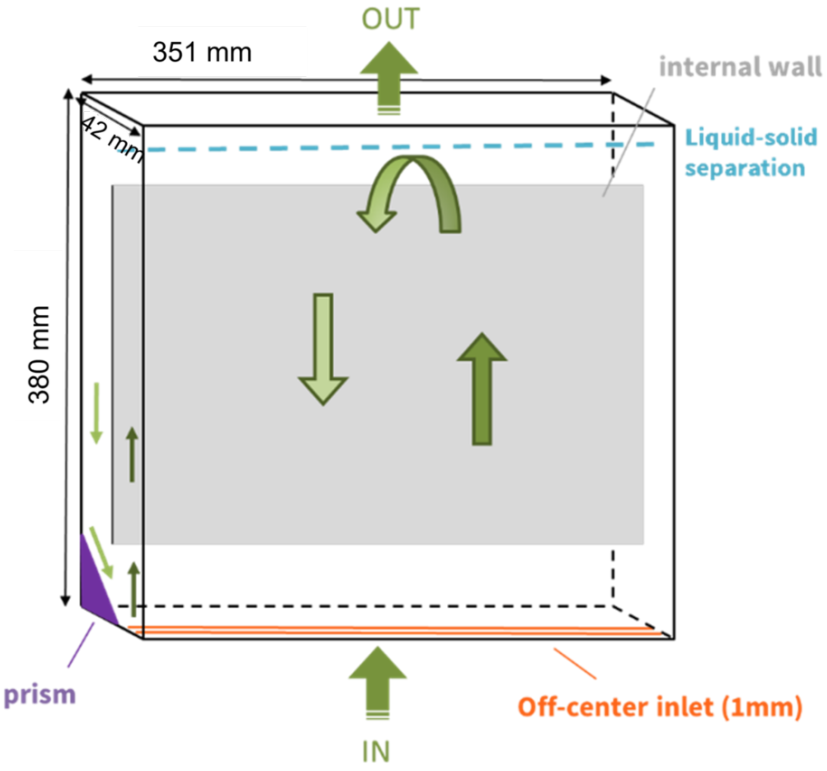

Figure 2.2 - Flow characteristics in the photobioreactor. A prism, an internal wall and an off-center inlet improve the beads circulation. A grid at the top of the reactor keeps solid with in the reactor while liquid is controlled in an external loop.

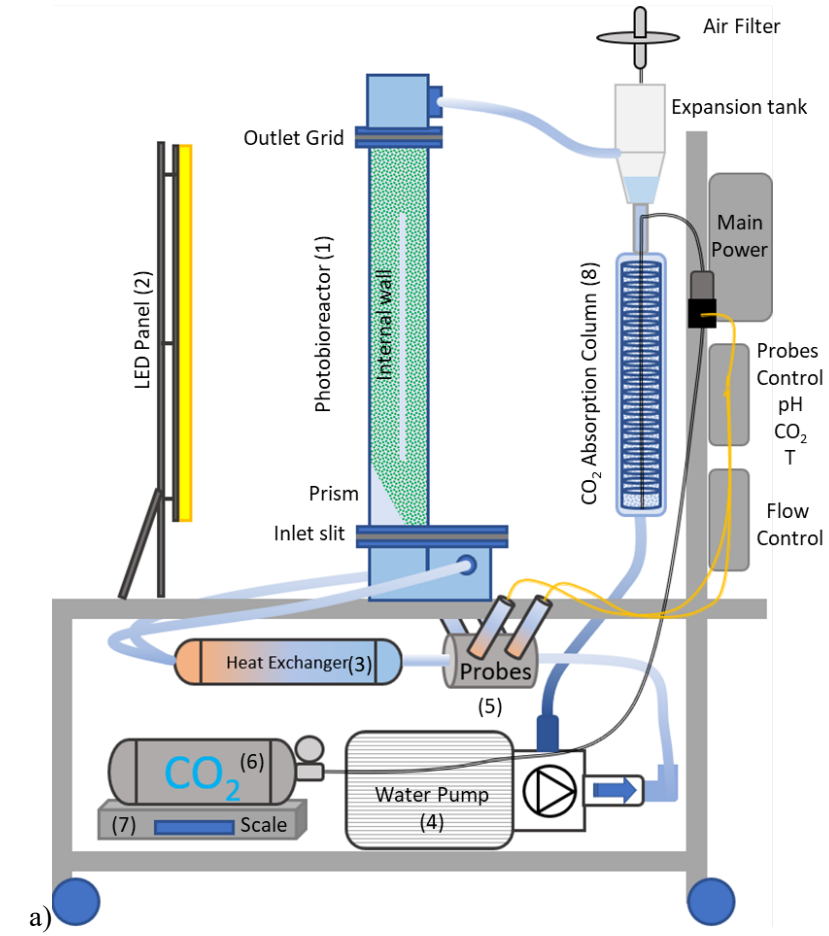

a)

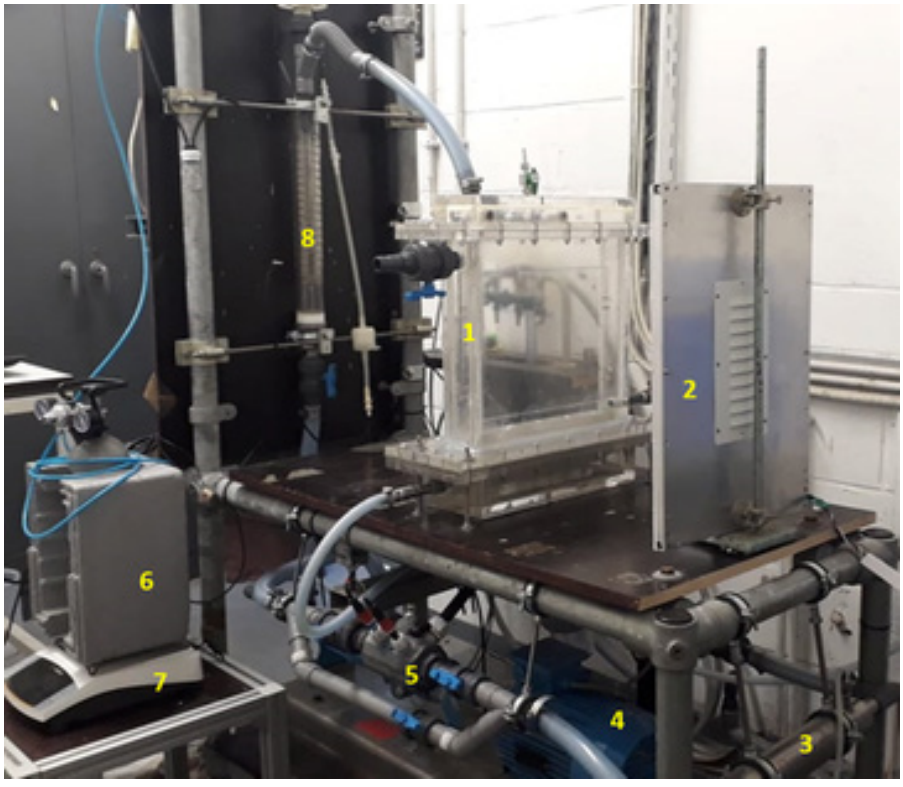

b)

Figure 2.3 – (a) Schema of the installation. (b) Photography of the installation. 1: reactor; 2: LED light; 3: heat exchanger; 4: pump; 5: pH, temperature and oxygen probes; 6: CO_2 bottle; 7: balance; 8: absorption column.

2.2.4 Biomass quantification

2.2.4.1 Free microalgae cultures

In free culture performed in flasks, the algae concentration (growth) monitoring is made by measuring the evolution of the culture optical density. The optical density (λ=750 nm) of cultures is measured using a spectrophotometer (Hach, DR 3900). The calibration is establishing the correlation between the optical density measured on different free cultures to their dry weight (Equation 2.1). The correlation is linear and is specific to the spectrophotometer and the strain used (Figure 2.4).

$$DW\ (g.L^{-1}) = \frac{OD\ (750\ nm)}{1.566} \qquad \textit{(Equation 2.1)}$$

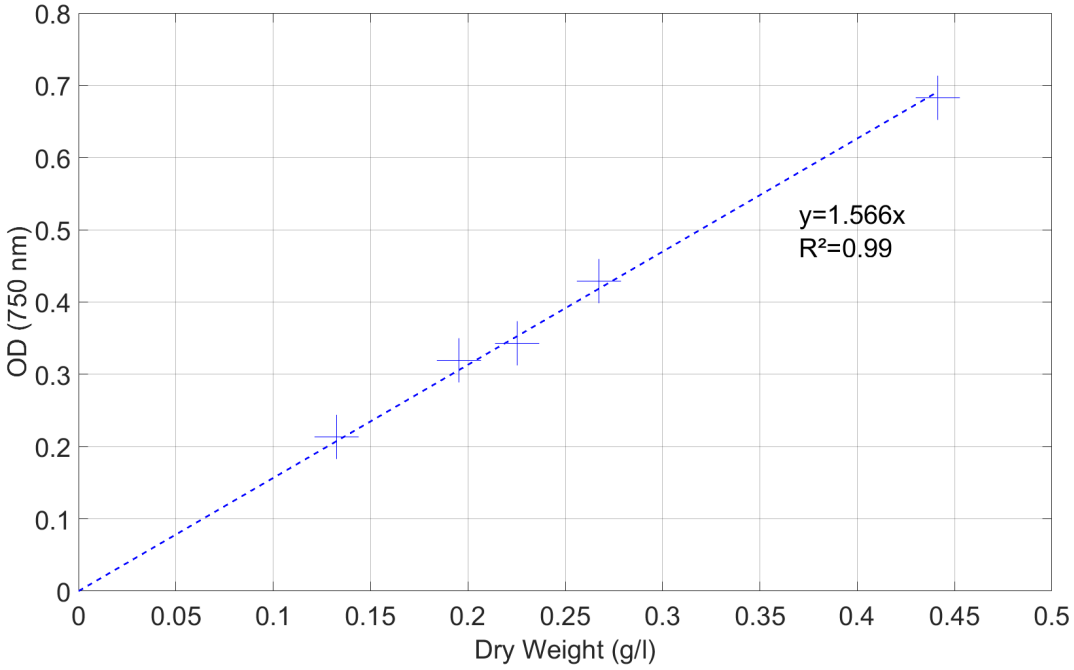

Figure 2.4 – Calibration curve between optical density at 750 nm and dry weight of Chlamydomonas reinhardtii for the spectrophotometer used (Hach, DR 3900). Linear regression through origin.

2.2.4.2 Encapsulated microalgae cultures

The protocol to measure biomass dry weight in encapsulated algae cultures is based on an optical density method similar to the one used for free algae described in Figure 2.4, adapted to prevent interference from the encapsulation matrix. Beads are first dissolved, then the optical density is measured. It requires a perfect dissolution of the alginate matrix, otherwise alginate fragments can absorb light and distort results. The dissolution protocol had to be optimized, as the method most often proposed in literature (trisodium citrate at room temperature) did not lead to satisfactory results.
A defined number of beads containing algae (10 to 50) are dissolved within 10 mL of trisodium citrate solution (0.25 M). To completely dissolve alginate, the mixture is heated during 2 h at 45 °C and then vigorously agitated at room temperature for 20 minutes. The optical density of the resulting solution is then measured by spectrophotometry at λ=750 nm, with trisodium citrate solution as blank.
If all beads are equivalent (same volume and same algae concentration) and if all beads are completely dissolved, the measured optical density should linearly increase with the bead concentration. Figure 2.5

shows that the linear regression is not perfect, while remaining very good, with a R^2 equal to 0.97. A microscopy observation of the resulting solution confirms the complete dissolution of alginate.
For comparison of free and encapsulated algae growth in flasks, 3 beads are dissolved par mL (9 beads in 3 mL) of trisodium citrate solution (0.25 M). Dry weight is calculated according to the total volume of solid (19 mL) and liquid (181 mL) in the flask. 1% of the total solid is removed in each sample, which is considered in the dry weight calculation.

In the photobioreactor, two duplicates of 9 beads in 3 mL are collected and dissolved before the measurement of optical density. Dry weight is calculated according to the volume of the bed bead (height < 350 mm) which corresponds to a volume of 4.5 L (while the volume of culture medium in the reactor is 15 L). The volume of beads removed every day (around 1 % of total volume of solid each day) is taken into account.

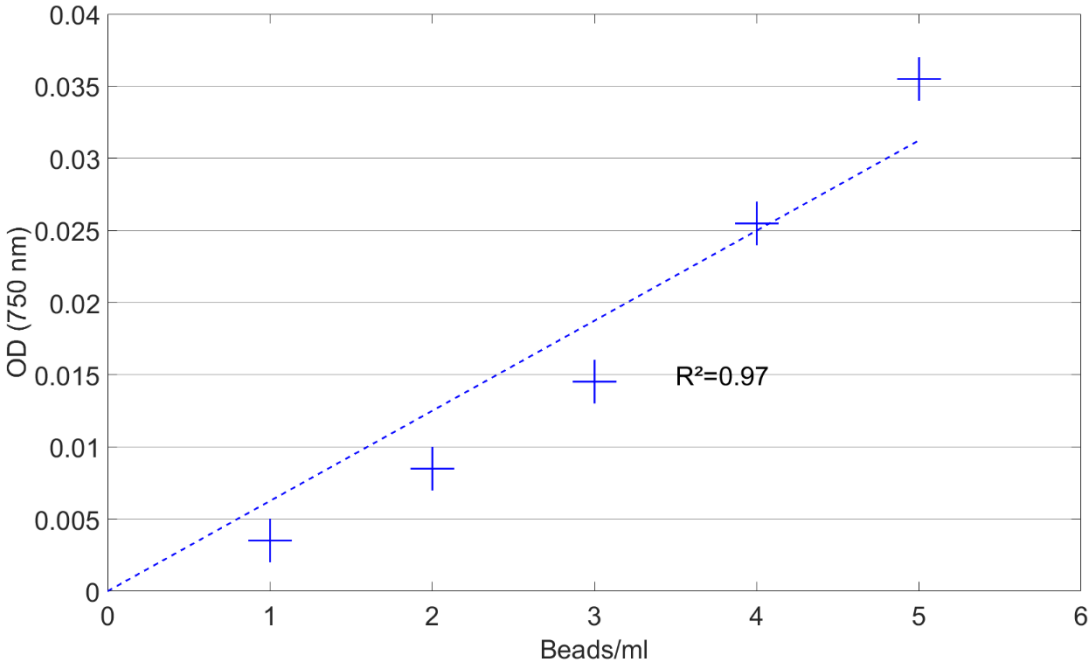

Figure 2.5 – Optical density measured by spectrophotometry at 750 nm for different number of beads per milliliters containing microalgae. Linear regression through origin.

2.2.4.3 Growth rate

Growth rate μ is calculated depending on the dry weights (C_{xi}) measured at different times t_i following the correlation (Equation 2.2). As dry weights are measured daily, intervals between two times are expressed in day.

$$\mu = \frac{\ln(C_{x2}) - \ln(C_{x1})}{t_2 - t_1} \qquad \textit{(Equation 2.2)}$$

2.2.5 Luciferase dosing

Luciferase is dosed by bioluminescence using the protocol described by Lauersen, Berger, et al., 2013; Shao & Bock, 2008. The samples used for measurement are either dissolved beads (6 beads in 2 mL of citrate) or culture medium sampled during culture. Optical density is measured by spectrophotometry and the sample is filtered (0.22 µm) to remove biomass before measuring luciferase concentration. Samples are kept at -20 °C for conservation. The impact of the volume of collected samples of beads and culture medium on measured luciferase concentrations is not taken into account, as it globally represents less than 3 % and 2 % of the total volumes of beads and culture medium, respectively.

Every sample is diluted in fresh culture medium with dilution ratios equal to 0.025, 0.05, 0.1, 0.175, 0.25, 0.5, 0.75 and 1 (ranging between 0.025 and 1). A blank containing only culture medium is also realized. 20 µL of sample is diluted in 125 µL of assay buffer (K_2HPO_4 100 mM, NaCl 500 mM, EDTA 1 mM, pH 7.6) in a 96 well-plate. 50 µL of coelenterazine (Roth, 4094.3) at 0.04 mM (after dissolution in ethanol), is added in each well (72 wells plate used). The plate is then placed in the dark for 5 min incubation. A plate reader (Synergy MX) is used to measure the relative luminescence unit (RLU).

This bioluminescence method is semi-quantitative and requires the use of a standard. It is not possible to use a commercial standard with a known concentration because of costs reasons. Indeed, the cost of 100 µg of luciferase powder is 225 $ (Nanolight, ref. 321-100) which is the quantity required for 3 tests only. Results are then expressed as relative and not absolute results, using a standard with an unknown concentration. Luminescence signal is plotted according to the sample dilution (Figure 2.6), allowing to determine the dilution ratio range in which the correlation is linear. A linear regression is made on this zone. For culture medium samples (from free and encapsulated cultures), the linear zone is between 0.175 and 0.75 dilution ratios, while it ranges between 0.1 and 0.5 dilution ratios for dissolved beads and standard. The concentration in the sample is extrapolated from the regression obtained on this linear zone for a dilution ratio equal to 0.5 and the y-intercept is subtracted. The luminescence of a standard, which corresponds to the supernatant of a 3 day-culture of free microalgae, is measured each 3 samples (2 lines of standard per well plate of 8 lines). As the second standard value has not a constant variation (was slightly higher or lower) compared to the first standard value, the average of both values is taken. The results of a plate are expressed as a percent of this averaged standard. However, the difference between two standards of one plate is generally of 30 % (vary from 2 to 90 %). Hence the error of the method is high and enables to only get main tendencies.

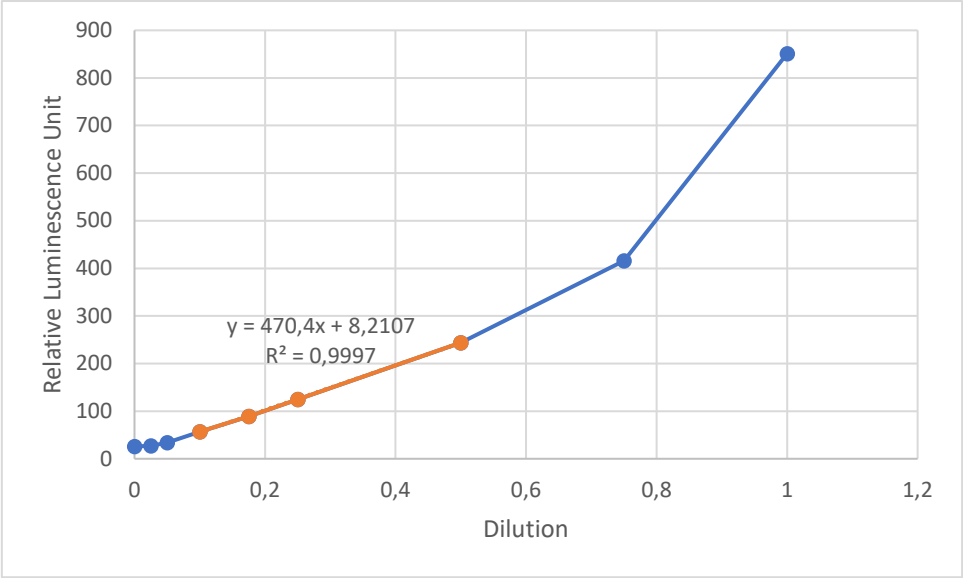

Figure 2.6 – Example of data processing of luminescence signal. Sample of dissolved beads on day 6, made using PDADMAC and cultivated in TMP. The linear regression is made between dilution 0.1 and 0.5 for this sample of dissolved beads. The value in absolute RLU for a dilution of 0.5 using the regression is 243. The y-intercept (8.2107) is subtracted and the result is multiply by the dilution (0.5). The absolute value in RLU is thus 118 and the mean value of the standards was 4942 for this plate so the value in RLU (%standard) is 2.4 %.

2.2.6 Nutrient dosing

Ammonium and phosphate ion concentrations are measured by a colorimetric method using a spectrophotometer (Hach, DR 3900). Phosphates are measured (spectrophotometric measurement at 890 nm) using the PhosVer method proposed by Hach: powder pillows of ascorbic acid are added in 10 mL samples. After swirling, the reaction is allowed to run for two minutes. For each sample, a blank is realized with sample without acid, submitted to the same swirling and reaction protocols. The method allows dosing up to 2.5 $mg.L^{-1}$ of PO_4^{3-}.

Ammonium is dosed using the Nessler method (spectrophotometric measurement at 425 nm). Reagents provided by Hach are used: mineral stabilizer (3 drops), polyvinyl alcohol dispersing agent (3 drops) and Nessler reagent (1 mL) are added to 25 mL samples. After swirling, the reaction is allowed to run for one minute. The same protocol and reagents are used for the blank (distilled water). The result is considering nitrogen and must be multiplied by 1.29 to be expressed as $mg.L^{-1}$ ammonium (NH_4^+). The method range is up to 2.5 $mg.L^{-1}$. Culture medium samples are diluted by 250 to be in the method range.

2.3 Results

2.3.1 Cultures in flasks

2.3.1.1 Luciferase production

One of the aims of the project is to recover in the culture medium luciferase secreted by encapsulated algae, to avoid separation of the metabolite from the algae, which is one benefit from encapsulation (chapter 1). There is a multi-scale process occurring: production of luciferase by the cells, extracellular secretion of part of luciferase, diffusion through the encapsulation matrix. To understand the process performances (luciferase concentration in the culture medium), each step must be analyzed. Luciferase

concentration in beads is thus measured. Growth is simultaneously evaluated to calculate a specific production of luciferase. Then, the comparison of luciferase concentration in beads and in the culture medium allows to evaluate luciferase diffusion through the encapsulation material. The impact of different parameters on each step is analyzed.

2.3.1.1.1 Luciferase production in beads

The concentration of luciferase in beads cultivated in flasks is followed for 6 days and measured on day 1, 2, 3 and 6. The influence of different parameters on secretion is studied. Different culture medium are tested (TAP, TMP, TMP 2x). For each medium, two flasks are used: one containing bead made from a reticulation solution with $CaCl_2$ and PDADMAC and one made using a reticulation solution with $CaCl_2$ only (Figure 2.7).

In beads formed using PDADMAC, a higher luciferase production is measured with TAP medium (between 9 and 41 %standard) than using TMP 2x medium (4 - 26 %standard). Similarly, luciferase concentration is more important using TMP 2x medium than TMP medium (1 - 3 %standard).

The influence on the secretion of luciferase of adding a polycation (PDADMAC, 0.4 %) in the reticulation solution (containing $CaCl_2$) is studied. In TAP medium, the concentration of luciferase inside the beads formed with PDADMAC (between 9 and 40 %standard) is higher than using $CaCl_2$ only (between 2 and 8 %standard) (Figure 2.7). This shows the high influence of the encapsulation material on the secretion of luciferase even inside the beads, due a modification of the local conditions around microalgae. However, in TMP 2x medium, the beads formed with or without PDADMAC produce a similar quantity of luciferase. Finally, the beads formed using PDADMAC and cultivated in TAP medium and the beads formed without using PDADMAC and cultivated in TMP 2x medium produce the most luciferase inside the beads.

It can be observed that luciferase concentration decreases after day 3 inside beads for all samples. Besides, optical density measurements of dissolved beads shows that encapsulated algae growth reaches stationary phase on the same day (day 3), indicating a potential correlation between secretion of luciferase and growth.

It must be noticed that the optical density is directly correlated to the dry weight, but these experiments are made with a spectrophotometer for which the correlation is unknown. This is the reason why results are expressed in OD (optical density).

Similar correlation is observed by other ValoAlgue partners. Moreover, Lauersen, Vanderveer, et al., 2013 highlights the same pattern on this strain when cultivated as free algae. They show an accumulation of recombinant protein at day 2 and 3 which corresponds to the period of exponential growth. After that, they observe a drastic decrease of recombinant protein. Hence the strain secretes luciferase only during its growth phase. Moreover, the luciferase concentration does not remain constant but decreases, meaning that during stationary phase no luciferase is secreted and the luciferase produced during the growth phase is degraded. This also is noticed by Lauersen, Vanderveer, et al., 2013.

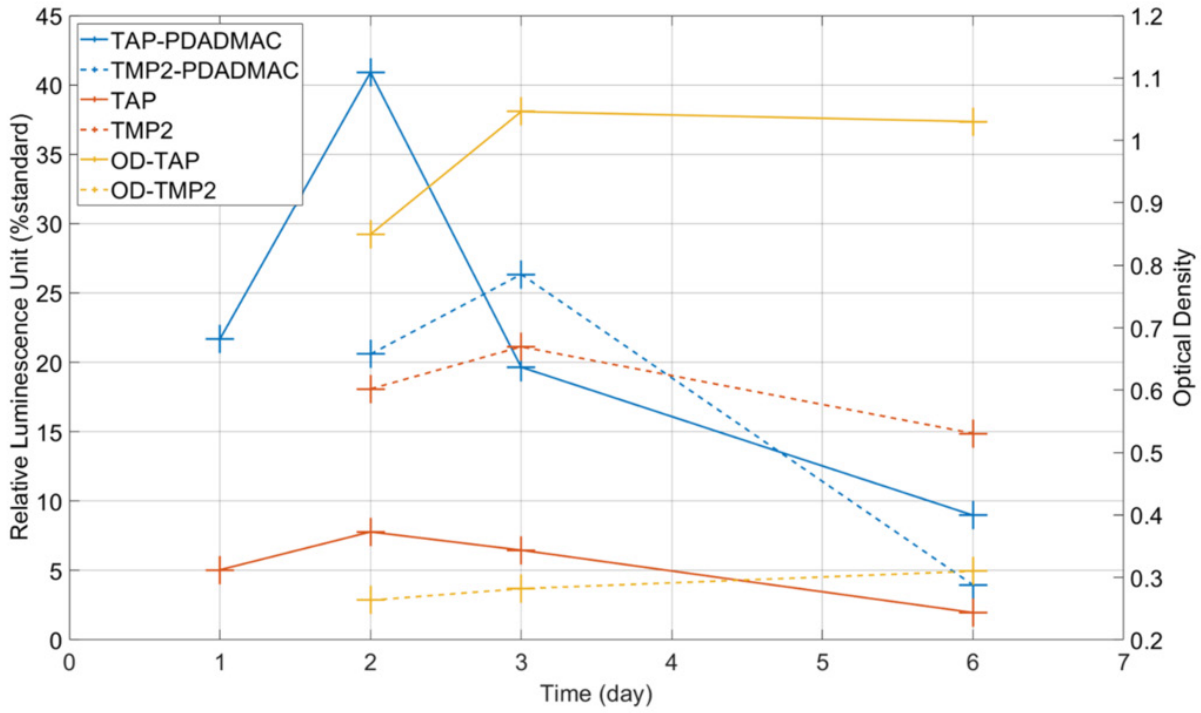

Figure 2.7 – Influence of the culture medium (TAP, TMP, TMP 2x) on the secretion of luciferase inside beads formed with (solid line) and without PDADMAC (dashed line). Optical density of the cultures in every medium is indicated (dotted line). For TAP and TMP2x, a mean optical density in cultures made with and without PDADMAC is calculated.

As more biomass is produced with TAP medium, the secretion of luciferase in TAP flasks is more important. The concentration of luciferase (%standard) is divided by the optical density for every culture medium to get information on the specific production of luciferase, i.e. normalized by a quantity (OD) directly related to the biomass concentration.

The specific production (ratio RLU/OD) obtained in TMP medium concentrated two times (TMP 2x) is more important than using TAP or TMP medium in any case (Figure 2.8). During day 2 and 3, it reaches the double of luciferase secreted by algae cultivated in TAP medium, inside beads formed with or without polycation. The specific production is significantly lower in TMP medium as well. Hence even if TAP medium allows to get a higher dry weight, TMP 2x medium enables to get higher luciferase specific production.

As working in mixotrophic conditions, when using TAP medium, results in higher bacterial proliferation, this culture mode is very difficult to manage in photobioreactor and must be avoided. It is thus promising that TMP 2x presents good results for luciferase production.

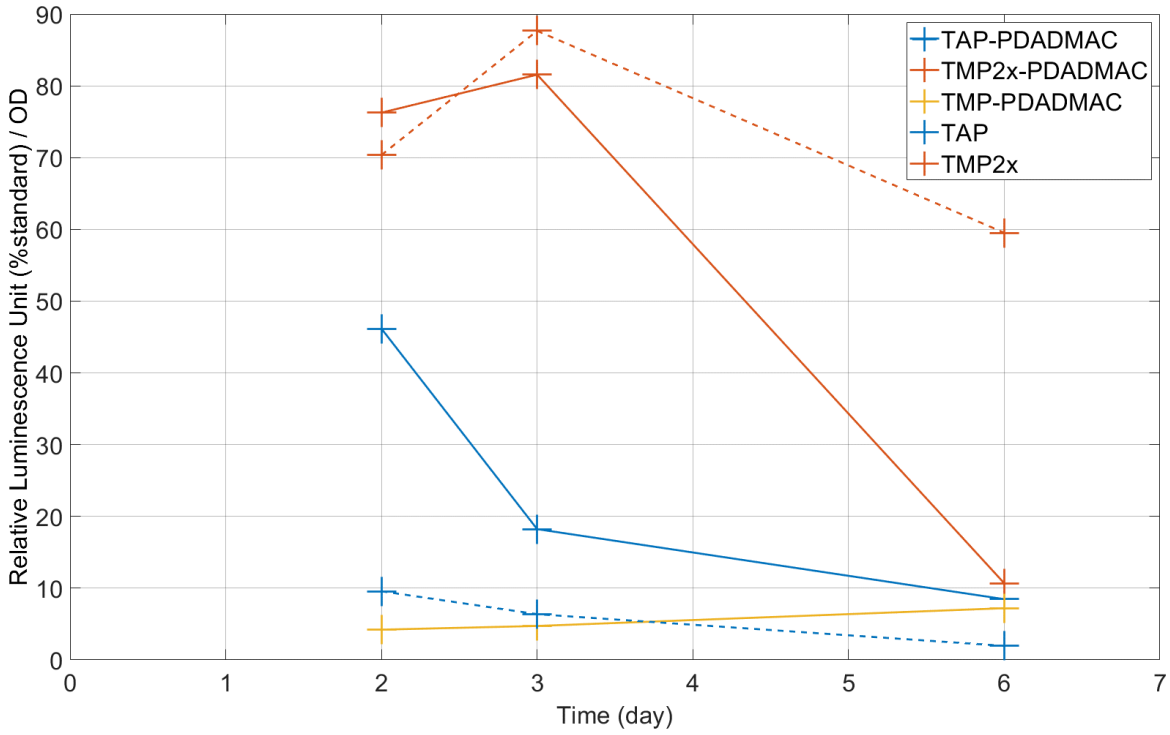

Figure 2.8 - Influence of the culture medium on the specific secretion of luciferase inside beads formed with and without PDADMAC. The relative luminescence is divided by the optical density measured by spectrophotometry.

2.3.1.1.2 Impact of the encapsulation matrix on luciferase diffusion in culture medium

The aim of the project is to design a process, allowing the continuous recovering of metabolite in the culture medium. To achieve this, the metabolite must be excreted by cells and then diffused through the beads. In free cultures, around 40 % of the total production of secreted luciferase is excreted by cells (results not published from our partner from the Laboratory of Bioenergetics of the University of Liege). Then the extracellularly secreted luciferase must be transferred to the culture medium, by diffusion through the bead material. This is the reason why a special attention is paid to the evolution of luciferase concentration in the culture medium as well as in beads. Figure 2.9 shows concentration values measured on days 1, 2, 3, and 6 in beads and in the culture medium. For all culture medium, luciferase concentration is always significantly lower in culture medium than in beads (factor 2 to 400), indicating a retention of luciferase inside alginate beads.

Results obtained without using PDADMAC in the reticulation solution shows the same, luciferase concentration in culture medium is always lower than in beads

The decrease of luciferase concentration with time is visible in the culture medium as it is in beads. The degradation of luciferase (decreasing and not stable concentration) can also be noticed. In TAP medium, the higher concentration in beads is measured on day 2 while it is on day 3 in culture medium. This could be due to the time required for the luciferase to diffuse through the encapsulation material.

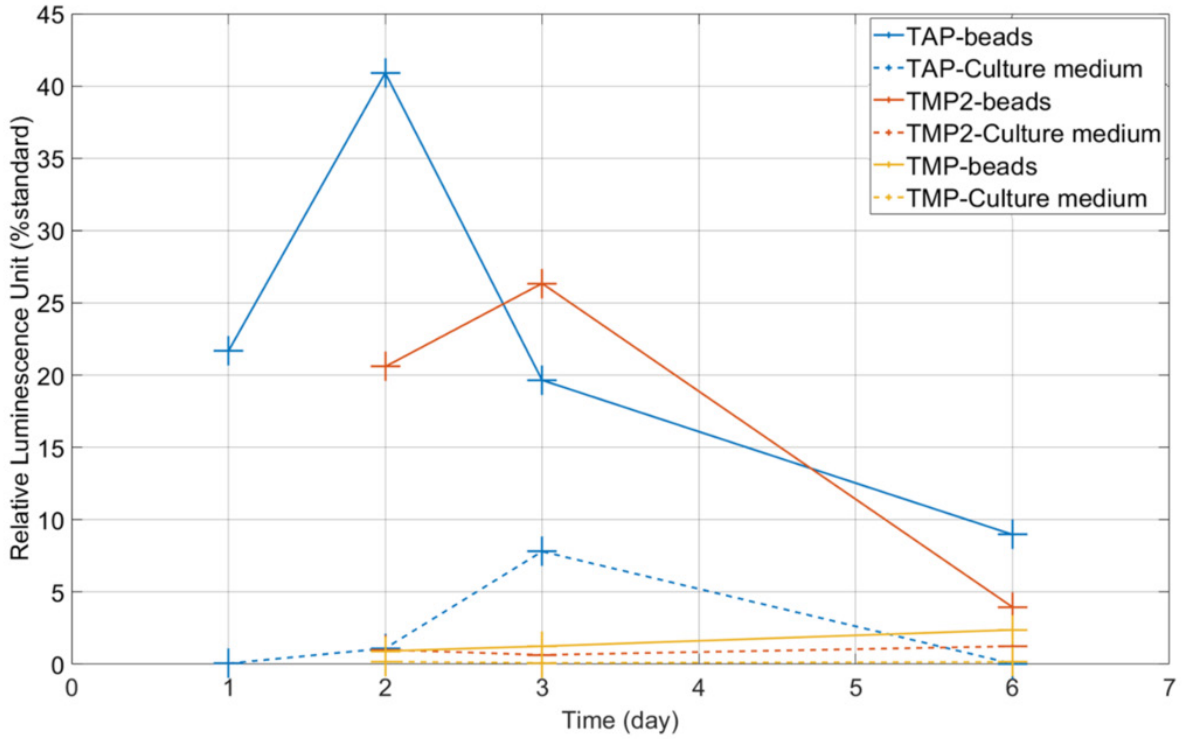

Figure 2.9 – Secretion of luciferase inside beads and culture medium. Cultures conducted in TAP, TMP 2x or TMP medium in flasks. Reticulation solution containing PDADMAC.

Gaussia luciferase secreted by *Chlamydomonas reinhardtii* has a molecular weight of approximately 50 kDa (Lauersen, Berger, et al., 2013). Assuming the protein is spherical, it corresponds to a 5 nm diameter. The pore size distribution and the pore volume of the encapsulation material was characterized by a team of the CMI laboratory (University of Namur) working on ValoAlgue project (Desmet et al., 2015), leading to a pore size distribution between 10 and 80 nm. Hence the pore size cannot completely explain the retention of luciferase inside the beads.

According to our partner from the University of Namur, possible explanations of the diffusion limitation is the physico-chemical properties of the material which have the most important influence on luciferase diffusion. Hydrophilic or hydrophobic sites as well as positive or negative charges can have an influence depending on the affinity of these sites with the metabolite (Rooke et al., 2011).

The impact of using PDADMAC during cross-linking of beads on the diffusion of luciferase in the culture medium is studied. The concentration of luciferase in the culture medium (TAP) without PDADMAC is more important except for day 3 (Figure 2.10). But the quantity of luciferase is low (a few percent of standard) and the error of the method is important as explained in the Methods (2.2.5), so it is difficult to draw conclusions.
Hence no impact of adding PDADMAC on the diffusion of luciferase through the beads can be observed. The luciferase concentration in beads made with PDADMAC is higher but concentration in culture medium is equivalent, indicating perhaps even a worse diffusion using PDADMAC. The above-mentioned study also showed that a higher porous volume is obtained if no PDADMAC is added to the reticulation solution (Desmet et al., 2015). Even if the pore size may not explain the luciferase retention in beads, a reticulation solution without PDADMAC is used, as it leads to a higher porosity and thus potentially to a better diffusion. Moreover, the beads without PDADMAC are sufficiently resistant.

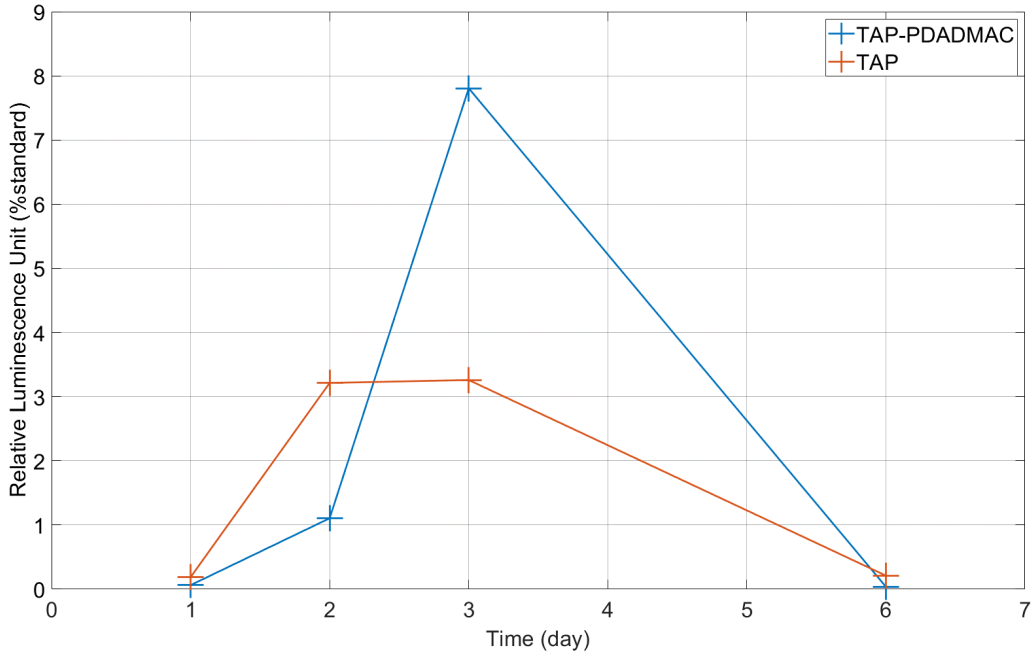

Figure 2.10 - Influence of the addition of PDADMAC in the reticulation solution on the diffusion of luciferase in the culture medium. Cultures conducted in TAP medium.

As the quantity of luciferase in the culture medium is significantly lower than the luciferase dosed in the beads, the conclusions drawn inside the beads are confirmed. The secretion of luciferase takes place during the growth phase only and is rapidly degraded. The luciferase is not well diffused through alginate beads made with this protocol. Improvements on encapsulation material have to be performed but are not the subject of this thesis. Results obtained at small scale show that the method (this strain encapsulated with this material) cannot be used to produce luciferase in the culture medium in the photobioreactor, so luciferase is not dosed in the photobioreactor. Despite this, the results obtained on photobioreactor are still valuable as the aim of the global project is to validate its design as a proof of concept for cultivating encapsulated microalgae at pilot scale, in the perspective of using it to cultivate other strains. Some strains have been previously used to secrete smaller metabolites through alginate beads. As detailed in the introduction of this chapter, *Haematococcus pluvialis* was used to produce vanillin (Tripathi et al., 2002) and *Haslea ostrearia* to secrete marennine (Lebeau et al., 2002). Moreover, the studied strain is used to test photobioreactor performances as knowledge on *Chlamydomonas reinhardtii* behavior has been accumulated and it is considered as a model alga. This green alga can be easily manipulated genetically which can results in extracellular secretion of metabolites. *Chlamydomonas reinhardtii* has been encapsulated to produce glycolate (Vílchez et al., 1991), glycerol (León & Galván, 1994) and hydrogen (Homburg, Kruse, et al., 2019).

Based on the results obtained in this section, it is chosen to study the strain growth with a reticulation solution containing no PDADMAC and with a culture medium TMP 4x (concentrated 4 times) in view of promising results with TMP 2x. Moreover, cultures can be more rapidly limited by nutrients using CO_2 input as in the photobioreactor.

2.3.1.2 Comparison of free and encapsulated microalgae growth

Microalgal growth in photobioreactor is potentially lower than in flasks, which is the main challenge of scale-up. For the purpose of cultivating encapsulated microalgae in photobioreactor, two potential negative impacts on growth must be taken into account: encapsulation and scale-up. Since the 5 L

photobioreactor does not allow cultivating free algae, it cannot be used to compare growth of free and encapsulated cells. Thus, the impact of encapsulation is evaluated based on biomass growths measured in cultures in TMP 4x performed in flasks agitated on orbital shaker. Three Erlenmeyer flasks of free and encapsulated algae are cultivated. Cultures are performed for 10 days.

The normalized dry weight evolution is presented on Figure 2.11. Dry weights are divided by their initial concentration as they are slightly different (0.02 $g.L^{-1}$ for free cultures and 0.03 $g.L^{-1}$ for encapsulated algae). It must be noticed that the biomass in flasks of encapsulated algae is situated only in the beads. There are thus two areas with different concentration: a high local concentration in the beads and a null concentration in the culture medium. A same initial concentration of free and encapsulated cultures corresponds to two different spatial distributions as free microalgae are almost uniformly distributed. After 10 days (237 hours) of culture, the normalized dry weight obtained in free algae cultures (13.9) is significantly higher (4 times higher) than the normalized dry weight measured with encapsulated algae (3.5).

If measured between day 0 and 8 (before the stationary phase is reached for encapsulated algae), the growth rate is 0.31 day^{-1} for free algae and 0.16 day^{-1} for encapsulated algae. This represents a growth inhibition of 49 %, higher than in the literature: between 13 and 36 % (Ferro et al., 2012; Homburg, Venkanna, et al., 2019). However, a longer lag phase for encapsulated algae than for free algae can be noticed the first two days. If the exponential growth phase of encapsulated cells is considered between day 2 and 8, the growth rate is 0.15 day^{-1} for encapsulated algae and 0.19 day^{-1} for free algae, corresponding to a 19 % difference, in better agreement with inhibition values reported in literature for *Chlamydomonas reinhardtii* (Ferro et al., 2012). It is important to note that these results strongly depend on the strain, the culture conditions, the encapsulation material, the time of reticulation and the concentration of the reticulation solution, the needle diameter, the height of the needle compared to the reticulation beaker… All these parameters have an influence on bead diameter and permeability thus an influence on the growth. Hence results obtained here are in the same order of magnitude than in literature but results of studies using different conditions cannot be accurately compared.

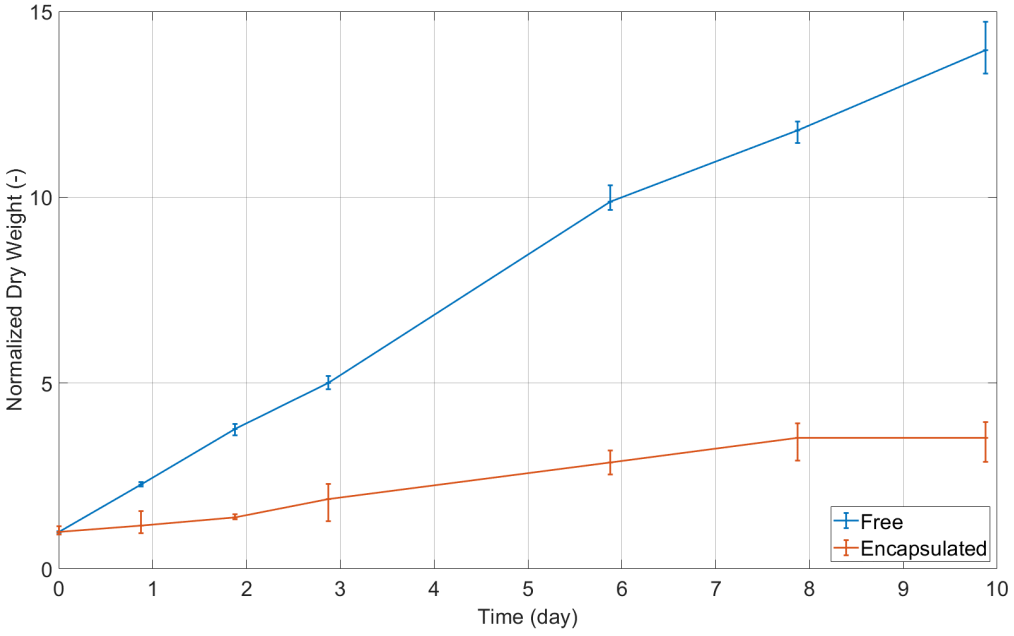

Figure 2.11 – Growth of Chlamydomonas reinhardtii cultivated in flasks as free or encapsulated in alginate (without PDADMAC in the reticulation solution). Mean dry weight of three free and three encapsulated cultures in TMP 4x. Dry weights are normalized (divided by the initial dry weight).

2.3.2 Culture in photobioreactor

2.3.2.1 Growth

Two cultures are realized successively in the 5 L photobioreactor (Figure 2.12). Different parameters are followed during the cultures: dry weight, temperature, pH, dissolved oxygen and nutrients concentration. Cultures are stopped when algae can be visually detected in the culture medium due to cell leakage from beads. Cell leakage occurred slightly from day 19 and more importantly on day 24 (end of culture) for culture 1. During culture 2, few algae grow in the culture medium from day 17. The culture is stopped on day 21. Hence the cultures lasted more than 20 days, even if no PDADMAC (commonly used to obtain a more robust material) is used. It is a longer time than most of other cultures of encapsulated algae in alginate in photobioreactor described in the literature, which last maximum 10 days (Cheirsilp et al., 2017; Kitcha & Cheirsilp, 2014; Lam & Lee, 2012; Ross & Pott, 2021). It should be taken into account that this time depends obviously on the initial cell concentration and the duration of growth, which is particularly long in this case due to a low light intensity input. This prolonged time shows that the encapsulation material is adapted to the conditions used for the culture. Moreover, it suggests that the designed photobioreactor provides low shear stress which could damage the beads.

Beads of encapsulated algae are sampled every day to measure the dry weight in the 5 L photobioreactor (as explained in Methods 2.2.4.2). Growth curves of culture 1 and 2 show a long lag period of 2 days. Then a low growth occurs during day 3 and 4 before a fast growth between day 4 and 6. Then, an almost constant growth occurs until the end of the growth, on day 20.

It can be noticed that final dry weights are globally low. This can be explained by a rather low light intensity (60 $\mu E.m^{-2}.s^{-1}$ on the reactor wall) and the low concentration in biomass at the beginning of the cultures.

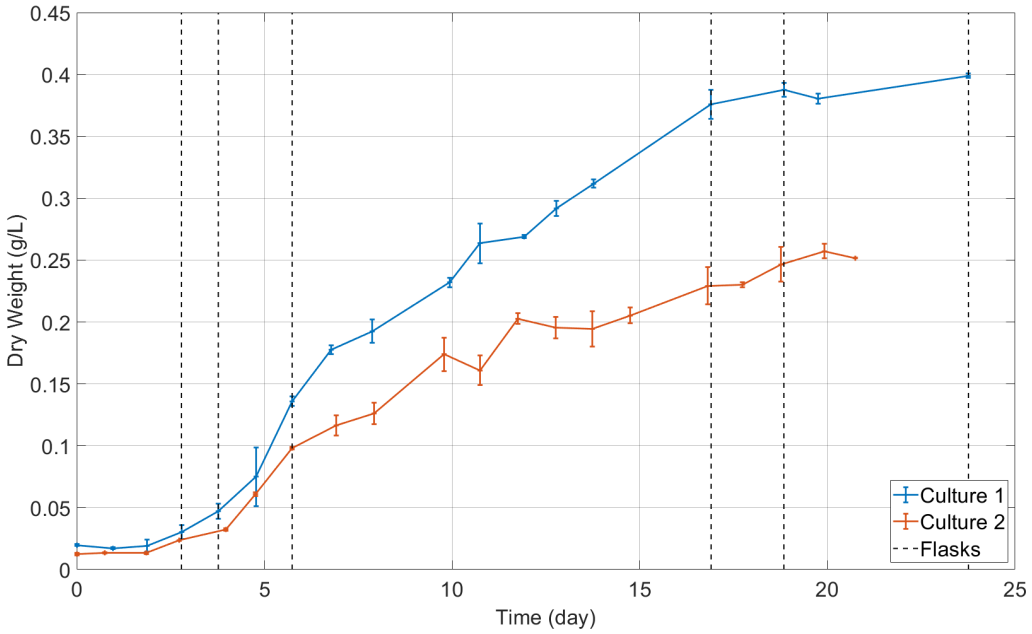

Figure 2.12 - Growth of Chlamydomonas reinhardtii encapsulated in alginate cultivated in a 5 L photobioreactor. Error bars correspond to the two duplicates of 9 beads used to measure dry weight.

Hence, not only the encapsulation material is robust enough to cultivate the algae more than 20 days but also has a suitable permeability to nutrients and transparency to grow algae. Indeed, the microscopic

observation of a cross section of a bead indicates that algae grow in the center of the bead as well as near their surface (Figure 2.13). A lack of nutrients or light in the center of the bead would lead to the death of cells. Furthermore, the photobioreactor provides a low shear stress but allows a sufficient mixing, which has an impact on mass transfer and light access for beads, to grow well this alga. It is a challenge in cultivating encapsulated microalgae. The encapsulation material and the design of the reactor are thus effective to grow encapsulated algae.

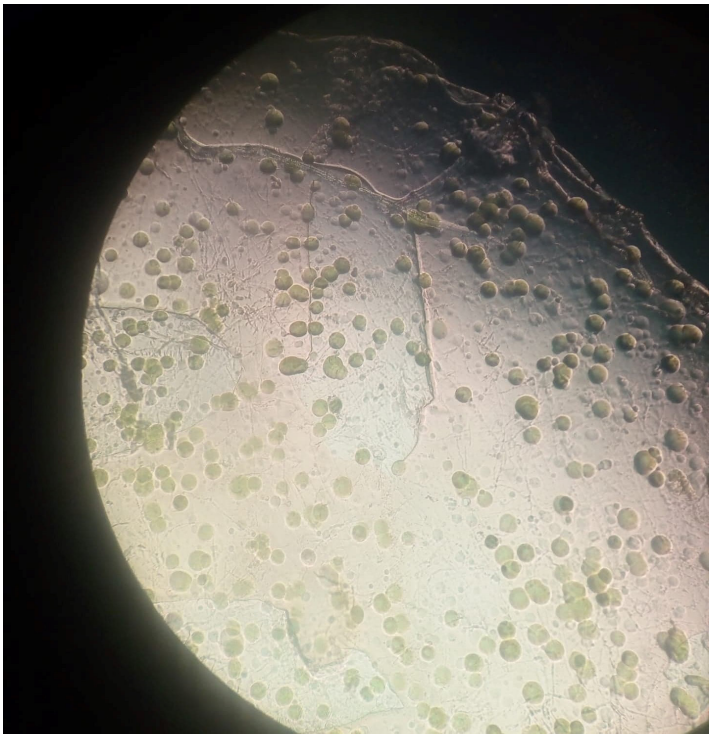

Figure 2.13 – Cross section of an alginate bead (obtained by cross-linking with $CaCl_2$) of around 3 mm of diameter containing encapsulated Chlamydomonas reinhardtii. The bead has been cut using a scalpel.

Measured dry weight of culture 2 is significantly lower than the dry weight of culture 1 (Figure 2.12). However, it should be noticed that the volume of solid in the reactor is unintentionally different for both cultures. The volume of solid in culture 1 is 4.3 % while the volume in culture 2 is 3.8 %. As the dry weight is calculated according to the total volume of solid in the reactor, this has an impact which can explain the dry weight difference between both cultures. Dry weights are normalized (divided by their initial concentration) to be compared (Figure 2.14). Once normalized, growth curves of dry weights are very close. This shows the very high influence of initial dry weight on the growth. The growth rate of culture 1 between day 4 and day 17 is 0.16 day^{-1} while it is 0.15 day^{-1} for culture 2. Between day 4 and 19, growth rate is 0.14 day^{-1} for both cultures. Hence, even if only two cultures are performed, experimental results are highly repeatable.

From the beginning of culture 2, some beads (approximately evaluated at ¼ of the total) are less colored (contained less algae) than most beads and this difference remained visible during the entire culture. These beads are not isolate from the others before the dissolution and measurements of dry weight. Then the proportion of light beads is random in the two duplicates of 9 beads used to measure dry weight. The uncertainty of the measure is then higher than for culture 1 and can perhaps explain the fluctuating dry weights measured on day 10, 11, 12.

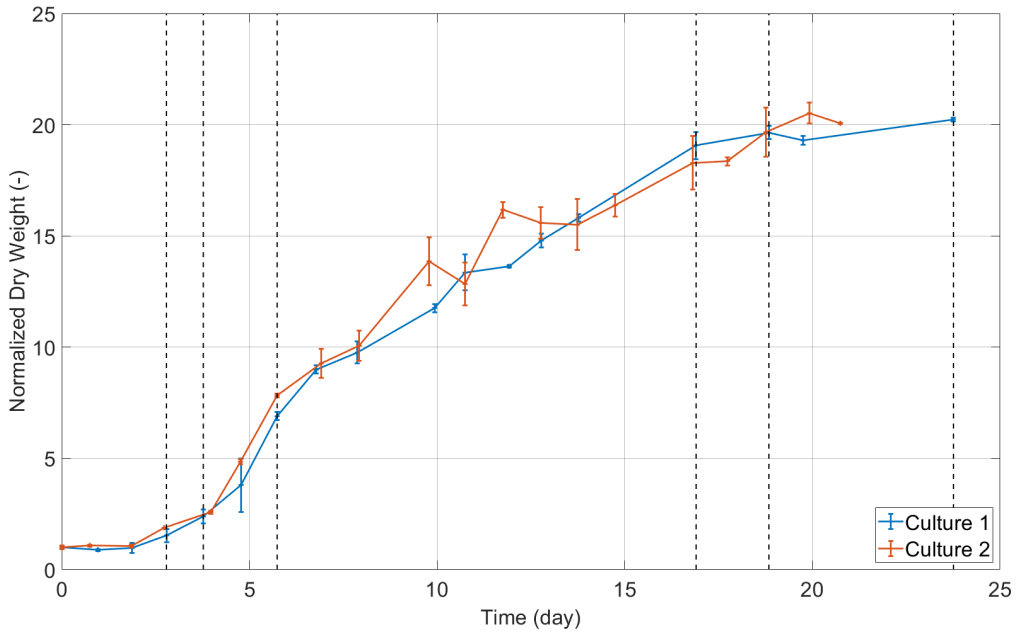

Figure 2.14 – Normalized dry weights of two cultures of Chlamydomonas reinhardtii encapsulated in alginate cultivated in 5 L photobioreactor. Error bars correspond to the two duplicates of 9 beads used to measure dry weight.

Bacterial proliferation is observed as the culture medium becomes turbid from day 3 in both cultures (Figure 2.15). Microscopic observation validated this assumption, but bacteria cannot be identified. They can come from the inoculum or the reactor. This one was sterilized using bleach but must be rinsed 5 times with filtered distilled water because of dead zones of the reactor. Bacterial proliferation in microalgae culture is quite usual, even in closed systems (Fulbright et al., 2018). In the studied photobioreactor, where the culture medium and algae are not mixed, bacteria are particularly visible compared to a classic photobioreactor used for the culture of free microalgae. Moreover, bacterial proliferation is favored by the absence of algae in the culture medium (no competition for nutrients). The UV disinfection system (25 W) situated in the external liquid loop is not sufficient to stop bacterial proliferation in this case. The impact of bacteria on algae growth is not well known. Some studies observed a negative impact of bacteria for algae because of competition for limiting nutrients or secretion of inhibitory compounds by bacteria (pigments or substances which cause algal lysis) (Cole, 1982; Mayali & Azam, 2004). Bacteria are often considered as contaminants in photobioreactor. However, a positive impact of bacteria on microalgae growth was measured by several teams (Amin et al., 2009; Foster et al., 2011; Kazamia et al., 2012). For example, vitamin B12 or iron synthetized by bacteria are used by algae. Delucca-1977 found a positive impact of two bacteria on growth of a *Chlamydomonas* strain but an inhibition when co-culturing both bacteria. Hence the influence of bacterial proliferation on microalgae growth really depends on the bacteria and algae strains. Without identification of the bacteria, which could be different in both cultures, and a comparison with an axenic culture, no conclusions can be drawn on the impact of bacteria on growth of this alga.

a) 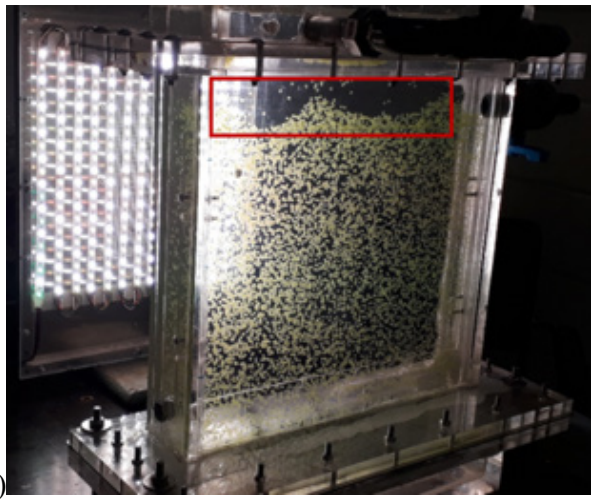 b) 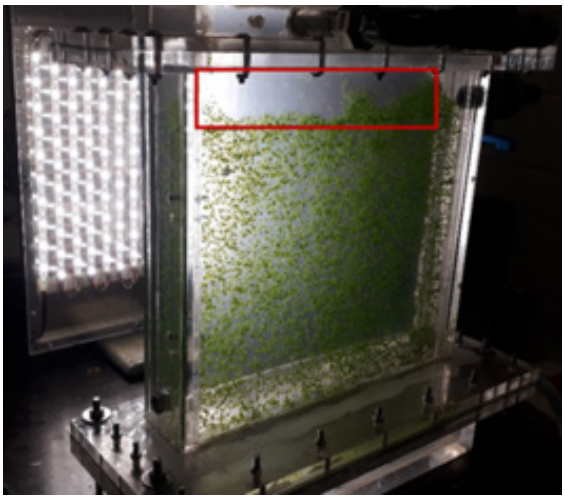

Figure 2.15 – Photographs of the 5 L photobioreactor containing encapsulated Chlamydomonas reinhardtii. Pictures taken during culture 1 on day 1 (a) and day 5 (b) to show turbidity of the culture medium due to bacterial proliferation on day 5. Zones where bacteria are visible are indicated by a red rectangle.

2.3.2.2 Culture conditions

2.3.2.2.1 Temperature

The temperature of the culture medium is followed in the external loop. The temperature is regulated at 25 °C using a heat exchanger and a thermostatically controlled bath. For the culture 1, the regulation is fine (mean of 24.5 °C), even if the temperature difference between night and day is around 2 °C (Figure 2.16). However, for the second culture, the ambient temperature is higher and the regulating system is not able to cool the medium sufficiently. A technical problem made unable to save data between day 1 and 5. The culture begins around 27 °C and increases around 30 °C. The mean temperature of culture 2 is 28.1 °C.

The influence of temperature on alginate polymerization is well known. High temperature depolymerized alginate (Moe et al., 1992). The difference of 3.6 °C between the two cultures could explain that cell leakage occurs earlier in culture 2 because of alginate degradation due to higher temperature. However, it seems not to impact growth as both cultures have similar growth. The temperature can also have an influence on bacterial proliferation in the reactor (Antoniou et al., 1990; Pomeroy & Wiebe, 2001).

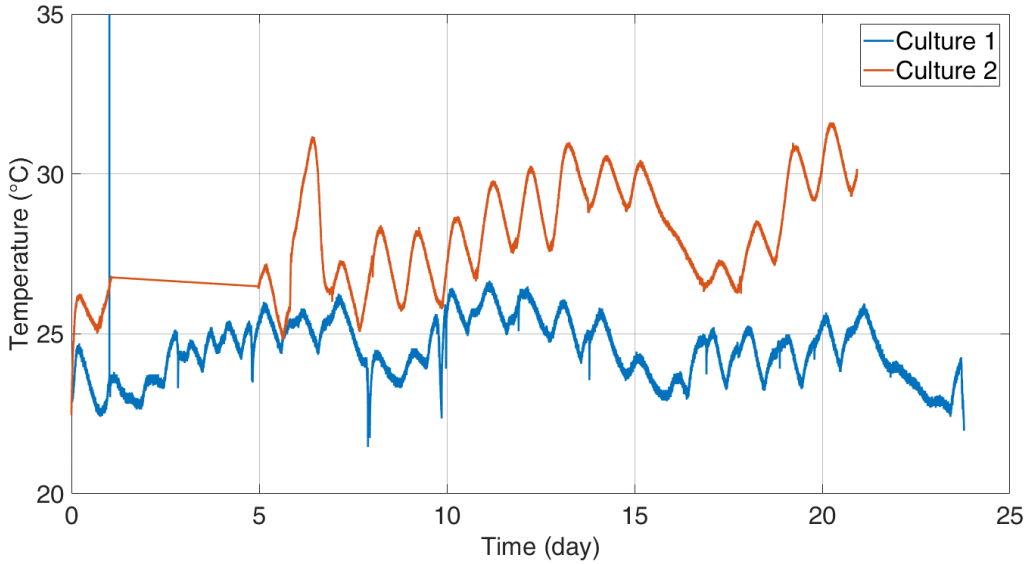

Figure 2.16 – Evolution of the temperature (°C) of the culture medium of culture 1 and 2.

2.3.2.2.2 pH

pH is regulated by CO_2 at pH 7.2. However, the volume of liquid (15 L) is much higher than the volume of solid containing microalgae (220 mL). Hence the photosynthesis of the microalgae is not sufficient to increase pH, at least after day 2 (Figure 2.17). This is why CO_2 is not injected to decrease the pH. On the contrary, after bacterial proliferation on day 2, pH decreases drastically to around 6.7. The same phenomenon is observed in culture 2 but cannot be studied in detail due to a technical issue to save data from day 1 to day 5. This suggests bacteria acidify the culture medium. Sudden pH increases are due to manual injection of NaOH in order to increase pH (day 5 and 8 of culture 1 or day 12 of culture 2). Gradually increase of pH due to photosynthesis can be observed between day 13 and 16 of culture 1 and between day 15 and 17 of culture 2.

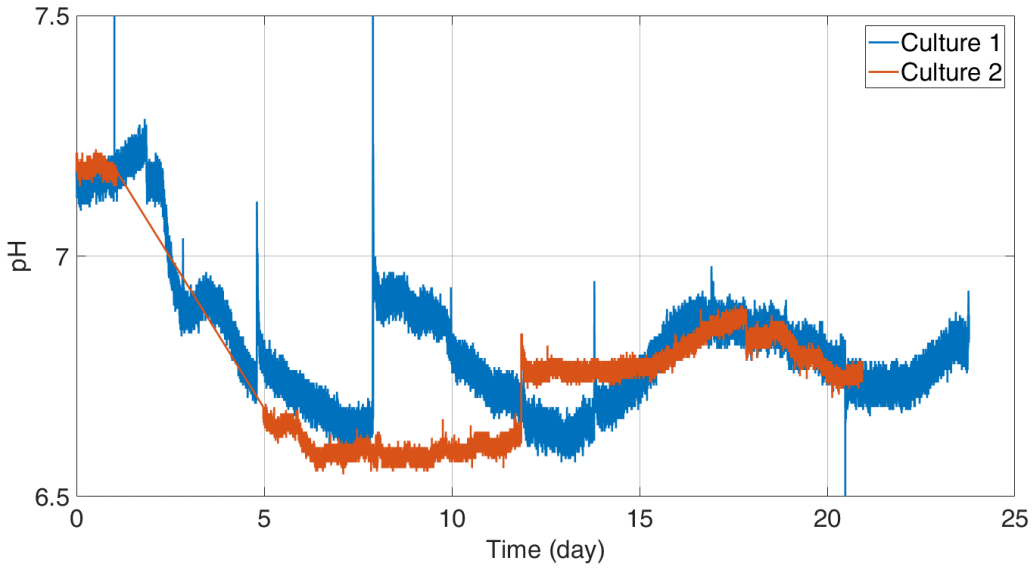

Figure 2.17 - Evolution of the pH of the culture medium of culture 1 and 2.

2.3.2.2.3 Dissolved oxygen

In the studied reactor, the dissolved oxygen decreases drastically (Figure 2.18). Conclusions which can be drawn from dissolved oxygen evolution in culture 1 are the same as the ones discussed for pH. Due to technical reasons, oxygen concentration in culture 2 is not followed. Dissolved oxygen concentration approximately follows pH evolution. It increases the two first days before it falls between day 2 and 3. This corresponds to the appearance of bacteria in the culture medium, which means that the bacteria present in the culture medium are most likely aerobic. Dioxygen concentration remains then low except straight pics due to pump stops for injection of NaOH to increase pH. Between day 14 and 17, a lower increase of oxygen can be observed which corresponds to an increase of the pH associated to microalgae metabolism (between day 13 and 16). The same appears at the end of the culture in days 23 and 24. Once again, the low volume of solid thus of algae (220 mL) compared to the volume of culture medium, thus bacteria (15 L), can explained this unusual result.

Few studies are dealing with the influence on low concentration of oxygen on the microalgae growth as the situation is unusual in photobioreactors, but it is worth noting that the studied reactor is under continuous illumination, thus algae do not need oxygen for respiration. One may note that, in applications related to wastewater treatment, microalgae are deliberately grown simultaneously to bacteria (Bilanovic et al., 2016; Vargas et al., 2016). These studies are based on a symbiotic relationship between bacteria and microalgae, as supposed in the studied 5 L photobioreactor, where the oxygen produced by algae helps bacteria growth which produces CO_2 useful for algae. This enables to obtain a higher growth rate, a better removal of ammonium and nitrogen and to prevent accumulation of oxygen in the system. These studies highlight the growth inhibition of low oxygen concentration for bacteria but not on microalgae. Hence, in any case, it can be assumed that no inhibition should occur because of low dissolved oxygen concentration.

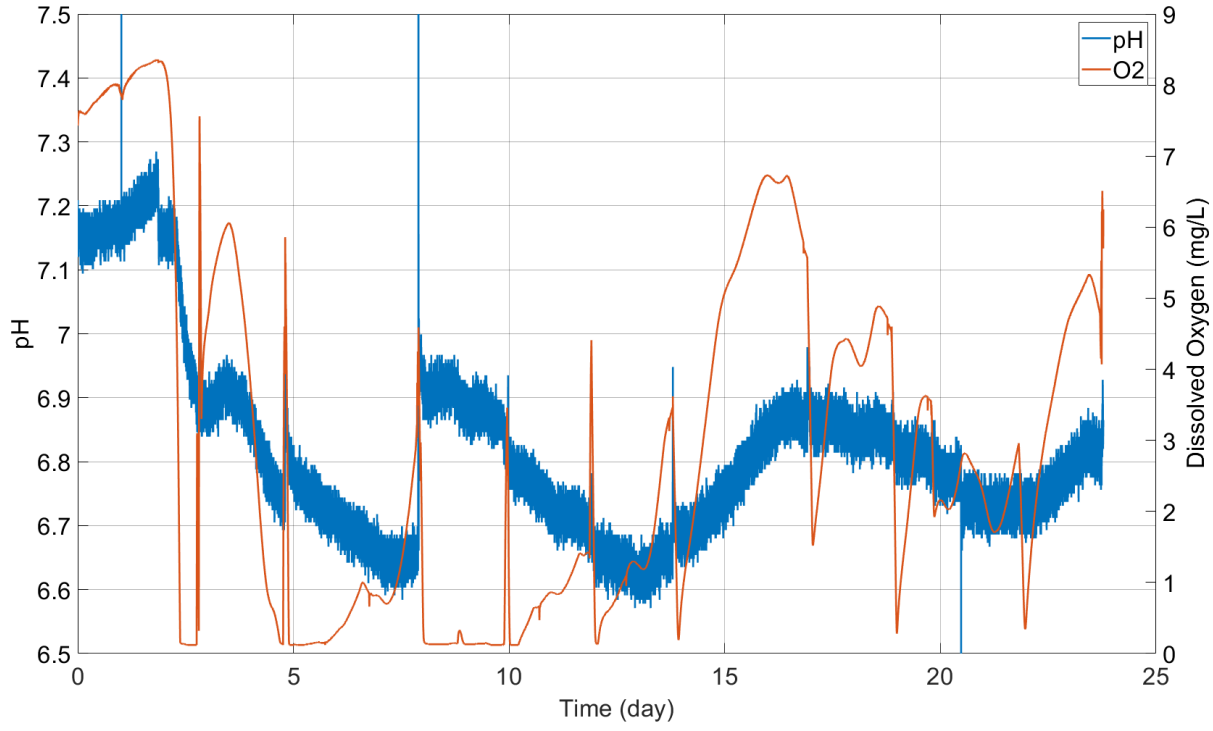

Figure 2.18 - Evolution of the dissolved oxygen and pH in the culture medium of culture 1.

2.3.2.3 Nutrients

TMP 4x (TMP concentrated 4 times) is used in the culture in the reactor of 5 L. PO_4^{3-} and NH_4^+ ions are dosed at the beginning and at the end of each culture (Table 2.3). Concentrations at the beginning of the culture are closer to TMP 2x (310 $mg.L^{-1}$) for PO_4^{3-} and TMP (400 $mg.L^{-1}$) for NH_4^+ than TMP 4x even if concentrations of stock solutions correspond to TMP 4x. It must be noticed that a standard is used for PO_4^{3-} but not for NH_4^+ ions so absolute values of NH_4^+ concentration are not reliable. These unexpected concentrations can be due to precipitation because of low temperature conservation or precipitation on the 0.22 µm filter.

Nutrient concentrations logically decrease during both cultures, but residual concentrations, at the end of cultures, are still quite high, not so far from the initial ones. In culture 1, PO_4^{3-} and NH_4^+ decrease by 33 % and 31 % respectively. In culture 2, PO_4^{3-} and NH_4^+ decrease by 19 % and 25 % respectively. Higher consumptions in culture 1 are related to a higher biomass. These results show the cultures are not limited by nitrogen or phosphorus nutrients as concentrations at the end of the culture are still close to TMP medium. As the volume of liquid is significantly higher than the volume of solid, unexpected low concentrations at the beginning of the culture do not impact the culture.

Table 2.3 – Evolution of phosphates and ammonium during culture 1 and 2 in the photobioreactor of 5 L.

Day	Concentration ($mg.L^{-1}$)	
	PO_4^{3-}	NH_4^+
Culture 1		
3	300	460
10	210	340
19	200	320
Culture 2		
1	350	490
21	280	360

2.3.3 Comparison of growth in photobioreactor and flasks

It is possible to compare the growth of encapsulated algae in flasks and in the photobioreactor as the same strain is used, encapsulated in the exact same conditions. However, it is important to notice that the algae are not grown in the exact same culture conditions. Nutrients concentration in culture medium are different in flasks and in the photobioreactor as the volume of culture medium in the reactor is more important due to the external loop. But nutrients concentrations of the TMP 4x medium used in flasks are really close to the one used by Takache, 2010. They measured that this nutrient concentration allows to reach a dry weight of 2 $g.L^{-1}$ (0.1 $g.L^{-1}$ is reached in flasks) and is not limiting culture below this biomass concentration. Nutrient limitation or inhibition in flasks is thus highly unlikely. The temperature of the room where the flasks are agitated is not easily controlled (between 20 °C and 25 °C) and not recorded, so is difficult to compare with the reactor. Bacteria proliferate in the reactor but are not visible in flasks. Supplement of CO_2 is finally not added in the reactor so the CO_2 comes from transfer with atmosphere, as in flasks. The exchange surface between atmosphere and culture medium is higher in case of flasks compared to the total volume of medium. The culture medium of the reactor containing no TRIS (buffer used in flaks to keep a pH equal to 7.2) as the pH regulation is supposed to occur with CO_2. The light sources are different as neon tubes are used to enlighten flasks and LED panel is used for the reactor. The light intensity on the orbital shaker of flasks is 70 $\mu E.m^{-2}.s^{-1}$ while it is 60 $\mu E.m^{-2}.s^{-1}$

on the illuminated side of the reactor. However, the light attenuation by glass cannot be quantified in the flasks. The light attenuation through beads is not the same as the thickness of the bead bed is different. The light goes through maximum 2 beads in flasks while it is attenuated by up to 8 beads in the reactor. Hence differences can be identified between the culture in flasks and in photobioreactor, but they are mostly in favor of growth in flasks (CO_2 and light). The main difference, that cannot be evaluated, is the presence of bacteria.

Several differences can be highlighted between growth curves obtained in flasks and in the photobioreactor (Figure 2.19). Dry weights are normalized to be compared. The lag phase (between day 0 and 2) is more important in the photobioreactor (growth of -0.01 day^{-1} (negative growth in culture 1) and 0.03 day^{-1} in culture 2) than in flasks (0.17 day^{-1}). However, the growth in flasks ends on day 8 while it ends on day 17 in the photobioreactor. Moreover, the growth rate between day 2 and 8 (exponential phase) in flasks is lower (0.16 day^{-1}) than the ones of the culture 1 (0.38 day^{-1}) and 2 (0.37 day^{-1}) in the photobioreactor. Cultures in photobioreactor enables also to get higher final dry weights. The algae grow thus more efficiently in the photobioreactor than in flasks, even if conditions are mostly more favorable in flasks (except for the impact of bacteria which cannot be evaluated). Hence the design of the photobioreactor is very satisfactory and suitable for the culture of encapsulated algae.

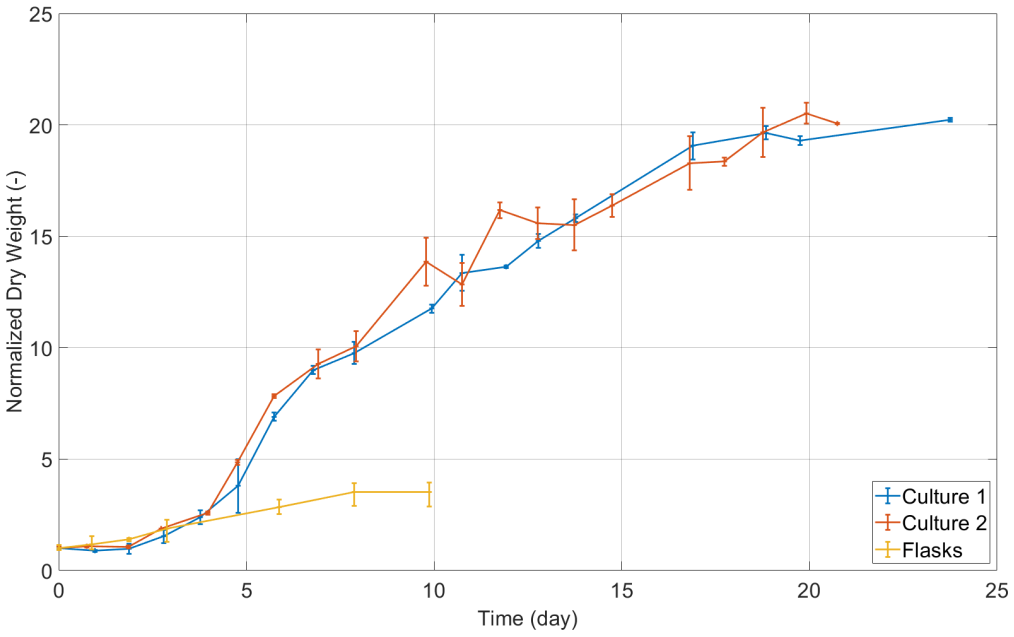

Figure 2.19 – Comparison of growth of Chlamydomonas reinhardtii encapsulated in alginate cultivated in 5 L photobioreactor (culture 1 and 2) and flasks.

2.4 **Conclusions**

The aim of this chapter is to improve knowledge of encapsulated microalgae behavior in terms of growth, metabolite extracellular secretion and culture at large scale. A strain of *Chlamydomonas reinhardtii*, which is genetically modified to secrete extracellularly *Gaussia princeps* luciferase, is studied. Microalgae are encapsulated in alginate beads by cross linking with $CaCl_2$. An innovative photobioreactor is tested in which beads are fluidized with liquid (culture medium) only.

Depending on the strain or encapsulation conditions, encapsulation can have a beneficial effect but have, most of the time, a negative impact on growth. Growth of free and encapsulated *Chlamydomonas reinhardtii* are compared in flasks. During the exponential phase, a 19 % growth inhibition for encapsulated algae is measured, similar to results obtained in the literature.

While they are mostly used in wastewater treatment, encapsulated algae can be used to produce high added value metabolites. Encapsulated *Chlamydomonas reinhardtii* is cultivated to recover luciferase in the culture medium. The secretion occurs during the growth phase only. It is shown that the encapsulation material is not adapted for recovering luciferase in the culture medium. The strain is nevertheless cultivated at a larger scale as a proof of concept but only the algae growth is monitored, and luciferase is not dosed.

A challenge for the culture of encapsulated microalgae is the scale-up. In this chapter, the biological characterization of a fluidized bed photobioreactor of 5 L is performed. The reactor is efficient to cultivate microalgae as it enables to grow them during almost 20 days without cell leakage, which proves it provides low shear stress but enables sufficient mixing.

Bacteria proliferate in the reactor despite chemical sterilization. They are identified and their impact on microalgae growth cannot be evaluated. Two cultures are performed and show very close growth curves after normalization. This shows the good repeatability of experiments. As the volume of culture medium is important compared to the volume of beads containing microalgae and because of bacterial proliferation, the pH and dissolved oxygen decrease most of the time. As the pH is kept in acceptable range (over 6.6), this has not a significant negative impact on the culture.

Hence, it was possible to cultivate a genetically modified strain of *Chlamydomonas reinhardtii*, encapsulated in alginate, in a 5 L photobioreactor. Even if the comparison is uncertain, as conditions are not exactly the same, growth in the photobioreactor is more efficient than in flasks. Growth lasts for almost 20 days which shows the efficiency of the encapsulation material and of the photobioreactor. This biological characterization is useful for developing a global model of the reactor. The experimental results can be used to fit the parameters of the biological model and to validate the global model.

3 Hydrodynamic characterization of the liquid phase

This chapter corresponds to the article entitled “Hydrodynamic Characterization of a Non-conventional Photobioreactor” (Klara Weck, Sébastien Calvo, Angélique Delafosse, Dominique Toye) published in Chemical Engineering & Technology, Volume 44, pp. 1803-1813. https://doi.org/10.1002/ceat.202100076

3.1 Introduction

As the attention in microalgae products is increasing worldwide, photobioreactor scale-up is becoming a wide challenge for microalgae culture. Indeed, microalgae growth in large-scale photobioreactor does not reach the growth achieved at small scale (flasks). This is explained by the changes of microenvironment experienced by microalgae: temperature, pH, nutrient intake, mass transfer of CO_2 and O_2 and light supply. These parameters are largely influenced by hydrodynamics (Takache, 2010). Indeed, the latter has a key role in photobioreactor performance as it influences directly mixing (thus nutrient availability and CO_2 transfer) and light supply to microalgae. Mass transfer of gas and nutrients can be a critical scale-up parameter if mixing at large scale is inefficient. Growth depends mainly on light supply but light distribution is a function of biomass concentration thus cannot be easily controlled inside the photobioreactor. Indeed there is a light gradient inside a photobioreactor due to microalgae absorption and scattering (self-shading of algae). The zone close to the reactor walls is strongly illuminated, while the region far from the walls is a darker zone, where the light can potentially not penetrate if the algae concentration is high. Light absorption can be characterized but is hard to optimize in culture with high biomass concentration. This is the reason why light is most often considered as the most limiting scale up parameter (Legrand, 2016). According to Molina Grima et al., 1999, the global characterization of the time spent by algae cells in illuminated and in dark zones is not sufficient to fully quantify a photobioreactor productivity. A special attention must also be paid on the frequencies at which cells go from an illuminated to a darker zone. To get information and control these frequencies, a deep knowledge of the algae circulation is required. This can be achieved by studying the hydrodynamics in the reactor (Luo & Al-Dahhan, 2004).

The need to perfectly describe hydrodynamics in photobioreactors has led researchers to use models of increasing complexity to characterize the flow inside them (Bitog et al., 2011; Nauha & Alopaeus, 2015; Pires et al., 2017). Computational Fluids Dynamics (CFD) has proved to be a powerful and accurate tool to simulate and describe concentration gradients of nutrients and CO_2 in the reactor. Moreover it can be used to describe cell trajectories, and thus times and frequencies they spend in light or dark zones, and ultimately improve photobioreactor scale-up.

The objective of the present work is to develop a 3D CFD model to describe hydrodynamics in a fluidized bed photobioreactor specifically designed to cultivate encapsulated microalgae. Encapsulation consists in algae entrapment in a polymeric matrix to form spherical beads of around 3 mm of diameter. It facilitates the microalgae harvest and the recovery of metabolites of interest if excreted out of the encapsulation matrix, without requiring any further downstream processing except concentration. It is thus a promising solution to switch to continuous processes, while limiting contamination risks (Cheirsilp et al., 2017; Vílchez et al., 1997). However, the industrial feasibility of this innovative production technology is not yet assessed due to the lack of large-scale experiments involving encapsulated microalgae. A fluidized bed technology has been chosen for the culture of encapsulated algae because it allows a good distribution and circulation of beads in the photobioreactor. Gas as well as liquid can be used to fluidize the encapsulated microalgae, liquid has been chosen in the present case. The photobioreactor has been thus designed as a two-phase liquid (culture medium) - solid (beads) reactor. The reactor has proved to be effective to grow *Chlamydomonas reinhardtii* genetically modified to secrete *Gaussia* luciferase (recombinant protein). As microalgae are encapsulated and thus protected, hydrodynamics has no particular effect on them except via the influence of the latter on nutrient distribution. On the contrary excessive hydromechanical stress may significantly affect the encapsulation matrix, leading to bead breakage and algae leakage.

The flow regime in the reactor is laminar but unsteady. This kind of regime is mostly studied either in microreactors, pipes or to study waterhammer phenomena (Brunone et al., 2004; Dreher et al., 2009; Schohl, 1993; Yuan & Isaac, 2017; Zalc et al., 2002). Studying unsteady laminar flow in a rectangular flat reactor of this volume using a low viscosity fluid as water is thus rather unusual. The occurrence of

this kind of flow regime in the present case is most probably due to instabilities induced by the reactor configuration (internal panel and off-centered inlet) similar to Von Karman vortex shedding (Park et al., 1994).

To validate the CFD model, Particle Image Velocimetry (PIV) measurements have been performed in the photobioreactor filled with water. PIV gives access to an Eulerian characterization of the fluid flow. A transparent reactor is needed to use this non-intrusive technique, which is not limiting in the case of photobioreactors. PIV is a well-known method to validate CFD models, on the basis of velocity field comparisons (Alimohammadi et al., 2016; de Lamotte et al., 2018; Lamberto et al., 1999; Xie et al., 2018). Both methods are complementary: using simulations reduces time and costs of numerous experiences and PIV enables to obtained information on hydrodynamics truly happening in the reactor (as long as the experimental error is considered). It is particularly important when using a non-conventional reactor geometry as in the present work. As a first step, the CFD model is developed and validated for a single-phase flow (liquid only). As the bead density (1018 $kg.m^{-3}$ at 20 °C) is very close to water density, the assumption is made that the beads motion almost follows the liquid flow and has a minor influence on it. In the context of an initial analysis, a single-phase approach gives thus a representative idea of the liquid flow within the reactor. Moreover, it will give information on the solid global behavior.

3.2 Materials and methods

3.2.1 Photobioreactor setup

The photobioreactor is a two-phase flow fluidized bed reactor (Figure 2.3) involving beads of encapsulated microalgae as solids and culture medium as liquid. It is a flat, rectangular reactor of 38 cm height, 34 cm width and 4 cm depth, made of transparent Plexiglas. The working volume is around 5 L and the wall thickness is 8 mm. Liquid is pumped in an external loop and injected at the reactor bottom through an off-centered slit. The slit is 1 mm thick and extends over the entire reactor width. This liquid upflow ensures the fluidization of beads. A liquid flow rate of 400 $L.h^{-1}$ has been chosen, which corresponds to the one required to fluidize a 4 %v solid volume fraction. An internal wall of 6 mm thickness enables to control the circulation inside the reactor and the homogeneous distribution of beads. As a consequence of the off-centered liquid inlet and the internal panel, the flow is ascending on one side of the internal panel and descending on the other side. A prism is set at the bottom of the reactor to avoid the formation of a dead zone and forces the circulation of the beads at the reactor bottom. At the top of the reactor, the beads are kept in the reactor thanks to a grid. The external loop is also used to control the culture medium conditions (pH and temperature regulation).

3.2.2 PIV setup

The camera used is a CDD camera (Dantec Dynamics, Flowsense EO 4M-32, 2048_2048 pixel, 32 Hz) equipped with a macro lens (Zeiss, Makro-Planar T* 2/50 ZF, 50 mm, f/2.0) and an orange filter (527-532 nm wavelength). The pulsed laser used is a YAG laser (Litron, DualPower 65-15, 2x65 mJ at 15 Hz, 532 nm). The camera and the laser are synchronized using a trigger unit (Berkeley Nucleonics Corporation, Model 575 Pulse/Delay Generator). The time between laser pulses (i.e. between two images used to calculate instantaneous velocities) used is 10 ms. The images are processed using the Dantec software (DynamicStudio 2015) to enhance the contrast between the polyamide tracer particles and the liquid. Adaptative PIV method is used to calculate velocities in 64x64 $pixel^2$ interrogation areas, which corresponds to 11.8x11.8 mm^2. Results are then further analyzed using Matlab codes (Matlab R 2018 A).

To perform PIV measurements, the reactor was filled with water (density and viscosity very closed to culture medium) seeded with polyamide particles with diameters of 1-20 µm and a density of 1030 $kg.m^{-3}$. PIV measurements were realized on the liquid phase only. The global flow motion is similar in a single or two-phase flow configuration, in the ascending section as well as in the descending section. As the beads density is close to water (1014 $kg.m^{-3}$ at 20 °C), the liquid flow will not be impacted by the solid.

PIV measurements are performed in 5 planes distributed along the depth of the reactor: planes 1, 2 and 3 are situated in the descending section, while planes 4 and 5 are in the ascending section (Figure 3.1). The laser is flashing orthogonally to the reactor depth, while the camera is placed orthogonally to the reactor front. Plane 1 is the closest to the camera. It is positioned at 3 mm from the reactor wall. Planes 2, 3, 4 and 5 are positioned at 8, 18, 28 and 34.7 mm from the reactor wall, respectively.

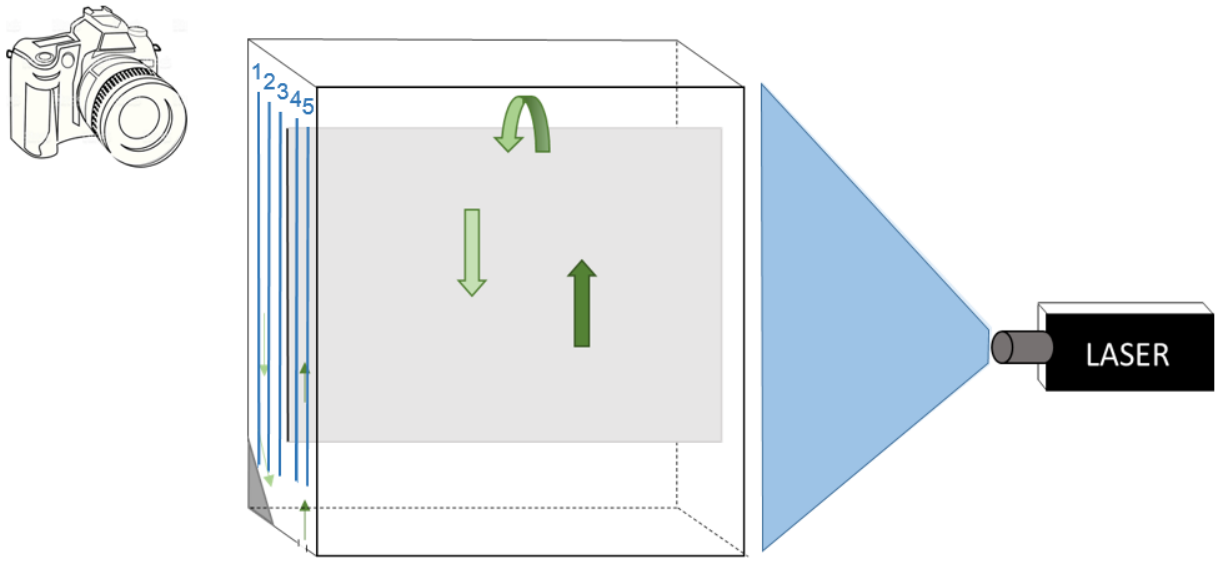

Figure 3.1. PIV setup to characterize the photobioreactor. A laser flashes towards the depth of the reactor while camera is taking photos in front of the reactor. Five planes have been characterized by PIV: two in the ascending section and three in the descending flow section.

3.2.3 CFD parameters

CFD simulations are performed using Fluent software (ANSYS, 2019 version R3). The geometry was drawn on DesignModeler software (ANSYS, 2019 version R3). The inlet slot has been drawn as a cubic inlet, with a 1 mm side. The mesh was developed using Meshing software. The grid was optimized to get accurate results in a reasonable computation time. It is composed of around one million of hexahedrons. The mean edge size of the mesh is 1.7 mm (minimum size: 0.8 mm and maximum size: 2.7 mm). A “mass flow inlet” and a “pressure outlet” boundary conditions are used. Pressure and velocity are coupled using the SIMPLE scheme. To solve the momentum equation, a second order upwind scheme is adopted while PRESTO! is used for pressure. Time is discretized using a bounded second order implicit method. The optimal time step is found to be 0.02 seconds which leads to a Courant number of 0.3. The flow inside the photobioreactor is solved using the “laminar model”.

3.3 Results

3.3.1 PIV results

3.3.1.1 PIV data treatment

Figure 3.5 presents an example of instantaneous velocity field measured by PIV on plane 3. Color scale represents velocity values ($m.s^{-1}$). It is worth noticing that inlet velocities (at the reactor bottom – white zone on the figure) cannot be measured by PIV due to the prism set at the bottom of the reactor which hides the liquid flow in this part from the camera view (below 50 mm height).

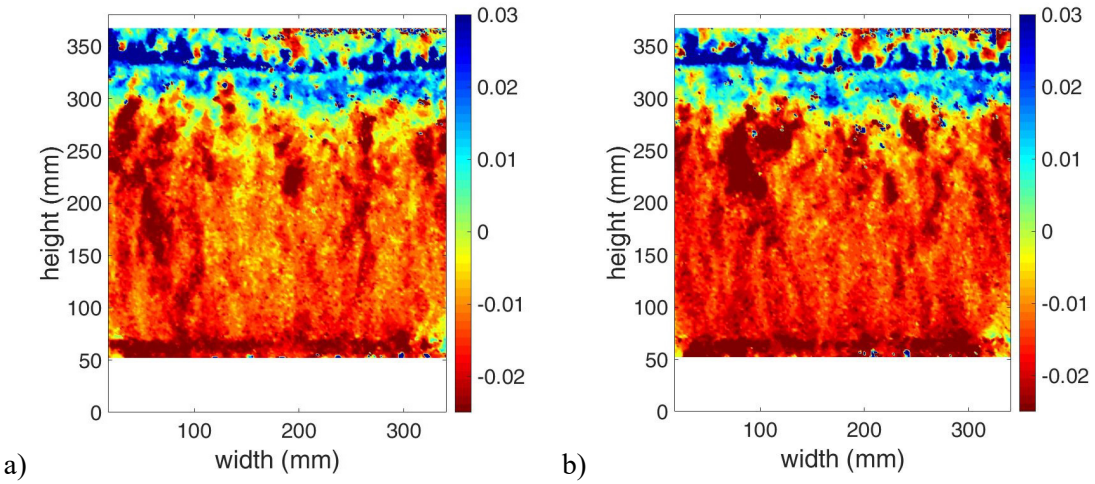

Figure 3.2. Instantaneous velocity field ($m.s^{-1}$) measured by PIV in plane 3 situated at 18 mm from the front reactor wall.

Velocity values in this plane are mainly negative as plane 3 is situated in the descending section of the reactor. The time evolution of velocities measured in different points of the plane shows that velocities oscillate between a minimum and a maximum value, without ever reaching a constant steady state value (Figure 3.3). Hence PIV results indicate the flow is unsteady.

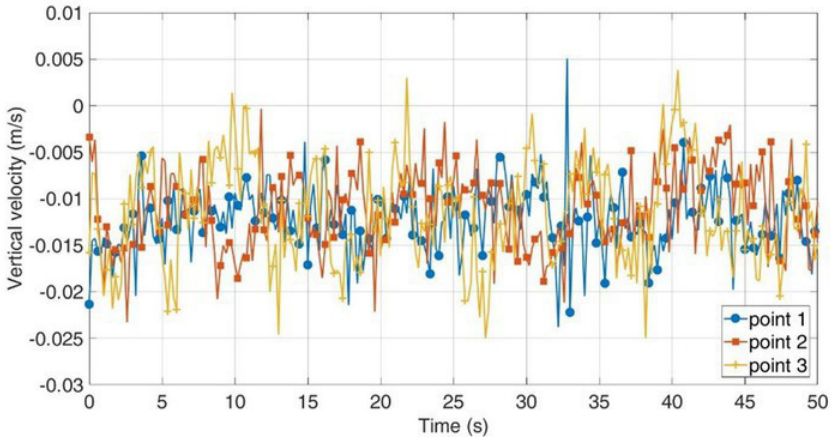

Figure 3.3 - Vertical velocities fluctuations as a function of time for 3 points on plane 3 obtained by PIV. The coordinates (mm) of the three points studied are: 1(175,150), 2(175,200), 3(175,250).

As the flow is unsteady, it cannot be analyzed based on a single instantaneous velocity field. Statistically representative time averaged velocities and time averaged fluctuations around these time averaged velocities can be calculated provided that a sufficient number of images are considered. To this aim, velocity fluctuations have been analyzed as a function of the number of images considered for the average calculation. This enables to determine the minimum number of images required to obtain an average value which is representative. Each instantaneous velocity (u(t)) is decomposed as a sum of a mean velocity ($\bar{u}$) and of a fluctuating component (u'(t)) (Reynolds decomposition) (Equation 3.1):

$$u(t) = \bar{u} + u'(t) \qquad \textit{(Equation 3.1)}$$

To test the convergence of statistical values, the influence of the number of images on the mean ($\bar{u}$) and on the root mean square (rms) of the fluctuating component ($\sqrt{\overline{u'^2}}$) is analyzed in six measurement points distributed in plane 3 (Figure 3.4). Values significantly fluctuate until 300 images is reached. Values between 300 and 500 images fluctuate in a range of +/- 7 % for every point. A 500 images mean has thus been considered satisfactory.

a)

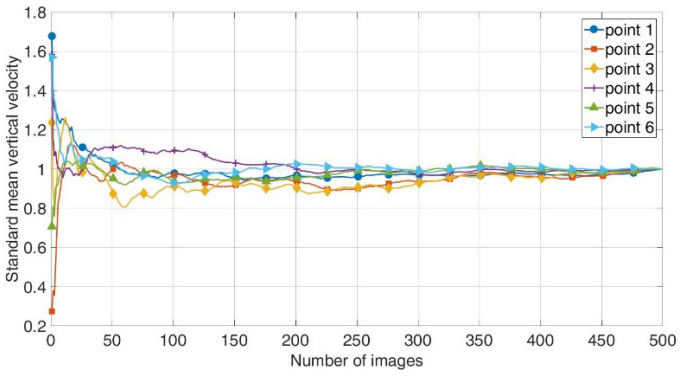

b)

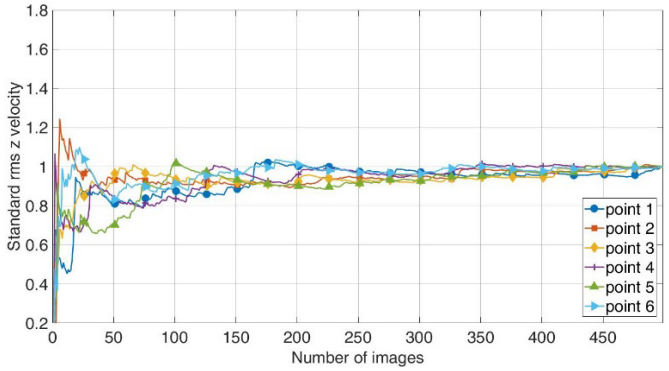

Figure 3.4. Influence of the number of images taken to compute averaged velocity fields in PIV. The mean velocity component is normalized by its final value on the left. The rms velocity is normalized by its final value on the right. The coordinates of the six points studied are 1(175,150), 2(175,200), 3(175,250), 4(25,50), 5(25,150), 6(325,150).

In the following, all results have been processed by calculating time averaged over 500 images (global time = 100 s). Moreover, Figure 3.5 shows that the flow is quite uniform along the width. Hence profiles are obtained by spatially averaging, in time averaged velocity fields, velocity over the width of the reactor. In the following, they will be called “mean profiles”, “mean” standing for time average over 500 images and for spatial average over the reactor width.

The study of the mean velocity profiles of the corresponding horizontal and vertical components of the same velocity field shows that the horizontal velocity component is almost constant over the reactor width and very small if compared to the vertical one. Moreover, the assumption was made that the normal (“out-of-plane”) velocity is negligible due to the reactor configuration. Thus, only the vertical velocity components will be considered for comparison.

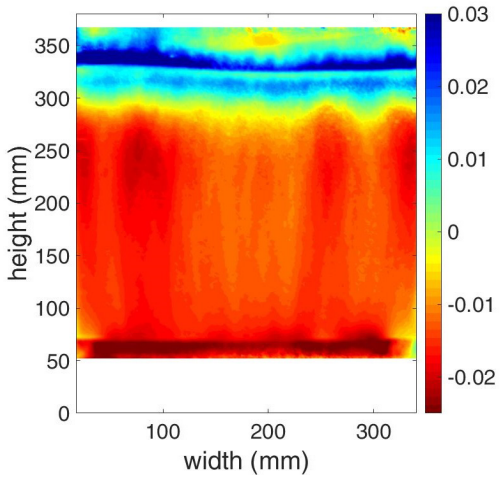

Figure 3.5. Mean vertical velocity ($m.s^{-1}$) of plane 3.

3.3.1.2 Experimental error on PIV measurements

To evaluate the experimental error associated with PIV measurements, two sets of PIV measurements have been performed on plane 3 on two different days in the same operating conditions. The reactor was not moved between the two measurement campaigns.

The mean profiles of vertical velocities for the two experimental sets are analyzed (Figure 3.6). The error is lower than 1.5 % on most of the reactor height (between 75 mm and 300 mm). Below 75 mm and above 300 mm, error increases to 3.5 %. Below 75 mm, this error is due to light refraction and reflection on the prism installed at the reactor bottom. Above 300 mm, the error increases near the top edge of the internal panel, due to the change of the flow direction perpendicularly to the measurement plane (recirculation loops) that cannot be properly caught by PIV.

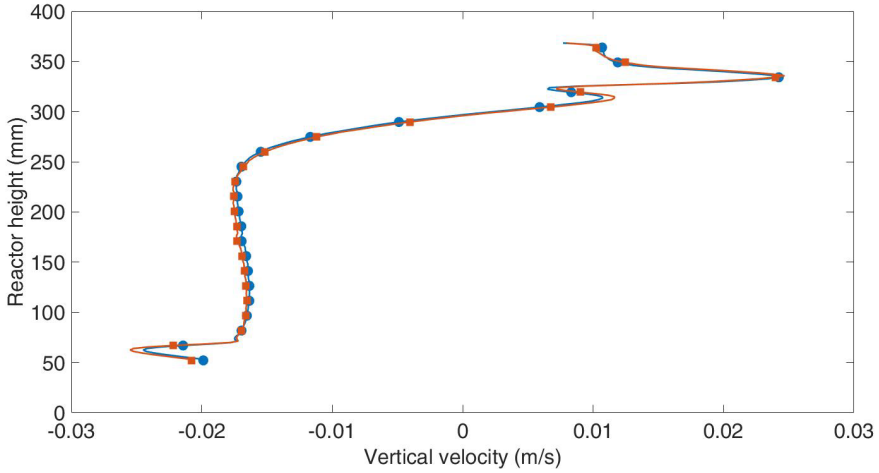

Figure 3.6 - Vertical velocity profiles of two different PIV sets on plane 3 situated at 18 mm of the reactor wall towards the camera.

3.3.1.3 Analysis of the flow in the reactor

As explain in section 3.2.2, PIV measurements have been performed on five planes in the reactor distributed along the depth of the reactor. Planes 1, 2 and 3 are situated in the zone where the flow is descending while planes 4 and 5 are in the ascending section (Figure 3.1). The vertical velocity fields of each of these planes are presented in Figure 3.7.

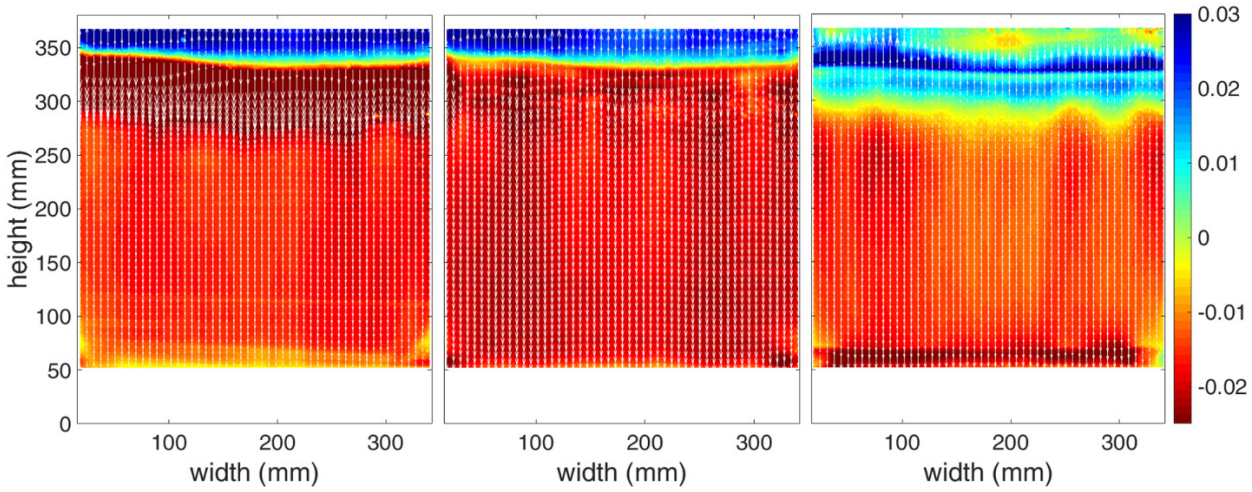

a) Descending section

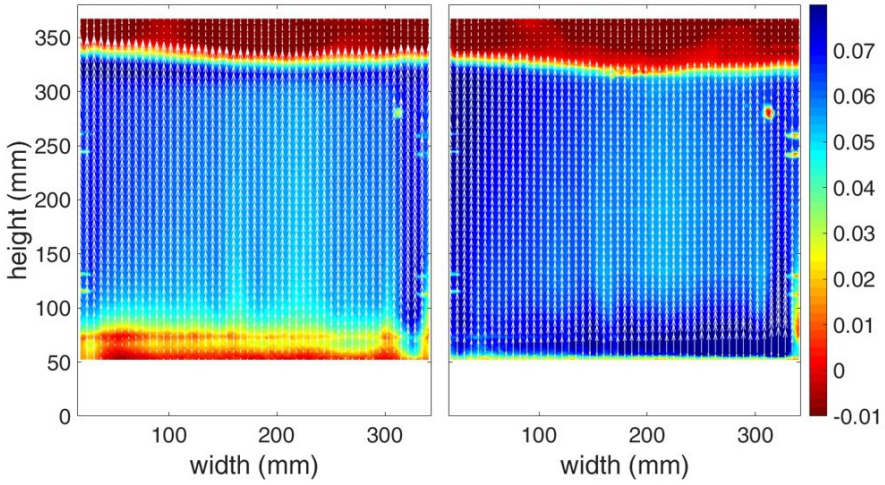

b) Ascending section

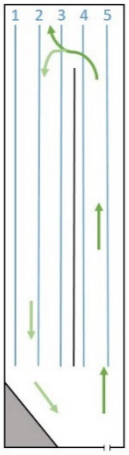

c)

Figure 3.7 - Vertical velocity fields (m/s) of planes 1, 2 and 3 from left to right (a) situated respectively at 3, 8, 18 mm of the reactor wall towards the camera. Vertical velocity fields (m/s) of planes 4 (left) and 5 (right) situated respectively at 28 and 34.7 mm of the reactor wall towards the camera (b). Velocity fields obtained by PIV. Schematic representation of the depth of the reactor (c). Dimensions are not true to scale.

Flow structures in Plane 1 and plane 2 are very similar: negative velocity values below 340 mm and positive values above. This corresponds to the top edge of the internal panel which has thus a significant impact on flow velocities. Plane 1 presents a zone with more negative velocities (up to -4×10^{-2} m.s^{-1}) between 280 and 340 mm. Plane 3 is situated in a mainly descending flow section, close to the internal panel. The velocities are thus negative along the panel except at the top of the panel where velocities are

null or have low positive values. Above the panel, velocities have higher positive values and this part of the flow corresponds to liquid leaving the reactor. According to velocity profiles in planes 1, 2 and 3, the mean value of the vertical velocity in the descending section (between 70 and 250 mm) is around -1.5×10^{-2} m.s^{-1} (Figure 3.8).

Planes situated in the ascending section are more difficult to characterize by PIV. Indeed the transparent internal panel inside the reactor is situated between the camera and the laser. Thus, the internal panel adds an additional barrier for light transmission. Unfortunately, due to the reactor configuration, it cannot be moved.

This influence can be observed on PIV results mostly on plane 5 close to the walls (screws used to fix the panel can be detected as well as a circular damage on the panel on the upper right part of the plan).

Planes 4 and 5 present the same flow structure with positive velocities below a 340 mm height and negative or null velocities above. The strong impact of the internal panel can also be noticed in this zone. As plane 5 is closer to the inlet jet than plane 4, velocity values in plane 5 ($+7\times10^{-2}$ m.s^{-1}) are higher than in plane 4 ($+4\times10^{-2}$ m.s^{-1}) at the bottom of the reactor. According to velocity profiles in planes 4 and 5, the mean vertical velocity in the ascending section (between 100 and 300 mm) approximately equals $+6\times10^{-2}$ m.s^{-1} (Figure 3.8).

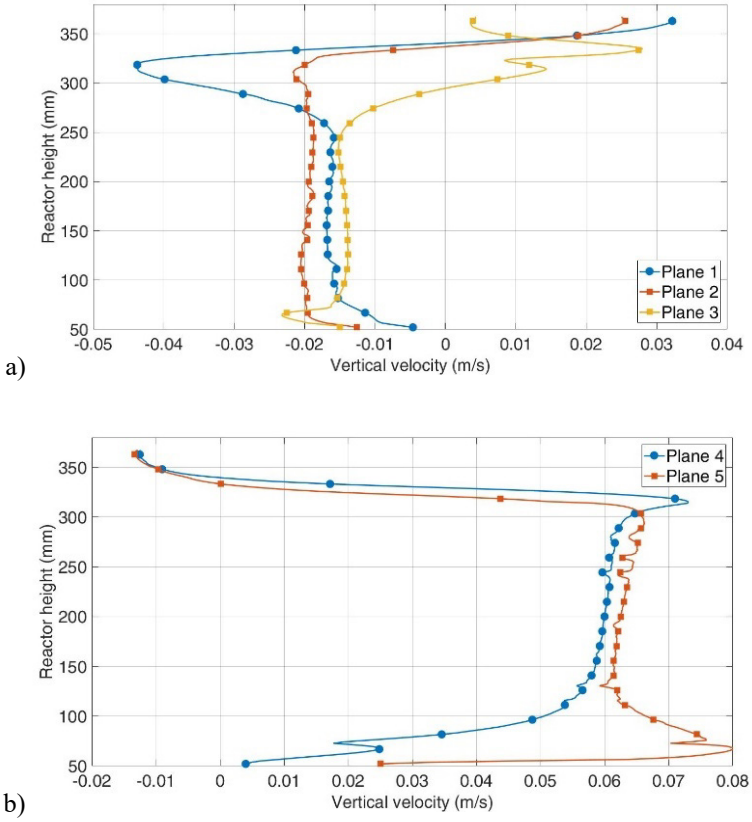

Figure 3.8 - Mean vertical velocity profiles obtained by PIV: on planes 1, 2 and 3 (a) (descending section) and 4 and 5 (b) (ascending section).

To characterize this unsteady flow, studying mean velocity fields is predominant but do not lead to a full characterization of the flow. This is the reason why, in addition to the analysis of time averaged velocity fields, fluctuations have been analyzed on the basis of root mean square values of the fluctuating

component $\sqrt{\overline{u'^2}}$ (rms velocity). Fluctuating velocities u'(t) have been calculated using the Reynolds decomposition (Equation 3.1). u'(t) values are considered as following a normal (Gaussian) distribution around 0. Values which are not in a +/- 4 root mean square interval centered on 0 have been considered as noise and ignored. The rms velocity $\sqrt{\overline{u'^2}}$ has been divided by the mean velocity component $|\bar{u}|$ to evaluate the part of fluctuations on the mean flow. These will be called normalized rms velocities in the following.

In plane 3, normalized rms velocities are around 0.2 below a 250 mm height - in most of the measurement plane - demonstrating the influence of fluctuations is low in this zone. Fluctuations are very high (200 %) close to a vertical position equal to 300 mm and above 350 mm (Figure 3.9). In plane 4, normalized rms velocities are below 0.2 between 75 and 340 mm. Large fluctuations are observed around 340 mm. At these heights, recirculation loops appear due to the internal panel, leading to almost null vertical flow or to liquid velocity vectors perpendicular to the measurement plane. In plane 3, recirculation loops height is lower due to the vicinity of the internal panel. On the PIV images, the time delay between two frames (10 ms) is set to optimally capture the main flow behavior (between 50 and 250 mm height), and not this kind of recirculation.

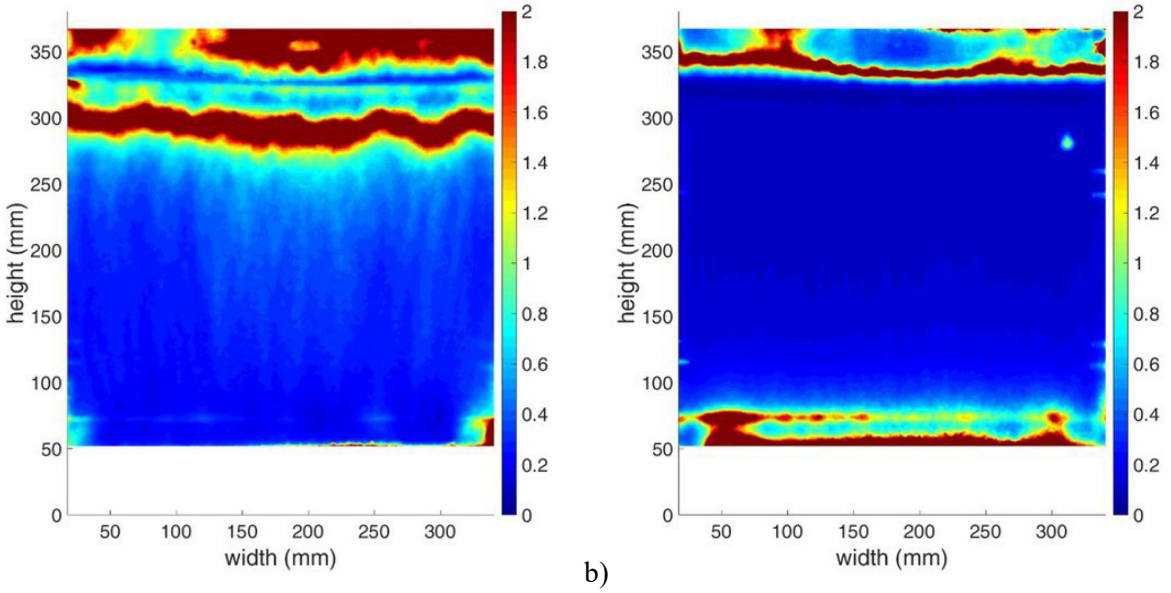

Figure 3.9 - Rms velocities divided by mean velocities on plane 3 (a) and plane 4 (b) situated at 18 and 28 mm from the reactor front wall. Mean on 500 images obtained by PIV.

3.3.1.4 Flow regime analysis

The Reynolds number is used to characterize the flow regime. It can be calculated as follows: $Re = u_l \rho_l D_h / \eta$; $D_h = 4A_s/P_s$.

where ρ_l is the fluid density, u_l is the (liquid) velocity, D_h is the hydraulic diameter and η is the dynamic viscosity. The hydraulic diameter was calculated using A_s, the cross (rectangular) section area and P_s the perimeter of this area.

Different Reynolds numbers may be estimated in different zones in the reactor. At the reactor inlet, the Reynolds number has been calculated through the slit. The inlet velocity has been calculated as the pump volumetric flow rate (400 $L.h^{-1}$) divided by the slit cross section area (3.4 cm^2).

The mean vertical velocities in the ascending and descending sections have been estimated according to PIV measurements. The hydraulic diameter values are evaluated for each zone on the basis of the reactor geometry.

Reynolds number values vary between 650 and 1430 (Table 3.1), which are characteristic of a laminar regime in this kind of geometry (rectangular duct section), as the critical Reynolds number of a transitory regime is estimated between 2300 and 2800 (Hanks & Ruo, 1966). Despite the unsteady nature of the flow in the reactor evidenced by PIV measurements, Reynolds number indicate that it could nevertheless be considered as laminar.

Table 3.1 - Reynolds numbers calculated in different zones of the reactor.

	Hydraulic diameter (m)	Velocity ($m.s^{-1}$)	Reynolds number
Slit	0.002	0.330	650
Ascending section	0.024	0.060	1430
Descending section	0.045	0.015	670

3.3.2 CFD validation by PIV

As PIV results highlight a non-stationary flow, and Reynolds number values seem to indicate a laminar regime in the reactor, it has been decided to test a turbulent as well as a laminar approach for CFD simulations.

Considering vertical velocity evolution on one random point enables to demonstrate CFD simulations using turbulent (k-ε model) or transitory regimes do not represent properly flow characteristics described by PIV. Using these models, velocity indeed reach a constant value after a few seconds while PIV velocity is oscillating. On the contrary, using a laminar model leads to simulated flow with similar characteristics as those measured by PIV: very close velocity values and similar range of fluctuations (Figure 3.10). This good agreement further confirms the laminar nature of the flow in the reactor.

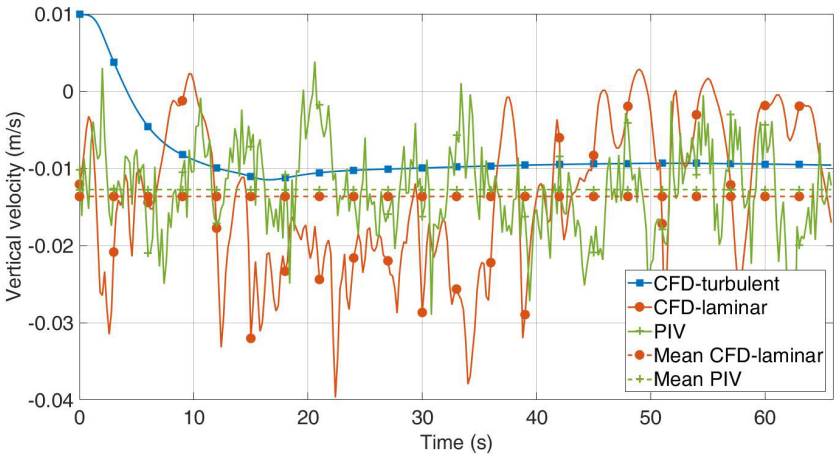

Figure 3.10. Vertical velocities fluctuations as a function of time (the time between two images is 0.2 seconds) obtained by CFD and PIV on one point (175mm, 250 mm).

To compare and validate CFD simulations using PIV measurements, it is important to use the same number of images, taken with the same frequency during the same period. Thus, the frequency used to sample images in CFD (every 10 time steps: 0.2 s) is equal to the trigger rate used in PIV (5 Hz). Rms velocities have been calculated on the same six points as for PIV (Figure 3.11). First, fluctuations are important and then decrease until 400 images, to finally reach a +/- 10 % range between 400 and 500 images. This range is considered satisfactory to show velocity fluctuations are stable using 500 images.

a)

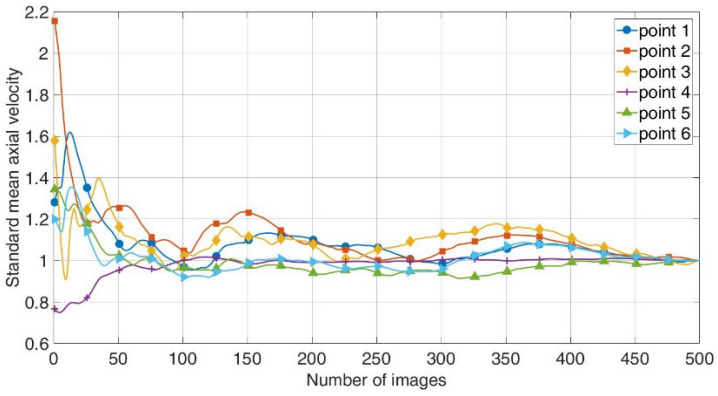

b)

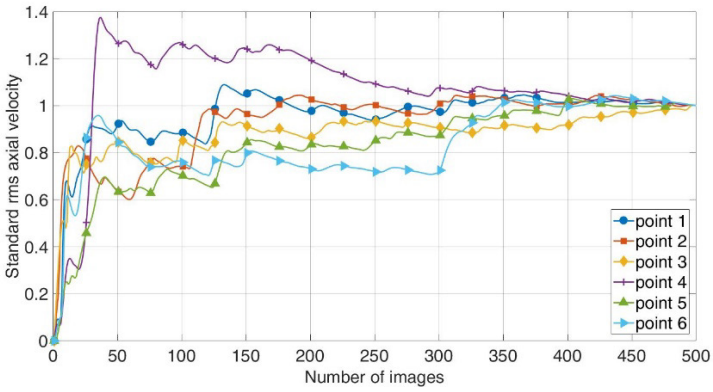

Figure 3.11 - Influence of the number of images taken to compute time averaged velocity fields in CFD. The mean velocity component is normalized by its final value (a). The rms velocity is normalized by its final value (b). The coordinates (mm) of the six points studied are: 1(175,150), 2(175,200), 3(175,250), 4(25,50), 5(25,150), 6(325,150).

3.3.2.1 Qualitative comparison

Vertical velocity fields have been simulated by CFD in the same planes as those investigated by PIV. CFD model represents very well the influence of the internal panel on the flow structure (Figure 3.12). Negative velocities below a height of 340 mm and positive values above this zone are represented on plane 1 and 2. As well as in PIV results, the model evidences the higher negative values between 280 and 340 mm in plane 1. Regarding plane 3, CFD describes correctly the three flow zones in the plane (downflow, null and upflow) highlighted by PIV. CFD fully describes the flow structure in the ascending section as well. For both planes 4 and 5, an upflow zone below 340 mm and a downflow zone above this height are similarly observed in CFD simulations and in PIV results. Hence the flow structure is correctly represented by CFD if compared to PIV results, allowing a qualitative validation of the numerical approach.

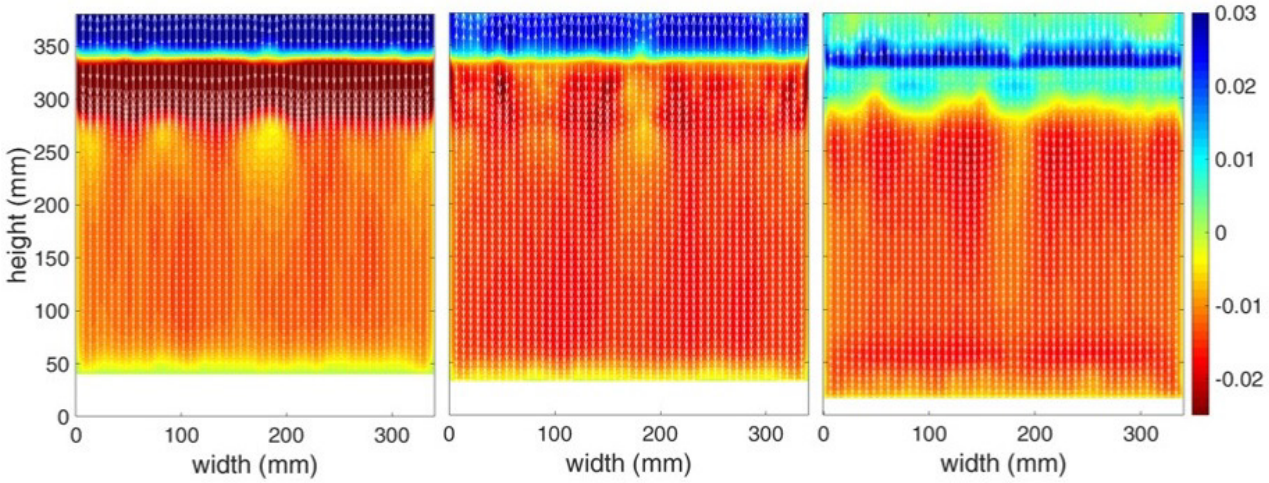

a) Descending section

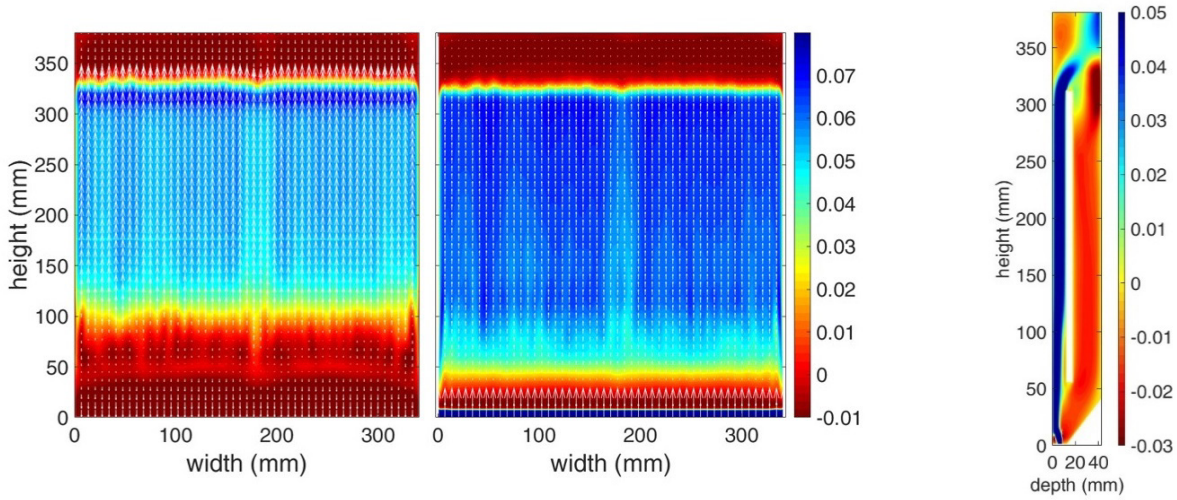

b) Ascending section c)

Figure 3.12 - Vertical velocity fields (m/s) of planes 1, 2 and 3 from left to right (a) situated respectively at 3, 8, 18 mm of the reactor wall towards the camera. Vertical velocity fields (m/s) of planes 4 (left) and 5 (right) situated respectively at 28 and 34.7 mm of the reactor wall towards the camera (b). Vertical velocity fields (m/s) in the depth of the reactor (c). Velocity fields obtained by CFD.

3.3.2.2 Comparison of mean velocity profiles

Mean vertical velocity profiles are obtained by CFD in the same way as PIV results, meaning vertical velocity fields have been temporally and spatially (over the width) averaged using Matlab codes.

To perform a quantitative assessment, vertical velocity profiles simulated by CFD and measured by PIV (Figure 3.13) are compared. The discrepancy between them is evaluated on the basis of a "difference error percentage". This "difference error percentage" ($x_{\%diff}$) between two sets is calculated as the absolute difference between two velocity values (u1 and u2) divided by a characteristic velocity (u_{eq}) (Equation 3.2). This characteristic value is a weighted mean of descending and ascending velocities in the reactor and equal to 0.03 $m.s^{-1}$. The use of this quantity allows avoiding (near)-zero division at some points in the reactor where velocity values are close to zero.

$$x_{\%diff} = \frac{|u1-u2|}{u_{eq}} \times 100 \qquad \textit{(Equation 3.2)}$$

Regarding plane 1 and plane 2, the difference between model and experiment is lower than 20 %. In both cases, velocity values are underestimate by CFD. In the downflow zone of plane 3, CFD and PIV velocities are close. The difference is lower than 5 %. Within the upflow zone, the discrepancies are higher (up to 30 %). As explained in 3.3.1.2, the area between 290 and 340 mm is not optimally characterized by 2D PIV due to very low (positive) velocity values. Higher than 340 mm, velocities are getting closer, and the difference is lower than 7 %.

Regarding the ascending section, difference percentage between CFD and PIV are higher. The highest discrepancies on the velocity profiles are observed at the bottom of the reactor. On plane 4, over a 150 mm height, a difference of less than 20 % is observed while it reaches 50 % between 100 and 150 mm to finally achieve 150 % below 100 mm. In plane 5, discrepancies between velocity fields are lower, especially at height higher than 100 mm, reaching maximum 10 %. Below 100 mm, the difference increases up to 90 % at 50 mm.

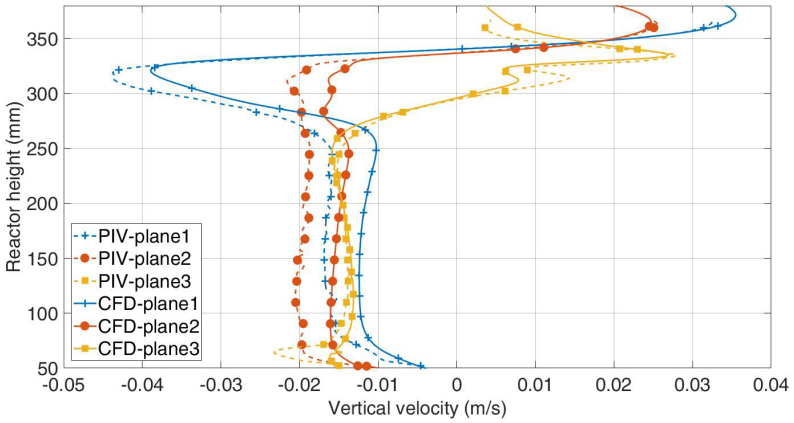

a) Descending section

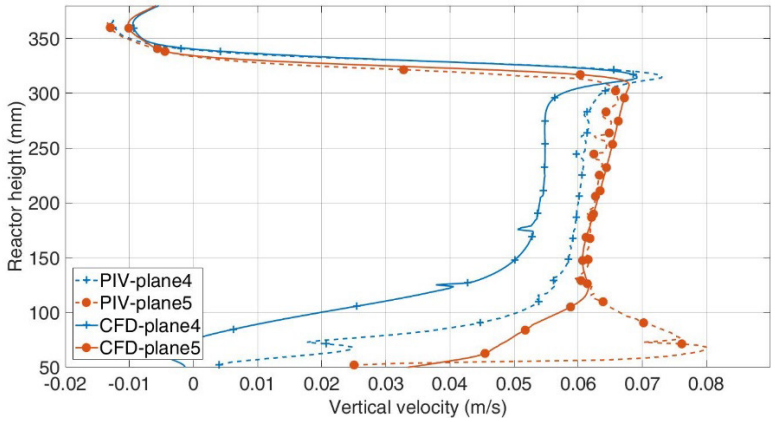

b) Ascending section

Figure 3.13 - Vertical velocity profiles in the descending zone (a) of plane 1, plane 2 and plane 3 obtained by PIV and CFD. Vertical velocity profiles in the ascending section (b) of plane 4 and plane 5 obtained by PIV and CFD.

3.3.2.3 Rms velocity profiles comparison

The full characterization of the flow requires not only the analysis of mean velocities, but also the study of fluctuations around these mean velocities. To this end, rms velocities have been calculated from CFD results. Normalized rms velocities have been calculated on plane 3 and 4 (Figure 3.14). The results obtained are similar to PIV with low values (below 0.2) in most parts of the planes (below 280 mm for plane 3 and between 100 and 340 mm for plane 4). High normalized rms velocities are obtained in zones where the mean velocities are low: over 280 mm for plane 3 and below 100 and around 340 mm for plane 4.

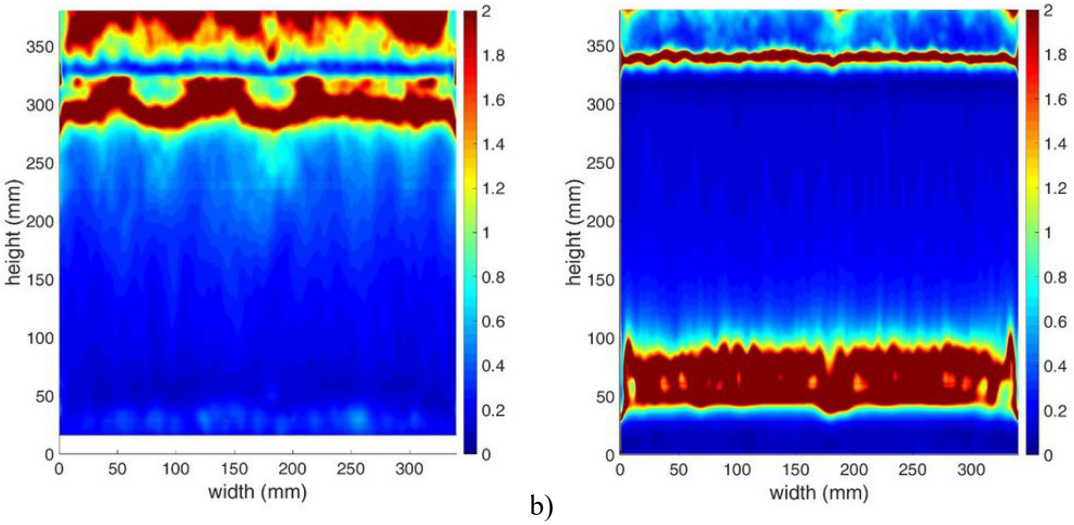

Figure 3.14 - Rms vertical velocities divided by mean vertical velocities on plane 3 (a) and plane 4 (b) situated at 18 and 28 mm of the reactor wall towards the camera. Mean on 500 images obtained by CFD.

Regarding PIV results, it has been hypothesized that the high influence of fluctuations (high value of $\sqrt{\overline{u'^2}}/\bar{u}$) was the result of the change of the flow direction perpendicularly to the measurement plane (recirculation loops). The influence of the "out-of-plane" velocity (perpendicular to the measurement plane) on the flow is not reachable by PIV but can be studied thanks to CFD. This shows the complementarity of both methods. Figure 3.15 shows the vertical profiles of the three components of velocity in plane 3 (left) and the field of the normal component of velocity in a transversal section of the reactor (along the depth). Near the reactor bottom (height below 50 mm) and at heights between 260 and 300 mm, the negative normal velocities (-0.005 $m.s^{-1}$) are not negligible compared to the vertical velocities (-0.015 $m.s^{-1}$). Moreover, above the internal panel (between 310 and 350 mm), the normal and the vertical velocities both reach their maximum values, but the normal component (0.040 $m.s^{-1}$) is larger than the vertical one (0.025 $m.s^{-1}$) in the descending section. These zones correspond to high influence fluctuations zones i.e. where the rms velocities are high compare to mean velocities in PIV and CFD. Recirculation loops which cause a significant normal velocity can thus be considered as a reason of high fluctuating velocities in this reactor.

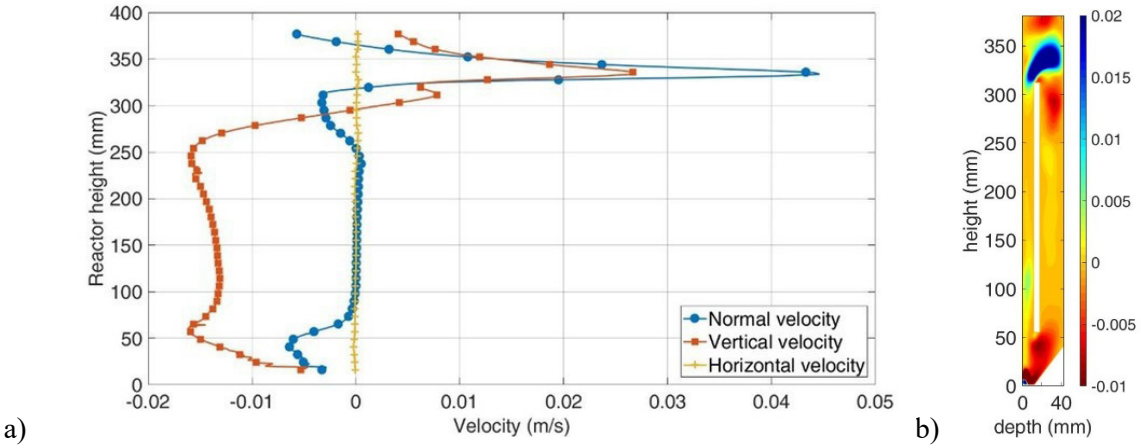

Figure 3.15. Vertical, horizontal and normal velocity profiles of plane 3 obtained by CFD (a) and normal velocity fields (m.s^{-1}) in the depth of the reactor obtained by CFD (b).

Rms velocity profiles obtained by CFD and PIV have also been compared in plane 3 and plane 4 (Figure 3.16). In plane 3, the heights at which rms velocities are very high are similar in PIV and CFD: height between 290 and 310 mm and above 340 mm. The same applies on plane 4, high rms velocities are observed in the same zones in PIV results and in CFD simulations: at a height of 340 mm and below 100 mm. Rms velocities calculated by CFD are slightly higher than those computed from PIV between 100 and 300 mm.

Hence, the CFD model enables to perfectly describe qualitatively the behavior of the fluctuating flow. Discrepancies observed between PIV and CFD are mainly due to the PIV experimental error. Based on these considerations, the CFD model is adequate to describe the rms fluctuating velocities. Moreover, this confirms that the laminar regime model used in CFD is appropriate to describe the flow.

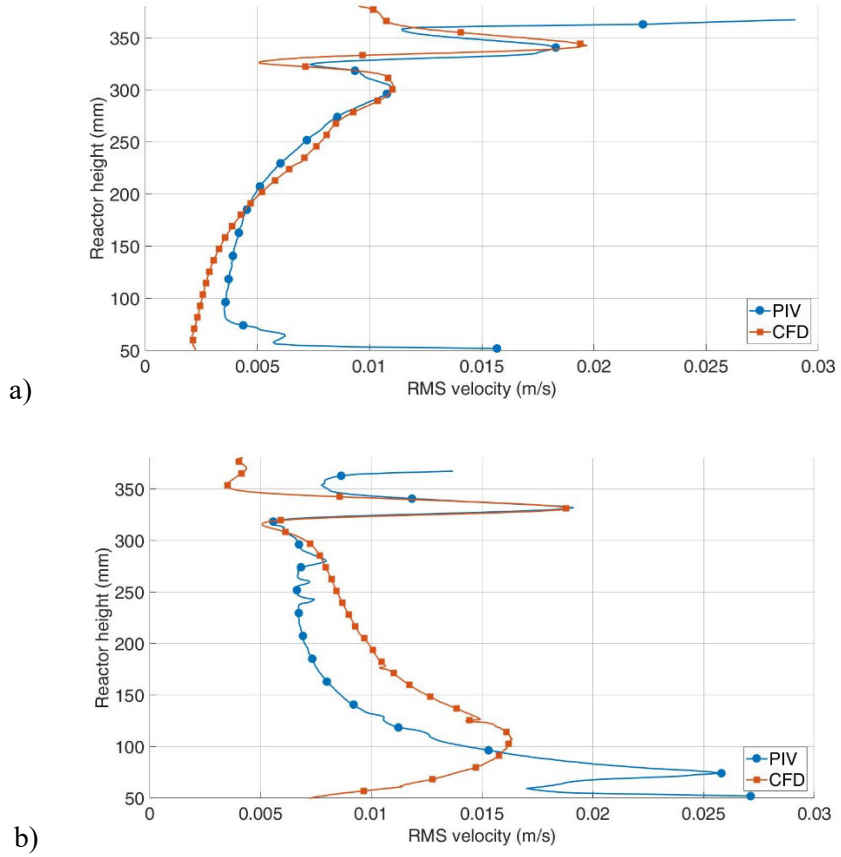

Figure 3.16. Comparison of rms velocity profiles of plane 3 (a) and plane 4 (b) obtained by CFD and PIV.

3.4 Factors influencing results

The CFD model is able to satisfactorily describe the unsteady laminar flow in the reactor. Mean and rms vertical velocity profiles have been compared to experimental results obtained by PIV. Results are in fair agreement. However, discrepancies between PIV and CFD have been observed. The aim of this section is to try to explain them.

3.4.1 Pump flow rate influence

The liquid flow rate delivered by the circulation pump at the reactor inlet is not perfectly known. Under the studied conditions, the pump flow rate presents an experimental uncertainty of +/- 3 %, if measured with three different flow meters. The impact of this uncertainty on the flow velocities in the reactor is studied to determine if it may explain the discrepancies observed between CFD and PIV results. It is studied using CFD (Figure 3.17). Plane 3 has been used as a reference plane. An increase of 3 % on the inlet mass flow rate (from 0.1111 $kg.s^{-1}$ to 0.1144 $kg.s^{-1}$) has been tested. The impact on vertical velocity values is between 3 and 8 % depending on the vertical position in the reactor. This has been considered in the previous sections which means that all simulations described in this chapter were performed using an inlet mass flow rate of 0.1144 $kg.s^{-1}$. Nevertheless, the single influence of this physical parameter cannot explain the discrepancies between CFD and PIV.

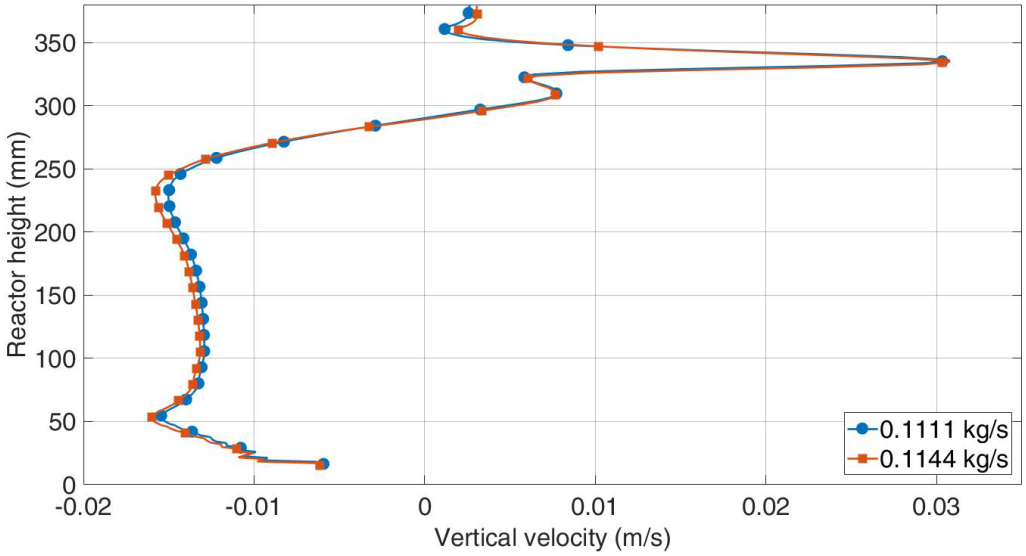

Figure 3.17 - Vertical velocity profiles of plane 3 situated at 18 mm of the reactor wall towards the camera for two different inlet mass flow rates (0.1111 and 0.1144 kg.s^{-1}). The profiles have been obtained by CFD simulations.

3.4.2 Variation of the velocity field along the reactor depth

It has been noticed that the flow field (measured by PIV or simulated by CFD) is strongly influenced by the position, along the reactor depth, of the plane which is considered. This can be explained by the small depth of the reactor and by presence of the internal panel, which makes the "wall effect" significant in all reactor planes.

This high sensitivity to plane position has to be accounted for when comparing different sets of experimental results or experimental results to simulations, because one has to be sure that results are relative to the exactly the same plane in the reactor.

When performing PIV measurements, the measurement plane position is sometimes not defined very accurately as it depends on the relative positions of the camera, the laser and the reactor which may slightly change when reactor is moved (for filling, cleaning…). Moreover, the laser sheet thickness equals up to 2 mm which also leads to an uncertainty on the plane which is explored.

Due to these uncertainties on the measurement plane position and to the finite number of elements used to describe the reactor geometry in CFD, it appears very complex to get experimental data and simulations relative to exactly the same plane when comparing PIV to CFD.

In order to quantify the potential effect of this uncertainty, CFD simulations have been further analyzed. Simulation results were extracted from 2x2 planes close to plane 3 and plane 4, respectively. These planes were chosen to get information on the impact of the plane position in the descending and ascending sections. The distance between these new planes and plane 3 and 4 was set to 2 mm, which corresponds to the PIV laser sheet thickness. The CFD mesh refinement is such that the different planes correspond to different mesh elements.

Plane 3-1, plane 3-2 and plane 3-3 were thus respectively situated at 16, 18 and 20 mm from the front reactor wall. Discrepancies between mean vertical velocities in the different planes are measured at every height (Figure 3.18). The impact on vertical velocities in the zone situated between 50 and 250 mm height can be evaluated at 10 % between plane 3-1 and plane 3-2. A lower impact on velocities can be noticed between plane 3-2 and plane 3-3 (5 % difference). As plane 3-3 is really close to the internal

panel, the decrease of velocities is due to the wall effect induced by it. A higher impact on velocities can be noticed above 250 mm (between 8 and 16 %).

Discrepancies between CFD and PIV on plane 3 are lower than 5 % below 250 mm while the influence of the plane position is evaluated between 5 and 10 %. Above 300 mm, the CFD model presents 7 % of difference with PIV while the influence of the plane position reaches 16 %. Hence discrepancies between CFD and PIV are lower than the uncertainty on plane position, indicating a quantitative validation of the CFD model for plane 3.

Below 250 mm, CFD model of plane 1 and plane 2 presents respectively 20 % and 16 % difference at the maximum with PIV which is comparable, even if a bit higher, to the impact of the plane position (10 %). It should be notice that this influence has been calculated on plane 3 only and that values can be slightly different for these planes.

Plane 4-1, plane 4-2 and plane 4-3 are respectively situated at 27, 28 and 30 mm from the front reactor wall. As plane 4 is situated closer than 2 mm from the internal panel, plane 4-1 is only 1 mm away from plane 4-2. This is the reason why velocity discrepancies between plane 4-2 and plane 4-3 are higher than between plane 4-2 and plane 4-1 (Figure 3.18). Indeed a difference lower than 35 % can be calculated between plane 4-2 and plane 4-1 while the difference with plane 4-3 is evaluated between 80 and 120 % below 250 mm. This is explained by the strong influence of the inflow jet on velocity fields. Hence the position of the plane has even a higher influence in the ascending section due to the vicinity of the inlet.

CFD model of plane 4 which is situated in the ascending section presents high discrepancies (between 20 and 150 %) with PIV experiments. CFD model of plane 5 which is situated in the same zone shows between 10 and 90 % difference with PIV. These significant discrepancies are due to the strong influence of the inlet flow jet on the position of the plane as it has been proved using CFD on plane 4 (influence up to 120 % on velocity fields).

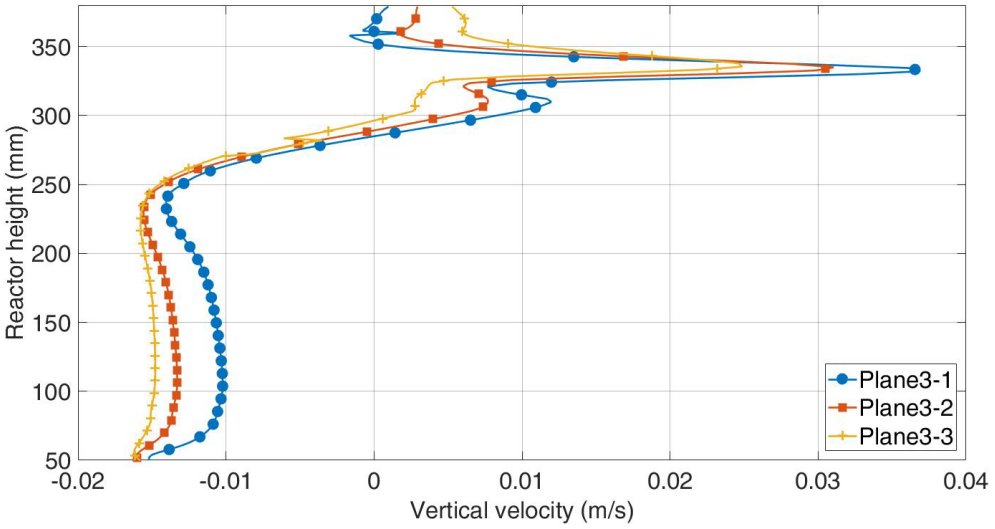

a)

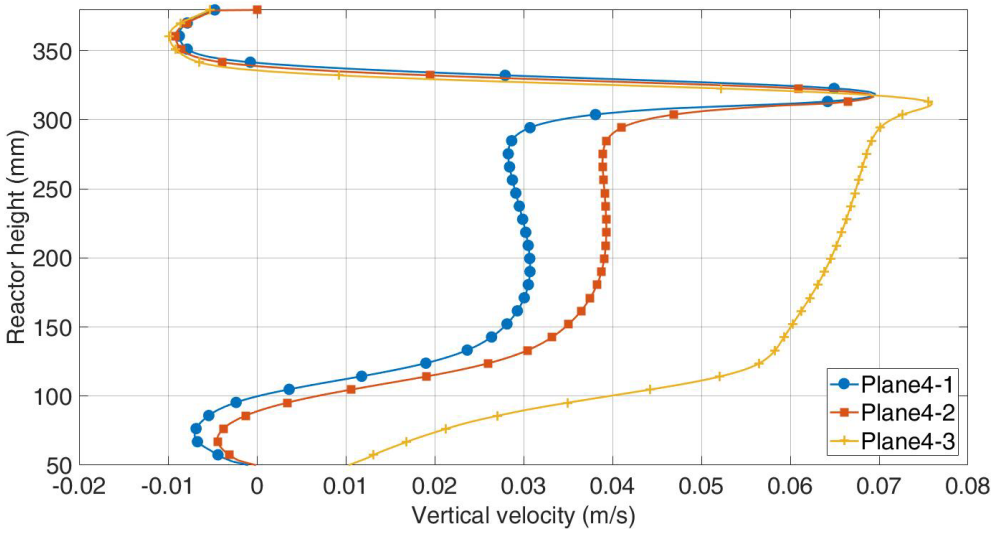

b)

Figure 3.18. Vertical velocity profiles of three planes around plane 3 (a) situated at 16, 18 and 20 mm from the front reactor wall and around plane 4 (b) situated at 27, 28 and 30 mm from the front reactor wall. The profiles have been obtained by CFD simulations.

Hence discrepancies between CFD and PIV seem important and may cast doubt on the validity of the numerical approach. However, these discrepancies can be explained by the high influence of the plane position along the depth of the reactor on flow velocities and the difficulty to model by CFD exactly the same planes as those used for PIV measurements.

CFD model is thus validated on ascending planes as well as descending planes as the CFD model describes quantitatively the flow in an uncertainty range of plane positions of 2 mm within the depth of the reactor.

3.5 Conclusions

This chapter aims to characterize the hydrodynamics in a photobioreactor. Hydrodynamics has a key role in microalgae culture as it influences light distribution and nutrient transfer, two main parameters in microalgae growth. The photobioreactor is designed to cultivate encapsulated microalgae i.e. microalgae entrapped in beads of polymer. Hence the reactor has been designed as a fluidized bed reactor using a liquid flow to fluidize solid (beads). In this chapter, only the liquid flow is studied.

Both experimental PIV and CFD modelling are used to characterize the reactor flow. Contrary to what might seem, the two approaches are not redundant. They bring complementary information as PIV gives access to the true velocity fields required to validate CFD model, while 3D-CFD simulations give access to information unreachable by 2D-PIV such as the normal velocity component.

PIV results proves the fluid flow regime to be laminar, but unsteady, and this is correctly modeled by CFD as it describes in the same way fluctuations over time as PIV. The analysis of vertical velocity fields on five planes shows that the flow structure (upflow, null and downflow zones) is accurately described by the CFD model compared to PIV. Zones where flow direction is changing correspond to the bottom and the top of the internal panel use to control the circulation of the beads. Hence the CFD model represents well the strong influence of the internal panel on the flow. The analysis of mean and rms vertical velocity profiles shows a good agreement (difference lower 20 %) between CFD and PIV results alongside the internal panel. However, discrepancies are observed below and beyond the panel (up to 150 %).

The main reason for these discrepancies, among the different potential sources of error, is determined. The impact of the experimental uncertainty on the pump flow rate (3 %) does not explain these discrepancies. The difficulty to study a single plane in PIV makes difficult to evaluate the influence of the measurement plane position on velocities. To this end, velocity profiles in two planes situated 2 mm apart from a given descending or a given ascending plane have been analyzed on the basis of CFD flow fields. Finally the discrepancies between CFD and PIV are in the same order of magnitude or lower than the error due to the plane position. This error is significant (up to 120 % for plane 4) due to the high influence of the plane position on velocity fields, especially in the ascending section. In this zone, high velocities are measured due to the flow inlet (up to 0.08 $m.s^{-1}$). Not only mean velocities measured by PIV and CFD correspond but also rms velocities. Indeed rms velocity profiles obtained by PIV and CFD have been compared in plane 3 (descending) and plane 4 (ascending). The CFD model describes accurately rms velocities. Discrepancies between the experimental method and simulations are low compared to the error due to the plane position. Hence CFD correctly model fluctuations as well as mean velocities.

The single-phase CFD model is thus qualitatively and quantitatively validated by PIV. The model enables to give information to characterize the flow in the three dimensions. This chapter described a complementary method using PIV and CFD to characterize hydrodynamics and develop a reliable CFD model on a reactor operating with an unusual flow: laminar and unsteady.

This study enables to describe accurately the hydrodynamics in a photobioreactor. A 3D-CFD model has been developed to describe the liquid flow within the reactor as a first step. As the reactor is designed to fluidized beads of 3 mm, the next step is to include solid in this model. This cannot be validated by PIV as two-phase PIV is difficult to develop because of the laser light scattering due to solid, especially using high solid fraction (10 %). Another experimental method has to be employed to determine solid distribution within the reactor as light attenuation. It will validate a two-phase CFD model which is being developed.

4 Hydrodynamic characterization of the solid phase

4.1 Introduction

Few studies are dealing with the culture of encapsulated microalgae at a pilot scale. Different reactor types can be used. A liquid-solid fluidized bed reactor designed to cultivate microalgae encapsulated in beads is chosen in this study to enhance light supply. Liquid-solid fluidized bed reactors are used from metallurgical processes to wastewater treatment (Bello et al., 2017; Sha et al., 2018). They are particularly interesting in biochemical processes as they provide high heat and mass transfers but a low shear stress which can be damageable for cell cultures (Ghatage et al., 2014; Panneerselvam et al., 2007). Knowledge on liquid-solid fluidized bed reactors is less significant than three-phase (gas-liquid-solid) or two-phase (gas-solid) reactors (Corona, 2008; Kalaga et al., 2012; Panneerselvam et al., 2007). Knowledge on gas-solid fluidized beds cannot be used directly on liquid-solid reactor as the flow regime is different. Indeed liquid-solid or gas-solid fluidized beds are not driven by the same flow regime. Mixing of gas-solid fluidized bed are controlled by collisions (high Stokes number) while liquid-solid are controlled by hydrodynamic interaction between particles (low Stokes number) (Corona, 2008). This is due to the higher density difference between gas and solid. Liquid-solid fluidized beds are more uniform as gas-solid fluidized beds are characterized by non-homogeneous voidage distribution (Zheng & Zhu, 2000).

Numerical modeling of multiphase flows can be performed using two different approaches: Euler-Lagrange and Euler-Euler. The Euler-Lagrange approach considers the fluid phase as a continuum using an Eulerian approach, while the dispersed phase flow is solved for each particle individually with a Lagrangian approach. This is achievable only if the solid phase volume fraction is low (below 10 %). In our case, the solid volume fraction (≈ 4 %) and the number of particle (less than 2.10^4) could allow to use this type of model. However, computation times would be long. Moreover, the Lagrangian approach is not successful to model continuously suspended particles in a close reactor (the liquid phase enters and comes out continuously in the studied reactor but the solid phase is kept inside). An Euler-Euler approach must thus be used. In this kind of approach, each phase is solved using an Eulerian treatment. Both phases are considered as interpenetrating continua and a volume fraction of each phase is calculated in every cell of the mesh. Two models can be used: mixture model (one fluid model) and the Eulerian model (two fluids model). The mixture model is used to model multiphase flow where phases move with a close velocity or density. In this model, the continuity, momentum and the energy equations are solved for the whole mixture. This model cannot be used in this context as velocities of both phases are not close enough. The Eulerian model is more complicated and requires higher computation times but gives a better description of the flow. The pressure field is solved for all phases while momentum and continuity equations are solved for each phase. The Eulerian model is recommended for fluidized beds and is used in this work.

Most CFD studies on liquid-solid fluidized bed compare solid holdup (or voidage) and/or solid or liquid velocities with experimental results to validate the model (Cornelissen et al., 2007; Davarnejad et al., 2014; Ghatage et al., 2014; Panneerselvam et al., 2007; Wang et al., 2012).

To characterize experimentally a two-phase flow, different non-intrusive experimental methods are available. Electrical resistance tomography gives information about solid distribution (Carletti et al., 2014; Hosseini et al., 2010) while computer aided radioactive particle tracking (CARPT) gives access to solid velocities (Dudukovic, 2000; Guha et al., 2007). These methods were not available, can cause health issues and are costly.

Two-phase Particle Image Velocimetry (PIV) can be used to obtain velocity of both phases (Virdung & Rasmuson, 2007). However, some limitations occur using this technique as laser light must penetrate through the liquid-solid dispersion and not be too much distorted. Two-phase PIV must thus be used with a low solid volume fraction (less than one percent) of transparent particles or with liquid-solid dispersion in which both phases have matching refractive indexes (Micheletti & Yianneskis, 2004; Montante et al., 2012; Unadkat et al., 2009). Hence it is complex to set up this technique on the studied

reactor, filled with a relatively high solid volume fraction of 4.35 % (for two-phase PIV), and particularly with beads having a high diameter (3 mm).

In this work, a light attenuation technique is chosen to characterize the solid distribution (Delafosse et al., 2018; Tamburini et al., 2013). This method allows to access to the solid concentration through the reactor depth, using a light source and a camera placed on each side of the reactor. It has been successfully used previously to validate CFD model on other types of reactors.

Density of solids in this thesis (1010-1020 $kg.m^{-3}$) is lower than in most studies in which the solid density is between 1050 and 2900 $kg.m^{-3}$ (Kalaga et al., 2012; Thombare et al., 2019). Nirmala & Muruganandam, 2013 studied global solid holdup and solid circulation rate of a liquid-solid fluidized bed involving alginate beads with a density of 1010 $kg.m^{-3}$. Maestri et al., 2019 developed a CFD-DEM model and compared results using CARPT method for a liquid-solid fluidized bed using alginate beads of 1027 $kg.m^{-3}$. Good agreements between the experimental method and the model were found studying bed expansion, solid distribution, time averaged velocity fields and axial dispersion coefficients. In this thesis, as the solid density is low and close to water density, the influence on density on the flow is particularly studied. As Panneerselvam et al., 2007; Wang et al., 2010 showed the particle size has an influence on the flow, the influence of the bead diameter on the flow is studied as well in this thesis.

Liquid-solid fluidized beds are usually cylindrical columns (Corona, 2008; Ghatage et al., 2014; Kalaga et al., 2012; Wang et al., 2010). Liquid is uniformly injected at the bottom of the column through a distributor as a perforated plate. The configuration of the studied reactor is very different as the column is rectangular and the liquid is injected through an off-centered slit. This causes an unusual bead motion which needs to be characterized.

The single phase (liquid) behavior of the reactor has been studied in a previously (chapter 3), to get a first insight on the flow behavior in the reactor. It has been shown that the flow regime in the reactor is laminar and unsteady. A CFD model was developed and validated by an experimental method (PIV). This model allows to describe liquid mean and rms velocity fields. In this thesis, it is used as a basis for the two-phase model.

The aim of this chapter is to develop a two-phase 3D-CFD model of the reactor in order to get information about the liquid and the solid phase behavior. An experimental method based on light attenuation is used to validate this model based on solid distribution. The influences of bead diameter and density on the flow are quantified. The impact of the presence of solid on the liquid flow is studied.

4.2 Materials and methods

4.2.1 Photobioreactor setup

The reactor characterized in this chapter is the same as in the previous chapters and the complete configuration of the reactor is described in chapter 2. The photobioreactor is a flat rectangular fluidized bed reactor of around 5 L (Figure 4.1). Solids (beads) are fluidized by liquid (distilled water in this chapter) entering at the reactor bottom by a slit of 1 mm thick extending over the whole reactor width. An internal panel allows delimiting two zones in the reactor, with ascending and descending flows, respectively. The solid fraction in the reactor is fixed at 4.35 % of beads in this chapter. A flow rate of 0.1310 $kg.s^{-1}$ (470 $L.h^{-1}$) is needed to completely fluidize this solid volume fraction in the ascending zone section and to allow beads reaching the upper part of the photobioreactor and to go behind the internal panel to the descending section. Beads sediment at the bottom of the photobioreactor and recirculate above the slit by means of the bottom prism. Flow is characterized in five vertical planes situated at 3, 8, 18, 28 and 34.7 mm, respectively, from the reactor wall maintaining the prism, beginning by plane 1 in the descending flow zone.

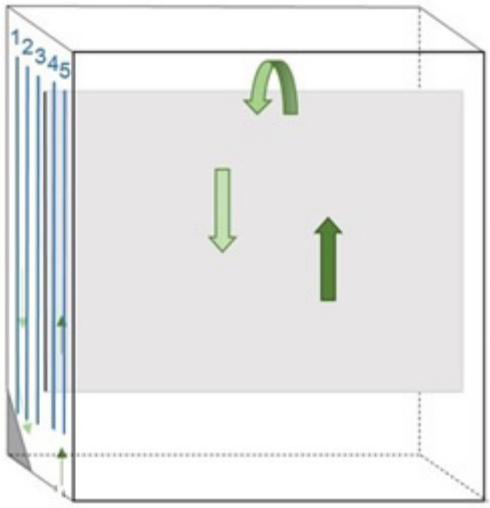

Figure 4.1 – Photobioreactor configuration. Five planes are used to characterize the hydrodynamics: two in the ascending section (plane 4 and 5) and three in the descending flow section (planes 1,2 and 3). Green arrows represent the flow.

4.2.2 Beads characterization

4.2.2.1 Bead making

Solids used in this chapter are beads made from sodium alginate. Since only hydrodynamics is studied in this chapter, beads are not filled with algae. However, to obtained beads with the same properties as the ones containing algae, the protocol to make beads is the same as described in chapter 2. A 3.75 %wt. solution of sodium alginate ($C_6H_7NaO_6$) is diluted with 20 % of distilled water just before cross-linking (this step balances the addition of microalgae in the solution in the encapsulation process). The solution is pumped through a needle and dripped in a beaker filled with reticulation solution ($CaCl_2$: 0.1 mol/L) to form beads.

4.2.2.2 Bead diameter measurement

As alginate beads absorb water, dry and wet bead densities and diameters are very different. Thus, bead density and diameter have to be measured in "real conditions" (in water solution) to get their characteristics once fluidized in culture medium. Culture medium is thus considered as water as the assumption is always made in literature about photobioreactor modeling (Nauha & Alopaeus, 2013). Bead diameter is measured using digital photographs (Sony camera, α450) of alginate beads in water. Beads are put on a black background to enhance contrast. Each picture contains more than one hundred beads which do not touch one another. 8 pictures containing new beads are considered which corresponds to approximately 1024 beads in average. Picture spatial resolution corresponds to 0.06 mm/pixel. Pictures are processed using Matlab R2020b including Image Processing Toolbox 11.2. A binarization step enables to convert pictures in black and white with a thresholding algorithm using Otsu method. A morphological opening (erosion followed by dilatation) is used to crop isolated pixels (Figure 4.2). Beads have not exactly a spherical but ellipsoidal shape. An equivalent diameter is used to characterize bead size, calculated as $\sqrt{\frac{4\times Area}{\pi}}$. Objects with diameter below 2 or above 4 mm are considered as noise, dust or light reflection artefacts, and removed. Using this method, the average bead diameter equals 2.80 ± 0.10 mm (with a confidence interval of 95 %) (Figure 4.3).

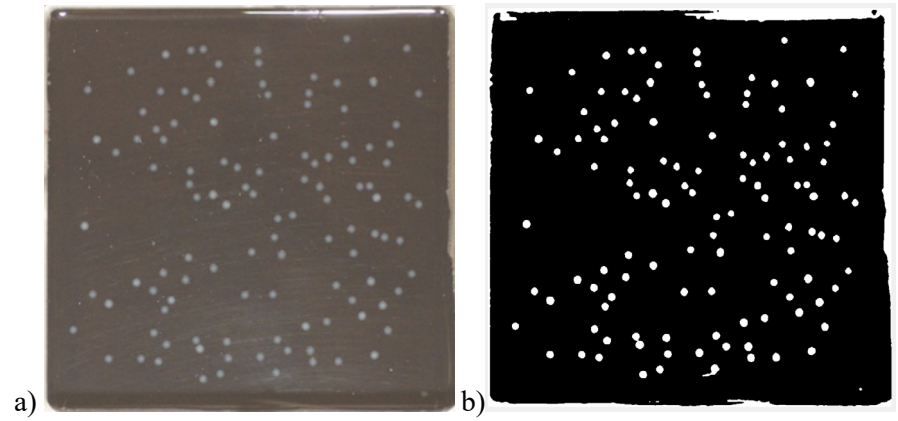

a) b)

Figure 4.2 – Photography of alginate beads (a). Same photography processed (binarization, erosion and dilatation) using Matlab (b).

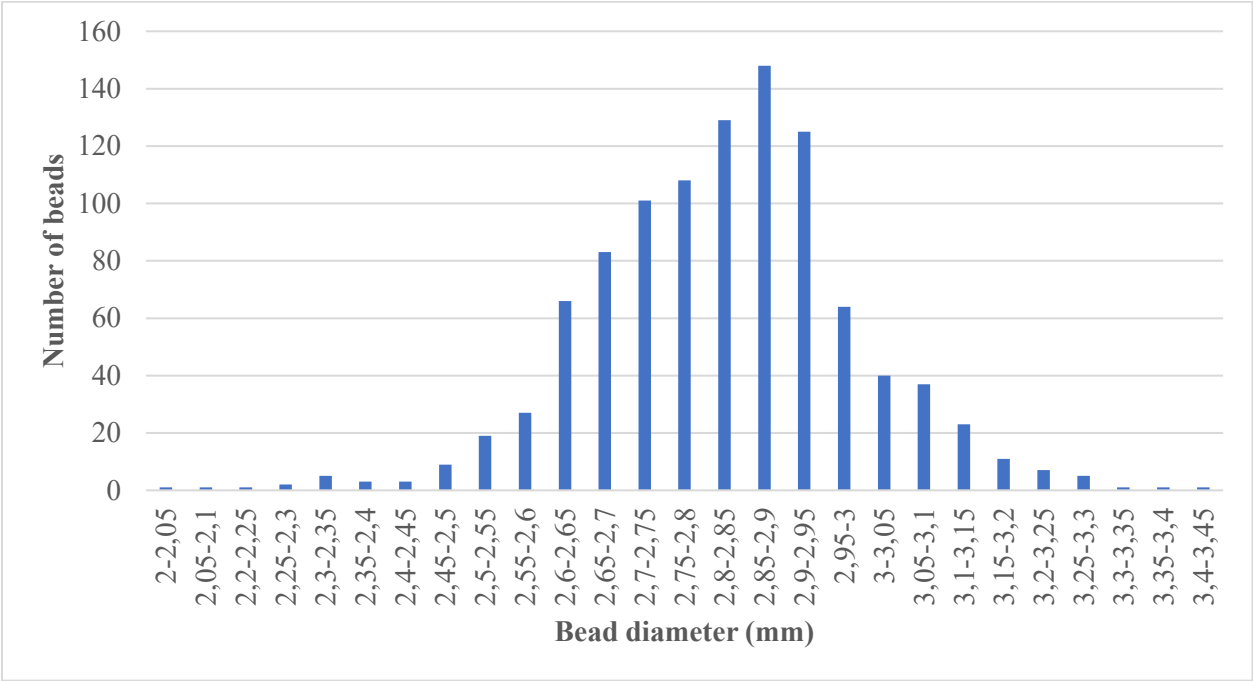

Figure 4.3 – Bead diameter distribution measured with images processed using Matlab. Total number of 1024 beads.

4.2.2.3 Bead density measurement

As bead density is close to water and must be measured inside water (4.2.2.2), measurement of bead density is not straightforward. Density is measured using settling velocities of 70 beads in a 1-meter-high column filled with distilled water (18 °C). The attenuation light method is performed in a room at 20 °C thus a close temperature. Column diameter is 30 times larger than bead diameter, so the influence of wall can be neglected (Malhotra & Sharma, 2014). When a single spheroidal particle (density ρ_s, diameter d_p) is settling with a constant speed ($u_{T,0}$) in a fluid at rest (velocity u_L, equal to 0 in this case, density ρ_l, cinematic viscosity ν_l), the force balance on the bead, considering the drag force and the buoyant force may be written as in (Equation 4.1).

$$C_D \rho_l {u_{T,0}}^2 = \frac{4}{3}(\rho_s - \rho_l) g d_p \quad \text{(Equation 4.1)}$$

Where the drag coefficient C_D depends on the particulate Reynolds number (Equation 4.2).

$$Re_p = \frac{d_p(u_{T,0} - u_L)}{\nu_l} \quad \text{(Equation 4.2)}$$

Using the measured settling velocities (average: 2.240 cm.s^{-1}, standard deviation: 0.077 cm.s^{-1}), a mean Reynolds number is calculated ($Re_p = 60$). As $1 < Re_p < 800$, the Schiller and Neumann correlation can be used to calculate C_D (Equation 4.3) and the bead density deduced from (Equation 4.1).

$$C_D = \frac{24}{\alpha_L Re_p}(1+0.15(\alpha_L Re_p)^{0.687}) \quad \text{(Equation 4.3)}$$

α_L is the liquid volume fraction and equal to 1 in this case.

As explained in 4.2.2.2, beads are not exactly spherical. The mean aspect ratio of the ellipsoidal beads, defined as the ratio between the minor and the major axis lengths (the aspect ratio of a sphere is equal to 1), equals 0.9. The influence of the spheroidal aspect of the beads on the flow is evaluated using a relation between the drag coefficient C_D and the elongation e (comparable to the aspect ratio in 3D) given by Bagheri & Bonadonna, 2016 (Equation 4.4). f is the fatness and equals to 1 in this case.

$$C_D = \frac{24 k_S}{Re_p}\left(1 + 0.125\left(Re_p \frac{k_N}{k_S}\right)^{\frac{2}{3}}\right) + \frac{0.46 k_N}{1 + \frac{5330}{Re_p \frac{k_N}{k_S}}} \quad \text{(Equation 4.4)}$$

$$\text{with } k_S = \frac{(fe^{1.3})^{\frac{1}{3}} + (fe^{1.3})^{-\frac{1}{3}}}{2}$$

$$k_N = 10^{\alpha_2(-\log(f^2 e))\beta_2}$$

$$\alpha_2 = 0.45 + \frac{10}{e^{2.5\,log\left(\frac{\rho_s}{\rho_l}\right)+30}}$$

$$\beta_2 = 0.45 - \frac{37}{e^{3\,log\left(\frac{\rho_s}{\rho_l}\right)+100}}$$

The drag coefficient C_D is 4.5 % higher with a particle with a 0.9 elongation, leading to velocities lower by 2.2 % (Equation 4.1). This is considered as a minor influence thus beads are considered as spherical in hydrodynamics characterization.

Using the settling velocities approach, the bead density is found to be 1018 ± 1 kg.m^{-3} at 18°C. If a 0.9 elongation is considered, the calculated density is 1 kg.m^{-3} higher.

4.2.3 Solid distribution measurement

The spatial distribution of the solid in the reactor is measured using an experimental method based on light attenuation and developed by Delafosse et al., 2018. The transparent alginate beads used to model the solid are compatible with this technique. Black and white photographs (greyscale images) of the reactor are taken by a CMOS camera (Figure 4.4). The reactor is illuminated on the other side by a white LED backlight (Phlox s.a., 70 000 cd.m²). Photographs of the entire column are thus taken through the depth of the reactor. The spatial resolution equals 6 pixels by mm. A "blank" image (reactor filled with distilled water) is taken when the bead bed is packed at the reactor bottom. Image processing is made using a homemade code on Matlab R2020b. Averages on 500 images (taken every 1 s) are calculated. On these blank images, the volume occupied by the packed bed (around 40 mm from the bottom of the image) approximately corresponds to the reactor volume next to the prism situated at the bottom of the reactor. Even when solid particles are dispersed in the reactor, this part of the image is unusable due to the strong light attenuation by the prism. Matlab software was used to crop and process images. For each image pixel, gray level is linked to light attenuation and then correlated with the local solid fraction.

a) 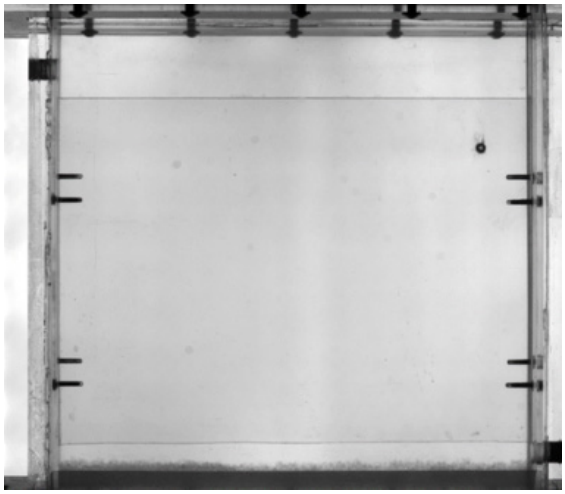 b) 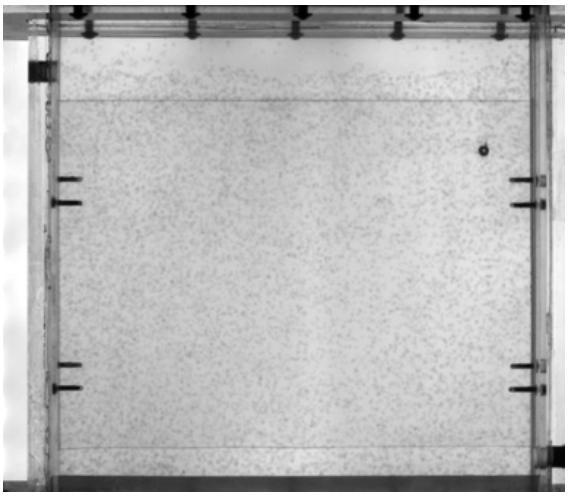

Figure 4.4 – Black and white photographs used for the attenuation light method. Image of empty reactor used as blank (a) and fluidized bed of alginate beads – 4.35 % of solid (b).

4.2.4 Two-phase flow modelling by CFD

CFD simulations are performed using Fluent software (ANSYS, 2019 version R3). The geometry, mesh and boundary conditions are similar to those used for single-(liquid) phase simulations (chapter 3). The geometry was drawn on DesignModeler software (ANSYS, 2019 version R3). The mesh is composed of around one million of hexahedrons. The mean edge size of the mesh is 1.70 mm (minimum size: 0.80 mm and maximum size: 2.70 mm). It is thus smaller than the mean bead size (2.80 ± 0.10 mm). This could seem inappropriate. However, using a larger cells size, which implies a lower number of cells, does not allow to properly describe the flow. Moreover, as an Euler-Euler approach is used, phases are considered as interpenetrating continua and volume fractions are calculated, so beads are not described individually in cells.

The liquid flow is laminar and unsteady. The optimal time step is found to be 0.02 seconds. A "mass flow inlet" and a "pressure outlet" boundary conditions are used. A single phase (liquid) initialization is first realized. Solids (4.4 % volume) is added after 10 seconds of flow simulation on the entire volume of the reactor using a patch on Fluent.

An Eulerian multiphase model is used to simulate the two-phase behavior. The pressure is solved for all phases while momentum and continuity equations are solved for each phase. Momentum and continuity equations are given by Navier-Stokes equations modified to take into account interphase momentum transfer. The continuity equations on both phases allow to calculate the volume fraction of each phase: liquid-L symbol (Equation 4.5) and solid-S symbol (Equation 4.6), with the sum of phase volume fractions equal to 1 (Equation 4.7).

$$\frac{\partial}{\partial t}(\propto_L \rho_L) + \nabla \cdot (\propto_L \rho_L \overrightarrow{u_L}) = 0 \qquad \textit{(Equation 4.5)}$$

$$\frac{\partial}{\partial t}(\propto_S \rho_S) + \nabla \cdot (\propto_S \rho_S \overrightarrow{u_S}) = 0 \qquad \textit{(Equation 4.6)}$$

$$\propto_S + \propto_L = 1 \qquad \textit{(Equation 4.7)}$$

The momentum conservation equations for liquid and solid phases are established as

(Equation 4.8) and

(Equation 4.9):

$$\frac{\partial}{\partial t}(\propto_L \rho_L \overrightarrow{u_L}) + \nabla \cdot (\propto_L \rho_L \overrightarrow{u_L . u_L}) = -\propto_L \nabla \mathrm{p} + \nabla \cdot (\propto_L \mu_L (\nabla \overrightarrow{u_L} + (\nabla \overrightarrow{u_L})^T)) + \propto_L \rho_L \vec{g} + K_{SL}(\overrightarrow{u_L} - \overrightarrow{u_S}) - \overrightarrow{F_{lift}} - \overrightarrow{F_{vm}} \qquad \textit{(Equation 4.8)}$$

$$\frac{\partial}{\partial t}(\propto_S \rho_S \overrightarrow{u_S}) + \nabla \cdot (\propto_S \rho_S \overrightarrow{u_S . u_S}) = -\propto_S \nabla \mathrm{p} - \nabla p_s + \nabla \cdot (\propto_S \mu_S (\nabla \overrightarrow{u_S} + (\nabla \overrightarrow{u_S})^T)) + \propto_S \rho_S \vec{g} + K_{SL}(\overrightarrow{u_S} - \overrightarrow{u_L}) + \overrightarrow{F_{lift}} + \overrightarrow{F_{vm}} \qquad \textit{(Equation 4.9)}$$

The fluid-solid exchange coefficient K_{SL} used in the momentum equation to model the drag force is calculated as:

$$K_{SL} = \frac{\propto_S \rho_S f_d}{\tau_S} \qquad \textit{(Equation 4.10)}$$

With the particle relaxation time τ_S calculated as:

$$\tau_S = \frac{\rho_S {d_p}^2}{18 \mu_L} \qquad \textit{(Equation 4.11)}$$

K_{SL} depends on the drag function f_d which includes the drag coefficient C_D calculated by (Equation 4.3). The function used in this work is the one proposed by Huilin Gidaspow (Gidaspow et al., 1992) (recommended for dense fluidized bed) which is a combination of Wen and Yu model (Wen & Yu, 1966) for $\alpha_L > 0.8$ (Equation 4.12) and Ergun equation (Ergun, 1952) for $\alpha_L < 0.8$ (Equation 4.13).

$$K_{SL} = \frac{3}{4} \mathrm{C_D} \frac{\propto_S \propto_L \rho_L (\mathrm{u_S} - \mathrm{u_L})}{d_p} \propto_L^{-2.65} \quad \textit{(Equation 4.12)}$$

$$K_{SL} = \frac{150\mu}{\mathrm{d_p}^2} \frac{(1-\varepsilon_\mathrm{b})^2}{\varepsilon_\mathrm{b}^3} \mathrm{u_L} + \frac{1.75\rho_\mathrm{L}}{\mathrm{d_p}} \frac{(1-\varepsilon_\mathrm{b})}{\varepsilon_\mathrm{b}^3} \mathrm{u_L}^2 \quad \textit{(Equation 4.13)}$$

A Granular phase is used to simulate the interactions between solids. It is based on kinetic theory of granular flow which considers the conservation of solid fluctuation energy. A solid pressure is calculated, composed of a kinetic and a particle collisions terms (Ding & Gidaspow, 1990). The solid pressure is used to calculate the pressure gradient term ∇p_s in the momentum equations relative to the solid phase (Equation 4.14).

$$p_s = \propto_S \rho_S T_S + 2\rho_S (1 + e_{ss}) \propto_S^2 g_{0,ss} T_S \quad \textit{(Equation 4.14)}$$

Where e_{ss} is the coefficient of restitution for particle collisions, T_S is the granular temperature energy which takes into account the particles fluctuating velocity and $g_{0,ss}$ is the radial distribution function which corrects the model of the probability of collisions between particles.
Lift force is calculated as:

$$\overrightarrow{F_{lift}} = C_l \rho_L \propto_S (\overrightarrow{u_L} - \overrightarrow{u_S}) (\nabla \times \overrightarrow{u_L}) \quad \textit{(Equation 4.15)}$$

The lift coefficient C_l is calculated according to Moraga model.

$$C_l = \begin{cases} 0.0767 \; if \; \varphi \leq 6000 \\ -(0.12 - 0.2e^{-\frac{\varphi}{3.6} \times 10^{-5}}) e^{\frac{\varphi}{3} \times 10^{-7}} \; if \; 6000 < \varphi \leq 5 \times 10^7 \\ -0.6353 \; if \; \varphi \geq 5 \times 10^7 \end{cases} \quad \textit{(Equation 4.16)}$$

Where $\varphi = Re_p Re_\omega$ with Re_ω the vorticity Reynolds number:

$$Re_\omega = \frac{(\nabla \times u_L) {d_p}^2}{\nu_l} \quad \textit{(Equation 4.17)}$$

Virtual mass force is calculated as:

$$\overrightarrow{F_{vm}} = -0.5 \propto_S \rho_L (\frac{d_L \overrightarrow{u_L}}{dt} - \frac{d_S \overrightarrow{u_S}}{dt}) \quad \textit{(Equation 4.18)}$$

The influence of virtual mass and lift forces are discussed in the results. As the density difference between phases is low, lift force can have a high influence (Malone 2006).

4.3 Results and discussion

4.3.1 Simulations results

4.3.1.1 Theoretical determination of the fluidization conditions (diameter and density)

As solid density ρ_S and particle diameter d_p play a key role in equations governing the flow (described in 4.2.4), uncertainties on the measurement of diameter and density of alginate beads can have a significant impact. A bead diameter of 2.80 ± 0.10 mm and a density of 1018 ± 1 kg.m^{-3} are estimated. Moreover, experimentally, it is determined that the minimum liquid mass flow inlet required to completely fluidize beads (1018 ± 1 kg.m^{-3}) equals 0.1138 kg.s^{-1}. But, on the basis of CFD simulations, it is observed that a bed of 1018 kg.m^{-3} beads cannot be entirely fluidized if a flow inlet equal to 0.1138 kg.s^{-1} is considered, while this flow allows a fluidization of 1014 kg.m^{-3} beads up to the top of the internal panel. Hence the influence of these bead characteristics (diameter 2.80 ± 0.10 mm, density 1014-1018 kg.m^{-3}) on the flow is first studied theoretically.

Richardson and Zaki law (Richardson & Zaki, 1997) describes the theoretical relation between the settling velocity of a single bead ($u_{T,0}$) and the hindered settling velocity of the bead bed (Equation 4.19).

$$u_b = u_{T,0} \times (1 - \overline{\alpha_s})^n \qquad \textit{(Equation 4.19)}$$

where n is an empirical coefficient.

For $1 < Re_p < 200$,

$$n = (4.45 + 18\frac{d_p}{D_h}){Re_p}^{-0.1} \qquad \textit{(Equation 4.20)}$$

where D_h is the hydraulic diameter.

As explained in 4.2.2.3, the bead diameter has a direct influence on the single bead settling velocity. Hence the theoretical influence of the bead diameter on the settling velocity of the bead swarm can be calculated combining (Equation 4.1) and (Equation 4.19).

For a given bead density, the settling velocity $u_{T,0}$ is calculated iteratively (as it depends on Re_p calculated from $u_{T,0}$) using equation (Equation 4.1) for different diameters d_p. Finally the settling velocity of the bed u_b is calculated as a function of d_p using Richardson and Zaki law (Equation 4.19). The solid volume fraction is 0.04. In reality, it is assumed to be between 0.03 and 0.06 in the bed due to local accumulation, but results are not influenced by these close solid fractions.

In these conditions, the measurement error on the bead diameter ± 0.1 mm, has a relative impact on the computed hindered settling velocity of ± 3.5 %, if a density equal to 1014 kg.m^{-3} is considered. Hence the impact of the error on the bead diameter is rather low when studying the fluidization conditions.

The influence of bead density on the fluidized bed is studied as well. The single bead settling velocity directly depends on the bead density. For a constant bead diameter, $u_{T,0}$ is calculated iteratively and u_b deducted from Richardson and Zaki law. For a solid volume fraction of 0.04, the influence of a density varying between 1014 and 1018 kg.m^{-3} on the hindered velocity is 14 %. Hence the bead density has a significant influence on the fluidization conditions of the beads.

4.3.1.2 Co-influence of interaction forces and density

As it is found to theoretically have a non-negligible influence on the flow, the impact of density on the flow is further studied using CFD simulations. Interaction forces (drag, virtual mass and lift) have an influence on fluidization as well (Table 4.1). Using only the drag force as interaction force, beads of 1018 $kg.m^{-3}$ cannot be fluidized using the experimental liquid flow rate of 0.1310 $kg.s^{-1}$ while beads of 1014 $kg.m^{-3}$ are fluidized (Table 4.1). However, using three interaction forces (drag, virtual mass and lift), beads of 1018 $kg.m^{-3}$ can be fluidized using the experimental liquid flow rate of 0.1310 $kg.s^{-1}$. In any case, beads of 1018 $kg.m^{-3}$ cannot be fluidized using a liquid flow rate of 0.1138 $kg.s^{-1}$ which is the minimum flow rate required to completely fluidize beads experimentally. Hence, both influences (density and interaction forces) are studied.

Using drag, virtual mass and lift interaction forces, the flow rate considered in the experimental part (4.3.1), equal to 0.1310 $kg.s^{-1}$, allows to fluidize 1018 $kg.m^{-3}$ beads. This value of liquid flow rate is thus used, in CFD simulations, to study the influence of density (1014-1018 $kg.m^{-3}$) on solid distribution.

To study influence of interaction forces, a density of 1014 $kg.m^{-3}$ must be used as the bed cannot be fluidized using a density of 1018 $kg.m^{-3}$ when lift is not considered.

Even if the influence is low, a bead diameter of 2.70 mm, within the uncertainty experimental range, is chosen in simulations as the liquid flow rate needed to fluidize the bed is higher to the experimental one.

As the global solid fraction in CFD (0.0440) and the experimental method (0.0435) is not exactly the same, results are normalized (divided by their mean global solid fraction) to be compared. It must be noticed that the global solid fractions are close and the difference has no influence on results described in this section.

Table 4.1 - Parameters of different simulations (CFD) used to study the influence of bead density and interaction forces. Total fluidization means a bed expansion up to the top of the internal panel.

Liquid flow rate ($kg.s^{-1}$)	Bead characteristics		Forces	Total Fluidization (Yes/No)
	Diameter (mm)	Density ($kg.m^{-3}$)	D: drag; VM: virtual mass; L: lift	
0.1310	2.70	1018	D	No
0.1310	2.70	1014	D	Yes
0.1310	2.70	1018	D + VM	No
0.1138	2.70	1018	D + VM + L	No
0.1138	2.70	1014	D + VM + L	Yes
0.1310	2.70	1014	D + VM + L	Yes
0.1310	**2.70**	**1018**	**D + VM + L**	**Yes**

4.3.1.2.1 Influence of density

The influence of bead density on the solid distribution is further evaluated using CFD simulations using drag, virtual mass and lift interaction forces. Two different densities are studied: 1014 and 1018 $kg.m^{-3}$. A liquid mass flow rate at the inlet equal to the experimental one (0.1310 $kg.s^{-1}$) is considered.

From 3D distributions simulated by CFD, vertical profiles of solid fraction are calculated by averaging over the reactor depth and width using Matlab. Null values due to the internal panel are not accounted for in the averaging process. Solid fractions are normalized (divided by the mean solid fraction in the reactor, equal to 0.044).

If density values equal to 1014 and 1018 kg.m^{-3} are successively considered, the 4 kg.m^{-3} difference has a low influence on the global solid fraction distribution (Figure 4.5). Solid fraction is higher (between 1 and 4 % relative difference) along the internal panel (z = 50 to 300 mm) using a bead density of 1018 kg.m^{-3}.

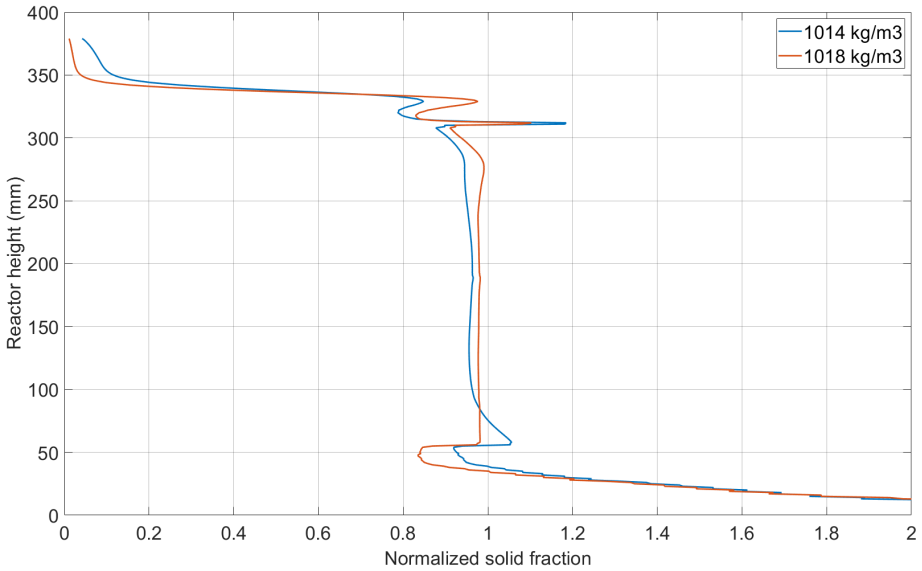

Figure 4.5 - Solid distribution profiles averaged over the reactor width and depth obtained by CFD using bead densities of 1014 or 1018 kg.m^{-3}. Liquid mass flow rate of 0.1310 kg.s^{-1} and bead diameter of 2.70 mm.

The influence of density is more significant at a local point of view. The bead density influence is indeed not negligible anymore if the solid distribution is studied on specific vertical planes. Studying plane 5 (Figure 4.6), the difference in solid distribution vertical profile (averaged over the reactor width) between a density of 1014 and 1018 kg.m^{-3} from z=100 to 300 mm leads to a relative difference in the solid distribution of 23 %. It has thus a major influence on the fluidized bed behavior.

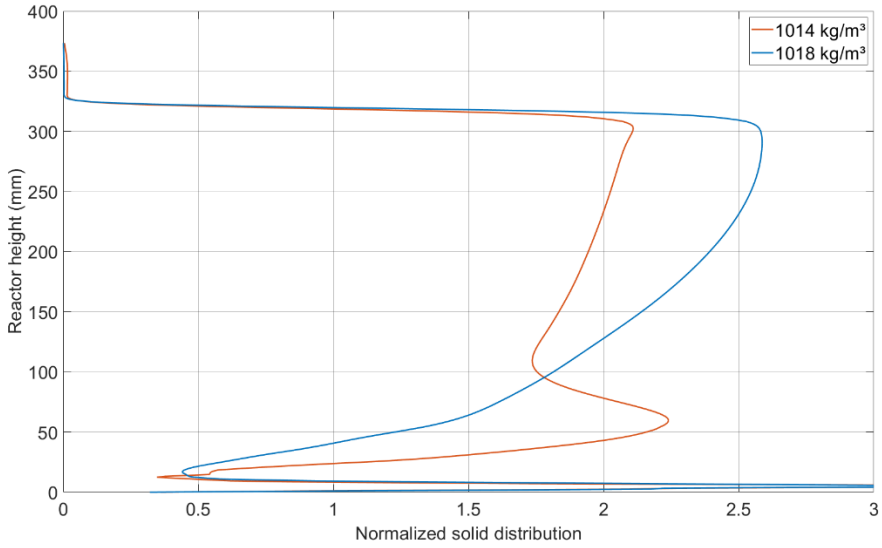

Figure 4.6 - Plane 5 solid distribution profile of the reactor obtained by CFD using bead densities of 1014 or 1018 kg.m^{-3}. Liquid mass flow rate of 0.1310 kg.s^{-1} and bead diameter of 2.70 mm.

4.3.1.2.2 Influence of the virtual mass and the lift force

In solid-liquid systems, different interaction forces can be considered. The mains are drag, virtual mass and lift (4.2.4). Drag is the most important and considered by default by Fluent. The virtual mass and the lift forces are sometimes neglected. In case of liquid-solid fluidized bed, most studies neglect the lift or the virtual mass force without justification (Zbib et al., 2018). However, Malone et al., 2006 found a significant influence of lift force due to a low density difference between phases as well as Koerich et al., 2018. On the contrary, the virtual mass force is more important and can be not negligible when the density difference is high (Wang et al., 2014). Hence, the influence of the virtual mass and the lift are studied in the present reactor. The study is performed using a bead diameter of 2.70 mm and a density of 1014 kg.m^{-3}. A liquid flow rate of 0.1310 kg.s^{-1} is used.

Solid distribution in the reactor depth is studied using drag force only; drag and virtual mass; drag, virtual mass and lift (Figure 4.7). Solid distribution is more homogeneous in the descending zone considering virtual mass and lift forces. Indeed, considering only the drag force, solid fraction is higher close to the internal panel and decreases near the reactor wall. Above the internal panel, solid behavior is different as well.

Horizontal profiles (solid distribution averaged over the reactor depth and height) are calculated using the different forces (Figure 4.8 a). There is no high influence of virtual mass or lift on horizontal profiles, except a higher side-effect of lateral walls using lift.

Vertical profiles (solid distribution averaged over the reactor depth and width) are studied (Figure 4.8 b). Virtual mass has a low influence on solid distribution. Simulations considering lift and virtual mass has a higher influence, showing a higher solid fraction along the internal panel, but a lower accumulation just at the top of the panel. One should notice that a density of 1014 kg.m^{-3} is used for these simulations which is lower than measured experimentally (1018 ± 1 kg.m^{-3}). The discrepancies with experimental results using a density of 1018 kg.m^{-3} is discussed in 4.3.3.

Hence, because using only drag does not allow to fluidize a bead bed of 1018 kg.m^{-3} density and due to their influence on the solid distribution (more homogeneous along the internal panel), the virtual mass and the lift force are considered in CFD simulations.

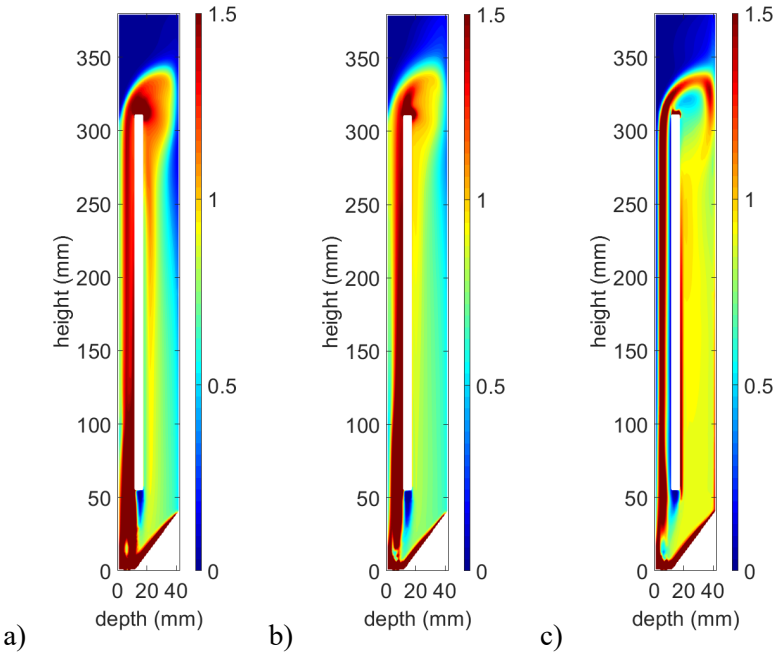

Figure 4.7 - Solid distributions obtained by CFD (mean on 500 images) normalized by the global solid fraction. 2D solid distributions in vertical planes (average over the reactor width) including drag force only (a), drag and virtual mass force (b), drag, virtual mass and lift force (c).

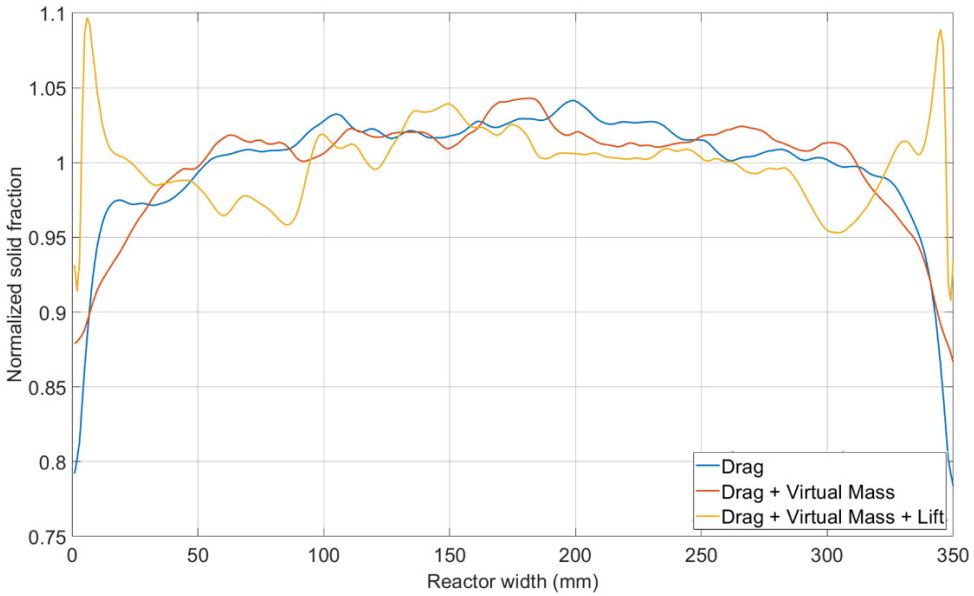

a)

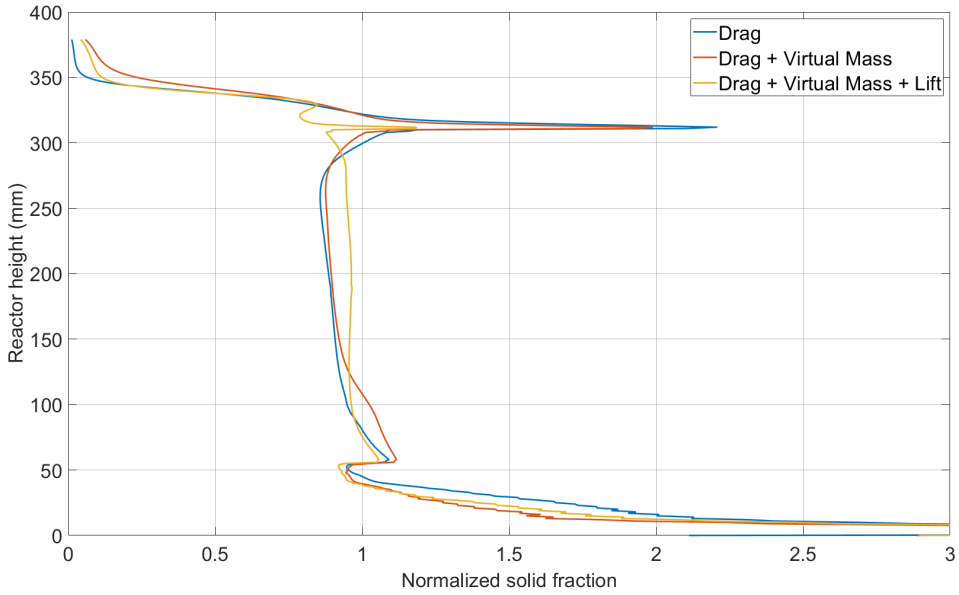

b)

Figure 4.8 – Solid distributions obtained by CFD (mean on 500 images) normalized by the global solid fraction. Horizontal profiles (averaged over the reactor depth and height) (a). Vertical profiles (averaged over the reactor depth and width) (b).

4.3.2 Experimental characterization of solid distribution

The aim of the experimental characterization is to study the bead behavior inside the reactor. The photobioreactor is filled with distilled water and beads, with a volume solid fraction equal to 4.35 %. The minimum liquid flow rate allowing a complete fluidization of solid particles (up to 35 cm height) equals 0.1138 $kg.s^{-1}$.

As presented in section 4.2.3, a light attenuation method is used to determine the solid distribution. The liquid flow rate is fixed at 0.1310 $kg.s^{-1}$. On Figure 4.4, one can observed that the bottom zone is

unreachable due to the prism. Solids are present in the whole reactor (below, along and over the internal panel) but solid fraction decreases at the top of the reactor.

Gray level values of pixels in black and white photographs can be directly related to the local solid concentration through the reactor depth. In a previous study, a calibration curve was drawn by Delafosse et al., 2018 for different solid fractions, based on measurements realized on homogeneous solid distributions inside a stirred tank. This kind of measurements cannot be performed here. However, as demonstrated by Delafosse et al., 2018, a linear relation between the log(A/A0) term and the solid fraction, as expressed in the Beer-Lambert law, is observed if the solid fraction is low enough (Equation 4.21).

$$-\log\left(\frac{A}{A_0}\right) = k_a\langle\propto_S\rangle \qquad \textit{(Equation 4.21)}$$

A and A_0 are the pixel gray level values in the fluidized bed reactor pictures and in the blank image (reactor filled with water), respectively.

k_a represents the absorption coefficient of alginate beads multiplied by the thickness of the liquid-solid dispersion. The attenuation of reactor walls and liquid (water) is subtracted in the blank.

$\langle\propto_S\rangle$ is the "local" volume solid fraction. It is relative to a given height and width in the reactor, but it is not related to a single point along the reactor depth, as the attenuation is integrated over the whole liquid-solid dispersion depth. Hence the "local" solid fraction is an average value over the reactor depth. k_a is related to the thickness of the liquid-solid dispersion. It is constant in all the reactor, except in the zone with the internal panel V_p (Figure 4.9), which occupies 13 % of the reactor depth. In this zone, k_a is thus considered 13 % lower.

4.3.2.1 Calibration of the technique

The global volume fraction of solids in the reactor ($\overline{\langle\propto_S\rangle}_T$) is equal to 0.0435 (Equation 4.23). Two zones are not reachable by the attenuation technique, the bottom zone below a height of 40 mm, V_b, due to the bottom prism, and the top zone above 350 mm, V_h, due to Plexiglass sheets used to close the reactor. The solid fraction cannot be measured, and some assumptions must thus be done relative to the solid fraction in these zones.

As a first step, the solid fraction in the bottom zone, $\overline{\langle\propto_S\rangle}_b$, is considered equal to the solid fraction just below the internal panel $\overline{\langle\propto_S\rangle}_1$ (Equation 4.24).
As the solid fraction is visually very low in the top zone, it is considered null (Equation 4.25).
These assumptions are integrated in the global mass balance (Equation 4.22) which relates the global solid fraction ($\overline{\langle\propto_S\rangle}_T$) in the reactor, to the solid fractions in the different zones of the reactor weighted by their corresponding volumes. $\overline{\langle\propto_S\rangle}_1$ and $\overline{\langle\propto_S\rangle}_p$ are replaced by their expressions as a function of light attenuation from Beer-Lambert law (Equation 4.21) to calculate the attenuation coefficient, k_a.
Finally, local values of solid fractions $\langle\propto_S\rangle$ are calculated from attenuation images according to Beer-Lambert (Equation 4.21).

$$\overline{\langle\propto_S\rangle}_T V_T = \overline{\langle\propto_S\rangle}_h V_h + \overline{\langle\propto_S\rangle}_2 V_2 + \overline{\langle\propto_S\rangle}_p V_p + \overline{\langle\propto_S\rangle}_1 V_1 + \overline{\langle\propto_S\rangle}_b V_b \qquad \textit{(Equation 4.22)}$$

$$\overline{\langle \alpha_S \rangle}_T = 0.0435 \qquad \textit{(Equation 4.23)}$$

$$\overline{\langle \alpha_S \rangle}_b = \overline{\langle \alpha_S \rangle}_1 \qquad \textit{(Equation 4.24)}$$

$$\overline{\langle \alpha_S \rangle}_h = 0 \qquad \textit{(Equation 4.25)}$$

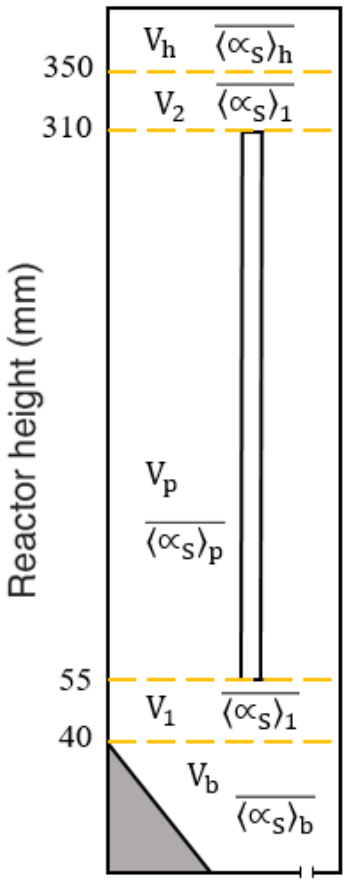

Figure 4.9 - Schematic representation of the depth of the reactor. Volume and solid concentration description. Dimensions are not true to scale.

4.3.2.2 Experimental results

Two kinds of solid profiles are computed by spatially averaging the solid distribution 2D images: vertical and horizontal profiles are obtained from averages over the reactor width and height, respectively (Figure 4.11). Vertical profiles indicate a rather homogeneous solid distribution in the reactor from 50 mm height to 250 mm. An accumulation of solids at z = 310 mm corresponds to the top edge of the internal panel. Vertical velocity decreases at this height as beads are changing direction (from upflow to downflow) which causes a bead accumulation.

Some high or low local values are also observed in other zones of the reactor (Figure 4.10). For example, at the left of the reactor (width < 30 mm) between z = 50 and 150 mm. They can be attributed to light reflections and are not due to local accumulations. Screws used to fix the internal panel can be detected

close to the lateral walls. They are not taken into account for the calculation of the profile. On horizontal profiles, experimental results obtained by the attenuation light show a higher solid fraction near the reactor walls. It should be noticed that the liquid injection under the slit of the reactor is coming from a horizontal pipe perforated with 7 holes of 7 mm of diameter distributed along the whole reactor width and fed with water by both ends. Hence the liquid flow rate is not perfectly uniform along the reactor width and is slightly higher near the reactor sides. It has been considered negligible in chapter 3 as it was less visible when observing only the liquid phase. However, it can be seen on PIV results (obtained on single liquid flow) if the color scale is specifically enhanced to evidence it (Figure 4.12).

The local solid distribution in the reactor is studied using two different liquid flow rates, for which the bed of particles is fluidized: 0.1310 $kg.s^{-1}$ and 0.1210 $kg.s^{-1}$. Regarding the solid profiles according to the height, the impact of the internal panel is visible exactly at the same height (310 mm). However, if a 0.1210 $kg.s^{-1}$ flow rate is used, the accumulation of solid is more significant in the lower part of the reactor (below 150 mm) and less important over that height compared to a 0.1310 $kg.s^{-1}$ flow rate. The relative difference is evaluated around 8% in the lower part as well as in the higher part. The difference can be explained as a higher flow rate enables to get a more uniform fluidized bed. The solid distribution along the reactor width differs as well, the solid accumulation is more important in the left side ($x < 50$ mm) using a 0.1210 $kg.s^{-1}$ flow rate.

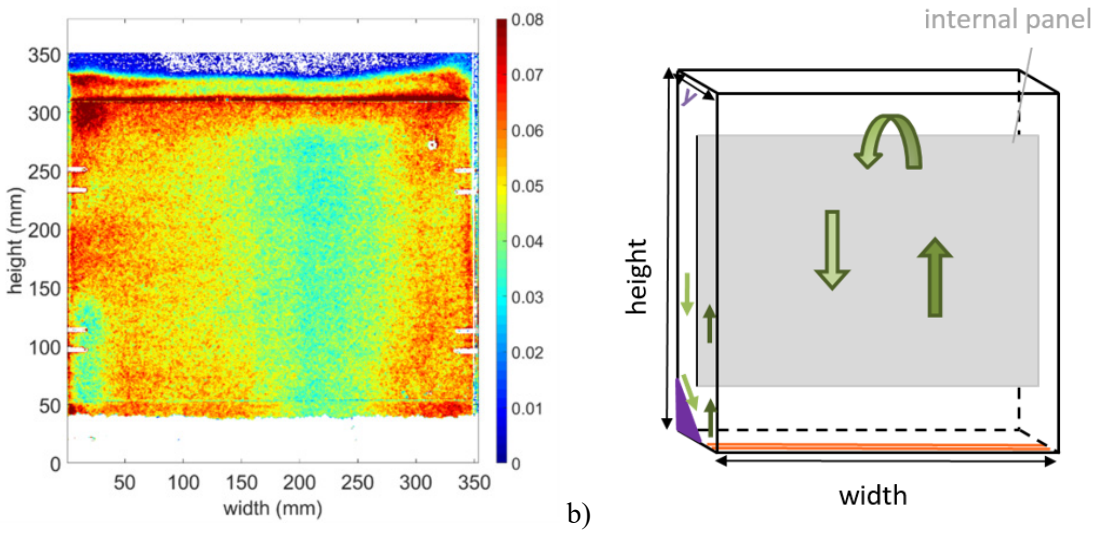

a) b)

Figure 4.10 - Solid distribution averaged over the reactor depth measured using attenuation light experimental method for a liquid flow rate of 0.1310 $kg.s^{-1}$ (a). Mean on 500 images. Schematic representation of the reactor set up (b).

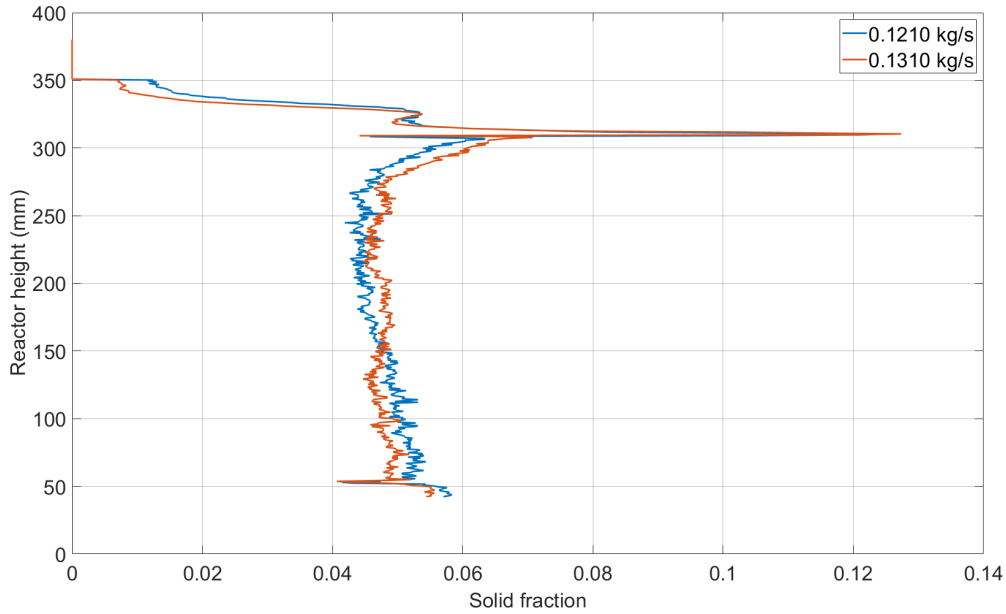

a)

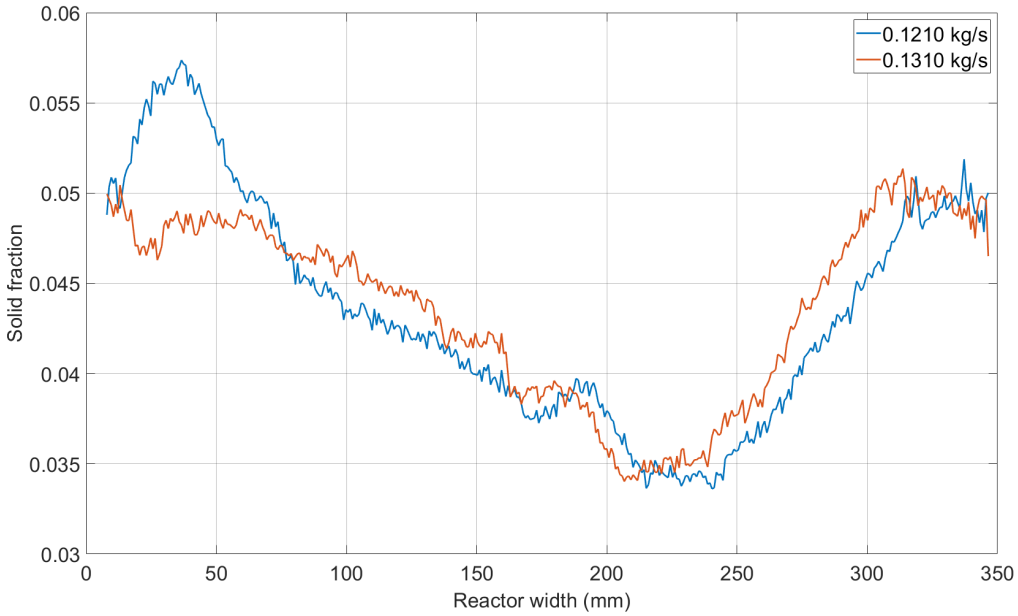

b)

Figure 4.11 –Solid fraction distribution profiles measured for two different liquid flow rates: 0.1310 kg.s^{-1} and 0.1210 kg.s^{-1}: vertical profiles obtained by averaging over the reactor width (a) and horizontal profiles obtained by averaging over the reactor height (b). Mean on 500 images.

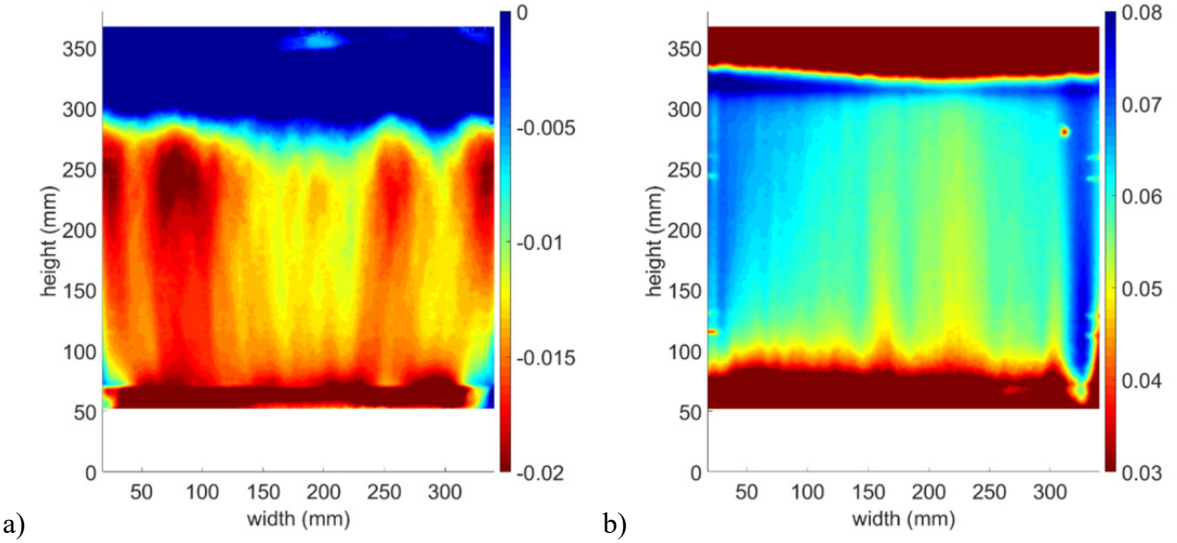

Figure 4.12 – 2D vertical velocity fields (m/s) measured by PIV in vertical planes: planes 3 (a) and plane 5 (b) situated respectively at 18 and 28 mm from the reactor wall towards the camera. Velocity fields obtained on single liquid flow.

4.3.2.3 Correction of experimental results

Using any density and including virtual mass and lift forces or not, an accumulation of solid at the bottom of the reactor (below 40 mm) is highlighted using CFD. The solid volume fraction in this zone is 0.108 (corrected by the experimental solid fraction which is slightly different than in CFD) which is really higher than in other parts of the reactor (0.0435 in total). This zone is not reachable by the attenuation light method (experimental results) due to the bottom prism in the reactor. Nevertheless, a visual accumulation of solids at the bottom of the reactor is noticed, due to the slowdown of beads on the prism.

As experimental results are calculated based on the total volume fraction (4.3.2.1), it has been calculated once more taking into account the accumulation of solid in the bottom of the reactor (Equation 4.26) instead of using a solid fraction equal to the one below the internal panel (Equation 4.24).

$$\overline{\langle \alpha_S \rangle}_b = 0.108 \qquad \textit{(Equation 4.26)}$$

CFD confirms that no solids are present at the top of the reactor (z > 350 mm). Hence this assumption in experimental results ($\overline{\langle \alpha_S \rangle}_h = 0$) is kept.

Vertical profiles (averaged over the width) using basic assumption and CFD correction are compared (Figure 4.13). Experimental results based on CFD correction gives logically a lower solid fraction in the other parts of the reactor as it is based on a higher fraction below 40 mm. The impact of this correction is significant as it presents 10 % of relative difference. The CFD correction is used in the following, even if it cannot be validated, as a higher solid fraction in the bottom part of the reactor is more realistic because visually noticed.

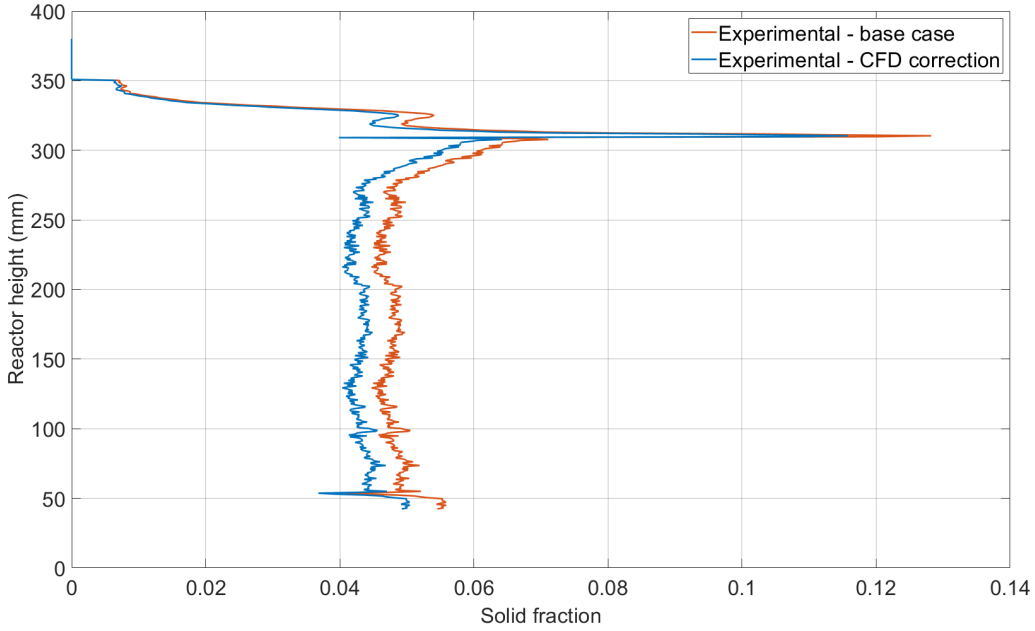

Figure 4.13 - Vertical solid fraction distribution profiles obtained by averaging over the reactor width, measured using a liquid flow rate of 0.1310 kg.s^{-1}. Solid fraction below 40 mm is estimated equal to the solid fraction below the internal panel (base case) or equal to the solid fraction calculated by CFD.

4.3.3 Comparison between experimental and simulations results

Experimental solid distributions are compared to simulations (liquid flow rate: 0.1310 kg.s^{-1}, density: 1018 kg.m^{-3}, diameter: 2.70 mm, drag, virtual mass and lift forces included). As the experimental method gives access only to the solid distribution values averaged over the reactor depth, simulations results are extracted and processed to be comparable. Local simulated solid distribution values are averaged over the reactor depth using Matlab. Null values due to the internal panel are not accounted for the average.

The solid distributions averaged over the reactor depth are presented on Figure 4.14 a b. Simulations and experiments both show an accumulation around z=310 mm which corresponds to the top of the internal panel. CFD solid distribution is more homogeneous than solid distribution obtained using the experimental method.

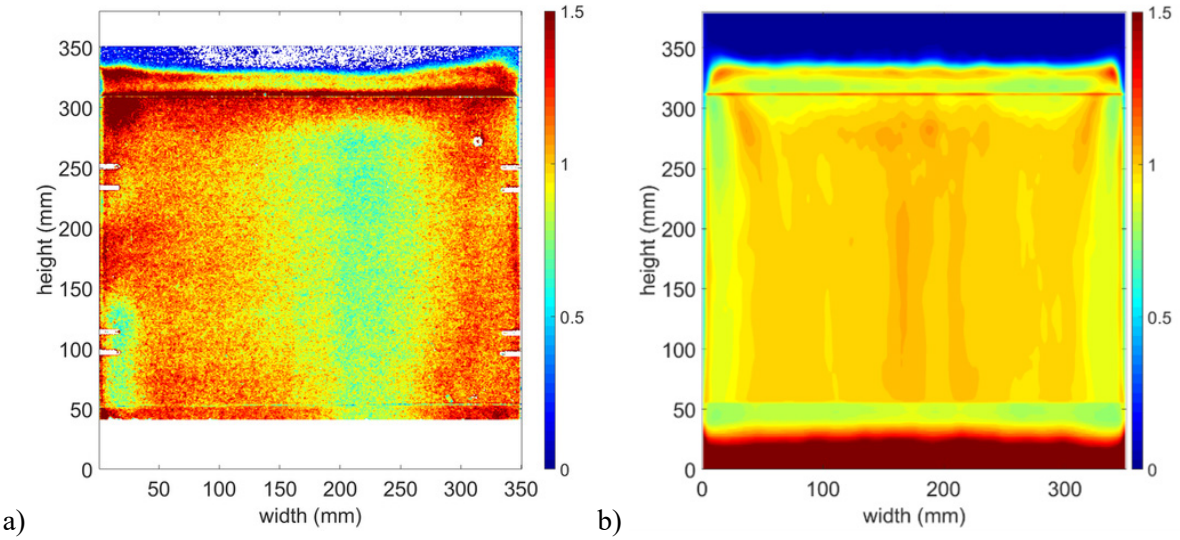

Figure 4.14 - Solid distribution averaged over the reactor depth measured using attenuation light experimental method (a). Solid distribution averaged over the reactor depth obtained by CFD (b) Mean on 500 images.

The analysis of profiles of solid distribution allows a more quantitative comparison between experimental and simulation results. Vertical profiles show solid distribution averaged over the reactor width (Figure 4.15 a). CFD results present a lower accumulation at the top of the internal panel than experiments. The solid distribution along the internal panel simulated by CFD is in good agreement with experiment. This confirms that the virtual mass and lift forces which lead to more homogeneous distribution must be taken into account (4.3.1.2.2). For heights between 50 and 250 mm, discrepancies between CFD and experimental are lower than 4 % in relative (as normalized values are considered).

However, comparison of horizontal profiles (averaged over the reactor height) indicates that the CFD results does not exactly match with experimental results (Figure 4.15 b). In CFD, horizontal profile oscillates between 0.95 and 1.05 normalized solid fraction, with a low accumulation of solid noticed in the center of the reactor and less solid present near the walls (probably due to the side-effect). On the contrary, on experimental profile, a lower normalized solid fraction is noticed in the right central zone (150 - 250 mm from the left). It is probably due to a higher flow rate on the reactor sides as the flow rate along the slit is non-uniform (4.3.2.2). In this zone, discrepancies with CFD reach a maximum of 24 % in relative.

Hence if the model describes well the solid distribution in the reactor height, experimental variations in the width cannot be predicted by the model.

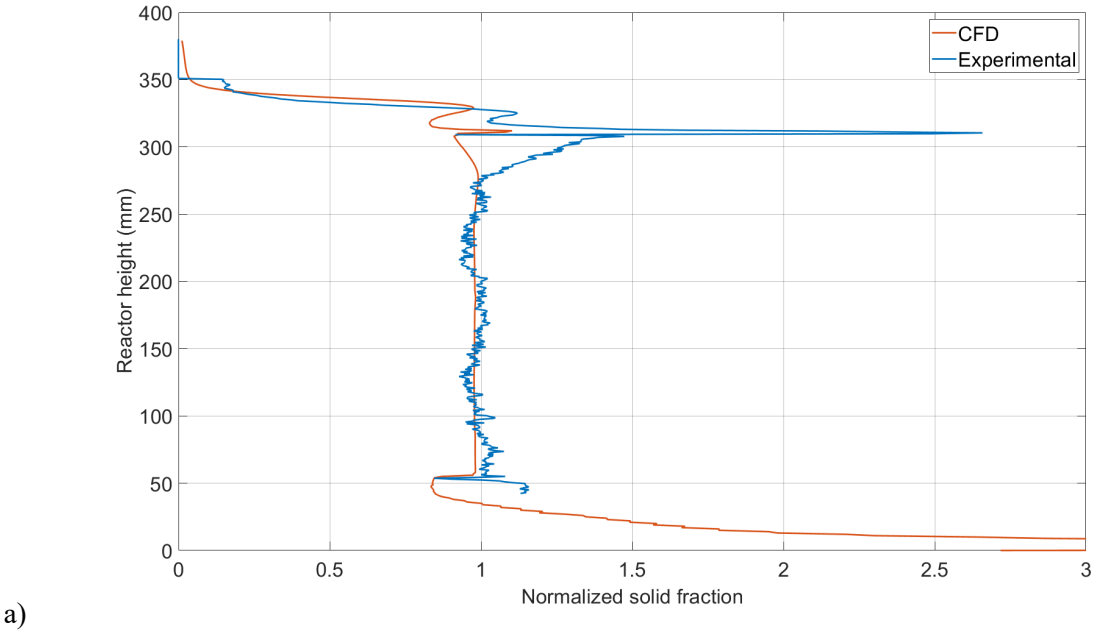

a)

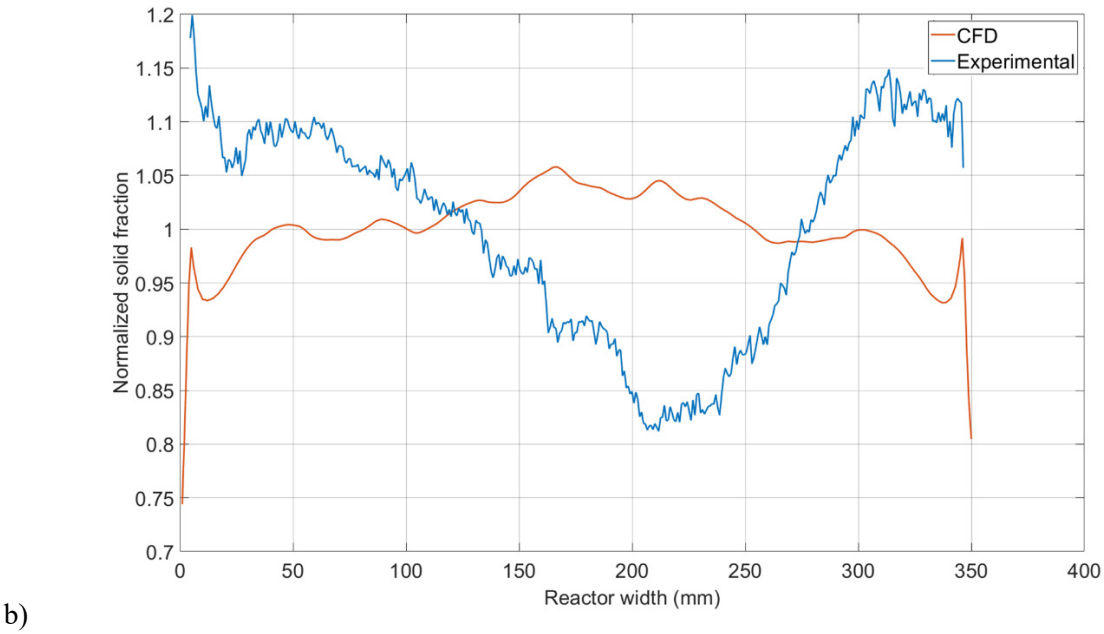

b)

Figure 4.15 - Solid fraction distribution profile obtained by calculating the mean along the reactor height (a) or width (b) using the experimental method or CFD. Mean on 500 images using both methods.

4.3.4 Solid distribution in the reactor

CFD allows to reach local solid distribution in the reactor while the experimental method only enables to access the solid distribution averaged over the reactor depth. Hence, CFD simulations allows to quantify the higher solid fraction in the ascending zone than in the descending zone (Figure 4.16). In plane 3, situated in the descending zone, the normalized solid fraction is close to 0.9 while it is higher than 1.5 in the plane 5 (ascending zone). This heterogeneous solid distribution has an influence on light attenuation by beads in the reactor thus on the biomass growth (chapter 5). This information is not

reachable using the attenuation light method as the latter only gives access to solid fractions values averaged over the reactor depth. Experimental results give access to global quantities which are considered sufficient to validate CFD. Different studies in literature use the same strategy validating CFD on global solid hold-up for example (Cornelissen et al., 2007; Davarnejad et al., 2014). In this way, CFD allows to access local values (of solid distribution and velocities) which are unreachable by experiments. CFD simulation and experimental method are thus not perfectly equivalent, but rather complementarity.

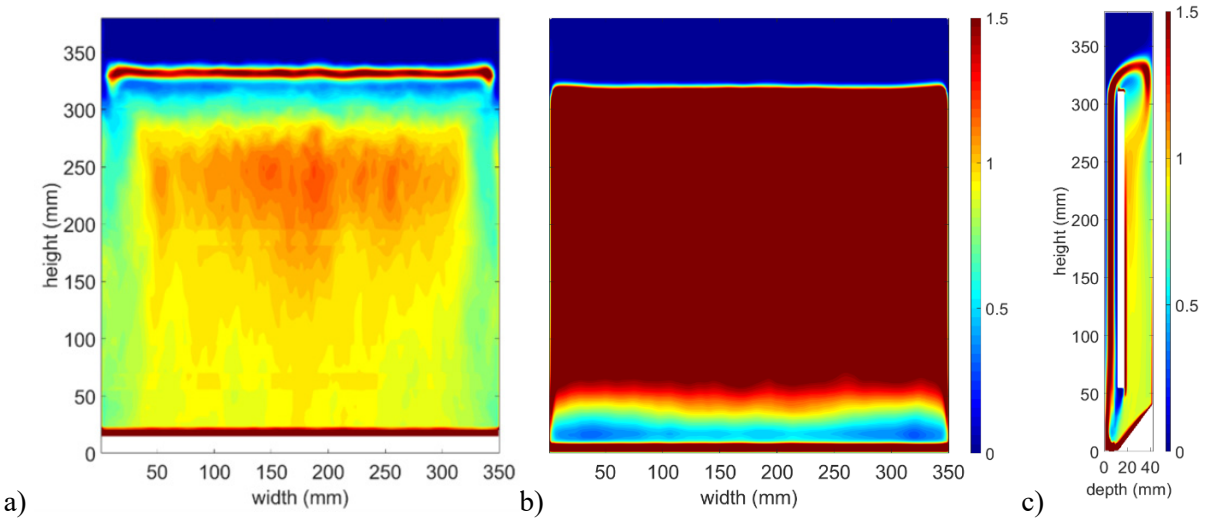

Figure 4.16 – Normalized solid fraction obtained by CFD in the descending zone: plane 3 (a) and in the ascending zone: plane 5 (b). Planes position is indicated in Figure 4.1. Normalized solid fraction obtained by CFD in the reactor depth (c). Liquid flow rate of 0.1310 kg.s^{-1}, bead diameter of 2.70 mm and density of 1018 kg.m^{-3}. Simulations including the drag, the virtual mass and the lift force.

4.3.5 Comparison of liquid and solid velocity fields

In order to develop a global model, it is useful to evaluate differences between solid and liquid flow behaviors. Because liquid and solid densities are close, global behaviors are expected to be similar but needs to be more precisely quantified. Liquid and solid flows have been compared based on vertical profiles of vertical components of velocities ("vertical velocity"). As explained in chapter 3, the horizontal component of velocity ("horizontal velocity") is negligible if compared to the vertical one. The normal component of velocity ('normal velocity") is also negligible everywhere except in the zone between 300 and 350 mm. So the vertical velocity is more representative of the entire flow. Vertical profiles (averaged over the reactor width) of vertical velocities of solid and liquid are compared in two planes: plane 3, situated in the descending zone, and plane 5, situated in the ascending zone (Figure 4.1). Solid perfectly follows the liquid flow: velocity profiles are similar in shape (Figure 4.17). But vertical profiles are shifted: solid velocity is higher (60 %) than liquid velocity in the descending zone, while it is smaller (17 %) in the ascending zone. This is obviously due to gravity, as solid density is slightly higher than liquid density. Hence displacements of beads containing algae (solid) cannot be completed modeled based on liquid velocities in this reactor. It must be noticed that the absolute difference of solid and liquid velocities (relative velocity) is around 0.018 m/s in plane 3 and between 0.013 and 0.016 m/s (depending on the height) in plane 5.

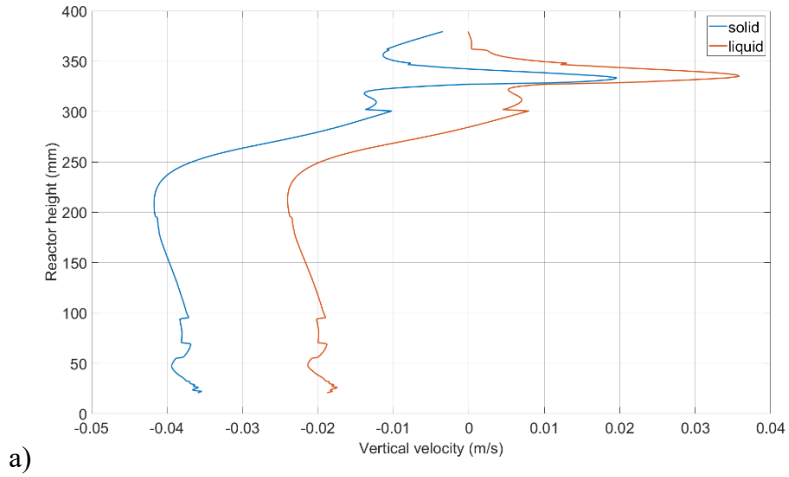

a)

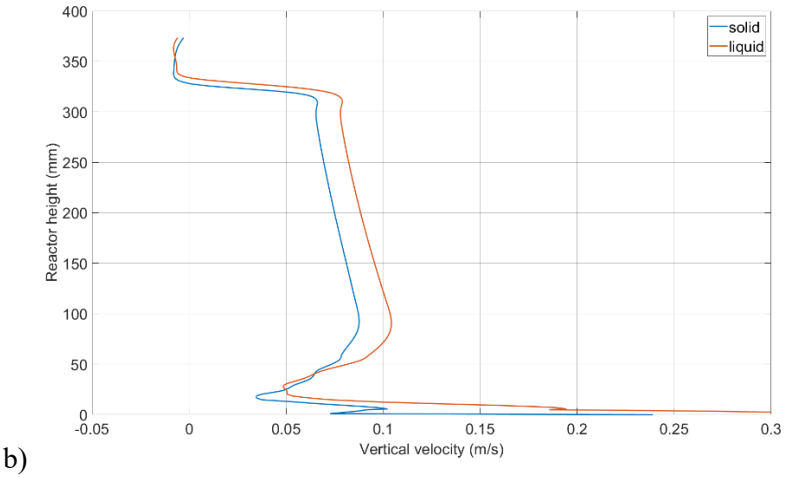

b)

Figure 4.17 – Vertical profiles of vertical velocity of liquid and solid in plane 3 (a) and plane 5 (b) obtained by CFD. Plane positions are indicated in Figure 4.1.

4.3.6 Influence of the solid on the flow

Vertical velocities of liquid in single-phase and two-phase flows are compared to evaluate the influence of the solid on the flow (Figure 4.18).

Figure 4.18 a b presents liquid vertical velocities in plane 3 (descending zone) simulated by CFD. They show that below z=300 mm, liquid velocities in single-phase flow are higher than in two-phase flow, except close to the reactor lateral walls. Indeed, null liquid velocities are predicted by CFD close to the reactor walls in two-phase flow (probably due to side-effect). This is due to the solid phase as they are not observed in single-phase simulations. Low positive velocities are even calculated on the left side. This can due to higher viscous friction forces present when particles get closer to walls, linked to the low gap between the particle and the wall (Ferchichi, 2013).

Figure 4.18 c d presents liquid vertical velocities in plane 5 (ascending zone) simulated by CFD. They show that liquid vertical velocities are lower in presence of solid between z = 100 and 300 mm, the solid probably slowing down the liquid flow. Below 100 mm, velocities are higher in two-phase flow. The liquid inlet is deviated in single-phase flow leading to negative velocities in plane 5 (between z = 15 and 20 mm). It is not visible on two-phase flow as the solid redirects the liquid flow to the internal panel. The solid fraction is indeed higher in this zone (Figure 4.16 c).

Hence, even if solid and liquid densities are very close, CFD simulations seem to show that liquid flow is influenced by the solid phase.

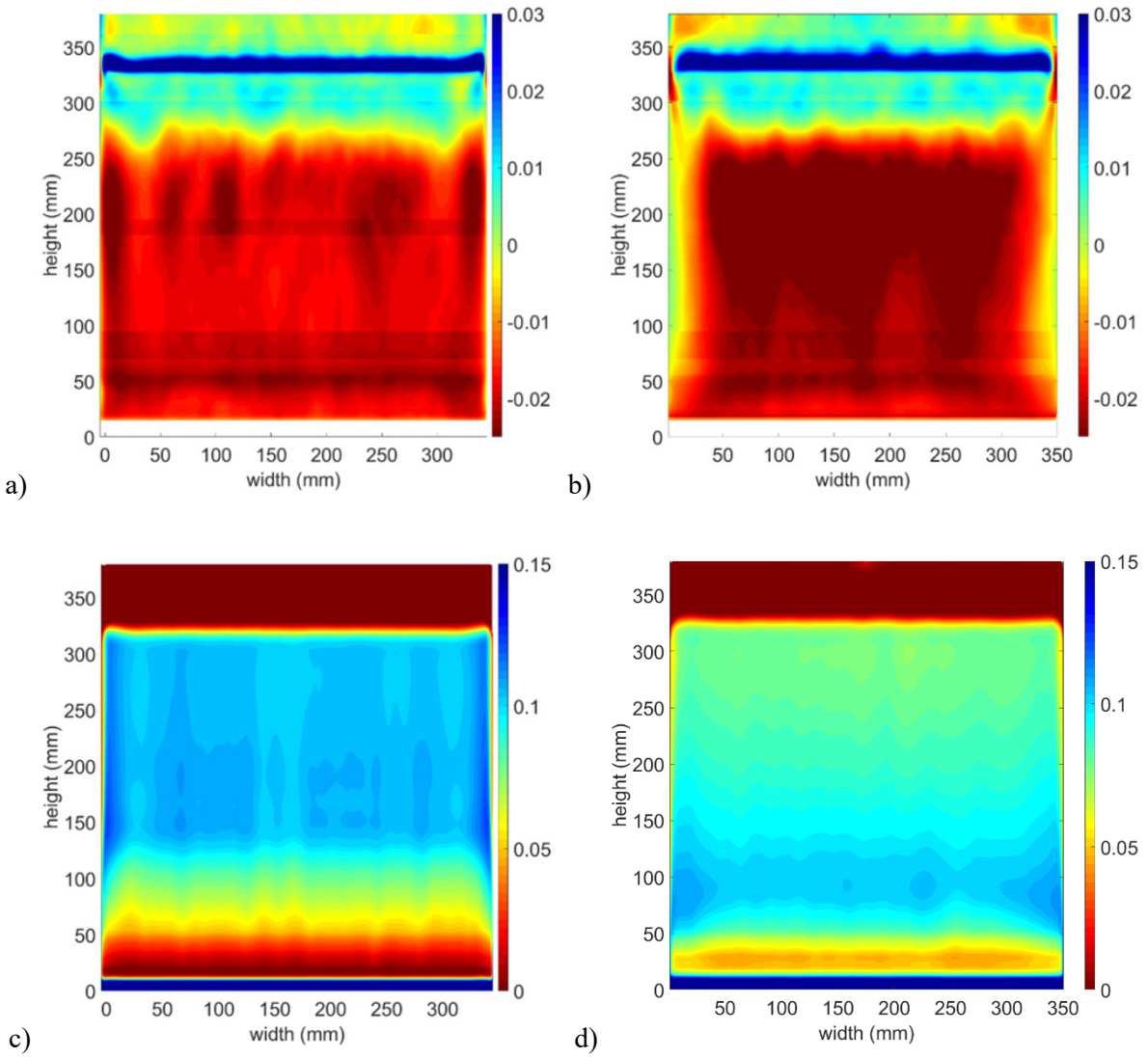

Figure 4.18 – Vertical liquid velocity fields (m/s) of plane 3 (a, b) and plane 5 (c, d) in single-phase (a, c) and two-phase (b, d) simulations.

The liquid vertical local root mean square (rms) velocities are computed from fluctuating components of vertical velocity $\sqrt{\overline{u'^2}}$, in single-phase and two-phase flows. Fluctuating components are calculated according to Reynolds decomposition as explained in chapter 3 (Equation 3.1). They are then divided by the corresponding local mean value, $\bar{u}$, to identify zones with high influence of fluctuations on the flow.

Figure 4.19 presents local normalized rms velocities in single-phase flow and two-phase flow in two planes: plane 3 (descending zone) and plane 5 (ascending zone).

In plane 3, high normalized rms are calculated for a height over 280 mm in single-phase as well as in two-phase flow, corresponding to the change of the flow direction perpendicularly to the measurement plane (recirculation loops) (chapter 3). In two-phase flow, zones close to the walls present high rms values, corresponding to small recirculation loops where negative velocities (in the central part) shift to

null or low positive velocities (close to the lateral walls). This high rms values zone is not present in the single-phase simulation as the impact of the walls is not visible on velocities (Figure 4.18 b).

In plane 5, a high rms zone is observed between z = 15 and 20 mm, in the single-phase flow field (Figure 4.19 c). It is certainly due to the recirculation loop observed in single phase (Figure 4.18 c). It is logically not present in the rms distribution simulated two-phase flow (Figure 4.19 d) as the recirculation loop is neither observed in Figure 4.18 d.

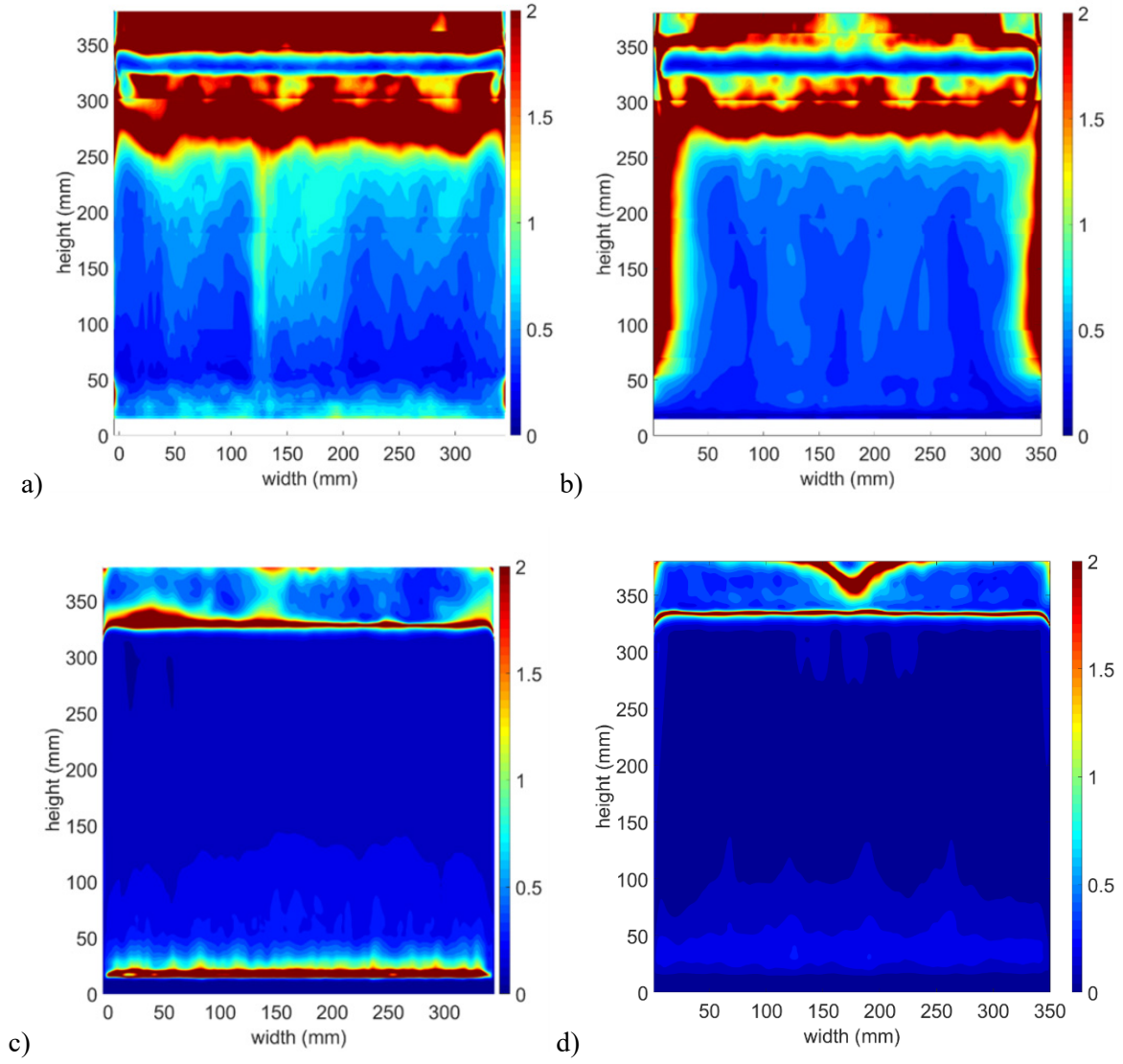

Figure 4.19 – Local rms vertical liquid velocities divided by local mean velocity of plane 3 (a, b) and plane 5 (c, d) obtained by CFD in single phase flow (a, c) and two-phase flow (b, d).

Solid velocities are studied as well using CFD. Mean and rms vertical velocity fields are calculated in plane 3 and plane 5 (Figure 4.20). A lower influence of the walls on solid flow than on liquid flow is noticed if vertical velocities are considered. Indeed, solid is slowed down near the walls but no null or positive velocities are predicted by CFD in plane 3 (descending zone) as for liquid velocities (Figure 4.20 a). Similarly, no high rms are calculated in plane 3 near the walls as for liquid flow (Figure 4.20 b). In plane 5, there is no influence of lateral walls (Figure 4.20 c). High rms are calculated over 320 mm which are not present in liquid phase (Figure 4.20 d). However, solid fraction at this height is almost null (Figure 4.16), thus these high rms are calculated on really few data.

The influence of liquid flow on solid can theoretically be characterize using the Stokes number (Equation 4.27). It is calculated as:

$$St = \frac{\rho_s d_p^{\,2} u_L}{18 \mu_L D_H} \qquad \textit{(Equation 4.27)}$$

with D_H the hydraulic diameter.

If the Stokes number is lower than 1, the flow is controlled by hydrodynamic interactions thus solid follows the liquid flow. A Stokes number higher than 1 means the inertia of particles is high and solid trajectory does not have time to change according to the liquid flow (Corona, 2008; Delafosse et al., 2018). In the descending zone, the Stokes number is equal to 0.2 while in the ascending zone it is equal to 0.9. The Stokes number is then slightly below 1 everywhere in the reactor. As it has been noticed studying velocity profiles, solid indeed follows the liquid flow (Figure 4.17). However, solid inertia is sufficient to be only lowly impacted by liquid local velocities. Indeed, low positive values of liquid velocities near lateral walls (Figure 4.20 b) do not lead to positive values of solid velocities in the descending zone even if solid is slow down.

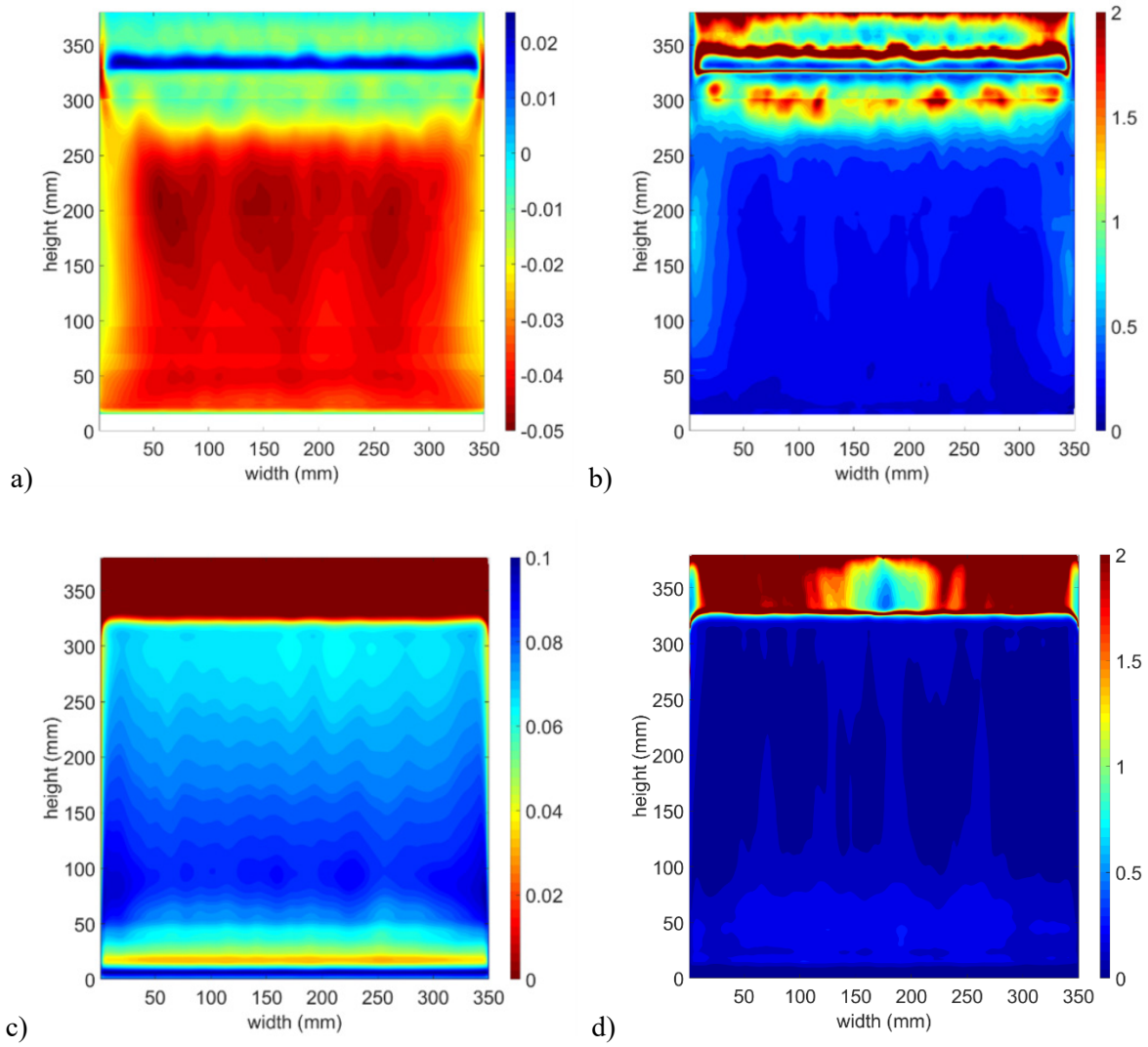

Figure 4.20 - Vertical solid velocity fields (m/s) (a, c) and normalized rms vertical solid velocities (b, d) in plane 3 (a, b) and plane 5 (c, d) obtained by CFD.

4.4 Conclusions

After studying the liquid flow within the reactor in chapter 3, the aim of this chapter is to characterize the solid behavior and its influence on the liquid flow. As the microalgae are contained in this solid phase when cultivated (which is not the case in this chapter), this step is preponderant to describe well the algae trajectories.

First, beads (solid phase) are characterized measuring their diameter and density. The uncertainty of the density measure is high as bead density is close to water density and must be measured in water. As a useful tool, CFD is used to study the influence of solid density on the flow. Solid distributions using densities of 1014 and 1018 $kg.m^{-3}$ are compared. If the density has not a high impact on global solid distribution, it has a higher influence on local solid fractions.

CFD allows to study the influence of virtual mass and lift forces on the flow. Results show a high influence of the lift force, and of virtual mass to a lesser extent, on the solid distribution. This is why they are taken into account in CFD simulations.

Solid phase distribution is then studied experimentally using a light attenuation method. Gray level values of pixels in black and white photographs and solid fraction are correlated based on Beer-Lambert law. This method gives access to the local solid fraction, at a given vertical and horizontal position in the reactor, but integrated over the reactor depth. Results show an accumulation of solid at the top of the internal panel. An accumulation of solid on the left and right sides is highlighted by experiments, which is due to a higher liquid flow rate injected from the bottom on reactor sides. Results are compared to CFD simulations. Bead density and diameter are set (2.70 mm and 1018 $kg.m^{-3}$) within the uncertainty range of measurement. Vertical profiles of solid fractions (averaged over the reactor width and depth) obtained by CFD and experiments match well. However, horizontal profiles (averaged over the reactor height and depth) show larger discrepancies, which may be explained by the fact that, in CFD an uniform liquid inlet along the slit is considered, which leads to a flatter horizontal solid distribution.

CFD allows to study solid distribution in the depth. It enables to quantify the higher solid fraction in the ascending zone than in the descending zone. Moreover, CFD gives access to liquid and solid velocities. Mean vertical velocity fields as well as rms velocity fields are calculated on plane 3 (descending zone) and plane 5 (ascending zone). Solid follows the liquid movement. However, solid velocity is lower in the ascending zone and higher in the descending zone due to gravity, despite the low difference of densities between the liquid and solid phases. Finally, CFD enables to study the influence of solid on liquid flow. The presence of solid leads to null or low positive liquid flow in the descending zone near the reactor lateral walls in the descending zone. Solid is slowed down near the walls but velocity values remain negative near the walls in the descending zone.

5 Global model based on compartmental approach

5.1 Introduction

Microalgae has become a potential feedstock in a large range of commercial applications. To realize profitable and sustainable cultures in photobioreactors, microalgal growth must be fast and significant. Among all parameters which have an influence on microalgae growth in photobioreactors (temperature, pH, CO_2 input, …), light is the most limiting. While other parameters can be controlled and set at a given value (pH controlled by CO_2 addition, heat exchangers, excess of nutrients), managing light is more challenging (Legrand, 2016). Indeed, light is attenuated through the culture depth due to cells shelf-shading. Hence, the reactor can be divided in several regions: zones where the light can penetrate and dark zones. Cells situated far from the light source have a slower growth, but the light input cannot be too high near the reactor walls exposing cells to photoinhibition. Photoinhibition is an excess of light which causes damage to cells. So, microalgae growth depends on the time cells spend in each zone, but also on the frequencies cells move from illuminated zones to dark ones. This phenomenon is called light/dark (L/D) cycles. A positive effect on growth, called "flashing light effect", has been measured most of the time with high frequencies L/D cycles (minimum 1 Hz). It has been highlighted by different teams using different methods as flashing LEDs or shading parts of the photobioreactor (Janssen et al., 2003; Liao et al., 2014; Matthijs et al., 1996). However, frequencies truly experienced by cells in photobioreactors are mostly lower than 1 Hz (cycles of several seconds). Some research teams have studied the impact of these medium-duration L/D cycles experienced by cells. Janssen et al., 2000 measured a negative impact on growth of medium-duration L/D cycles (between 6 and 24 s) on *Chlamydomonas reinhardtii*. Hence it is crucial to precisely determine the frequencies between expositions to dark and illuminated zones to evaluate their impact on growth.

To globally characterize a photobioreactor, it is thus important to take different aspects into account. On the one hand, light attenuation through the reactor depth has a major role and must be characterized. Light attenuation can be described using different models. Beer-Lambert law is the simplest, as it only considers cell absorption. Other models as two-flux model or Radiative Transfer Equation take into account scattering as well. However, studying encapsulated algae, Beer-Lambert law is considered sufficient in this study (chapter 1). On the other hand, hydrodynamics (describing the flow) within the reactor is decisive as it has an impact on mixing, renewal of cells in the illuminated zone and frequencies of this renewal. To develop a global model of the photobioreactor, both aspects (light and hydrodynamics) must be combined to get the "light history" of cells. Adding a biological model on this history enables to predict microalgal growth. It is essential to note that light and growth are dually coupled as light is limiting growth and microalgal growth influences light attenuation due to cells' shelf-shading.

A CFD model was developed to fully characterized hydrodynamics of a photobioreactor designed for the culture of encapsulated microalgae. First, a monophasic model describing liquid flow in the reactor has been experimentally validated by PIV (chapter 3). Then a two-phase model considering liquid and solid (beads) has been validated by an attenuation light method (chapter 0). CFD enables to precisely describe local flow behavior far better than macromixing models such as perfectly stirred-tank or plug-flow reactor models (Weber et al., 2019). However, CFD simulations require high computing power and is time consuming. Moreover, it is difficult to include a biological model in CFD model and this requires even longer calculation times. One of the biggest challenges is the difficulty to couple flow hydrodynamics and cell growth due to different timescales: seconds for hydrodynamics and days for growth.

Compartment models are developed to overcome these bottlenecks. In these models, geometry of the reactor is modeled by compartments, larger than CFD cells but small if compared to the reactor size, which are considered perfectly mixed. Basic compartment models are based on global hydrodynamic quantities (mixing time, flow number…) which leads to a high loss of information compared to CFD models. This is why CFD-based compartment models have been developed and are increasingly used

(Delafosse et al., 2014; Krychowska et al., 2020; Weber et al., 2019). Compartments consist in CFD cells grouped together. Flow rates between compartments are calculated based on simulation results (CFD velocity fields). Biological kinetic equations can be easily implemented in compartment models as compartments are considered as perfectly mixed and ordinary differential equations are used to calculate the evolution of variables inside compartments.

In the development of global models of photobioreactors, different biological models exist. Simple correlations between growth and light intensity have been proposed but they highly depend on the system. Some models combine these correlations with an attenuation law. However, these models do not consider light history of cells. Among more complex models, PhotoSynthetic Factory (PSF) are mostly used (Béchet et al., 2013). They are simplified models of cell metabolism but have proven to give good prediction of biomass growth (X. Gao et al., 2018; Nauha & Alopaeus, 2013; Wu & Merchuk, 2001). They consider that biomass can be in three states (resting, activated or inhibited) depending on the light received. They take into account L/D cycles. In the form of ordinary differential equations, they are particularly suitable to be combined with compartment models (Nauha & Alopaeus, 2013; S. Papacek et al., 2007). Light attenuation can also easily be implemented in algebraic equation.

The aim of this chapter is to develop a global model predicting the growth in a photobioreactor designed for the culture of encapsulated microalgae. The model describes bead displacements using a compartment model based on CFD results. The trajectories of beads are determined by a stochastic model based on solid fluxes between compartments. While a Eulerian approach was used in previous chapters (3 and 0) to compare experiments and model, the approach used in this chapter to determine trajectories is Lagrangian. In each compartment encountered by the bead on its trajectory, the light intensity is calculated using Beer-Lambert law. Simultaneously, a biological PSF model is applied thus light/dark cycles experienced by cells are taken into account. This enables to report light history of a bead. The results of the model are compared to experimental results of growth in the reactor.

5.2 Methods

5.2.1 Hydrodynamics

5.2.1.1 CFD-based compartment model

A CFD-based compartment model is developed on Matlab (MATLAB R2020b) and adapted from a model developed by Delafosse et al., 2014 which have proven to describe satisfactorily hydrodynamics in a stirred tank reactor. Compartments group together CFD cells. Exchanges between compartments are calculated as mean and fluctuant flow rates (Figure 5.1). As microalgae are encapsulated, their displacements in the reactor are those of beads. The study is thus focused on solid flow. As explained in chapter 2, the experimental bead diameter used for algae encapsulation equals 3.3 ± 0.1 mm (different from the non-sterile beads used for CFD validation in chapter 0 as a slightly different fabrication setup must be used). Hence the compartment model was based on CFD simulations of beads of 3.3 mm diameter and 1018 $kg.m^{-3}$ density, using a liquid flow rate of 0.1444 $kg.s^{-1}$. It can be noticed that the bead density could slightly change with biomass growth, but this is not considered. Moreover, bead density is measured at 18.0 °C (chapter 0) while culture is performed at 24.5 °C (chapter 2). As beads absorb water and the relative difference of water density at these temperatures is 0.16 %, it is considered negligible.

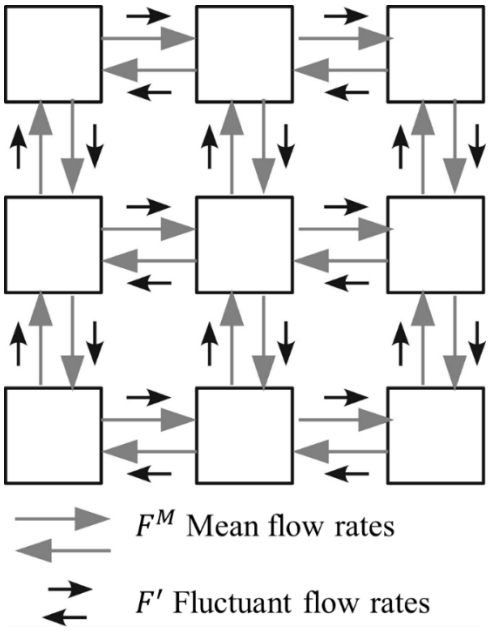

Figure 5.1 - 2D schematic representation of the model structure. Reproduced from (Delafosse et al., 2014) *with authorization*.

Solid flow rates between CFD cells must first be calculated in all directions from velocity fields simulated by CFD (Figure 5.2 a). Mean solid velocity fields are used to calculate mean flow rates ($f^M_{\alpha\beta}$) (Equation 5.1) and rms solid velocity fields (obtained by Reynolds decomposition: $u'=u - \overline{U}$) are used to calculate fluctuant flow rates ($f'_{\alpha\beta}$) (Equation 5.2). As each CFD cell is spatially in contact with six others, six mean flow rates and six fluctuant flow rates can be calculated for each cell.

$$f^M_{\alpha\beta}=A_{\alpha\beta}\frac{\overline{U}_i^{\alpha}+\overline{U}_i^{\beta}}{2} \qquad \textit{(Equation 5.1)}$$

with $f^M_{\alpha\beta}$ the mean flow rate between α and β cells, $A_{\alpha\beta}$ the exchange surface between α and β cells, $\overline{U}_i^{\alpha}$ and $\overline{U}_i^{\beta}$ mean velocities in α and β cells respectively with i = x, y or z.

$$f'_{\alpha\beta}=A_{\alpha\beta}\frac{\overline{u'}_i^{\alpha}+\overline{u'}_i^{\beta}}{2} \qquad \textit{(Equation 5.2)}$$

with $f'_{\alpha\beta}$ the fluctuant flow rate between α and β cells, $A_{\alpha\beta}$ the exchange surface between α and β cells, $\overline{u'}_i^{\alpha}$ and $\overline{u'}_i^{\beta}$ rms velocities in α and β cells respectively with i = x, y or z.

Compartments are built by agglomerating CFD cells. Two methods exist to this end. Building compartments according to their coordinates and get a uniform network or agglomerating cells with similar flow properties which allows to lose less information on the flow (Tajsoleiman et al., 2019). Delafosse et al., 2010 obtain the same results for both methods using this model in stirred tank reactor. Hence, in the studied reactor, compartments are built according to their coordinates as it is easier and faster.

Flow rates between adjacent compartments are calculated by summing flow rates on CFD cells situated at the interface between two compartments (Figure 5.2 b). Positive flow rates are considered as inflow (Equation 5.3) while negative flow rates are considered as outflow (Equation 5.4). Fluctuant flow rates are similarly calculated (Equation 5.5) (Equation 5.6).

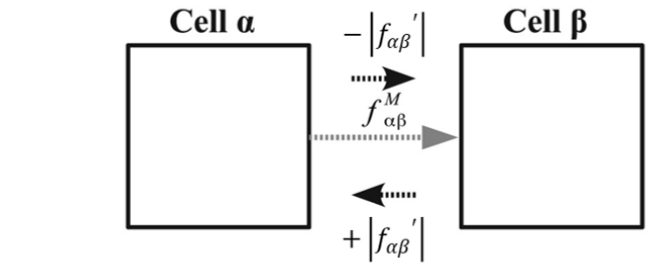

a)

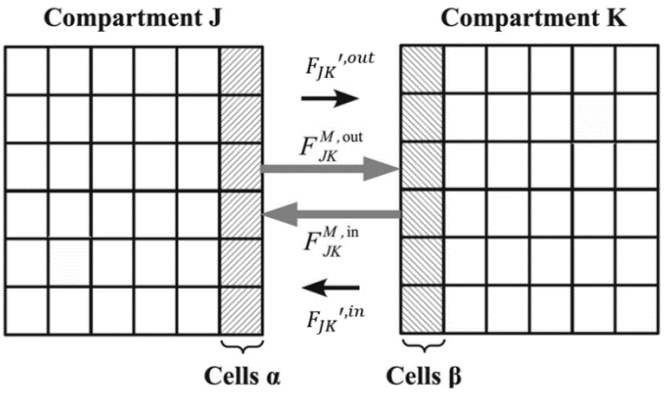

b)

Figure 5.2 – Description of the CFD-based compartment model. CFD mean and fluctuant flow rates calculation (a). Determination of flow rates between two adjacent compartments (b). Reproduced from (Delafosse et al., 2014) *with authorization*.

$$F_{JK}{}^{M,in} = \sum_{\alpha} f_{\alpha\beta}{}^{M} \qquad \textit{(Equation 5.3)}$$

with $f_{\alpha\beta}{}^{M} > 0$, $\alpha \in J$, $\beta \in K$

$$F_{JK}{}^{M,out} = \sum_{\alpha} f_{\alpha\beta}{}^{M} \qquad \textit{(Equation 5.4)}$$

with $f_{\alpha\beta}{}^{M} < 0$, $\alpha \in J$, $\beta \in K$

$$F_{JK}{}^{',in} = \sum_{\alpha} +\left|f_{\alpha\beta}{}'\right| \qquad \textit{(Equation 5.5)}$$

with $\alpha \in J$, $\beta \in K$

$$F_{JK}^{',out} = \sum_{\alpha} -\left|f_{\alpha\beta}^{'}\right| \qquad \textit{(Equation 5.6)}$$

with $\alpha \in J$, $\beta \in K$

5.2.1.2 Stochastic model

A stochastic approach is used to model bead movement between compartments. The model developed here is adapted from the one proposed by Delafosse et al., 2015. A Continuous-Time Markov Chain (CTMC) is programmed on Matlab (MATLAB R2020b). A Markov chain consists in generating a random variable which corresponds to a state. In this case, the state of a given bead corresponds to the compartment it is in. When a bead moves, the compartment of arrival is thus random but based on probabilities calculated according to flow rates between compartments. In a CTMC, the time at which a bead leaves a compartment is also random. Thus, the time it spends in this compartment is random as well. It follows a decreasing exponential probability distribution (in agreement with the residence time distribution in a perfectly mixed continuous stirred tank). Hence, there are two random processes: one in space (moving direction) and one in time (moving time). The system takes into account neither previous states (previous compartments), nor the times spent in them. The system has no memory.

The stochastic model is described with matrices as CTMC algorithm is based on matrix calculation. The probabilities of movement and residence times in compartments are thus calculated from a transition matrix. The transition matrix Q_C groups together solid flow rates between compartments (Equation 5.7). Each row is dedicated to one compartment. The outflow rates from a compartment J to a compartment K ($Q_{J\text{-}K}$) are set positive. The total inflow rate in a compartment J ($Q_{J\text{-}J}$) is placed in the diagonal and is set negative (Equation 5.12). Hence in each compartment, the mass balance is conserved (total inflow equals total outflow).

$$Q_C = \begin{bmatrix} Q_{1\text{-}1} & Q_{1\text{-}2} & \cdots & Q_{1\text{-}NC} \\ Q_{2\text{-}1} & Q_{2\text{-}2} & \cdots & Q_{2\text{-}NC} \\ \vdots & \vdots & \ddots & \vdots \\ Q_{NC\text{-}1} & \cdots & \cdots & Q_{NC\text{-}NC} \end{bmatrix} \qquad \textit{(Equation 5.7)}$$

Mean outflow rates are calculated according to the compartment model (Equation 5.11). An inhomogeneous CTMC is used which takes into account a random fluctuant flow rate $\propto_{J\text{-}K}$. This one follows a normal distribution centered on 0 with a standard deviation equals to the mean fluctuant flow rate $Q^{',out}_{J\text{-}K}$ (Equation 5.8) (Equation 5.9) (Equation 5.10). As $\propto_{J\text{-}K}$ can be negative, the sum with the mean outflow rate can be negative. It is thus considered as an outflow rate for compartment J. The transition matrix Q_C is non-stationary in this case thus must be calculated every time step.

$$Q_{J-K}=Q^{MT}{}_{J-K}+Q^{MT}{}_{K-J} \qquad \textit{(Equation 5.8)}$$

$$Q^{MT}{}_{J-K}=\begin{cases} Q^{M,out}{}_{J-K}+\propto_{J-K} & \text{if } (Q^{M,out}{}_{J-K}+\propto_{J-K})>0 \\ 0 & \text{if } (Q^{M,out}{}_{J-K}+\propto_{J-K})<0 \end{cases} \qquad \textit{(Equation 5.9)}$$

$$Q^{MT}{}_{K-J}=\begin{cases} 0 & \text{if } (Q^{M,out}{}_{K-J}+\propto_{K-J})>0 \\ -(Q^{M,out}{}_{K-J}+\propto_{K-J}) & \text{if } (Q^{M,out}{}_{K-J}+\propto_{K-J})<0 \end{cases} \qquad \textit{(Equation 5.10)}$$

$$Q^{M,out}{}_{J-K} = -F_{JK}{}^{M,out} \qquad \textit{(Equation 5.11)}$$

$$Q_{J-J}= -\sum_{J\neq K}^{Nc} Q_{J-K} \qquad \textit{(Equation 5.12)}$$

The transition matrix Q_C finally enables to calculate the residence time distribution (S_J) of a bead in the compartment J and the probability (p_{J-K}) of bead movement from compartment J to compartment K (Equation 5.13) (Equation 5.14). V_J is the volume of the compartment.

$$S_J=\exp\left(-\frac{|Q_{J-J}|}{V_J}t\right) \qquad \textit{(Equation 5.13)}$$

$$p_{J-K}=\frac{Q_{J-K}}{|Q_{J-J}|} \qquad \textit{(Equation 5.14)}$$

The resolution of the CTMC is divided in two iterative loops. First, the CTMC model calculates when the bead leaves the compartment. This probability follows a decreasing exponential (Equation 5.15). Then, the compartment where the bead goes is determined according to the probability p_{J-K} (Equation 5.16). Two random numbers $\beta_1(i)$ and $\beta_2(i)$, calculated from a standard uniform distribution, are used.

$$T(i+1) = T(i) - \frac{V_J}{|Q_{J-J}|}\ln(\beta_1(i)) \qquad \textit{(Equation 5.15)}$$

$$C=\left\{\begin{array}{c} 1 \text{ if } 0<\beta_2(i)\leq p_{J-1} \\ 2 \text{ if } p_{J-1}<\beta_2(i)\leq p_{J-1}+p_{J-2} \\ \vdots \\ NC \text{ if } \sum_{j=1}^{NC-1} p_{J-K}<\beta_2(i)\leq 1 \quad K\neq J \end{array}\right\} \qquad \textit{(Equation 5.16)}$$

5.2.2 Light model

5.2.2.1 Equations

As explained in chapter 1, light attenuation through the reactor depth is modeled with Beer-Lambert law. This one will have to be modified at each time step to take into account the evolution of biomass concentration in the reactor. One may notice that no natural light or light/day alternation is modeled as a constant artificial light was used in experiments.

Due to the presence of the internal panel, the reactor volume is divided in 4 regions (Figure 5.3). For simplicity, the prism is not considered.

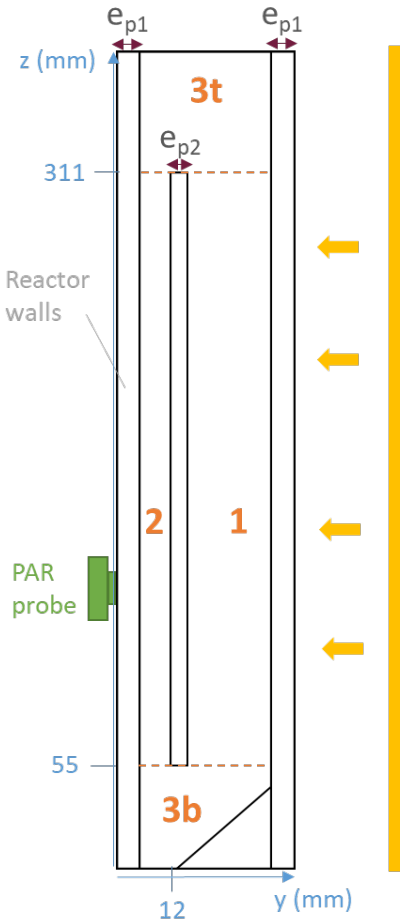

Figure 5.3 – Schematic representation of light path in the reactor depth. Thickness of the reactor walls is referred by e_{p1} and e_{p2} for the internal panel. The interior of the reactor is divided in 4 regions to calculate light attenuation. Dimensions are not true to scale.

It must be noticed that the y-axis is oriented the wrong way compared to the light source. This is the reason why y_t is used in the following equations. It is calculated to flip the y-axis (Equation 5.17).

$$y_t = y_{max} - y \qquad \textit{(Equation 5.17)}$$

$$y_{max} = 0.04 \text{ m}$$

As the light passes through external and internal reactor walls made of Plexiglas, the light attenuation by this material must be considered (Equation 5.18) (Equation 5.19). The thickness of each wall must also be accounted for.

For region 1 (55 mm < z < 311 mm, y_t < 25 mm) and 3 (z < 55 mm or z > 311 mm),

$$I = I_0 . e^{-\varepsilon_p e_{p1} - (\varepsilon_b . C_x . f_{ti} - \varepsilon_w . y_t)} \qquad \textit{(Equation 5.18)}$$

For region 2 (55 mm ≤ z ≤ 311 mm, $y_t \geq 25$ mm),

$$I = I_0 . e^{-\varepsilon_p e_{p1} - \varepsilon_p e_{p2} - (\varepsilon_b . C_x . f_{ti} - \varepsilon_w . (y_t - e_{p2}))} \qquad \textit{(Equation 5.19)}$$

with I the light intensity, I_0 the incident light intensity at the reactor surface (values in section 5.2.2.2), C_x the biomass concentration (dry weight), ε_b, ε_w and ε_p the absorption coefficients of biomass, water and Plexiglas, respectively. e_{p1} and e_{p2} are the thickness of the reactor walls and of the internal panel respectively. f_{ti} is introduced to consider the influence of the solid fraction of beads in each compartment between the light source and a given position in depth y_t (Equation 5.20).

The beads are not uniformly distributed along the height of the reactor. Above a height z > 350 mm, the solid fraction, and thus the biomass concentration, is almost null (chapter 0). As a consequence, the biomass concentration (C_x) of the culture is measured every day as explained in chapter 2: dry weight is calculated according to the volume of the bed bead (z < 350 mm) (the volume of the reactor above 350 mm and of the external loop are not considered). Results of culture 1 are considered (chapter 2). Moreover, C_x is considered as a global quantity, uniform in the reactor (all beads have the same concentration). In other words, each bead of each trajectory is considered representative of the global dry weight in the whole reactor. This assumption is made as the mixing time of beads is fast compared to growth. Moreover, light attenuation depends on several beads thus a mean concentration must be used.

Hence, in the model, the local biomass concentration depends only on the solid fraction. Indeed, beads are also not uniformly distributed over the depth of the reactor. It is higher in the ascending zone than in the descending zone and this has an influence on light attenuation through the reactor depth. For each compartment, a normalized solid fraction is calculated dividing the solid fraction of the compartment α_{Sj} (obtained by CFD) by the mean solid fraction of the bead bed $\overline{\langle \alpha_S \rangle}_{bed}$. Then, for each height and width, the normalized solid fraction is integrated over the depth between the studied compartment and the light source in order to consider the light attenuation due to non-uniform concentration.

$$f_{ti} = \sum_{j=1}^{N_{yi}} \frac{\alpha_{Sj}}{\langle \alpha_S \rangle_{bed}} . (y_{t_{j+1}} - y_{t_j}) \qquad \textit{(Equation 5.20)}$$

$$\text{with } 1 \leq N_{yi} \leq N_y$$

With N_y the total number of compartments along the depth of the reactor and N_{yi} the number of compartments in depth between the light source and a given compartment.

ε_w is equal to 0.8 m^{-1} (Pope & Fry, 1997) as culture medium is assimilated to water. To avoid refraction due to scratches on walls, ε_p (13.7 m^{-1}) was measured with a reactor only filled with culture medium and the influence of culture medium was subtracted. ε_b is calculated according to experimental results as explained in (section 5.2.2.2).

5.2.2.2 Experimental measurements

To measure light attenuation through the reactor depth, light intensity (in $\mu E.m^{-2}.s^{-1}$) is measured every day during a microalgal culture discussed in chapter 2. It is measured using a PAR probe (KIPP & ZONEN, PQS 1 PAR Quantum Sensor) on the side of the reactor opposite to the light source, on 9 points distributed on the reactor's surface (Figure 5.4 a). Light attenuation of beads is considered homogeneous. Intensities are automatically recorded for one minute (one measure every two seconds) for each point using a data logger (KIPP & ZONEN, Meteon) and a software (Meteon software V 4.0.0.1). The light attenuation by a bed of beads containing no algae is measured using a PAR probe. Measurements show no attenuation due to empty beads (according to the precision of the probe which is 1 $\mu E.m^{-2}.s^{-1}$).

As the LED panel is not significantly larger than the reactor, the incident light is not homogeneous at the reactor surface: light intensity is higher at the center of the reactor (Figure 5.4 b). Incident light intensity is measured in the 9 same points as light attenuation, but on the side of the light source. This is taken into account in the light attenuation model (Beer-Lambert law) (Equation 5.18) (Equation 5.19) and in the calculation of the absorption coefficient of biomass.

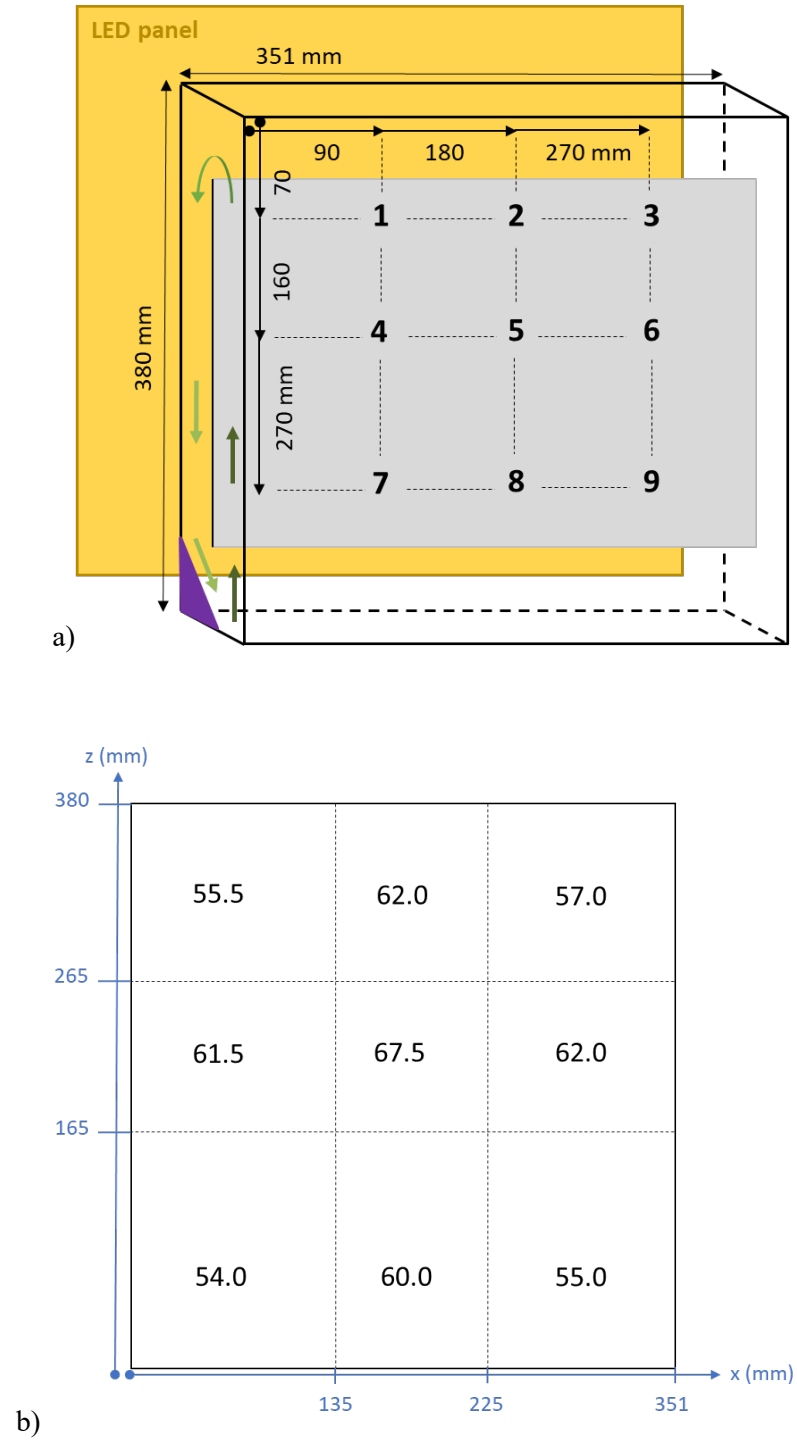

Figure 5.4 – Position of the 9 points used to measure light attenuation through the reactor using a PAR probe (a). Value of the incident light intensity (I_0) in $\mu E.m^{-2}.s^{-1}$ according to the position of the probe (b). Dimensions are not true to scale.

The absorption coefficient of biomass (ε_b) depends on the microalgal strain. It thus must be experimentally determined from measurements of light attenuation as a function of biomass dry weight. As light attenuation through the reactor is measured every day as well, the absorption coefficient of the biomass ε_b can be calculated every day according to Beer-Lambert law (Equation 5.21). As I_0 depends on the position of the probe, 9 different ε_b coefficients are calculated. In reality, solid fraction is higher in the ascending zone (chapter 0). However, as light attenuation can only be measured through the whole

reactor depth and not inside the reactor, attenuation of both zones cannot be determined independently. Hence, f_{ti} is not considered for calculation of ε_b and replaced by e_l in (Equation 5.19), which represents the whole thickness of liquid in the reactor. For each of the 9 points, ε_b is calculated for a given value of I_0 and measured value of I depending on C_x.

$$\varepsilon_b = \frac{1}{C_x}\left(-\frac{\ln\left(\frac{I}{I_0}\right)+\varepsilon_p\left(2e_{p1}+e_{p2}\right)}{e_l}-\varepsilon_w\right) \qquad \textit{(Equation 5.21)}$$

The presence of bacterial contamination has an influence on culture medium turbidity (chapter 2). Hence the turbidity of the culture medium was measured every day on the 9 same points, after a complete settling of the bed. It was found that the maximum influence of bacteria on light attenuation was equal to 2 $\mu E.m^{-2}.s^{-1}$ (5 % of light intensity while biomass attenuation represents between 44 and 57 %), thus it has been neglected.

The absorption coefficient of biomass (ε_b) value is calculated as a mean of the 9 ε_b measured in different positions (Figure 5.5). The mean absorption coefficient is calculated between day 6 and day 19. Indeed, the 5 first days the low light attenuation (because of very low concentration of biomass) leads to a high error, thus the absorption coefficient is not considered. Using this method ε_b is equal to 90 $L.g^{-1}.m^{-1}$. It must be noticed that from day 6, the absorption coefficient is still not constant as the pigment content (chlorophyl) in the cells is changing due to photoacclimation.

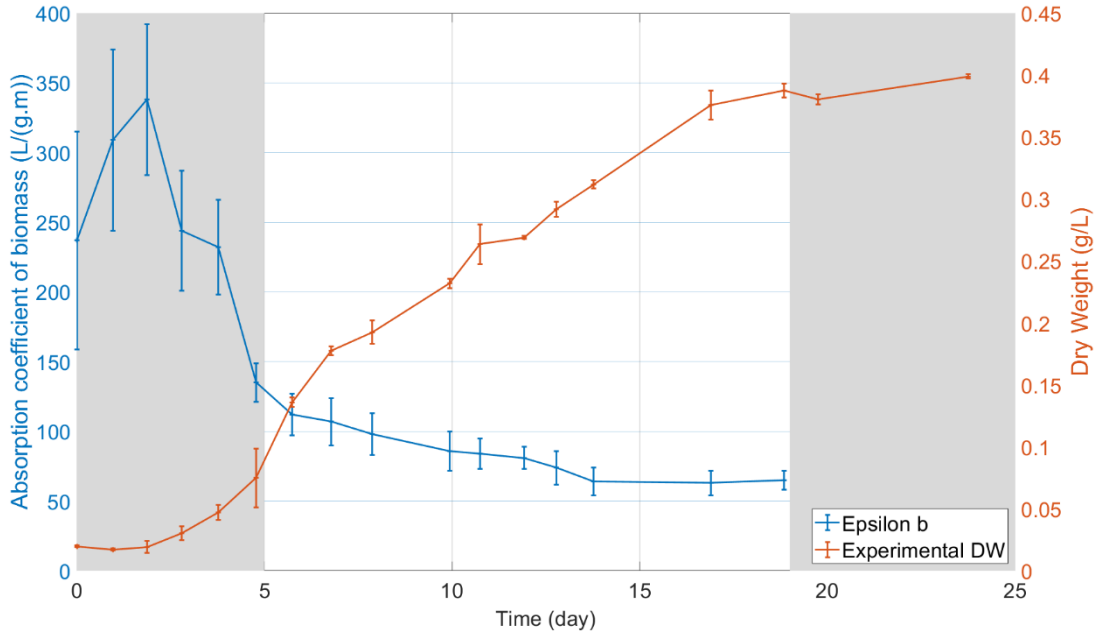

Figure 5.5 – Evolution of the biomass absorption coefficient calculated every day according to experimental measurements of light attenuation (error bars represent twice the standard deviation calculated on the 9 positions) and biomass concentration (error bars represent the minimum and maximum of the measurements). Values in grey zones are not considered.

5.2.3 Biological model

5.2.3.1 Equations

The assumption is made that growth is limited only by light as there is no nutrients (N, P) limitation in the studied culture (chapter 2). pH never increases above 7.3, which is favorable for CO_2 dissolution. Photosynthetic Factory (PSF) model is used to model growth of cells limited by light (Eilers & Peeters, 1988; Wu & Merchuk, 2001). The model considers that the biomass is distributed in three states: inactive (designated by scalar x_1), active (x_2) and inhibited (x_3) (Figure 5.6). The proportion of biomass in each state is calculated according to light intensity and empirical parameters $\propto$, β, γ and δ (Equation 5.22) (Equation 5.23) (Equation 5.24) (Equation 5.26). The biomass growth μ is calculated according to the biomass from state 2 going back to state 1 (Equation 5.25). This equation has been modified by Wu & Merchuk, 2001, to add the parameter M_e (maintenance term) to enable a negative growth rate (due to dark reactions) which led to more accurate results. Moreover, they add a parameter k which depends on the system (photobioreactor and culture conditions), while γ parameter takes into account the strain characteristics.

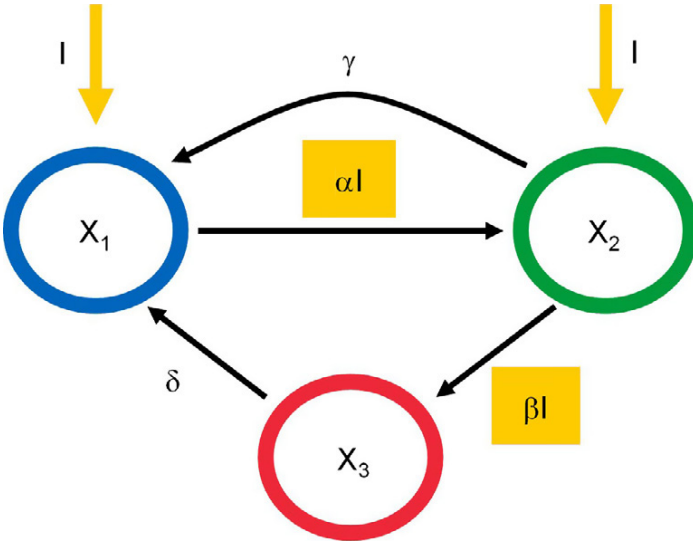

Figure 5.6 – Structure of PhotoSynthetic Factory (PSF) model. x1, x2 and x3 represent the resting, activated and inhibited state respectively. Reproduced from (Nauha & Alopaeus, 2013) with authorization.

$$\frac{dx_1}{dt} = -\propto Ix_1 + \gamma x_2 + \delta x_3 \quad \textit{(Equation 5.22)}$$

$$\frac{dx_2}{dt} = \propto Ix_1 - \gamma x_2 - \beta x_2 \quad \textit{(Equation 5.23)}$$

$$\frac{dx_3}{dt} = \beta Ix_2 - \delta x_3 \quad \textit{(Equation 5.24)}$$

$$\mu = k\gamma x_2 - M_e \quad \textit{(Equation 5.25)}$$

$$x_1 + x_2 + x_3 = 1 \quad \textit{(Equation 5.26)}$$

5.2.3.2 Parameter fitting

The PSF model of Wu & Merchuk, 2001 depends on 6 different parameters ($\propto$, β, γ, δ, k, M_e) which must be fitted on experimental results. Parameters are fitted by the method of least squares. Experimental results are limited as only one global value of biomass dry weight is measured each day for the entire reactor. A strategy is thus needed to fit parameters on these results. Initial parameters used are the one of Wu & Merchuk, 2001. As it very difficult to fit all parameters at the same time, the most impacting parameters are first estimated. The identification of these "major" parameters is performed according to a sensitivity analysis. This analysis is made one parameter at a time, meaning the combined impact of other parameters is not studied. Each parameter one by one is increased by 5 % and the difference of the sum of squares with the initial curve (without changing parameters) is calculated. The analysis time is a culture of 24 days (time step 1 s). The parameters which have the most important impact are k, M_e and $\propto$ (Table 5.1). Then, the parameter fitting is realized in decreasing order of impact. The global model is used to calculate biomass growth on 1 trajectory. Parameters are iteratively replaced in the model. Method of least squares is used to decrease the dry weight difference between the experimental and the simulated curve by the model. The method is made 1 parameter at a time. γ, β and δ parameters are not fitted as it leads to unrealistic values. This could be explained as least squares method is applied only on 16 points (corresponding to experimental results). Moreover, β and δ parameters are related to photoinhibition and the studied conditions do not allow to study it. As these parameters have less influence on the model, parameters from Wu & Merchuk, 2001 are used.

Table 5.1 - Parameter values of PSF model by order of sensibility on the model. The sensibility is performed by applying a 5 % change in sum of squares. Values are compared with literature using relative difference percentages.

Parameters (units)	5 % change in sum of squares	Wu & Merchuk, 2001	Values (% of difference with Wu & Merchuk, 2001)
k (-)	81 360	3.65×10^{-4}	4.42×10^{-4} (19 %)
Me (h^{-1})	46 709	1.64×10^{-5}	9.13×10^{-6} (57 %)
Alpha $\propto$ ($\mu E.m^{-2}$)$^{-1}$	44 651	1.94×10^{-3}	9.50×10^{-4} (68 %)
Gamma γ (s^{-1})	8 665	1.46×10^{-1}	1.46×10^{-1} (-)
Beta β ($\mu E.m^{-2}$)$^{-1}$	96	5.78×10^{-7}	5.78×10^{-7} (-)
Delta δ (s^{-1})	89	4.8×10^{-4}	4.8×10^{-4} (-)

5.2.4 Implementation in the global model

The global model is programmed on Matlab (MATLAB R2020b). Trajectories of beads are determined using the stochastic model based on calculations of the CFD-compartment model. The hydrodynamic model allows to calculate the normalized solid fraction between the light source and the studied compartment as well. Hydrodynamic is considered stable over time. This means the assumption is made that biomass growth does not impact bead properties (diameter, density) which have an influence on bead circulation. Moreover, the solid fraction in each compartment is considered constant over time and not influenced by the displacement of the beads.

Light attenuation and biomass growth are then computed following an iterative process (Figure 5.7). The time step is not constant as it depends on the time a particle spends in a compartment as calculated by the stochastic model. At each iteration, light attenuation is first calculated, then biomass growth is evaluated. Light intensity is calculated according to the depth, height and width positions of the bead in the reactor, and the global biomass concentration, i.e. the dry weight.

Obtained values of dry weight (C_x) and scalar x_1, x_2 and x_3 which represents the distribution in each biomass state (resting, activated and inhibited) according to PSF model, are used to initialize the next time step. The initial biomass concentration was fixed at the initial experimental value and biomass state equal to (x_1=1, x_2=0, x_3=0).

At each time step, the dry weight C_x is considered uniform in the reactor: the followed bead of the trajectory is considered representative of the global dry weight in the whole reactor. The program is run independantly for each different trajectory calculated by the compartment model (40 times in total). Each trajectory is repeated to last 25 days. Finally, dry weights of the 40 trajectoriesare meaned to get the final dry weight.

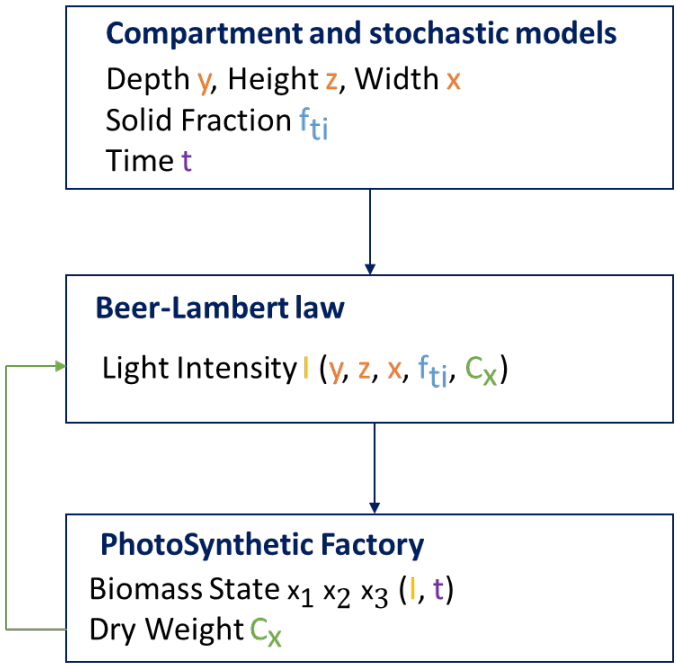

Figure 5.7 – Schematic representation of the program of the global model developed on Matlab.

5.3 Results

5.3.1 Hydrodynamics

5.3.1.1 CFD-based compartment and stochastic model

The hydrodynamic model has first to be built and then validated. The validation is based on a comparison of velocity fields and spatial distributions of solid simulated by CFD and by the compartment/stochastic approach.

The number of compartments must be optimized: using less compartments allows to save time, but a minimum number of compartments is required to keep an accurate description of the solid flow and of the solid spatial distribution.

The number of compartments in width (x) and height (z) are taken equal to 20 and 40, respectively, which is significantly smaller than the number of CFD cells in these directions (193 and 209), as the resolution in these directions has a lower impact on flow. Indeed, velocity varies less in these directions than along the depth (chapter 3).

Discretization along the reactor depth must be close to the number of CFD cells (24) to keep a sufficient level of accuracy for flow description, as velocity values are highly dependent on depth (chapter 3). Moreover, as light is attenuated through the depth, it is important to keep as many as possible of compartments in this direction to account for it and get a precise description in the global model.

The optimum number of compartments is determined by analyzing its influence of the simulated bead distribution (as a function of the reactor depth). The bead distribution is calculated according to the probability density function (Equation 5.27).

$$\upsilon_i = \frac{c_i}{N.w_i} \qquad \text{(Equation 5.27)}$$

with υ_i the bin (interval) final value, i.e. the probability density, c_i the number of elements (beads) in the bin, N the total number of elements (beads) for one height and w_i the width of the bin.

The bead distribution is studied at 3 different heights (Figure 5.8), situated in the different reactor regions.

If 10 compartments in depth are considered, 10^6 iterations enable simulating a 37 h trajectory, while the same number of iterations allows simulating only 29 h if 20 compartments are used. However, it can be noticed a bead distribution significantly different using 20 or 10 compartments in the reactor depth, especially near the reactor sides. Hence, it has been chosen to divide the reactor depth in 20 compartments to keep a satisfying flow description.

Hence the compartment model is based on CFD fluxes but is composed of 16 000 (20×20×40) elements (taking into account the internal panel and the prism) while CFD mesh is composed of 8.7×10^5 elements (reduction factor of 54).

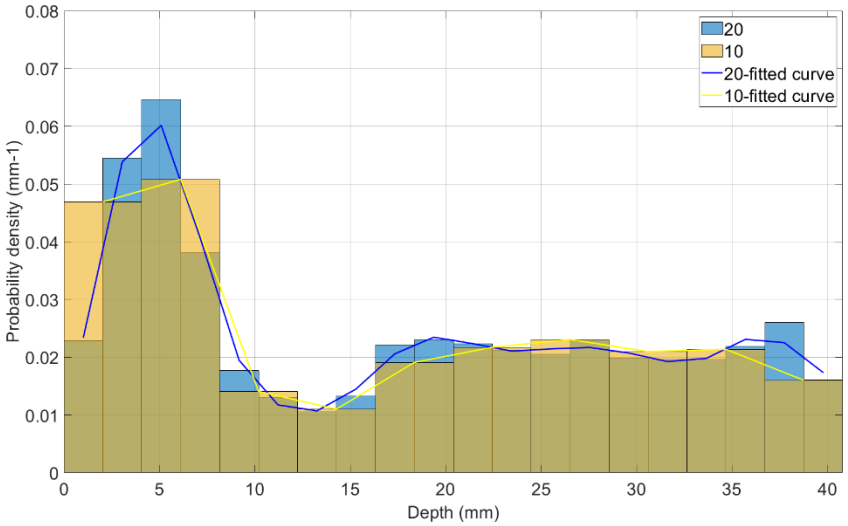

a)

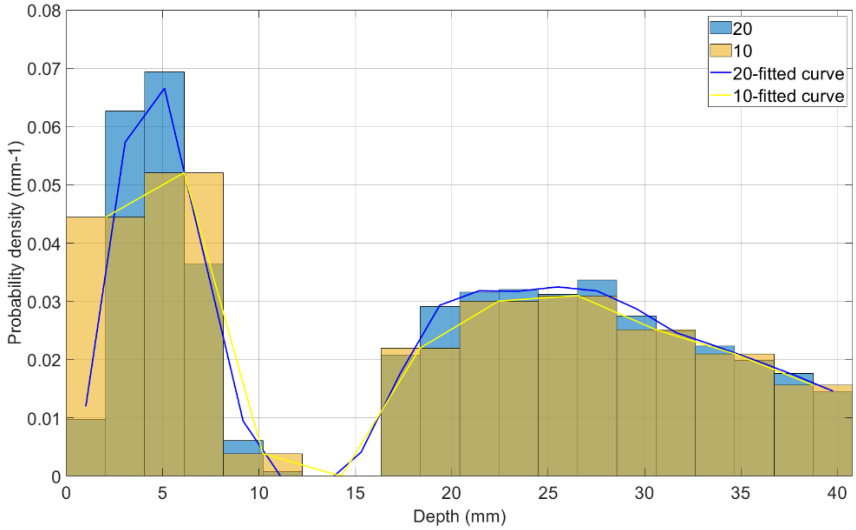

b)

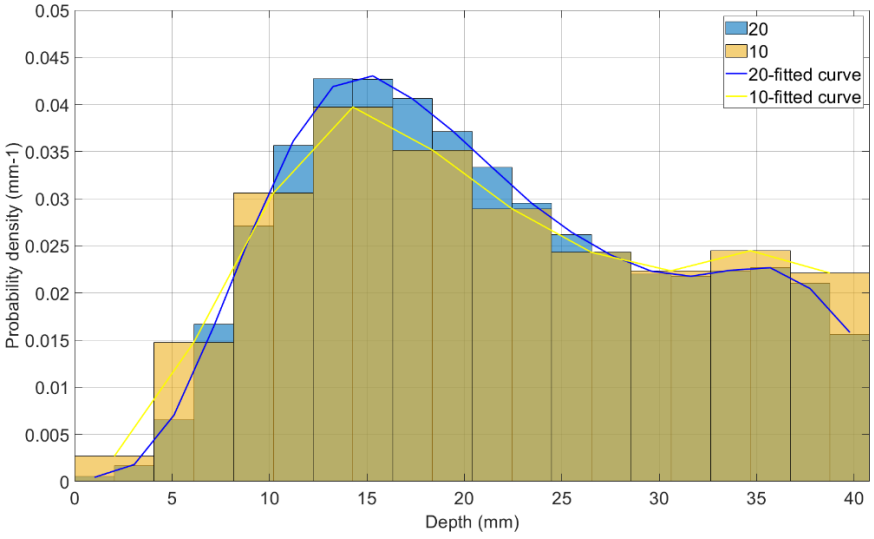

c)

Figure 5.8 – Beads distribution across the reactor depth at different heights: 0.04 m (a), 0.20 m (b), 0.33 m (c). The probability density is calculated by the probability density function.

5.3.1.2 Model validation

5.3.1.2.1 Velocity fields

The mean axial solid velocity fields of compartment and CFD models are compared to validate the stochastic model (Figure 5.11). The compartment model is composed of 20×20×40 compartments. In chapter 3, it was shown that the horizontal velocity (x) is negligible compared to the vertical velocity (z). The normal velocity (y) is negligible except above 300 mm height and under 50 mm. Planes 3 and 5 previously studied are used to compare CFD and compartment model. Velocity fields are close even if the spatial resolution is significantly lower than in CFD. Logically, local velocities are not always well described by the compartment model as at the top of the internal panel (height of 340 mm). In plane 5, velocities below z = 100 mm are overestimated by the compartment model up to 30 %. As a result, velocity fields of the compartment model are smoother.

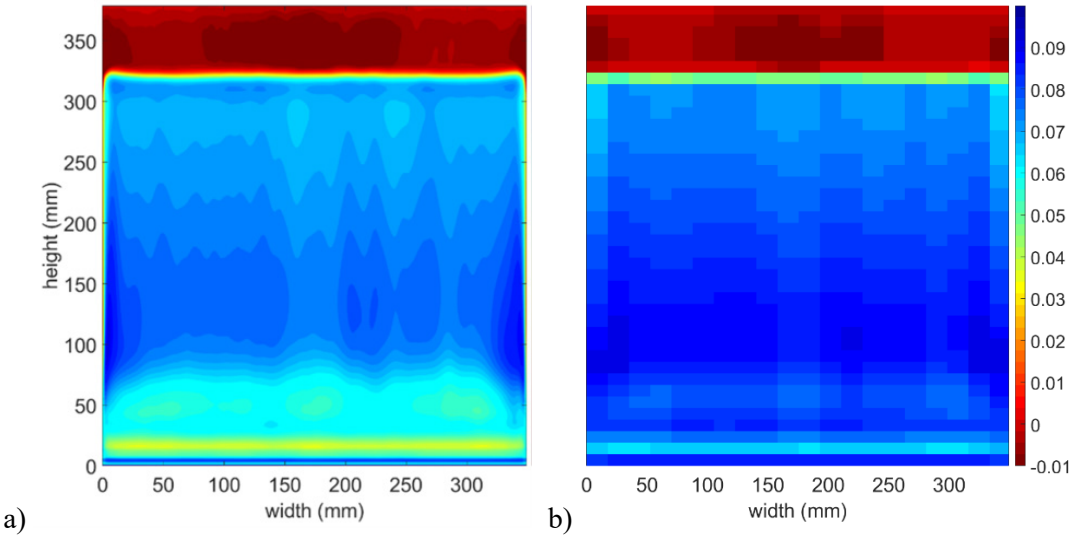

Figure 5.9 - Mean vertical (z) solid velocity fields ($m.s^{-1}$) of plane 5 situated in the ascending zone calculated by CFD (a) and compartment model (b). The numbers of compartments in the compartment model in x, y and z are 20, 20 and 40 respectively.

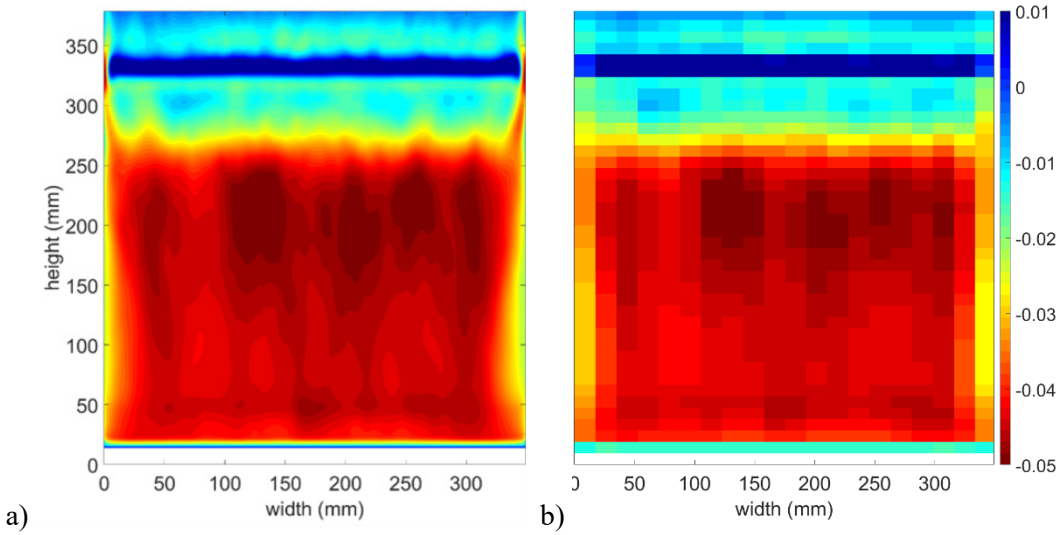

Figure 5.10 - Mean vertical (z) solid velocity fields (m.s^{-1}) of plane 3 situated in the descending zone calculated by CFD (a) and compartment model (b). The numbers of compartments in the compartment model in x, y and z are 20, 20 and 40 respectively.

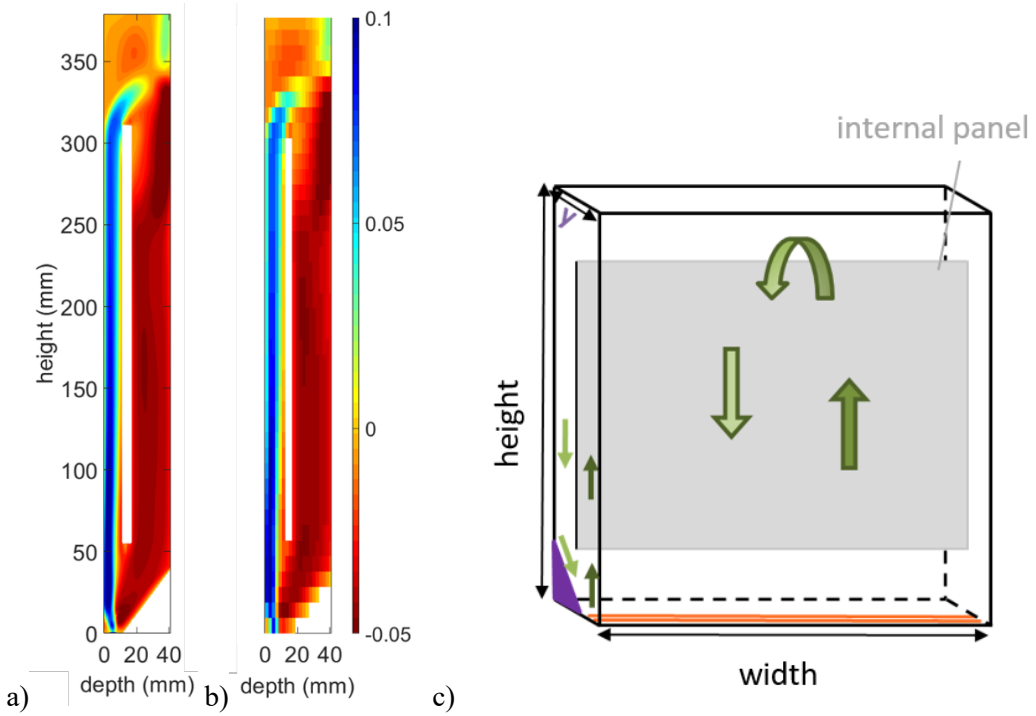

Figure 5.11 – Mean vertical solid velocity fields (m.s^{-1}) *in the reactor depth in a plane situated in the center of the reactor width, calculated by CFD (a) and compartment model (b). The numbers of compartments in the compartment model in x, y and z are 20, 20 and 40 respectively. Schematic representation of the reactor (c).*

5.3.1.2.2 Solid distribution

Solid distribution of CFD and compartment model are compared in planes 3 and 5 (Figure 5.13). Same conclusions as velocity fields can be drawn. Global solid distributions are well described by the compartment model even if local accumulations are not so correctly represented. Hence the information

lost using the compartment model compared to the CFD is low, if compared to the time saved: several days for a CFD simulation, compared to several hours for the compartment and stochastic models.

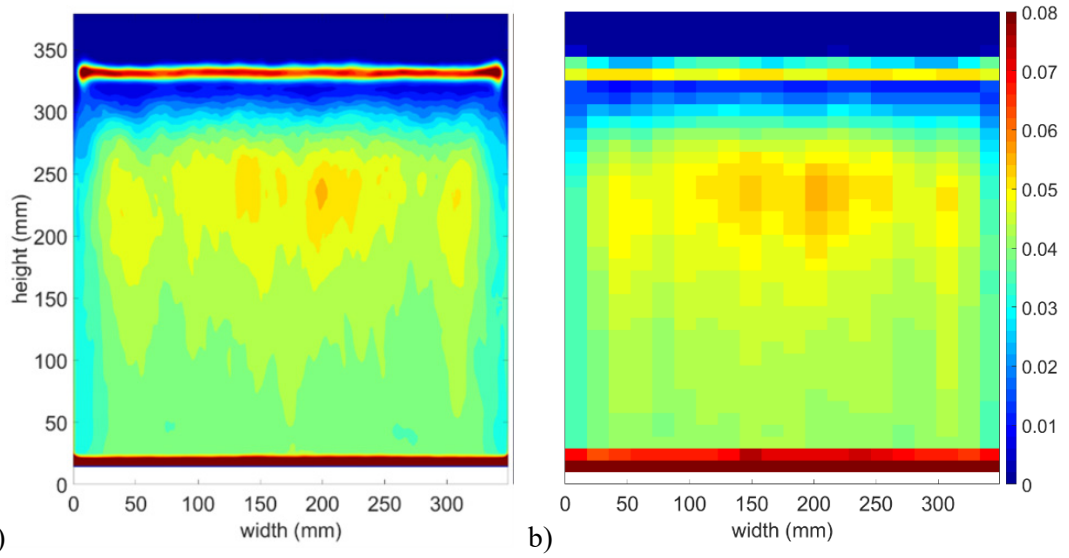

Figure 5.12 - Solid fraction distribution in plane 3 situated in the descending zone calculated by CFD (a) and compartment model (b).

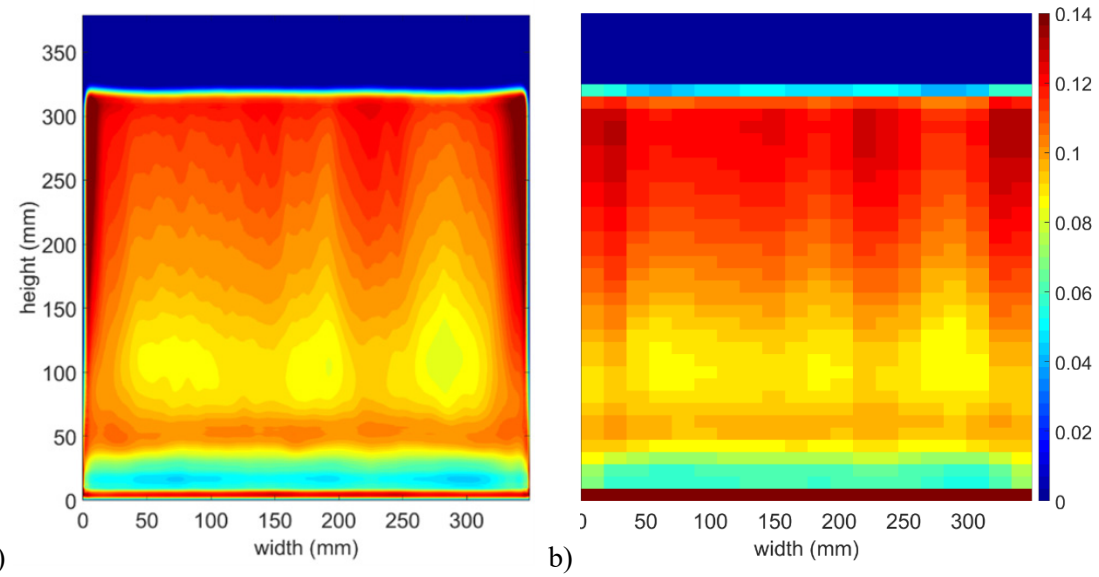

Figure 5.13 – Solid fraction distribution in planes 5 situated in the ascending zone calculated by CFD (a) and compartment model (b).

5.3.1.3 Bead trajectories

The CFD-based compartment model coupled to the stochastic model allows to determine realistic trajectories of beads. The trajectories are calculated in the 3 dimensions: depth (y), width (x) and height (z). The position of a bead (depth and, to a lesser extend, height and width) determines the light received by algae encapsulated in the bead. An example of a trajectory of a bead during 200 s is shown on Figure

5.14. On simulated trajectories, beads are going up and down on each side of the internal panel, which is in good agreement with visual observations. The bead depth hardly changes during the ascending or descending time while it increases or decreases rapidly above or under the internal panel. This represents physically well the bead trajectories observed visually.

As the position of a bead along the reactor width has an impact on the incident light intensity (Figure 5.4 b), it must also be considered. Moreover, the bead motion along the reactor width has a significant influence on the time needed for the bead to go up or down as well: diagonal/inclined trajectories are longer than straight/vertical ones. However, Figure 5.14 d shows that displacements along the width are less important than those along the depth and height.

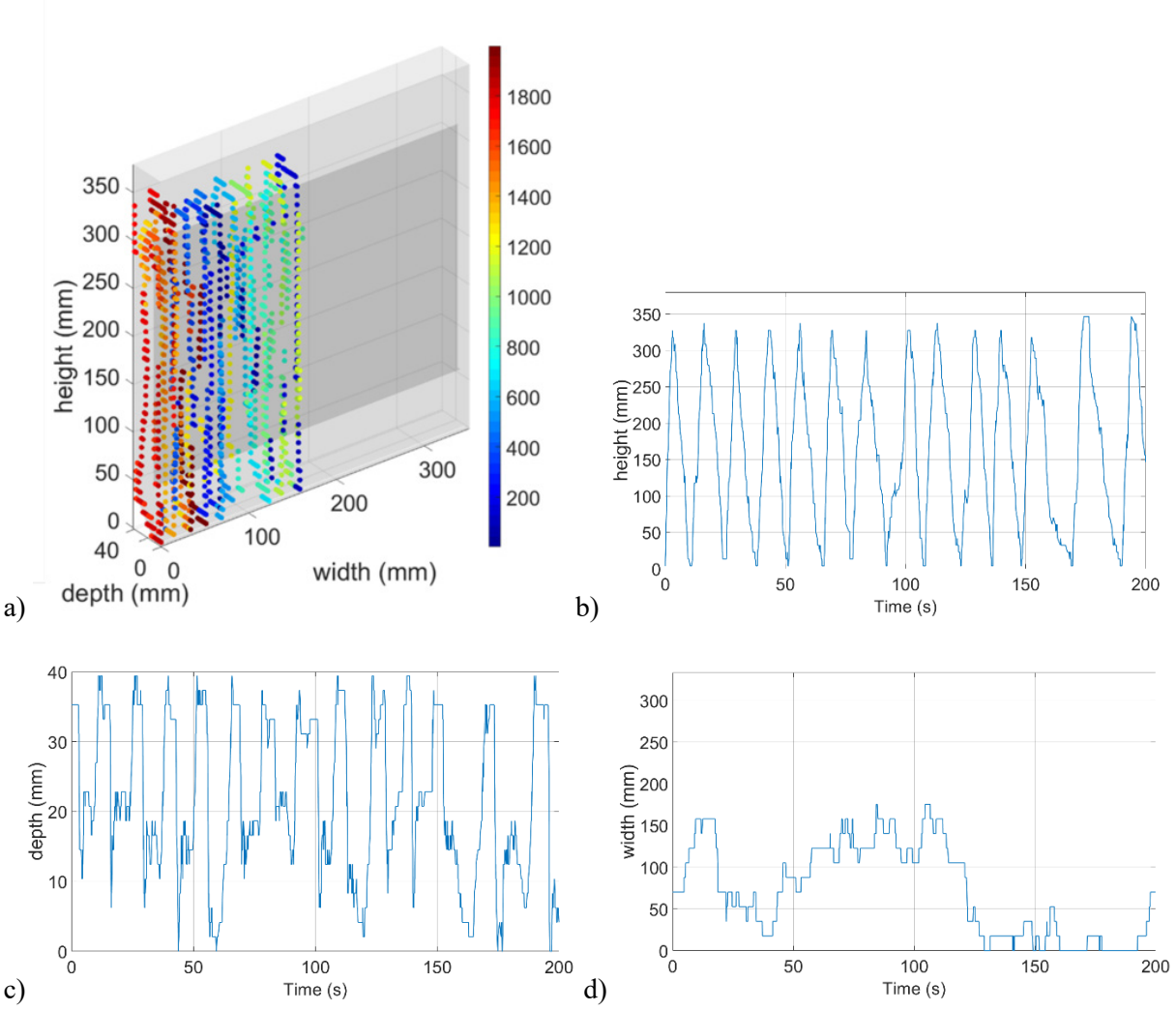

Figure 5.14 – Example of trajectory of a bead in the reactor in 3D during 200s (a). Color scale represents the time step (a). Trajectory of the same bead according to the reactor height (b), depth (c) and width (d).

The model enables to determine mean residence times (time spent by beads) in the four main regions of the reactor: in front (1), behind (2), over (3t) and below (3b) the internal panel (Figure 5.3). The residence times (Table 5.2) in the dark (region 2, 3.2 s) and illuminated zone (region 1, 5.6 s) are rather low leading to short medium-duration L/D cycles compared to other photobioreactors (between 6 and 24 s) (Janssen et al., 2000). However, they should not lead to any flashing light effect, observed only if the L/D cycle is shorter than 1s. Beads spend more time than expected below the internal panel regarding the volume of this region (region 3b, 3.1 s). This can be explained by a lower speed region, as beads are

slidding on the prism. Moreover, beads can sometimes be temporarily stuck in a small recirculation loop below the internal panel as observed in the reactor.

Table 5.2 – Mean residence time in the 4 main regions of the reactor.

Region	Mean residence time (s)	Volume (L)
1	5.6	2.25
2	3.2	1.08
3t	1.6	1.04
3b	3.1	0.61

5.3.1.4 Long time simulations

Even if time efficient, the stochastic model cannot be used to simulate the trajectories of beads on the whole duration of a culture (24 days), as it would lead to non-available computer memory capacity. To reduce calculation time, bead trajectories are studied to get a realistic representation of light conditions experienced by cells in the reactor. 3 zones are chosen in regions of the reactor where the flow and light attenuation differ (Figure 5.15 a). Zones corresponding to 1 compartment in depth and 4 compartments in height is delimited. 8 compartments are considered in width ($x < 135$ mm) due to different incident light intensities (Figure 5.4 b). The mean residence time, which corresponds to the mean time a bead spends in the zone, and the mean circulation time, which is the mean time needed for a bead to enter the zone again, are considered. The convergence of these values shows that the model is representative of the bead global movement in relation to light (Figure 5.15 b c). To get a statistically representative trajectory in a random Lagrangian approach, the number or the length of time of trajectories can be considered. In other words, once the trajectory does not depend on its initial position anymore, studying 40 random trajectories of 1 hour is statistically the same as studying 1 trajectory of 40 hours. It is chosen, for memory reasons, to study trajectories of 40 beads. Each trajectory is studied for 58 hours (2.10^6 iterations). It is found that after 29 hours (10^6 iterations), a satisfactorily convergence is obtained. Indeed, fluctuations in a range of ~ 1 % are observed between 10^6 and 2.10^6 iterations. Only results in zone s2 are presented in Figure 5.15. Results relative to zones s1 and s3 can be found in Appendices (Figure 0.1). Trajectory simulated on 29 hours is repeated, to get a trajectory simulated on 24 days which corresponds to the whole duration of the experimental culture.

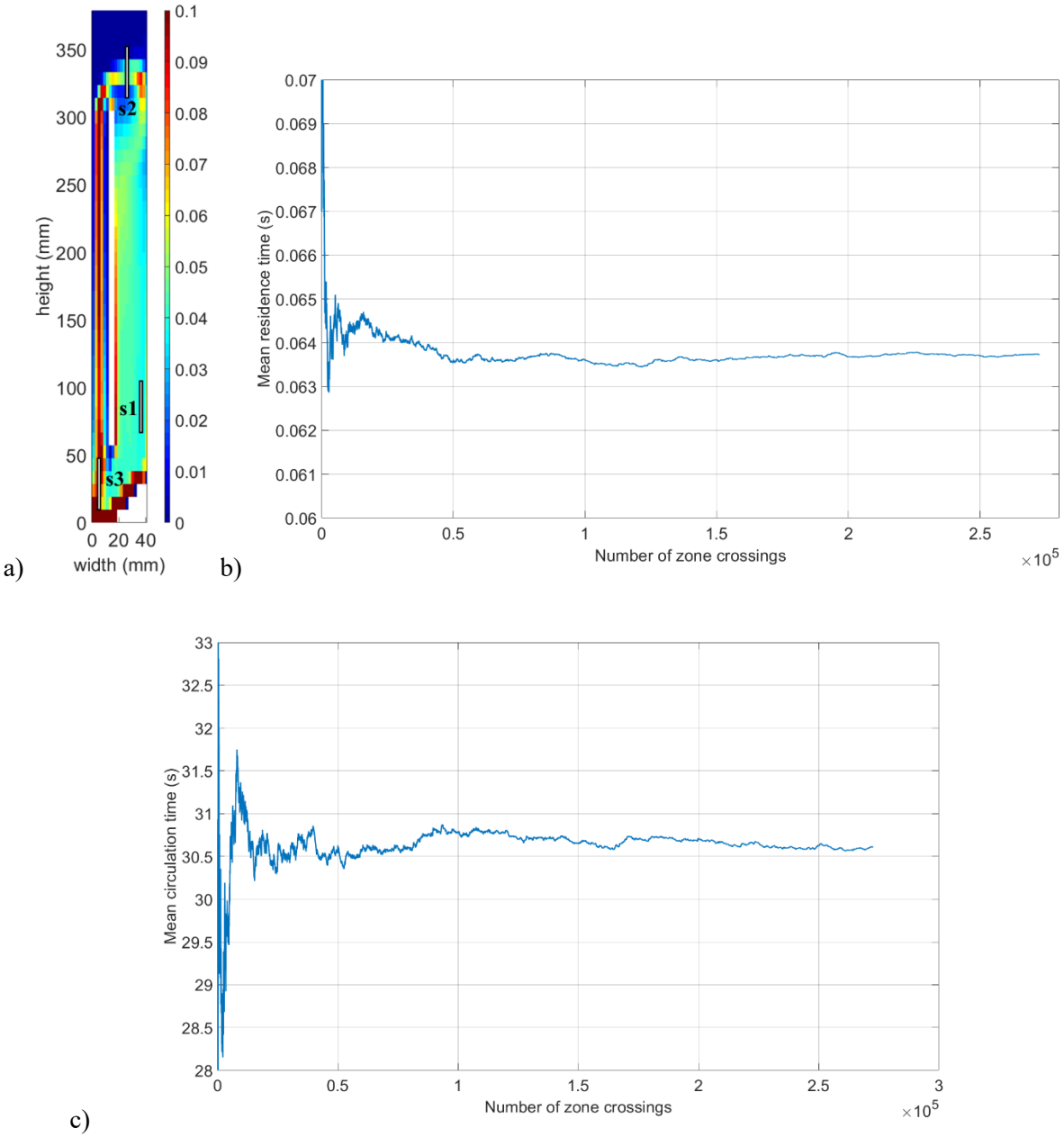

Figure 5.15 – Position of the three zones of the reactor used for mean residence and circulation times (a). The reactor width (x) below 135 mm is considered due to different incident light intensities (Figure 5.4 b). Mean residence time (b) and mean circulation time (c) in zone s2 obtained using the stochastic model. Mean on 40 beads (corresponding to different initial positions). Calculations correspond to a total time of 58 h in the reactor. 29 h (half of the total) is considered satisfactory to characterize trajectories.

5.3.2 Global model

5.3.2.1 Comparison with experimental results

Implementation of the light attenuation and the PSF model on trajectories enables to model the growth of biomass using the global model described in 5.2.4. Biomass dry weight as a function of time is used to compare experiments and model results. As the model cannot predict the lag phase of the culture which is particularly long for encapsulated algae (two days experimentally), calculations results are compared from the second day to the last day of the experimental ones.

A mean dry weight on 40 trajectories is calculated. Time steps of each trajectory is different as it depends on the time a particle spends in a compartment. As time step is low compared to light changes, for each iteration a mean dry weight and a mean time step are calculated. Few differences between dry weights calculated by different trajectories are highlighted (Figure 5.16). Considering one single bead could thus be fairly representative of all beads. Therefore error bars are not showed in the following.

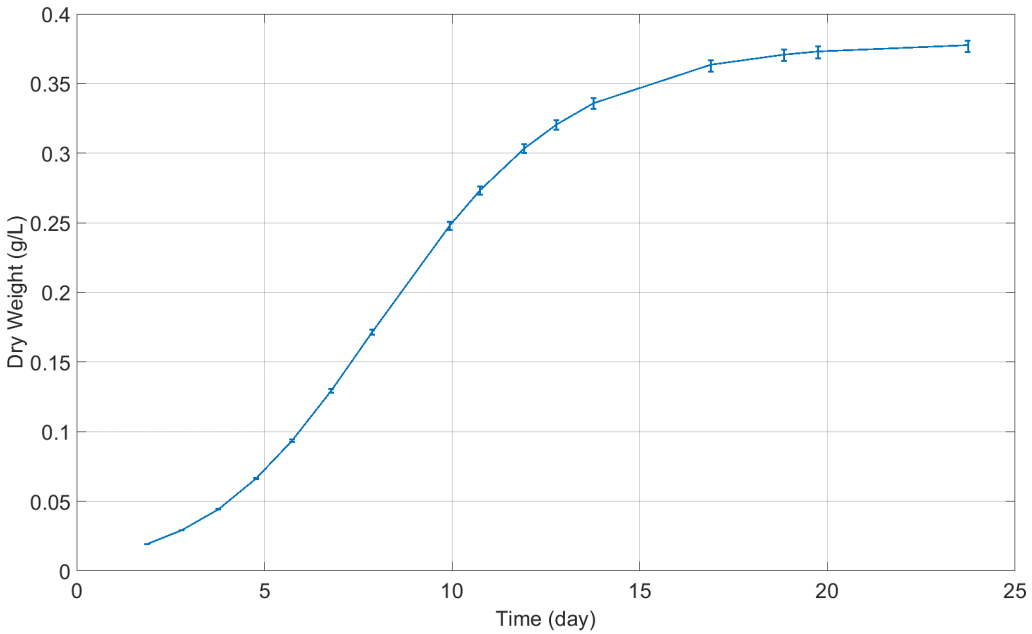

Figure 5.16 - Growth of encapsulated Chlamydomonas reinhardtii in a 5 L photobioreactor calculated with the global model. Mean on 40 particles. The error bars represent the minimum and maximum of the 40 trajectories for each day an experimental measure is made.

Results of the global model are then compared to experimental results (Figure 5.17). Model globally follows experimental results. The relative difference between both curve is 10 % in average (between 2 and 36 %). The fitting used (method of least squares, one parameter at a time) does not allow to get a lower difference. Indeed, the impact of decreasing the difference of the two curves between day 6 and 7 is to increase the difference on day 13 and 14. The final dry weight (between day 19 and 24) of the model (0.375 $g.L^{-1}$ in average) is close to the one measured experimentally (0.387 $g.L^{-1}$). The model describes globally well the experimental growth of biomass.

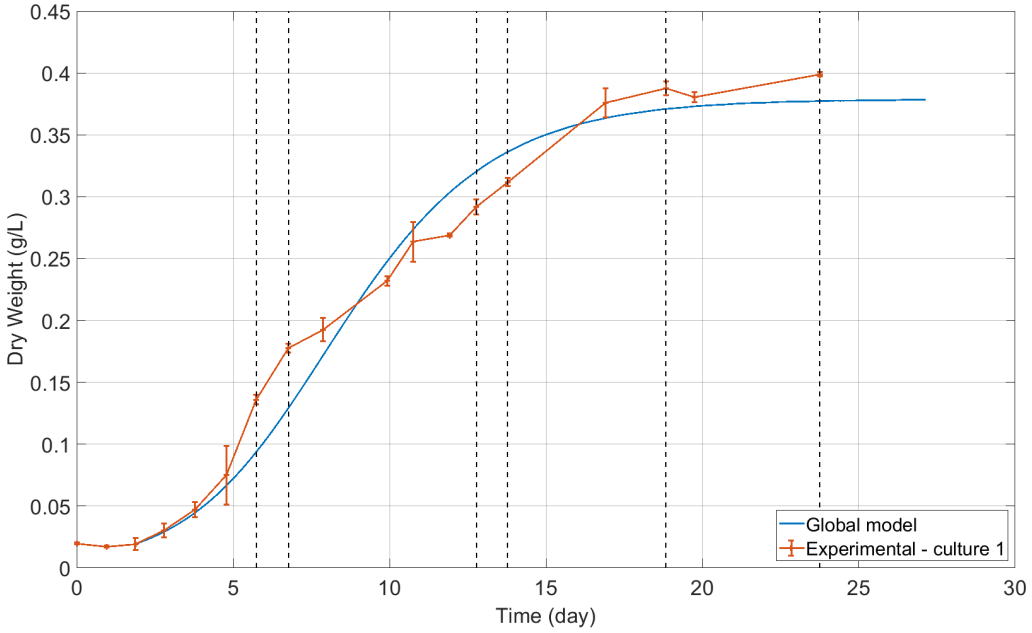

Figure 5.17 – Growth of encapsulated Chlamydomonas reinhardtii in a 5 L photobioreactor obtained experimentally and calculated with the global model. Mean on 40 particles with the model.

The repartition of biomass between the three potential states (x_1, x_2, x_3) calculated by the model (5.2.3.1) is studied on 1 trajectory (Figure 5.18). The change of biomass state is fast (around 10 s) leading to a spread range signal. The fraction in inhibited state (x_3) is very low (lower than 2 %) which is explained by the low light input. The fraction in the resting state (x_1) is around 74 % at the beginning of the culture and remains in this range in the illuminated zone of the reactor until the end while it increases in the dark zone from 78 % to 90 %. The fraction in the activated state (x_2) has logically an opposite behavior. Hence the mean fraction in the activated state x_2 decreases which leads to a slower growth.

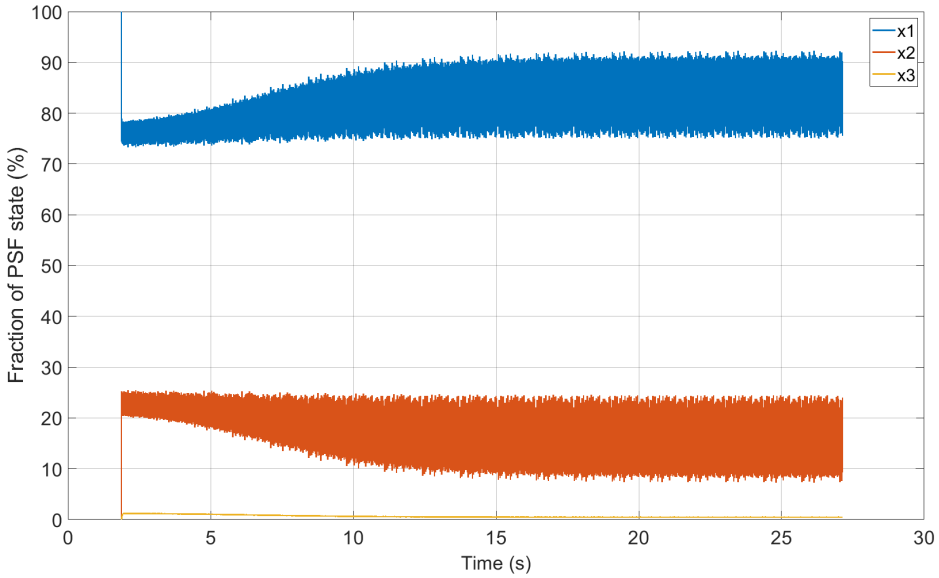

Figure 5.18 - Repartition in the 3 states of biomass in the PSF model for 1 trajectory. x1, x2 and x3 represent respectively to the resting, the activated and the inhibited state.

Figure 5.19 a shows a zoom on the repartition in the 3 states of biomass on day 10 for a given trajectory. Light intensity received by cells is plotted as well. Figure 5.19 b shows dry weight curve during the same time. The change of biomass state and dry weight clearly follows the light intensity: fraction in activated state (x_2) increases with light intensity. However, change of biomass state is not instantaneous and does not follow each fluctuation of light intensity. This shows that the model predicts a biomass growth following a partial integration according to light regime as explained in 1.4.1.3 (Takache, 2010). Hence biomass growth can certainly not be predicted easily predicted and a comprehensive study of flow and light is needed (Gernigon et al., 2019). This is confirmed in 5.3.2.3.2.

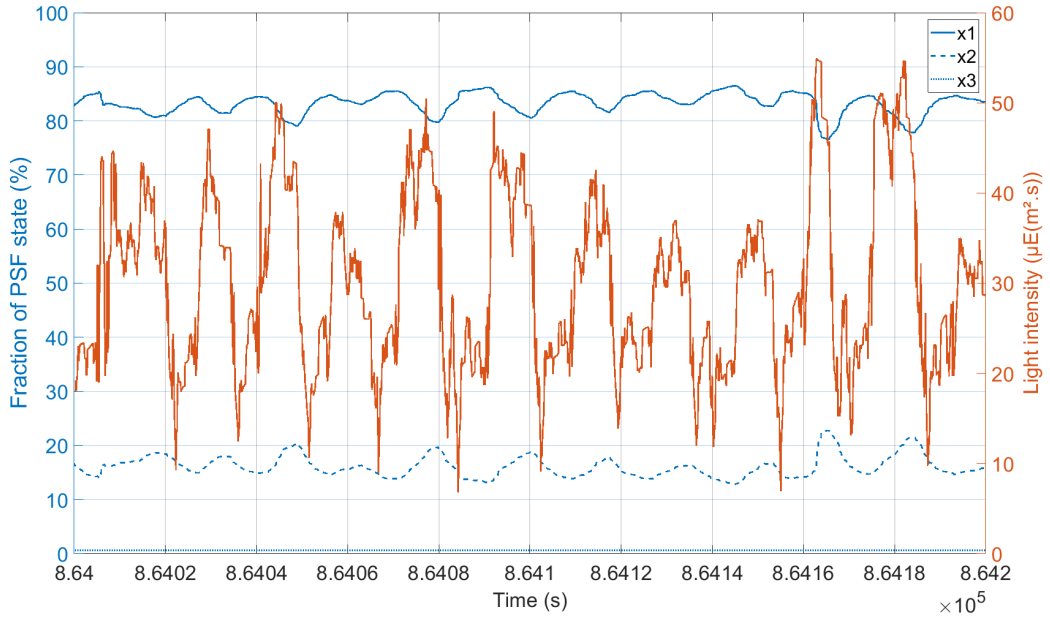

a)

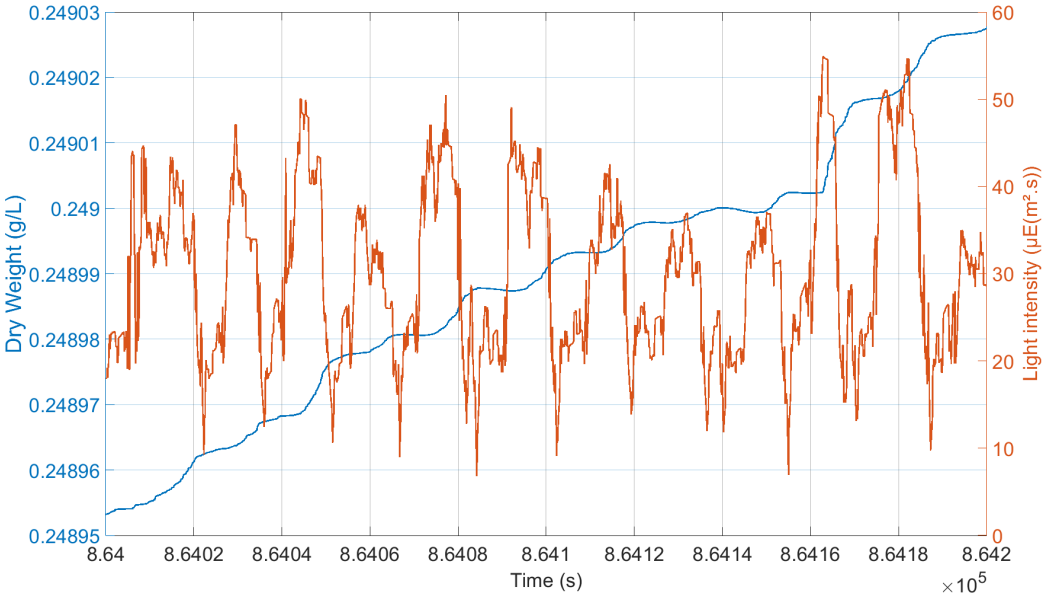

b)

Figure 5.19 – Zoom on light intensity and fraction in the 3 states of biomass in the PSF model for 1 trajectory on day 10. x1, x2 and x3 represent respectively the resting, the activated and the inhibited state (a). Zoom on light intensity and dry weight for 1 trajectory on day 10.

5.3.2.2 Influence of L/D cycles

The influence of L/D cycles on growth is studied using the model. Two simulations are compared: one considering local light values resulting to alternating periods of light and dark and another considering time evolution of mean light. The last thus does not considered L/D cycles.

A smoothed curve is computed to determine a moving mean light intensity (yellow curve) based on light fluctuations (blue curve). This represents a mean light received over a period of time significantly longer than the circulation time of the reactor. The method is a smoothed local regression using weighted linear least squares and a second degree polynomial model. A span of 30 % of the total number of data points

is used. It is available in Curve Fitting Toolbox in Matlab. The smoothed curve globally follows the fluctuating light without considering instantaneous fluctuations. An equation of time evolution of light can thus be used.

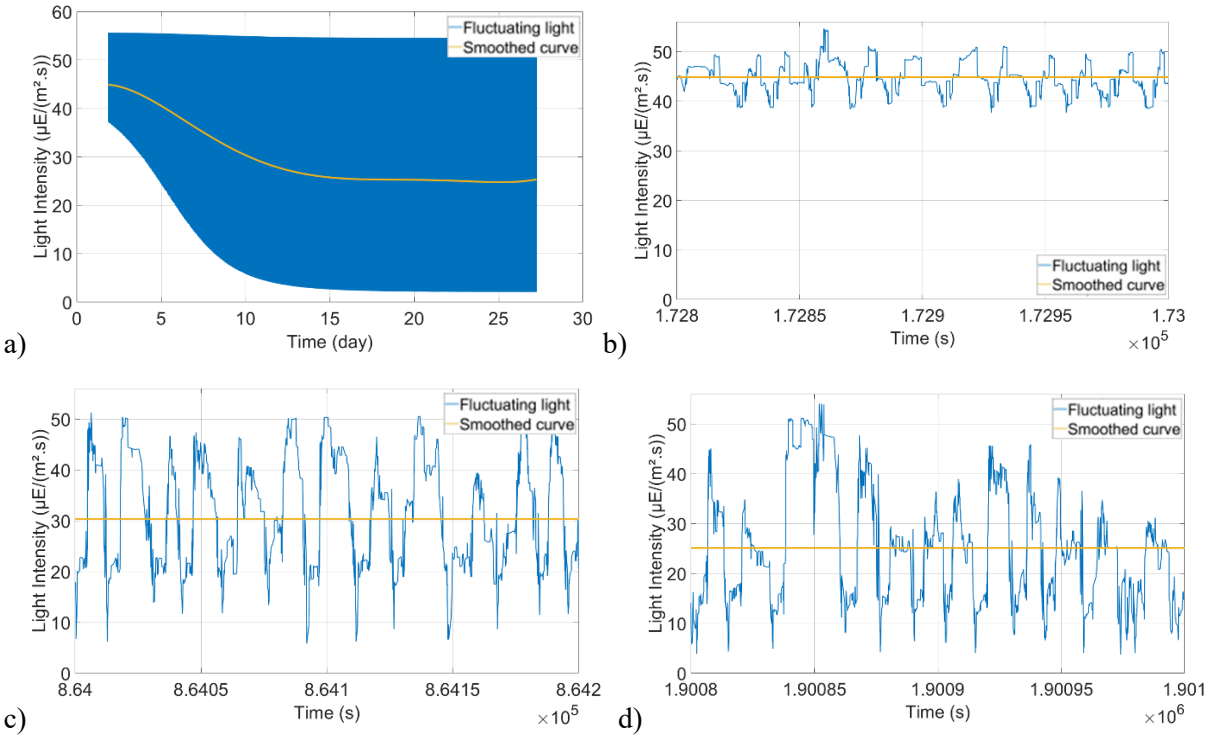

Figure 5.20 – Light received by cells using a realistic trajectory determined by the stochastic model (fluctuating light) or a smoothed curve calculated based on this fluctuating light (a). Zoom on fluctuating and smoothed curve on day 2 (b), day 10 (c) and day 22 (d).

The model is then used to calculate growth from both curves. Simulation results on 1 trajectory are presented on Figure 5.21. The growths under fluctuating or mean light are very close at the beginning of the culture until day 6 when it begins to slightly differ. The difference increases as the attenuation becomes more important, until the end of the culture with a dry weight difference of 10 %, i.e., 0.339 $g.L^{-1}$ for the mean light intensity against 0.374 $g.L^{-1}$ for the fluctuating light on day 23. Hence the model takes light history (and L/D cycles) into account, and it has a positive impact on growth (in this case). This confirms that it is essential to consider algae circulation and thus hydrodynamics to globally characterize a photobioreactor.

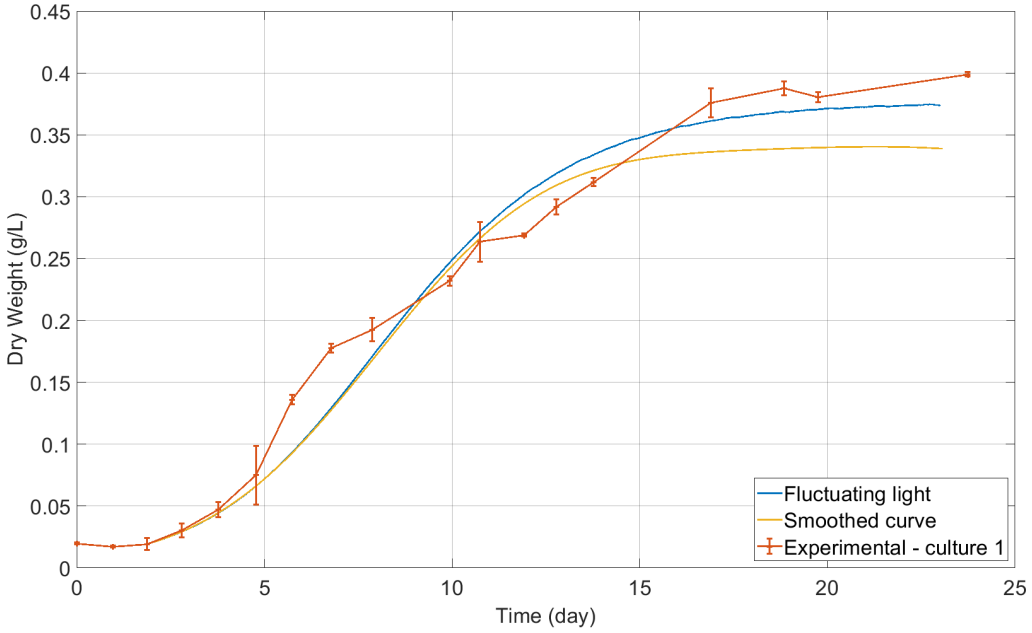

Figure 5.21 - Growth of encapsulated Chlamydomonas reinhardtii in a 5 L photobioreactor calculated using a realistic trajectory determined by the stochastic model (fluctuating light) or a mean light calculated as a smoothed curve on 1 trajectory.

5.3.2.3 Simplifications of the model

5.3.2.3.1 Influence of solid distribution

As explained in chapter 0, the solid fraction is not homogeneous in the reactor (higher in the ascending zone) and this can have an influence on light attenuation in the reactor depth. The influence of introducing the f_{ti} ratio (Equation 5.20) which takes into account the different local solid fractions is studied (Figure 5.22). Biomass growth is calculated based on the same trajectory using two different light attenuation methods: base case considering f_{ti} or homogeneous solid distribution (f_{ti} is replaced by y_t in (Equation 5.18) (Equation 5.19). Results considering or not f_{ti} show different dry weight curves thus the f_{ti} correction is not negligible. Hence solid distribution has an influence on light attenuation and thus on biomass growth. This shows the interest of developing this kind of advanced model, which can predict precisely solid distribution, for the studied system.

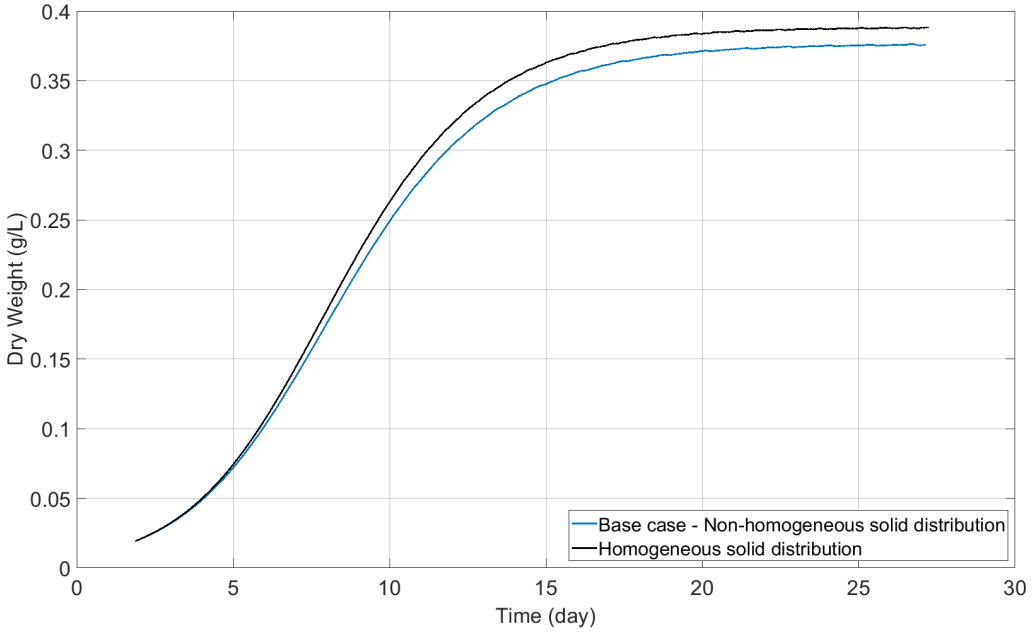

Figure 5.22 – Dry weight calculated by the global model considering non uniform solid distribution (considering fti) or considering a homogeneous solid distribution (not considering fti). 1 trajectory is considered.

5.3.2.3.2 Basic model

To determine the relevance of developing a global model taking accurately hydrodynamics into account, a basic model of the reactor is developed considering that no CFD study has been performed. The model is compared to the global model developed in this thesis. The basic model is based on residence times in the 4 main regions of the reactor (Figure 5.3, Table 5.2). The residence times used are the ones obtained by the stochastic model but could be measured experimentally. The 4 regions are considered perfectly mixed, considering no other information is reached on beads displacements. A trajectory is built alternating continuously the displacement in the 4 regions according to a logical scheme following this order: region 1, 3b, 2 and 3t (Figure 5.23). The light intensity in each region is integrated through the depth of the region (Equation 5.28) (Equation 5.29) (Equation 5.30). The bead is thus submitted to alternating periods of different light intensity according to the 4 main regions of the reactor. However, the mean light intensity received by algae during the culture is very close for both model, (28 $\mu E.m^{-2}.s^{-1}$ for the basic model and 30 $\mu E.m^{-2}.s^{-1}$ for the global model). The time step used to calculate the PSF model is 0.1 s which corresponds to the mean time step of the global model. Parameters fitted on the global model are used.

For region 1,

$$I=\frac{\int Idy}{e_{L1}}=\frac{I_0\times e^{-\varepsilon_p e_{p1}}(1-e^{-(\varepsilon_b X+\varepsilon_w)e_{L1}})}{e_{L1}(\varepsilon_b X+\varepsilon_w)} \qquad \textit{(Equation 5.28)}$$

For region 2,

$$I=\frac{\int Idy}{e_{L2}}=\frac{I_0\times e^{-\varepsilon_p e_{p1}}\times e^{-(\varepsilon_b X+\varepsilon_w)e_{L1}}\times e^{-\varepsilon_p e_{p2}}(1-e^{-(\varepsilon_b X+\varepsilon_w)e_{L2}})}{e_{L2}(\varepsilon_b X+\varepsilon_w)} \qquad \textit{(Equation 5.29)}$$

For region 3,

$$I=\frac{\int Idy}{(e_{L2}+e_{L1}+e_{p2})}=\frac{I_0\times e^{-\varepsilon_p e_{p1}}(1-e^{-(\varepsilon_b X+\varepsilon_w)\times(e_{L2}+e_{L1}+e_{p2})})}{(e_{L2}+e_{L1}+e_{p2})\times(\varepsilon_b X+\varepsilon_w)} \qquad \textit{(Equation 5.30)}$$

with e_{L1} and e_{L2} the depth of zone 1 and 2 respectively.

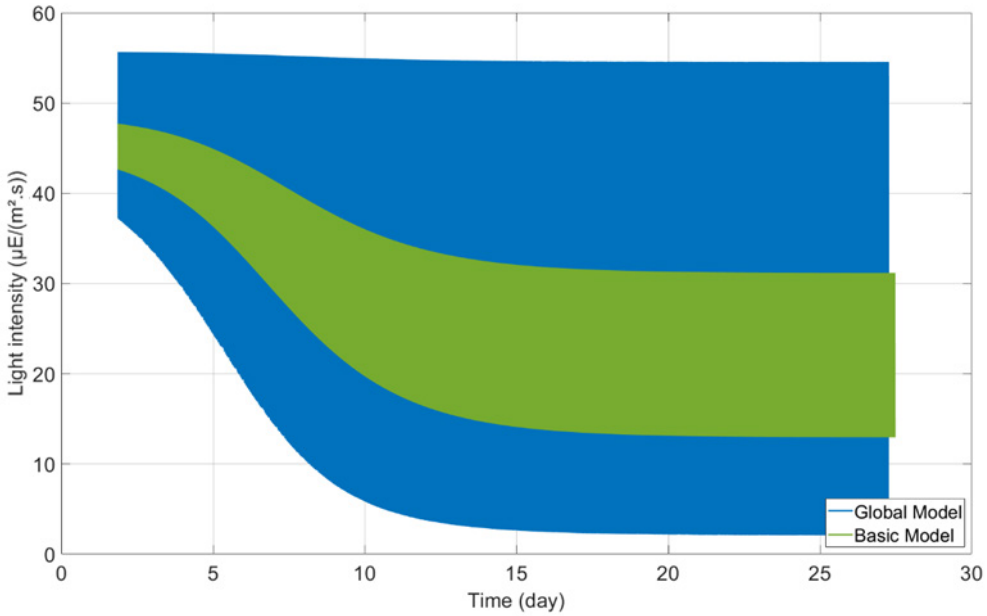

a)

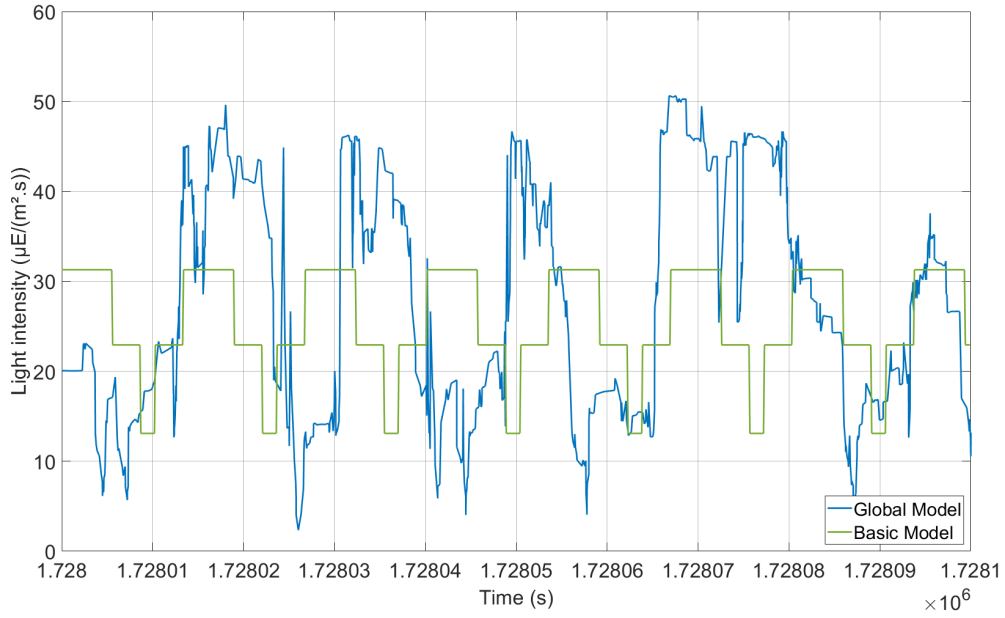

b)

Figure 5.23 – Light intensity received by algae calculated by the global model and a basic model based on residence times in 4 main regions of the reactor (a). Zoom on light intensity on day 20 (b).

The basic model does not give the same results as the global model (Figure 5.24). The final dry weight is highly overestimated by the basic model (0.478 $g.L^{-1}$) compared to the global model (0.377 $g.L^{-1}$) on day 23. Yet the mean light intensity received is close and even slightly higher for the global model. This shows again the high influence of L/D cycles and thus of hydrodynamics on the growth. In the basic model, cells experienced less extreme light intensities as the light is integrated through the depth. Even if lower light intensities are reached in the basic model in the illuminated zone, it does not seem to have a high influence. In the dark zone, higher light intensities are reached in the basic model (13 $\mu E.m^{-2}.s^{-1}$ against 2 $\mu E.m^{-2}.s^{-1}$ in the global model). The model considered thus that light intensity in the dark zone has more influence in this case.

However, the shape of the basic model curve is similar to the one of the global model. A wider range of experimental data which considers different conditions is needed to confirm the supremacy of the global model over the basic model.

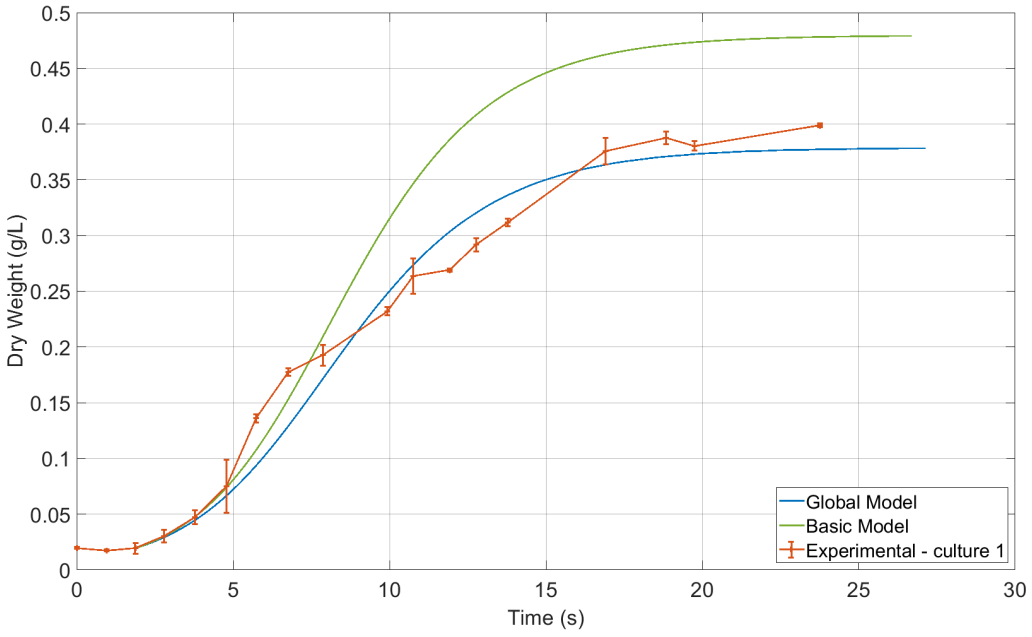

Figure 5.24 - Dry weight calculated by the global model and a basic model based on residence times in 4 main regions of the reactor.

5.3.3 Applications

5.3.3.1 Light

The influence of incident light intensity is evaluated (Figure 5.25). It must be noticed that these results are qualitative as experimental results at different light intensities would be required to fit accurately the biological model parameter in the whole range of light intensity and to obtain quantitative results. The model logically predicts a faster growth and a higher dry weight with an increasing light input. The model does not consider nutrients limitation which could happen in the case of higher dry weight. A continuous or fed-batch system should be used in this case.

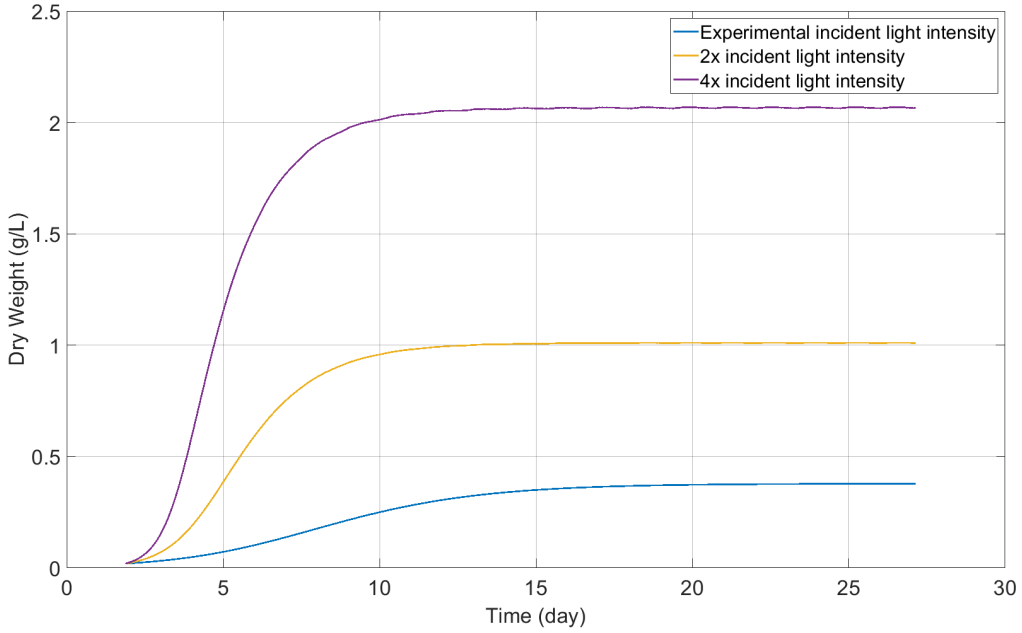

Figure 5.25 - Dry weight calculated by the global model for different incident light intensity (I0). The mean experimental light intensity is 60 µE.m^{-2}.s^{-1}, thus the 2x and 4x mean incident light intensity correspond to 120 and 240 µE.m^{-2}.s^{-1} respectively.

The model is also able to predict a high photoinhibition which fully hinders biomass growth after 25 days. However, this is achieved with a mean incident light intensity of 6600 µE/(m².s) which is higher than usually reported (2000 µE/(m².s)) (Wu & Merchuk, 2001). The model is thus able to qualitatively predict the photoinhibition but not quantitatively as the model is fitted on experiments using a low light intensity (60 µE/(m².s)) which does not allow to study photoinhibition. Experiments at higher light intensities are needed to fit these parameters in the actual model.

5.3.3.2 Hydrodynamics

The influence of hydrodynamics on biomass growth is evaluated using the model. Different inlet liquid flow rates are simulated using CFD, then the compartment and stochastic models and finally the global model are computed. As liquid fluidizes beads, liquid flow rate has a direct influence on the solid distribution and bead displacements.

Figure 5.26 shows the biomass curves calculated by the model using different liquid flow rate. A higher flow rate leads to a significant higher biomass dry weight. Indeed a 0.2000 kg.s^{-1} flow rate allows to reach a final dry weight of 0.431 g.L^{-1} (day 25) while a dry weight of 0.377 g.L^{-1} is reached using the base case model using a flow rate of 0.1444 kg.s^{-1}. This result is confirmed with a liquid flow rate of 0.1800 kg.s^{-1} (final dry weight of 0.414 g.L^{-1}). It must be noticed that the nutrient limitation is not considered by the model, thus only the influence of light access through hydrodynamics is taken into account.

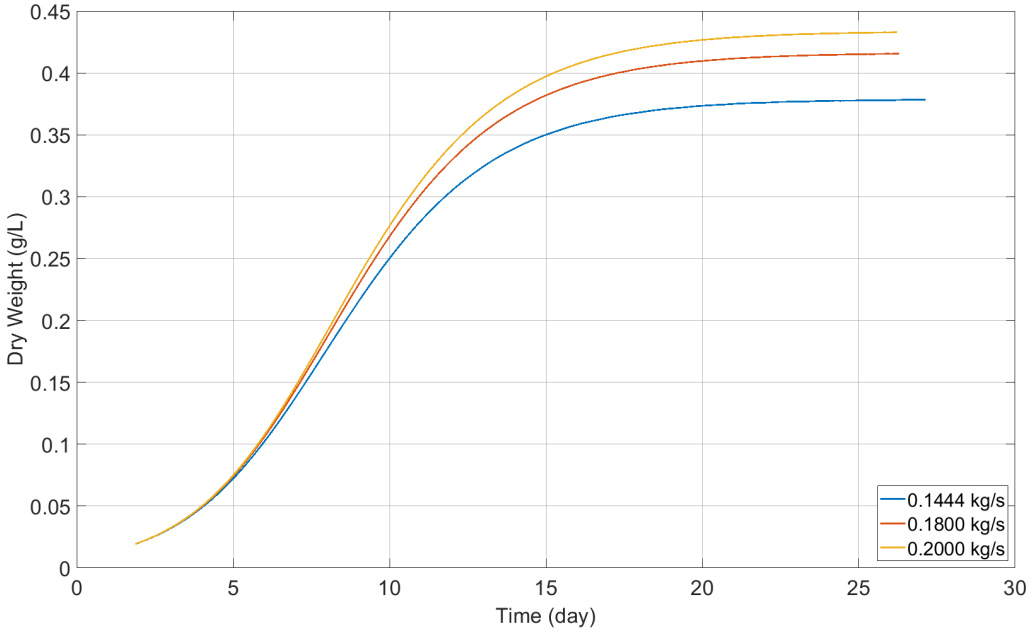

Figure 5.26 – Influence of the inlet liquid flow rate on the dry weight.

The solid distribution in the reactor height or width is not significantly impacted by the different flow rates. The solid distribution in the reactor depth using the different flow rates is slightly different, especially using a flow rate of 0.1444 $kg.s^{-1}$ (Figure 5.27). Figure 5.28 describes the solid distribution at a height of 200 mm. At a flow rate of 0.1444 $kg.s^{-1}$, a higher solid fraction is measured in the dark (ascending) zone (below a depth of 12 mm) which leads to a higher attenuation thus a lower growth rate. However, using other liquid flow rate values lead to similar solid distribution.

Residence times using a higher flow rate are lower leading to lower L/D cycles. These are favorable for biomass growth. The higher dry weights obtained by increasing liquid flow rate can thus be probably explained by lower L/D cycles. These primary results must be validated by experimental results but show the high theoretical influence of L/D cycles.

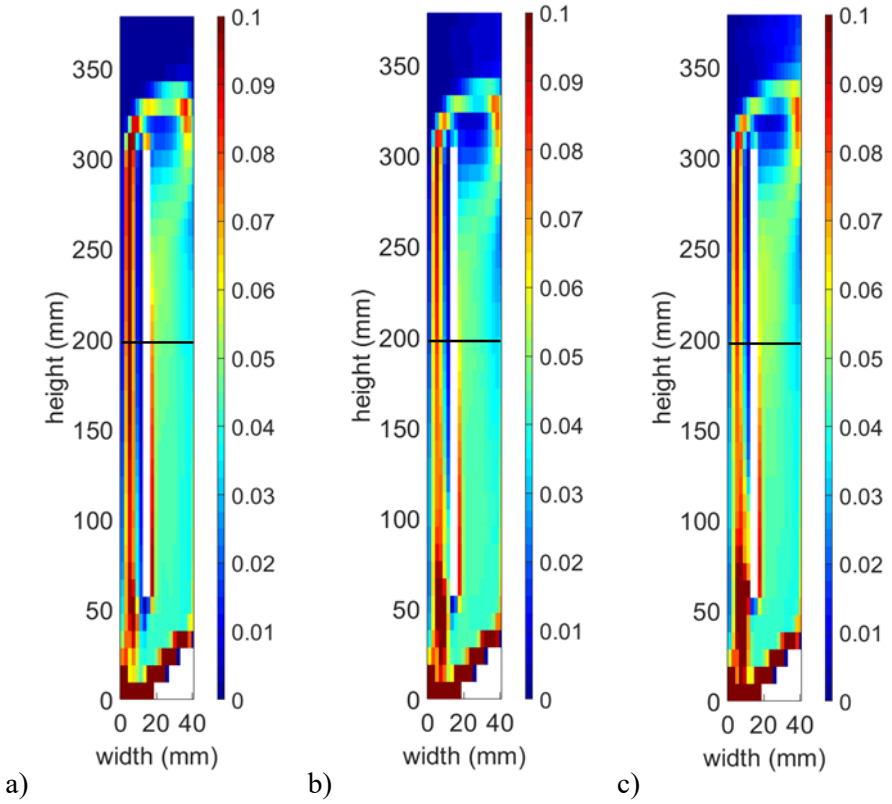

Figure 5.27 - Solid distribution in depth in a plane situated in the center of the reactor width calculated by the compartment model using a liquid flow rate of 0.1444 kg.s^{-1} (a), 0.1800 kg.s^{-1} (b) and 0.2000 kg.s^{-1} (c). The black line at 200 mm represents the height used in Figure 5.28.

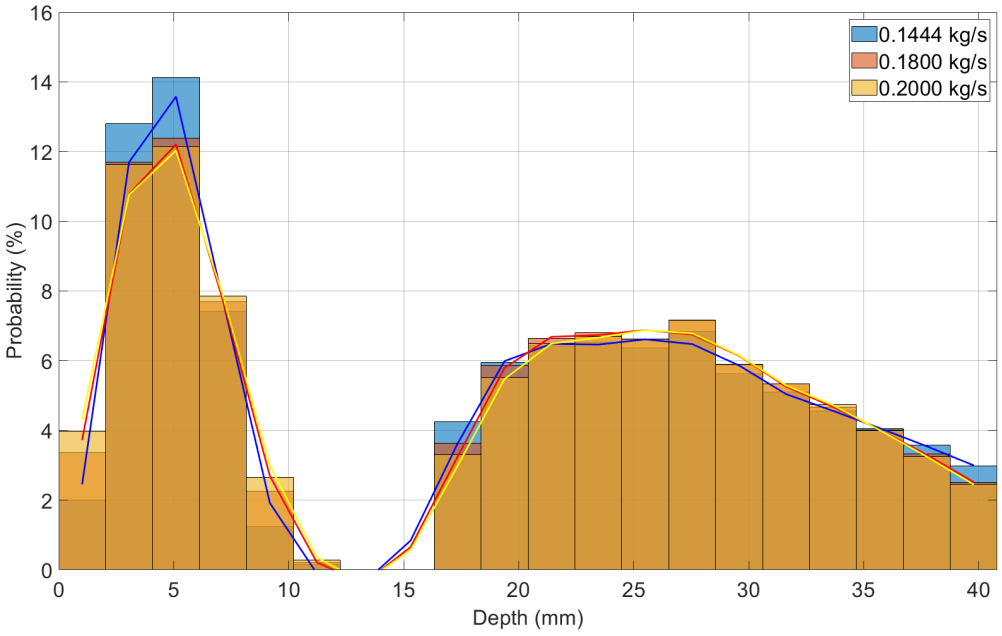

Figure 5.28 - Beads distribution across the reactor depth using different liquid flow rate at a height of 0.20 m.

5.4 Conclusions

A model is developed to predict biomass growth in a photobioreactor designed for the culture of encapsulated microalgae. The model is built using models describing hydrodynamics, light and biology. Hydrodynamics has an influence on light distribution in the reactor. Light and biomass concentration are dually coupled. Indeed, biomass growth directly depends on light and light attenuation through the photobioreactor depends on biomass growth.

Hydrodynamics is modeled using a CFD-based compartment model. The flow rates between adjacent compartments are calculated based on CFD flow rates. The number of cells is divided by 54 in the compartment model if compared to the CFD model, which allows to save computation time and memory. The compartment model nevertheless well describes global velocities. A stochastic model for bead displacements in the reactor is adapted based on flow rates of the compartment model. The stochastic model also allows describing the non-uniform spatial solid distribution.

A Beer-Lambert law is used to model light attenuation through the reactor. It takes into account attenuation of the reactor walls, culture medium and cells shelf shading, as well as of local values of solid fraction.

A PSF biological model enables to predict biomass growth. Parameters of the biological model are fitted, so the predictions of the global model which considers hydrodynamics, light and biology agree with experimental results obtained in chapter 2. Results agree globally well and allow to reach a final dry weight close to the experimental one (0.375 $g.L^{-1}$ compared to 0.387 $g.L^{-1}$ experimentally).

The model is able to predict qualitatively the influence of changing incident light. It is shown that using increased incident light leads to higher biomass and photoinhibition hinders growth for high intensities, but it is required to confirm with more accurate parameters for the biological model (fitted on the whole range of light intensities).

The high influence of hydrodynamics on biomass growth is highlighted several times using the model.

Using stochastic model in this thesis (using encapsulated algae) is particularly interesting as it enables to consider heterogeneity of solids in the reactor (solid fraction higher in the ascending zone) which have an influence on light attenuation and thus on biomass growth.

Growth is calculated using two different incident lights: a fluctuating light calculated by the global model based on stochastic trajectories and a light considering no fluctuations. While both mean intensities are the same, results show a final dry weight difference of 10 %. This proves the high influence of L/D cycles on biomass growth according to the model.

The model is used to qualitatively evaluate the impact of liquid flow rate on the reactor performance (biomass growth). Using a higher liquid flow rate to fluidize the beads leads to significant faster growth and higher dry weights. It must be noticed that the model does not considered damages caused by shear stress on cells, but they are limited by encapsulation.

General Conclusion and Outlooks

Culture of encapsulated microalgae

The first goal of the present thesis was to increase the knowledge about culture of encapsulated microalgae. It shows that the studied strain of *Chlamydomonas reinhardtii* is able to grow encapsulated in beads of alginate. According to experiments in flasks, it nevertheless grows more slowly than free culture using studied encapsulation material and culture conditions. The growth rate is 0.15 day^{-1} for encapsulated algae while it is 0.19 day^{-1} for free algae if the lag phase, which is longer for encapsulated algae, is not considered. The considered strain is able to secrete extracellularly *Gaussia* luciferase which is a high-added value metabolite. It is shown that, even if the strain secrete luciferase while encapsulated, the encapsulation material is not adapted for diffusion of luciferase in the culture medium.

The culture of the encapsulated strain is then scaled-up in a 5 L liquid-solid fluidized bed. Two cultures are performed in the reactor. The culture growth is followed by spectrophotometry (measurement of optical density) after complete dissolution of beads. Cultures last for 17 and 19 days without cell leakage and growth occurs all this time. This shows that the encapsulation material is robust and the reactor is suitable for the culture of encapsulated algae as it provides sufficient mixing but low shear stress. Both cultures show close growth curves when normalized which suggests a good repeatability of experiments. Even if results must be carefully compared as conditions are not exactly the same, the growth during exponential phase is faster in the reactor (0.37 day^{-1} for culture 2 and 0.38 day^{-1} for culture 1) than in flasks (0.16 day^{-1}). Hence the innovative liquid-solid fluidized bed composed of an off-center liquid inlet and an internal panel is well adapted for the culture of encapsulated microalgae.

Encapsulation in alginate beads allows to immobilize and grow *Chlamydomonas reinhardtii*. As the culture medium was clear during an extended period, the separation, which is the goal of encapsulation, is effective. The encapsulation material and the reactor have thus proved to be efficient to cultivate this alga.

Some technical challenges remain on the culture of encapsulated algae and have been faced in this thesis. One of the most crucial is the large-scale production of beads. The production is time consuming even using a semi-automatic process as in this thesis. Some fully automatic and faster methods are used but they can lead to more fragile and non-reproducible beads. This is an issue which needs to be solve for large-scale culture of encapsulated algae.

The culture of encapsulated algae can possibly leads to more bacterial proliferation than free cultures as experienced in this thesis. Alginate (often used as an encapsulation material) may be used as carbon source and promote bacteria proliferation. Furthermore, as there is no competition in the culture medium, bacteria can probably more easily proliferate than in free cultures. Using a UV system to clear the culture medium was not sufficient in this thesis. Another challenge faced is to introduce beads in the reactor while maintaining sterile conditions. Pilot or large-scale reactors cannot be installed under a laminar flow hood. Beads cannot be transferred by pumping (risks of crushing) and need a valve large enough to pass. In this thesis, transfer is realized as clean as possible: ethanol disinfection of the reactor valve and of the tubing on the transfer bottle, but can lead to contaminations.

Optimization of the encapsulation material is still crucial. The CMI laboratory (University of Namur) who works on the ValoAlgue project is developing hybrid carriers using simultaneously inorganic (as silica) and organic materials (Desmet et al., 2014). This increases the material resistance but the diffusivity of the material must be kept sufficient for CO_2 and nutrient transfer. Regarding the diffusion

of the secreted product, the encapsulation material must be optimized depending on the application. As observed in this thesis, diffusion of large metabolites as proteins can be an issue. Once in the culture medium, metabolites must be recovered. The Chemical and Biochemical Process group of the University of Mons, working on the ValoAlgue project, developed a method to concentrate luciferase in the culture medium using an ultrafiltration cassette.

This thesis focuses on one strain of *Chlamydomonas reinhardtii* but the encapsulation material (alginate) was used for a large amount of strains: *S. capricomutum* (Faafeng et al., 1994), *Tetraselmis suecica* (Pane et al., 1998), *Chlorella vulgaris* (Lau et al., 1997), *Phaeodactylum tricornutum* (Hertzberg & Jensen, 1989)… Moreover, the studied photobioreactor can be used to cultivate any strain. Different strains are interesting to encapsulate, especially for the secretion of high added value metabolites as *Haematococcus pluvialis* (Tripathi et al., 2002) and *Haslea ostrearia* (Lebeau et al., 2002).

Photobioreactor characterization and modeling

The second aim of this thesis was to characterize and develop a global model of the photobioreactor, able to predict algae growth. The hydrodynamics of the reactor is first characterized. As an initial analysis, the liquid flow is first studied. This initial analysis highlights the unusual flow regime in the reactor: laminar and unsteady. A first CFD model is developed and compared to velocity fields measured experimentally by PIV on five planes distributed along the depth of the reactor. Agreement between CFD and PIV is considered satisfactory as a high experimental error is measured, due to the high influence of plane position on the flow and the difficulty of performing CFD simulations in the exact same planes as PIV.

Solid is then considered in the CFD model (chapter 0). This two-phase model is experimentally validated as well using a simple and innovative method of light attenuation. This method enables to measure solid fraction through the reactor depth. It shows an accumulation at the top of the internal panel and no solid in the top zone of the reactor. Solid distribution in the reactor height is well described by CFD compared to experiments. CFD allows to quantify the solid accumulation in the bottom of the reactor and the higher solid fraction in the ascending zone, in agreement with observations. Some discrepancies can be seen in the reactor width between CFD and experiments. These can be explained as liquid inflow is described by CFD as uniform (ideal) through the width of the reactor while it is experimentally more important on the reactor sides. These results enable to increase knowledge on liquid-solid reactors containing beads of density close to water (density difference of 19 $kg.m^{-3}$ at 18 °C). The high influence of the lift interaction force on the flow is highlighted. Solid globally follows the liquid flow but influences it as well near the reactor lateral walls. Moreover, the unusual geometry of the reactor makes it particularly interesting to characterize (liquid-solid fluidized bed reactors are often cylindrical column with uniform liquid injection at the bottom of the column).

Results obtained by CFD enables to develop a CFD-based compartment model (chapter 5), based on solid velocity flow fields. It enables to globally describe the solid flow while using significantly less computing time due to a coarser discretization of the photobioreactor geometry. A stochastic Lagrangian model, superimposed on the CFD-based compartment model, is used to calculate bead trajectories. The particles movement between compartments is random but based on probabilities derived from fluxes calculated by the compartment model. This model gives access to information on solid displacements in the reactor, as residence times in different regions of the reactor. It could be used to study the liquid phase as well, evaluating gradients of pH or nutrients. It would be useful if nutrient limitation is considered in the model.

Light intensity is calculated in each compartment of the reactor based on a light attenuation law similar to the Beer-Lambert law. Light attenuation and dry weight measured every day of the culture of

encapsulated algae (chapter 2) enables to calculate absorption coefficients of biomass, water and Plexiglass to be used in the attenuation law. A biological three-states model (Photosynthetic Factory) is used to predict biomass growth.

The global model gives a good description of growth when compared to experimental results. The model predicts a high influence of hydrodynamics on biomass growth. Indeed the model considers heterogeneity of solids in the reactor (solid fraction higher in the ascending zone) and it has an impact on biomass growth. Moreover, a qualitative study enables to show that the model estimates higher growth rates when using higher liquid flow rates to fluidize solid.

To develop this model, some assumptions and simplifications are made. Their validity should be evaluated and other operating conditions, which are not studied by lack of time, should be tested. Regarding hydrodynamics, only one value of the total solid fraction is used. The photobioreactor can indeed be used to cultivate higher solid fractions. Considering a fluidized bed reactor, studying different solid fractions and their impact on flow and ultimately biomass growth is of great interest, but was out of the scope of the present thesis. Indeed it is very time-consuming as a new CFD simulation is needed for each solid fraction. Besides, the bead density is potentially changing with biomass concentration and it is not considered in this thesis. As the dry weight is low (0.39 $g.L^{-1}$ maximum) and the liquid flow rate needed to fluidize beads does not need to be changed, this probably does not have a significant impact on hydrodynamics in this thesis. However, the evolution of bead density could have more influence and would need to be quantified with higher dry weight. It could be obtained using higher solid fraction or higher light intensity. Reaching higher dry weight is of commercial interest as it allows to obtain more biomass which would secrete more metabolites.

Improvements in modeling light attenuation are also achievable. For simplicity reasons, the Beer-Lambert law is used to model light attenuation. As described in chapter 1, more precise models have been developed to take into account scattering. It would be worthwhile to verify if these models can be used for encapsulated algae. Light attenuation through the bead bed can be improved as well. The attenuation in the bead is not considered, meaning no difference is made between cells in the center and at the bead sides. If microscopy shows algae live in the center of beads (Figure 2.13), they might grow slower as they receive less light. Moreover, the attenuation of the bead bed is considered globally, i.e. light variations due to changes in the number of beads between light and the studied bead are averaged. It would be valuable to quantify and model these variations. Besides, the model does not consider day and night cycles nor natural light. Some models have been developed to predict light input from daily and seasonally variations of sun which could be easily implemented in the model (Nauha & Alopaeus, 2015). Furthermore, photoacclimation (pigment content adaptation of cells according to the light intensity) is a challenge to model but can have an influence on light attenuation and biomass growth (Souliès, 2014). As developed in chapter 5, experiments under higher light intensities could be used to precisely study the impact on dry weight and photoinhibition with the model.

From a biological point of view, this thesis proves the PSF model can be used to model growth of encapsulated algae even if growth curves can differ. Nutrient limitation is not considered as it is not the main limiting parameter. Under higher light intensity or using higher solid fraction in the reactor, nutrients limitation could have more influence and should be modeled. This would imply to describe the CO_2 and nutrients transfer through the encapsulation material.

References

Abdel-Raouf, N., Al-Homaidan, A. A., & Ibraheem, I. B. M. (2012). Microalgae and wastewater treatment. *Saudi Journal of Biological Sciences*, *19*(3), 257–275. https://doi.org/10.1016/j.sjbs.2012.04.005

Acien Fernandez, F. G., Fernandez Sevilla, J. M., Sanchez Perez, J. A., Molina Grima, E., & Chisti, Y. (2001). Airlift-driven external-loop tubular photobioreactors for outdoor production of microalgae: assessment of design and performance. *Chemical Engineering Science*, *56*, 2721–2732. https://doi.org/https://doi.org/10.1016/S0009-2509(00)00521-2

Acién Fernández, F. G., García Camacho, F., Sánchez Pérez, J. A., Fernández Sevilla, J. M., & Molina Grima, E. (1997). A model for light distribution and average solar irradiance inside outdoor tubular photobioreactors for the microalgal mass culture. *Biotechnology and Bioengineering*, *55*(5), 701–714. https://doi.org/10.1002/(SICI)1097-0290(19970905)55:5<701::AID-BIT1>3.0.CO;2-F

Adam, M., Lentz, K. E., & Loppes, R. (1993). Insertional mutagenesis to isolate acetate-requiring mutants in Chlamydomonas reinhardtii. *FEMS Microbiology Letters*, *110*(3), 265–268. https://doi.org/10.1111/j.1574-6968.1993.tb06332.x

Alimohammadi, S., Fanning, E., Persoons, T., & Murray, D. B. (2016). Characterization of flow vectoring phenomenon in adjacent synthetic jets using CFD and PIV. *Computers and Fluids*, *140*, 232–246. https://doi.org/10.1016/j.compfluid.2016.09.022

Amin, S. A., Green, D. H., Hart, M. C., Kupper, F. C., Sunda, W. G., & Carrano, C. J. (2009). Photolysis of ion – siderophore chelates promotes bacteria – algal mutualism. *Environmental Sciences*, *106*, 2–7. https://doi.org/https://doi.org/10.1073/pnas.0905512106

Andrews, J. F. (1968). A Mathematical Model for the Continuous Culture of Microorganisms Utilizing Inhibitory Substrates. *Biotechnology and Bioengineering*, *10*(6), 707–723. https://doi.org/https://doi.org/10.1002/bit.260100602

Antoniou, P., Hamilton, J., Koopman, B., Jain, R., Holloway, B., Lyberatos, G., & Svoronos, S. A. (1990). Effect of temperature and pH on the effective maximum specific growth rate of nitrifying bacteria. *Water Research*, *24*(1), 97–101. https://doi.org/https://doi.org/10.1016/0043-1354(90)90070-M

Aslanbay Guler, B., Deniz, I., Demirel, Z., Oncel, S. S., & Imamoglu, E. (2020). Computational fluid dynamics modelling of stirred tank photobioreactor for Haematococcus pluvialis production: Hydrodynamics and mixing conditions. *Algal Research*, *47*. https://doi.org/10.1016/j.algal.2020.101854

Babel, S., & Takizawa, S. (2010). Microfiltration membrane fouling and cake behavior during algal filtration. *Desalination*, *261*(1–2), 46–51. https://doi.org/10.1016/j.desal.2010.05.038

Bagheri, G., & Bonadonna, C. (2016). On the drag of freely falling non-spherical particles. *Powder Technology*, *301*, 526–544. https://doi.org/10.1016/j.powtec.2016.06.015

Bahadar, A., & Bilal Khan, M. (2013). Progress in energy from microalgae: A review. *Renewable and Sustainable Energy Reviews*, *27*, 128–148. https://doi.org/10.1016/j.rser.2013.06.029

Bahadur, B., Manchikatla, V. R., Sahijram, L., & Krishnamurthy, K. v. (2015). *Plant Biology and Biotechnology Volume II: Plant Genomics and Biotechnology* (Vol. 2). https://doi.org/10.1007/978-81-322-2283-5

Barrera, D. J., & Mayfield, S. P. (2013). High-value Recombinant Protein Production in Microalgae. In *Handbook of Microalgal Culture: Applied Phycology and Biotechnology* (pp. 532–544).

Barros, A. I., Gonçalves, A. L., Simões, M., & Pires, J. C. M. (2015). Harvesting techniques applied to microalgae: A review. *Renewable and Sustainable Energy Reviews*, *41*, 1489–1500. https://doi.org/10.1016/j.rser.2014.09.037

Bashan, Y., Hernandez, J. P., Leyva, L. A., & Bacilio, M. (2002). Alginate microbeads as inoculant carriers for plant growth-promoting bacteria. *Biology and Fertility of Soils*, *35*(5), 359–368. https://doi.org/10.1007/s00374-002-0481-5

Bayat, Z., Hassanshahian, M., & Cappello, S. (2015). Immobilization of Microbes for Bioremediation of Crude Oil Polluted Environments: A Mini Review. *The Open Microbiology Journal*, *9*, 48–54.

Béchet, Q., Shilton, A., & Guieysse, B. (2013). Modeling the effects of light and temperature on algae growth: State of the art and critical assessment for productivity prediction during outdoor cultivation. *Biotechnology Advances*, *31*(8), 1648–1663. https://doi.org/10.1016/j.biotechadv.2013.08.014

Bello, M. M., Abdul Raman, A. A., & Purushothaman, M. (2017). Applications of fluidized bed reactors in wastewater treatment – A review of the major design and operational parameters. *Journal of Cleaner Production*, *141*, 1492–1514. https://doi.org/10.1016/j.jclepro.2016.09.148

Benson, E., Harding, K., Ryan, M., Petrenko, A., Petrenko, Y., & Fuller B. (2018). Alginate encapsulation to enhance biopreservation scope and success: a multidisciplinary review of current ideas and applications in cryopreservation and non-freezing storage. *CryoLetters*, *39*(1), 14–18. http://www.cryo.org.ua/ipk_eng/unesco.html

Benvenuti, G., Bosma, R., Ji, F., Lamers, P., Barbosa, M. J., & Wijffels, R. H. (2016). Batch and semi-continuous microalgal TAG production in lab-scale and outdoor photobioreactors. *Journal of Applied Phycology*, *28*(6), 3167–3177. https://doi.org/10.1007/s10811-016-0897-1

Bilanovic, D., Holland, M., Starosvetsky, J., & Armon, R. (2016). Co-cultivation of microalgae and nitrifiers for higher biomass production and better carbon capture. *Bioresource Technology*, *220*, 282–288. https://doi.org/10.1016/j.biortech.2016.08.083

Bitog, J. P., Lee, I. B., Lee, C. G., Kim, K. S., Hwang, H. S., Hong, S. W., Seo, I. H., Kwon, K. S., & Mostafa, E. (2011). Application of computational fluid dynamics for modeling and designing photobioreactors for microalgae production: A review. *Computers and Electronics in Agriculture*, *76*(2), 131–147. https://doi.org/10.1016/j.compag.2011.01.015

Blanken, W., Janssen, M., Cuaresma, M., Libor, Z., Bhaiji, T., & Wijffels, R. H. (2014). Biofilm Growth of Chlorella Sorokiniana in a Rotating Biological Contactor Based Photobioreactor. *Biotechnology and Bioengineering*, *111*, 2436–2445. https://doi.org/10.1002/bit.25301/abstract

Borowitzka, M. A. (2013). High-value products from microalgae-their development and commercialisation. *Journal of Applied Phycology*, *25*(3), 743–756. https://doi.org/10.1007/s10811-013-9983-9

Bouabidi, Z. B., El-Naas, M. H., & Zhang, Z. (2019). Immobilization of microbial cells for the biotreatment of wastewater: A review. *Environmental Chemistry Letters*, *17*(1), 241–257. https://doi.org/10.1007/s10311-018-0795-7

Brandenberger, H., & Widmer, F. (1998). A new multinozzle encapsulation/immobilisation system to produce uniform beads of alginate. *Journal of Biotechnology*, *63*, 73–80. https://doi.org/https://doi.org/10.1016/S0168-1656(98)00077-7

Bravo-Fritz, C. P., Sáez-Navarrete, C. A., Herrera-Zeppelin, L. A., & Varas-Concha, F. (2016). Multi-scenario energy-economic evaluation for a biorefinery based on microalgae biomass with application of anaerobic digestion. *Algal Research*, *16*, 292–307. https://doi.org/10.1016/j.algal.2016.03.028

Brouers, M., & Hall, D. 0. (1986). Ammonia and hydrogen production by immobilized cyanobacteria. *Journal of Biotechnology*, *3*, 307–321. https://doi.org/https://doi.org/10.1016/0168-1656(86)90012-X

Brunone, B., Ferrante, M., & Cacciamani, M. (2004). Decay of pressure and energy dissipation in laminar transient flow. *Journal of Fluids Engineering, Transactions of the ASME*, *126*(6), 928–934. https://doi.org/10.1115/1.1839926

Cardon, Z. G., Gray, D. W., & Lewis, L. A. (2008). The Green Algal Underground: Evolutionary Secrets of Desert Cells. *BioScience*, *58*, 114–122. https://doi.org/10.1641/B580206

Carletti, C., Montante, G., Westerlund, T., & Paglianti, A. (2014). Analysis of solid concentration distribution in dense solid – liquid stirred tanks by electrical resistance tomography. *Chemical Engineering Science*, *119*, 53–64. https://doi.org/10.1016/j.ces.2014.07.049

Cheirsilp, B., Thawechai, T., & Prasertsan, P. (2017). Immobilized oleaginous microalgae for production of lipid and phytoremediation of secondary effluent from palm oil mill in fluidized bed photobioreactor. *Bioresource Technology*, *241*, 787–794. https://doi.org/10.1016/j.biortech.2017.06.016

Chen, F., & Johns, M. R. (1996). Heterotrophic Growth of Chlamydomonas reinhardtii on Acetate in Chemostat Culture. *Process Biochemistry*, *31*(6), 601–604. https://doi.org/https://doi.org/10.1016/S0032-9592(96)00006-4

Chen, Y.-C. (2001). Immobilized microalga Scenedesmus quadricauda (Chlorophyta, Chlorococcales) for long-term storage and for application for water quality control in fish culture. *Aquaculture*, *195*, 71–80. https://doi.org/https://doi.org/10.1016/S0044-8486(00)00540-8

Chevalier, P., & de la Noüe, J. (1988). Behavior of algae and bacteria co-immobilized in carrageenan, in a fluidized bed. *Enzyme and Microbial Technology*, *10*(1), 19–23. https://doi.org/10.1016/0141-0229(88)90093-2

Chisti, Y. (2013). Raceways-based production of algal crude oil. *Green*, *3*(3–4), 195–216. https://doi.org/10.1515/green-2013-0018

Choix, F. J., de-Bashan, L. E., & Bashan, Y. (2012). Enhanced accumulation of starch and total carbohydrates in alginate-immobilized Chlorella spp. induced by Azospirillum brasilense: II. Heterotrophic conditions. *Enzyme and Microbial Technology*, *51*(5), 300–309. https://doi.org/10.1016/j.enzmictec.2012.07.012

Chowdury, K. H., Nahar, N., & Deb, U. K. (2020). The Growth Factors Involved in Microalgae Cultivation for Biofuel Production: A Review. *Computational Water, Energy, and Environmental Engineering*, *09*(04), 185–215. https://doi.org/10.4236/cweee.2020.94012

Cinar, S. O., Chong, Z. K., Kucuker, M. A., Wieczorek, N., Cengiz, U., & Kuchta, K. (2020). Bioplastic production from microalgae: A review. *International Journal of Environmental Research and Public Health*, *17*(11). https://doi.org/10.3390/ijerph17113842

Cole, J. J. (1982). Interactions between bacteria and algae in aquatic ecosystems. *Annual Review of Ecology and Systematics*, *13*, 291–314. https://doi.org/https://doi.org/10.1146/annurev.es.13.110182.001451

Cornelissen, J. T., Taghipour, F., Escudié, R., Ellis, N., & Grace, J. R. (2007). CFD modelling of a liquid-solid fluidized bed. *Chemical Engineering Science*, *62*(22), 6334–6348. https://doi.org/10.1016/j.ces.2007.07.014

Cornet, J.-F., Dussap, C. G., Gros, J.-B., Binois, C., & Lasseur, C. (1995). A simplified monodimensional approach for modeling coupling between radient light transfer and growth kinetics in photobioreactors. *Chemical Engineering Science*, *50*(9), 1489–1500.

Corona, A. A. (2008). *Agitation des particules dans un lit fluidisé liquide. Etude expérimentale* [Université de Toulouse]. https://oatao.univ-toulouse.fr/6931/1/aguilar_corona.pdf

Costa, S. A., Azevedo, H. S., & Reis, R. L. (2005). Enzyme Immobilization in Biodegradable Polymers for Biomedical Applications. In *Biodegradable Systems in Tissue Engineering and Regenerative Medicine* (pp. 301–323).

Costerton, J. W., Lewandowski, Z., Caldwell, D. E., Korber, D. R., & Lappin-Scott, H. M. (1995). Microbial Biofilms. *Annual Review of Microbiology*, *49*, 711–745. https://doi.org/10.1146/annurev.mi.49.100195.003431

Danquah, M. K., Ang, L., Uduman, N., Moheimani, N., & Forde, G. M. (2009). Dewatering of microalgal culture for biodiesel production: Exploring polymer flocculation and tangential flow filtration. *Journal of Chemical Technology and Biotechnology*, *84*(7), 1078–1083. https://doi.org/10.1002/jctb.2137

Davarnejad, R., Eshghipour, R., Abdi, J., & Dehkordi, F. B. (2014). CFD modeling of a binary liquid-solid fluidized bed. *Middle - East Journal of Scientific Research*, *19*(10), 1272–1279. https://doi.org/10.5829/idosi.mejsr.2014.19.10.89

de Grahl, I., Rout, S. S., Maple-Grødem, J., & Reumann, S. (2020). Development of a constitutive and an auto-inducible high-yield expression system for recombinant protein production in the microalga Nannochloropsis oceanica. *Applied Microbiology and Biotechnology*, *104*(20), 8747–8760. https://doi.org/10.1007/s00253-020-10789-4

de Lamotte, A., Delafosse, A., Calvo, S., & Toye, D. (2018). Identifying dominant spatial and time characteristics of flow dynamics within free-surface baffled stirred-tanks from CFD simulations. *Chemical Engineering Science*, *192*(1999), 128–142. https://doi.org/10.1016/j.ces.2018.07.024

de-Bashan, L. E., & Bashan, Y. (2010). Immobilized microalgae for removing pollutants: Review of practical aspects. *Bioresource Technology*, *101*(6), 1611–1627. https://doi.org/10.1016/j.biortech.2009.09.043

Degen, J., Uebele, A., Retze, A., Schmid-Staiger, U., & Trösch, W. (2001). A novel airlift photobioreactor with baffles for improved light utilization through the flashing light effect. *Journal of Biotechnology*, *92*, 89–94. https://doi.org/https://doi.org/10.1016/S0168-1656(01)00350-9

Delafosse, A., Collignon, M. L., Calvo, S., Delvigne, F., Crine, M., Thonart, P., & Toye, D. (2014). CFD-based compartment model for description of mixing in bioreactors. *Chemical Engineering Science*, *106*, 76–85. https://doi.org/10.1016/j.ces.2013.11.033

Delafosse, A., Loubière, C., Calvo, S., Toye, D., & Olmos, E. (2018). Solid-liquid suspension of microcarriers in stirred tank bioreactor – Experimental and numerical analysis. *Chemical Engineering Science*, *180*, 52–63. https://doi.org/10.1016/j.ces.2018.01.001

Desmet, J., Meunier, C., Danloy, E., Duprez, M. E., Lox, F., Thomas, D., Hantson, A. L., Crine, M., Toye, D., Rooke, J., & Su, B. L. (2015). Highly efficient, long life, reusable and robust

photosynthetic hybrid core-shell beads for the sustainable production of high value compounds. *Journal of Colloid and Interface Science*, *448*, 79–87. https://doi.org/10.1016/j.jcis.2015.01.091

Desmet, J., Meunier, C. F., Danloy, E. P., Duprez, M. E., Hantson, A. L., Thomas, D., Cambier, P., Rooke, J. C., & Su, B. L. (2014). Green and sustainable production of high value compounds via a microalgae encapsulation technology that relies on CO2 as a principle reactant. *Journal of Materials Chemistry A*, *2*(48), 20560–20569. https://doi.org/10.1039/c4ta04659e

Dineshkumar, R., Kumaravel, R., Gopalsamy, J., Sikder, M. N. A., & Sampathkumar, P. (2018). Microalgae as Bio-fertilizers for Rice Growth and Seed Yield Productivity. *Waste and Biomass Valorization*, *9*(5), 793–800. https://doi.org/10.1007/s12649-017-9873-5

Ding, J., & Gidaspow, D. (1990). A bubbling fluidization model using kinetic theory of granular flow. *AIChE Journal*, *36*(4), 523–538. https://doi.org/10.1002/aic.690360404

Dreher, S., Kockmann, N., & Woias, P. (2009). Characterization of laminar transient flow regimes and mixing in t-shaped micromixers. *Heat Transfer Engineering*, *30*(1–2), 91–100. https://doi.org/10.1080/01457630802293480

Dudukovic, M. P. (2000). Opaque Multiphase Reactors: Experimentation, Modeling and Troubleshooting. *Oil & Gas Science and Technology*, *55*, 135–158. https://doi.org/10.2516/ogst

Eilers, P. H. C., & Peeters, J. C. H. (1988). A model for the relationship between light intensity and the rate of photosynthesis in phytoplankton. *Ecological Modelling*, *42*(3–4), 199–215. https://doi.org/10.1016/0304-3800(88)90057-9

Ergun, S. (1952). Fluid flow through packed columns. *Chemical Engineering Progress*, *48*, 89–94.

Ermilova, E. V., Zalutskaya, Z. M., Lapina, T. V., & Nikitin, M. M. (2003). Chemotactic behavior of Chlamydomonas reinhardtii is altered during gametogenesis. *Current Microbiology*, *46*(4), 261–264. https://doi.org/10.1007/s00284-002-3872-9

European Algae Biomass Association. (2021). *What are Algae?* https://www.what-are-algae.com/

Faafeng, B. A., van Donk, E., & Källqvist, S. T. (1994). In situ measurement of algal growth potential in aquatic ecosystems by immobilized algae. *Journal of Applied Phycology*, *6*(3), 301–308. https://doi.org/10.1007/BF02181943

Fasaei, F., Bitter, J. H., Slegers, P. M., & van Boxtel, A. J. B. (2018). Techno-economic evaluation of microalgae harvesting and dewatering systems. *Algal Research*, *31*, 347–362. https://doi.org/10.1016/j.algal.2017.11.038

Ferchichi, Y. (2013). *Étude expérimentale du mouvement d'une particule sphérique à l'approche d'une interface liquide/fluide*. https://tel.archives-ouvertes.fr/tel-01001954v1

Ferreira, L. S., Rodrigues, M. S., Converti, A., Sato, S., & Carvalho, J. C. M. (2010). A new approach to ammonium sulphate feeding for fed-batch Arthrospira (Spirulina) platensis cultivation in tubular photobioreactor. *Biotechnology Progress*, *26*(5), 1271–1277. https://doi.org/10.1002/btpr.457

Ferro, Y., Perullini, M., Jobbagy, M., Bilmes, S. A., & Durrieu, C. (2012). Development of a biosensor for environmental monitoring based on microalgae immobilized in silica hydrogels. *Sensors*, *12*, 16879–16891. https://doi.org/10.3390/s121216879

Foster, R. A., Kuypers, M. M. M., Vagner, T., Paerl, R. W., Musat, N., & Zehr, J. P. (2011). Nitrogen fixation and transfer in open ocean diatom-cyanobacterial symbioses. *ISME Journal*, *5*(9), 1484–1493. https://doi.org/10.1038/ismej.2011.26

Fouchard, S., Pruvost, J., Degrenne, B., Titica, M., & Legrand, J. (2009). Kinetic modeling of light limitation and sulfur deprivation effects in the induction of hydrogen production with Chlamydomonas reinhardtii: Part I. model development and parameter identification. *Biotechnology and Bioengineering*, *102*(1), 232–245. https://doi.org/10.1002/bit.22034

Fulbright, S. P., Robbins-Pianka, A., Berg-Lyons, D., Knight, R., Reardon, K. F., & Chisholm, S. T. (2018). Bacterial community changes in an industrial algae production system. *Algal Research*, *31*, 147–156. https://doi.org/10.1016/j.algal.2017.09.010

Gallaher, S. D., Fitz-Gibbon, S. T., Glaesener, A. G., Pellegrini, M., & Merchanta, S. S. (2015). Chlamydomonas genome resource for laboratory strains reveals a mosaic of sequence variation, identifies true strain histories, and enables strain-specific studies. *Plant Cell*, *27*(9), 2335–2352. https://doi.org/10.1105/tpc.15.00508

Gao, S., Yang, J., Tian, J., Ma, F., Tu, G., & Du, M. (2010). Electro-coagulation-flotation process for algae removal. *Journal of Hazardous Materials*, *177*(1–3), 336–343. https://doi.org/10.1016/j.jhazmat.2009.12.037

Gao, X., Kong, B., & Vigil, R. D. (2018). Simulation of algal photobioreactors: recent developments and challenges. *Biotechnology Letters*, *40*(9–10), 1311–1327. https://doi.org/10.1007/s10529-018-2595-3

Garcia-Gonzalez, J., & Sommerfeld, M. (2016). Biofertilizer and biostimulant properties of the microalga Acutodesmus dimorphus. *Journal of Applied Phycology*, *28*(2), 1051–1061. https://doi.org/10.1007/s10811-015-0625-2

Garg, S., Wang, L., & Schenk, P. M. (2015). Flotation separation of marine microalgae from aqueous medium. *Separation and Purification Technology*, *156*, 636–641. https://doi.org/10.1016/j.seppur.2015.10.059

Gernigon, V., Chekroun, M. A., Cockx, A., Guiraud, P., & Morchain, J. (2019). How Mixing and Light Heterogeneity Impact the Overall Growth Rate in Photobioreactors. *Chemical Engineering and Technology*, *42*(8), 1663–1669. https://doi.org/10.1002/ceat.201900102

Ghatage, S. V., Peng, Z., Sathe, M. J., Doroodchi, E., Padhiyar, N., Moghtaderi, B., Joshi, J. B., & Evans, G. M. (2014). Stability analysis in solid-liquid fluidized beds: Experimental and computational. *Chemical Engineering Journal*, *256*, 169–186. https://doi.org/10.1016/j.cej.2014.06.026

Gidaspow, D., Bezburuah, R., & Ding, J. (1992). Hydrodynamics of circulating fluidized beds: Kinetic theory approach. *7th Fluidization Conference*.

Gimpel, J. A., Hyun, J. S., Schoepp, N. G., & Mayfield, S. P. (2015). Production of Recombinant Proteins in Microalgae at Pilot Greenhouse Scale. *Biotechnology and Bioengineering*, *112*, 339–345. https://doi.org/10.1002/bit.25357/abstract

Gong, Y., Hu, H., Gao, Y., Xu, X., & Gao, H. (2011). Microalgae as platforms for production of recombinant proteins and valuable compounds: Progress and prospects. *Journal of Industrial Microbiology and Biotechnology*, *38*(12), 1879–1890. https://doi.org/10.1007/s10295-011-1032-6

Gonzalez, L. E., & Bashan, Y. (2000). Increased Growth of the Microalga Chlorella vulgaris when Coimmobilized and Cocultured in Alginate Beads with the Plant-Growth-Promoting Bacterium Azospirillum brasilense. *Applied and Environmental Microbiology*, *66*(4), 1527–1531. https://doi.org/10.1128/aem.66.4.1527-1531.2000

Granados, M. R., Acién, F. G., Gómez, C., Fernández-Sevilla, J. M., & Molina Grima, E. (2012). Evaluation of flocculants for the recovery of freshwater microalgae. *Bioresource Technology*, *118*, 102–110. https://doi.org/10.1016/j.biortech.2012.05.018

Guha, D., Ramachandran, P. A., & Dudukovic, M. P. (2007). *Flow field of suspended solids in a stirred tank reactor by Lagrangian tracking*. *62*, 6143–6154. https://doi.org/10.1016/j.ces.2007.06.033

Halim, R., Danquah, M. K., & Webley, P. A. (2012). Extraction of oil from microalgae for biodiesel production: A review. *Biotechnology Advances*, *30*(3), 709–732. https://doi.org/10.1016/j.biotechadv.2012.01.001

Hameed, M. S. A., & Ebrahim, O. H. (2007). Biotechnological Potential Uses of Immobilized Algae. *International Journal of Agriculture & Biology*, *9*, 183–192. http://www.fspublishers.org

Hanks, R. W., & Ruo, H. (1966). Laminar-Turbulent Transition in Ducts of Rectangular cross Section. *Industrial & Engineering Chemistry Fundamentals*, *5*(6), 558–561. https://doi.org/https://doi.org/10.1021/i160020a022

Harris, E. H., Stern, D., & Witman, G. (2009). *The Chlamydomonas Sourcebook Second Edition: Introduction to Chlamydomonas and its laboratory uses* (Vol. 1).

Hatanaka, Y., Kudo, T., Miyataka, M., Kobayashi, O., Higashihara, M., & Hiyama, K. (1999). Asymmetric reduction of hydroxyacetone to propanediol in immobilized halotolerant microalga Dunaliella parva. *Journal of Bioscience and Bioengineering*, *88*(3), 281–286. https://doi.org/10.1016/S1389-1723(00)80010-9

Hertzberg, S., & Jensen, A. (1989). Studies of Alginate-immobilized Marine Microalgae. *Botanica Marina*, *32*(4), 267–274. https://doi.org/10.1515/botm.1989.32.4.267

Homburg, S. V., Kruse, O., & Patel, A. v. (2019). Growth and photosynthetic activity of Chlamydomonas reinhardtii entrapped in lens-shaped silica hydrogels. *Journal of Biotechnology*, *302*, 58–66. https://doi.org/10.1016/j.jbiotec.2019.06.009

Homburg, S. V., Venkanna, D., Kraushaar, K., Kruse, O., Kroke, E., & Patel, A. v. (2019). Entrapment and growth of Chlamydomonas reinhardtii in biocompatible silica hydrogels. *Colloids and Surfaces B: Biointerfaces*, *173*, 233–241. https://doi.org/10.1016/j.colsurfb.2018.09.075

Hosseini, S., Patel, D., Ein-Mozaffari, F., & Mehrvar, M. (2010). Study of solid – liquid mixing in agitated tanks through electrical resistance tomography. *Chemical Engineering Science*, *65*(4), 1374–1384. https://doi.org/10.1016/j.ces.2009.10.007

Huang, Q., Yang, C., Yu, G., & Mao, Z. S. (2010). CFD simulation of hydrodynamics and mass transfer in an internal airlift loop reactor using a steady two-fluid model. *Chemical Engineering Science*, *65*(20), 5527–5536. https://doi.org/10.1016/j.ces.2010.07.021

Hyde, F. W., Hunt, G. R., & Errede, L. A. (1991). Immobilization of Bacteria and Saccharomyces cerevisiae in Poly(Tetrafluoroethylene) Membranes. *Applied and Environmental Microbiology*, *57*, 219–222.

Janssen, M., Janssen, M., de Winter, M., Tramper, J., Mur, L. R., Snel, J., & Wijffels, R. H. (2000). Efficiency of light utilization of Chlamydomonas reinhardtii under medium-duration light/dark cycles. *Journal of Biotechnology*, *78*, 123–137. https://doi.org/10.1016/s0168-1656(99)00233-3

Janssen, M., Tramper, J., Mur, L. R., & Wijffels, R. H. (2003). Enclosed outdoor photobioreactors: Light regime, photosynthetic efficiency, scale-up, and future prospects. *Biotechnology and Bioengineering*, *81*(2), 193–210. https://doi.org/10.1002/bit.10468

Jaycor, A. V. (1985). *Review and evaluation of immobilized algae systems for the production of fuels from microalgae*.

John, D. M., & Whitton, B. A. (2011). *The Freshwater Algal Flora of the British Isles. An Identification Guide to Freshwater and Terrestrial Algae Using aquatic plants to monitor water quality View project An Identification Guide to the Marine Plants of the United Arab Emirates View project*. http://protist.i.hosei.jp/index.

Kalaga, D. V., Reddy, R. K., Joshi, J. B., Dalvi, S. V., & Nandkumar, K. (2012). Liquid phase axial mixing in solid-liquid circulating multistage fluidized bed: CFD modeling and RTD measurements. *Chemical Engineering Journal*, *191*, 475–490. https://doi.org/10.1016/j.cej.2012.02.091

Kang, Z., Kim, B. H., Ramanan, R., Choi, J. E., Yang, J. W., Oh, H. M., & Kim, H. S. (2015). A cost analysis of microalgal biomass and biodiesel production in open raceways treating municipal wastewater and under optimum light wavelength. *Journal of Microbiology and Biotechnology*, *25*(1), 109–118. https://doi.org/10.4014/jmb.1409.09019

Karsten, U., Schumann, R., & Mostaert, A. (2007). Aeroterrestrial algae growing on man-made surfaces: What are the Secrets of their Ecological Success? In *Cellular Origin, Life in Extreme Habitats and Astrobiology - Algae and cyanobacteria in extreme environments* (pp. 585–599).

Katarzyna, L., Sai, G., & Avijeet Singh, O. (2015). Non-enclosure methods for non-suspended microalgae cultivation: Literature review and research needs. *Renewable and Sustainable Energy Reviews*, *42*, 1418–1427. https://doi.org/10.1016/j.rser.2014.11.029

Kazamia, E., Aldridge, D. C., & Smith, A. G. (2012). Synthetic ecology - A way forward for sustainable algal biofuel production? *Journal of Biotechnology*, *162*(1), 163–169. https://doi.org/10.1016/j.jbiotec.2012.03.022

Kazbar, A., Cogne, G., Urbain, B., Marec, H., Le-Gouic, B., Tallec, J., Takache, H., Ismail, A., & Pruvost, J. (2019). Effect of dissolved oxygen concentration on microalgal culture in photobioreactors. *Algal Research*, *39*, 101432. https://doi.org/10.1016/j.algal.2019.101432

Khetkorn, W., Rastogi, R. P., Incharoensakdi, A., Lindblad, P., Madamwar, D., Pandey, A., & Larroche, C. (2017). Microalgal hydrogen production – A review. *Bioresource Technology*, *243*, 1194–1206. https://doi.org/10.1016/j.biortech.2017.07.085

Kim, Z. H., Park, H., Hong, S. J., Lim, S. M., & Lee, C. G. (2016). Development of a floating photobioreactor with internal partitions for efficient utilization of ocean wave into improved mass transfer and algal culture mixing. *Bioprocess and Biosystems Engineering*, *39*(5), 713–723. https://doi.org/10.1007/s00449-016-1552-6

Kitcha, S., & Cheirsilp, B. (2014). Enhanced lipid production by co-cultivation and co-encapsulation of oleaginous yeast Trichosporonoides spathulata with microalgae in alginate gel beads. *Applied Biochemistry and Biotechnology*, *173*(2), 522–534. https://doi.org/10.1007/s12010-014-0859-5

Klinthong, W., Yang, Y. H., Huang, C. H., & Tan, C. S. (2015). A Review: Microalgae and their applications in CO2 capture and renewable energy. *Aerosol and Air Quality Research*, *15*(2), 712–742. https://doi.org/10.4209/aaqr.2014.11.0299

Koerich, D. M., Lopes, G. C., & Rosa, L. M. (2018). Investigation of phases interactions and modification of drag models for liquid-solid fluidized bed tapered bioreactors. *Powder Technology*, *339*, 90–101. https://doi.org/10.1016/j.powtec.2018.07.102

Kumar, S. V., Misquitta, R. W., Reddy, V. S., Rao, B. J., & Rajam, M. V. (2004). Genetic transformation of the green alga - Chlamydomonas reinhardtii by Agrobacterium tumefaciens. *Plant Science*, *166*(3), 731–738. https://doi.org/10.1016/j.plantsci.2003.11.012

Lam, M. K., & Lee, K. T. (2012). Immobilization as a feasible method to simplify the separation of microalgae from water for biodiesel production. *Chemical Engineering Journal*, *191*, 263–268. https://doi.org/10.1016/j.cej.2012.03.013

Lamberto, D. J., Alvarez, M. M., & Muzzio, F. J. (1999). Experimental and computational investigation of the laminar flow structure in a stirred tank. *Chemical Engineering Science*, *54*(7), 919–942. https://doi.org/10.1016/S0009-2509(98)00275-9

Lau, P. S., Tam, N. F. Y., & Wong, Y. S. (1997). Wastewater nutrients (N and P) removal by carrageenan and alginate immobilized chlorella vulgaris. *Environmental Technology*, *18*(9), 945–951. https://doi.org/10.1080/09593331808616614

Lauersen, K. J., Berger, H., Mussgnug, J. H., & Kruse, O. (2013). Efficient recombinant protein production and secretion from nuclear transgenes in Chlamydomonas reinhardtii. *Journal of Biotechnology*, *167*(2), 101–110. https://doi.org/10.1016/j.jbiotec.2012.10.010

Lauersen, K. J., Vanderveer, T. L., Berger, H., Kaluza, I., Mussgnug, J. H., Walker, V. K., & Kruse, O. (2013). Ice recrystallization inhibition mediated by a nuclear-expressed and -secreted recombinant ice-binding protein in the microalga Chlamydomonas reinhardtii. *Applied Microbiology and Biotechnology*, *97*(22), 9763–9772. https://doi.org/10.1007/s00253-013-5226-x

Lebeau, T., Gaudin, P., Moan, R., & Robert, J. M. (2002). A new photobioreactor for continuous marennin production with a marine diatom: Influence of the light intensity and the immobilised-cell matrix (alginate beads or agar layer). *Applied Microbiology and Biotechnology*, *59*(2–3), 153–159. https://doi.org/10.1007/s00253-002-0993-9

Lebeau, T., & Robert, J.-M. (2006). *Biotechnology of Immobilized Micro algae : a Culture Technique for the Future ?*

Lee, A. K., Lewis, D. M., & Ashman, P. J. (2009). Microbial flocculation, a potentially low-cost harvesting technique for marine microalgae for the production of biodiesel. *Journal of Applied Phycology*, *21*(5), 559–567. https://doi.org/10.1007/s10811-008-9391-8

Legrand, J. (2016). *Advances in Chemical Engineering. Photobioreaction Engineering* (1st Edition, Vol. 48).

Lengke, M. F., Fleet, M. E., & Southam, G. (2006). Morphology of gold nanoparticles synthesized by filamentous cyanobacteria from gold(I)-Thiosulfate and gold(III)-chloride complexes. *Langmuir*, *22*(6), 2780–2787. https://doi.org/10.1021/la052652c

León, R., & Galván, F. (1994). Halotolerance studies on Chlamydomonas reinhardtii: glycerol excretion by free and immobilized cells. *Journal of Applied Phycology*, *6*(1), 13–20. https://doi.org/10.1007/BF02185898

Liang, H., Gong, W., Chen, J., & Li, G. (2008). Cleaning of fouled ultrafiltration (UF) membrane by algae during reservoir water treatment. *Desalination*, *220*(1–3), 267–272. https://doi.org/10.1016/j.desal.2007.01.033

Liao, Q., Li, L., Chen, R., & Zhu, X. (2014). A novel photobioreactor generating the light/dark cycle to improve microalgae cultivation. *Bioresource Technology*, *161*, 186–191. https://doi.org/10.1016/j.biortech.2014.02.119

Lima, S., Schulze, P. S. C., Schüler, L. M., Rautenberger, R., Morales-Sánchez, D., Santos, T. F., Pereira, H., Varela, J. C. S., Scargiali, F., Wijffels, R. H., & Kiron, V. (2021). Flashing light emitting diodes (LEDs) induce proteins, polyunsaturated fatty acids and pigments in three microalgae. *Journal of Biotechnology*, *325*, 15–24. https://doi.org/10.1016/j.jbiotec.2020.11.019

Luo, H. P., & Al-Dahhan, M. H. (2004). Analyzing and Modeling of Photobioreactors by Combining First Principles of Physiology and Hydrodynamics. *Biotechnology and Bioengineering*, *85*(4), 382–393. https://doi.org/10.1002/bit.10831

Maestri, M., Salierno, G., Piovano, S., Cassanello, M., Cardona, M. A., Hojman, D., & Somacal, H. (2019). CFD-DEM modeling of solid motion in a water-calcium alginate fluidized column and its comparison with results from radioactive particle tracking. *Chemical Engineering Journal*, *377*, 120339. https://doi.org/10.1016/j.cej.2018.11.037

Malhotra, S., & Sharma, M. M. (2014). Experimental measurement of settling velocity of spherical particles in unconfined and confined surfactant-based shear thinning viscoelastic fluids. *Journal of Visualized Experiments*, *83*, 1–10. https://doi.org/10.3791/50749

Mallick, N. (2002). Biotechnological potential of immobilized algae for wastewater N, P and metal removal: A review. *BioMetals*, *15*(4), 377–390. https://doi.org/10.1023/A:1020238520948

Malone, K. F., Xu, B. H., & Fairweather, M. (2006). The Combined-Continuum-and-Discrete-Model (CCDM) for simulation of liquid-particle flows. *Computer Aided Chemical Engineering*, *21*, 227–232. https://doi.org/https://doi.org/10.1016/S1570-7946(06)80051-9

Mata, T. M., Martins, A. A., & Caetano, N. S. (2010). Microalgae for biodiesel production and other applications: A review. *Renewable and Sustainable Energy Reviews*, *14*(1), 217–232. https://doi.org/10.1016/j.rser.2009.07.020

Mata, T. M., Mendes, A. M., Caetano, N. S., & Martins, A. A. (2014). Sustainability and economic evaluation of microalgae grown in brewery wastewater. *Bioresource Technology*, *168*, 151–158. https://doi.org/10.1016/j.biortech.2014.04.091

Matthijs, H. C. P., Balke, H., van Hes, U. M., Kroon, B. M. A., Mur, L. R., & Binot, R. A. (1996). Application of light-emitting diodes in bioreactors: Flashing light effects and energy economy in algal culture (Chlorella pyrenoidosa). *Biotechnology and Bioengineering*, *50*(1), 98–107. https://doi.org/10.1002/(SICI)1097-0290(19960405)50:1<98::AID-BIT11>3.0.CO;2-3

Mayali, X., & Azam, F. (2004). Algicidal bacteria in the sea and their impact on algal blooms. *Journal of Eukaryotic Microbiology*, *51*(2), 139–144. https://doi.org/10.1111/j.1550-7408.2004.tb00538.x

Mendoza, J. L., Granados, M. R., de Godos, I., Acién, F. G., Molina, E., Heaven, S., & Banks, C. J. (2013). Oxygen transfer and evolution in microalgal culture in open raceways. *Bioresource Technology*, *137*, 188–195. https://doi.org/10.1016/j.biortech.2013.03.127

Merchant, S. S., Prochnik, S. E., Vallon, O., Harris, E. H., Karpowicz, S. J., Witman, G. B., Terry, A., Salamov, A., Fritz-Laylin, L. K., Maréchal-Drouard, L., Marshall, W. F., Qu, L. H., Nelson, D. R., Sanderfoot, A. A., Spalding, M. H., Kapitonov, V. v., Ren, Q., Ferris, P., Lindquist, E., … Zhou, K. (2007). The Chlamydomonas genome reveals the evolution of key animal and plant functions. *Science*, *318*(5848), 245–251. https://doi.org/10.1126/science.1143609

Metting, F. B. (1996). Biodiversity and application of microalgae. *Journal of Industrial Microbiology*, *17*, 477–489. https://doi.org/https://doi.org/10.1007/BF01574779

Micheletti, M., & Yianneskis, M. (2004). Study of fluid velocity characteristics in stirred solid – liquid suspensions with a refractive index matching technique. *Proceedings of the Institution of*

Mechanical Engineers. Part E, Journal of Process Mechanical Engineering, *218*, 191–204. https://doi.org/https://doi.org/10.1243/0954408042466945

Milledge, J. J. (2011). Commercial application of microalgae other than as biofuels: A brief review. *Reviews in Environmental Science and Biotechnology*, *10*(1), 31–41. https://doi.org/10.1007/s11157-010-9214-7

Miyamoto, K., Wable, O., & Benemann, J. R. (1988). Vertical Tubular Reactor for Microalgae Cultivation. *Biotechnology Letters*, *10*, 703–708.

Moe, S. T., Draget, K. I., Skjak-Braek, G., & Smidsrod, O. (1992). Temperature dependence of the elastic modulus of alginate gels. *Carbohydrate Polymers*, *19*, 279–284. https://doi.org/https://doi.org/10.1016/0144-8617(92)90081-Z

Molina, E., Fernández, J., Acién, F. G., & Chisti, Y. (2001). Tubular photobioreactor design for algal cultures. *Journal of Biotechnology*, *92*(2), 113–131. https://doi.org/10.1016/S0168-1656(01)00353-4

Molina Grima, E., Acién Fernández, F. G., García Camacho, F., & Chisti, Y. (1999). Photobioreactors: light regime, mass transfer, and scaleup. *Progress in Industrial Microbiology*, *35*(C), 231–247. https://doi.org/10.1016/S0079-6352(99)80118-0

Monod, J. (1949). The growth of Bacterial Cultures. *Annual Review of Microbiology*, *3*, 371–394. https://doi.org/https://doi.org/10.1146/annurev.mi.03.100149.002103

Montante, G., Paglianti, A., & Magelli, F. (2012). Analysis of dilute solid-liquid suspensions in turbulent stirred tanks. *Chemical Engineering Research and Design*, *90*(10), 1448–1456. https://doi.org/10.1016/j.cherd.2012.01.009

Moreno-Garrido, I. (2008). Microalgae immobilization: Current techniques and uses. *Bioresource Technology*, *99*(10), 3949–3964. https://doi.org/10.1016/j.biortech.2007.05.040

Muñoz, R., Köllner, C., Guieysse, B., & Mattiasson, B. (2004). Photosynthetically oxygenated salicylate biodegradation in a continuous stirred tank photobioreactor. *Biotechnology and Bioengineering*, *87*(6), 797–803. https://doi.org/10.1002/bit.20204

Murphy, T. E., & Berberoğlu, H. (2011). Effect of algae pigmentation on photobioreactor productivity and scale-up: A light transfer perspective. *Journal of Quantitative Spectroscopy and Radiative Transfer*, *112*(18), 2826–2834. https://doi.org/10.1016/j.jqsrt.2011.08.012

Naessens, M., Leclerc, J. C., & Tran-Minh, C. (2000). Fiber optic biosensor using Chlorella vulgaris for determination of toxic compounds. *Ecotoxicology and Environmental Safety*, *46*(2), 181–185. https://doi.org/10.1006/eesa.1999.1904

Naessens, M., Tran-Minh, C., & Biosensor, T.-M. (1999). Biosensor using immobilized Chlorella microalgae for determination of volatile organic compounds. *Sensors and Actuators B: Chemical*, *59*(3), 100–102. https://doi.org/10.1016/S0925-4005(99)00203-8ï

Nauha, E. K., & Alopaeus, V. (2013). Modeling method for combining fluid dynamics and algal growth in a bubble column photobioreactor. *Chemical Engineering Journal*, *229*(September), 559–568. https://doi.org/10.1016/j.cej.2013.06.065

Nauha, E. K., & Alopaeus, V. (2015). Modeling outdoors algal cultivation with compartmental approach. *Chemical Engineering Journal*, *259*(November), 945–960. https://doi.org/10.1016/j.cej.2014.08.073

Nirmala, G. S., & Muruganandam, L. (2013). Biosorption of cadmium in liquid-solid circulating fluidized bed. *International Journal of ChemTech Research*, *5*(1), 65–71.

Norton, T. A., Melkonian, M., & Andersen, R. A. (1996). Algal biodiversity. *Phycologia*, *35*(4), 308–326. https://doi.org/https://doi.org/10.2216/i0031-8884-35-4-308.1

Not, F., Siano, R., Kooistra, W. H. C. F., Simon, N., Vaulot, D., & Probert, I. (2012). Diversity and Ecology of Eukaryotic Marine Phytoplankton. In *Advances in Botanical Research* (Vol. 64, pp. 1–53). Academic Press Inc. https://doi.org/10.1016/B978-0-12-391499-6.00001-3

Pan, C., Hu, B., Li, W., Sun, Y., Ye, H., & Zeng, X. (2009). Novel and efficient method for immobilization and stabilization of β-d-galactosidase by covalent attachment onto magnetic Fe3O4-chitosan nanoparticles. *Journal of Molecular Catalysis B: Enzymatic*, *61*(3–4), 208–215. https://doi.org/10.1016/j.molcatb.2009.07.003

Pane, L., Feletti, M., Bertino, C., & Carli, A. (1998). Viability of the marine microalga Tetraselmis suecica grown free and immobilized in alginate beads. *Aquaculture International*, *6*(6), 411–420. https://doi.org/10.1023/A:1009279300596

Panneerselvam, R., Savithri, S., & Surender, G. D. (2007). CFD based investigations on hydrodynamics and energy dissipation due to solid motion in liquid fluidised bed. *Chemical Engineering Journal*, *132*(1–3), 159–171. https://doi.org/10.1016/j.cej.2007.01.042

Papacek, S., Stys, D., Dolınek, P., & Petera, K. (2007). Multicompartment/CFD modelling of transport and reaction processes in Couette-Taylor photobioreactor. *Applied and Computational Mechanics*, *1*, 577–586.

Park, D. S., Ladd, D. M., & Hendricks, E. W. (1994). Feedback control of von Kármán vortex shedding behind a circular cylinder at low Reynolds numbers. *Physics of Fluids*, *6*(7), 2390–2405. https://doi.org/10.1063/1.868188

Person, J. (2011). Livre Turquoise - Algues, Filières du Futur. In *Actes du Colloque Adebiotech 17-19 Novembre 2010, Romainville.*

Pierre, G., Delattre, C., Dubessay, P., Jubeau, S., Vialleix, C., Cadoret, J. P., Probert, I., & Michaud, P. (2019). What is in store for EPS microalgae in the next decade? *Molecules*, *24*(23). https://doi.org/10.3390/molecules24234296

Pires, J. C. M., Alvim-Ferraz, M. C. M., & Martins, F. G. (2017). Photobioreactor design for microalgae production through computational fluid dynamics: A review. *Renewable and Sustainable Energy Reviews*, *79*(September 2016), 248–254. https://doi.org/10.1016/j.rser.2017.05.064

Pomeroy, L. R., & Wiebe, W. J. (2001). Temperature and substrates as interactive limiting factors for marine heterotrophic bacteria. *Aquatic Microbial Ecology*, *23*, 187–204. https://doi.org/doi:10.3354/ame023187

Praveen, P., & Loh, K. C. (2015). Photosynthetic aeration in biological wastewater treatment using immobilized microalgae-bacteria symbiosis. *Applied Microbiology and Biotechnology*, *99*(23), 10345–10354. https://doi.org/10.1007/s00253-015-6896-3

Priyadarshani, I., & Rath, B. (2012). Commercial and industrial applications of micro algae - A review. *Journal of Algal Biomass Utilization*, *3*, 89–100.

Pruvost, J., Pottier, L., & Legrand, J. (2006). Numerical investigation of hydrodynamic and mixing conditions in a torus photobioreactor. *Chemical Engineering Science*, *61*(14), 4476–4489. https://doi.org/10.1016/j.ces.2006.02.027

Ramos Tercero, E. A., Sforza, E., Morandini, M., & Bertucco, A. (2014). Cultivation of Chlorella protothecoides with urban wastewater in continuous photobioreactor: Biomass productivity and nutrient removal. *Applied Biochemistry and Biotechnology*, *172*(3), 1470–1485. https://doi.org/10.1007/s12010-013-0629-9

Richardson, J. F., & Zaki, W. N. (1997). Sedimentation and fluidisation: Part I. *Chemical Engineering Research and Design*, *75*(1 SUPPL.), S82–S100. https://doi.org/10.1016/s0263-8762(97)80006-8

Romo, S., & Perez-Martinez, C. (1997). The use of Immobilization in Alginate Beads for long-term storage of Pseudanabaena galeata (cyanobacteria) in the laboratory. *Journal of Phycology*, *33*, 1073–1076. https://doi.org/https://doi.org/10.1111/j.0022-3646.1997.01073.x

Rooke, J. C., Léonard, A., Meunier, C. F., & Su, B. L. (2011). Designing photobioreactors based on living cells immobilized in silica gel for carbon dioxide mitigation. *ChemSusChem*, *4*(9), 1249–1257. https://doi.org/10.1002/cssc.201000442

Ross, B. S., & Pott, R. W. M. (2021). Hydrogen production by immobilized Rhodopseudomonas palustris in packed or fluidized bed photobioreactor systems. *International Journal of Hydrogen Energy*, *46*(2), 1715–1727. https://doi.org/10.1016/j.ijhydene.2020.10.061

Rossignol, N., Lebeau, T., Jaouen, P., & Robert, J. M. (2000). Comparison of two membrane - Photobioreactors, with free or immobilized cells, for the production of pigments by a marine diatom. *Bioprocess Engineering*, *23*(5), 495–501. https://doi.org/10.1007/s004499900186

Ruiz, J., Olivieri, G., de Vree, J., Bosma, R., Willems, P., Reith, J. H., Eppink, M. H. M., Kleinegris, D. M. M., Wijffels, R. H., & Barbosa, M. J. (2016). Towards industrial products from microalgae. *Energy and Environmental Science*, *9*(10), 3036–3043. https://doi.org/10.1039/c6ee01493c

Ruiz-Marin, A., Mendoza-Espinosa, L. G., & Stephenson, T. (2010). Growth and nutrient removal in free and immobilized green algae in batch and semi-continuous cultures treating real wastewater. *Bioresource Technology*, *101*(1), 58–64. https://doi.org/10.1016/j.biortech.2009.02.076

Sánchez Mirón, A., Cerón García, M. C., García Camacho, F., Molina Grima, E., & Chisti, Y. (2002). Growth and biochemical characterization of microalgal biomass produced in bubble column and airlift photobioreactors: Studies in fed-batch culture. *Enzyme and Microbial Technology*, *31*, 1015–1023. https://doi.org/10.1016/S0141-0229(02)00229-6

Santos-Rosa, F., Galván, F., & Vega, J. M. (1989). Photoproduction of ammonium by Chlamydomonas reinhardtii cells immobilized in barium alginate: a reactor feasibility study. *Applied Microbiology and Biotechnology*, *32*(3), 285–290. https://doi.org/10.1007/BF00184975

Sasso, S., Stibor, H., Mittag, M., & Grossman, A. R. (2018). The Natural History of Model Organisms: From molecular manipulation of domesticated Chlamydomonas reinhardtii to survival in nature. *ELife*. https://doi.org/10.7554/eLife.39233.001

Schohl, G. A. (1993). Improved approximate method for simulating frequency-dependent friction in transient laminar flow. *Journal of Fluids Engineering, Transactions of the ASME*, *115*(3), 420–424. https://doi.org/10.1115/1.2910155

Schulze, P. S. C., Brindley, C., Fernández, J. M., Rautenberger, R., Pereira, H., Wijffels, R. H., & Kiron, V. (2020). Flashing light does not improve photosynthetic performance and growth of green microalgae. *Bioresource Technology Reports*, *9*. https://doi.org/10.1016/j.biteb.2019.100367

Seibert, M., & Torzillo, G. (2018). *Microalgal Hydrogen Production Achievements and Perspectives* (Vol. 16). Royal Society Chemistry. https://doi.org/https://doi.org/10.1039/9781849737128

Serp, D., Cantana, E., Heinzen, C., Von Stockar, U., & Marison, I. W. (2000). Characterizetion of an encapsulation device for the production of monodisperse alginate beads for cell immobilization. *Biotechnology and Bioengineering*, *70*(1), 41–53. https://doi.org/10.1002/1097-0290(20001005)70:1<41::aid-bit6>3.0.co;2-u

Sha, J., Lei, H., Wang, M., Liu, B., & Shao, H. (2018). Comparison of Separation Performance of Liquid-Solid Fluidized Bed Separator and Dense Medium Cyclone for Cleaning Coal. *International Journal of Coal Preparation and Utilization*, *38*(2), 98–106. https://doi.org/10.1080/19392699.2016.1202824

Shao, N., & Bock, R. (2008). A codon-optimized luciferase from Gaussia princeps facilitates the in vivo monitoring of gene expression in the model alga Chlamydomonas reinhardtii. *Current Genetics*, *53*(6), 381–388. https://doi.org/10.1007/s00294-008-0189-7

Shitanda, I., Takada, K., Sakai, Y., & Tatsuma, T. (2005). Compact amperometric algal biosensors for the evaluation of water toxicity. *Analytica Chimica Acta*, *530*(2), 191–197. https://doi.org/10.1016/j.aca.2004.09.073

Sicard, C., Brayner, R., Margueritat, J., Hémadi, M., Couté, A., Yéprémian, C., Djediat, C., Aubard, J., Fiévet, F., Livage, J., & Coradin, T. (2010). Nano-gold biosynthesis by silica-encapsulated micro-algae: A "living" bio-hybrid material. *Journal of Materials Chemistry*, *20*(42), 9342–9347. https://doi.org/10.1039/c0jm01735c

Singh, G., & Patidar, S. K. (2018). Microalgae harvesting techniques: A review. *Journal of Environmental Management*, *217*, 499–508. https://doi.org/10.1016/j.jenvman.2018.04.010

Singh, J., & Saxena, R. C. (2015). An Introduction to Microalgae: Diversity and Significance. Diversity and Significance. In *Handbook of Marine Microalgae: Biotechnology Advances* (pp. 11–24). Elsevier Inc. https://doi.org/10.1016/B978-0-12-800776-1.00002-9

Singh, R. N., & Sharma, S. (2012). Development of suitable photobioreactor for algae production - A review. *Renewable and Sustainable Energy Reviews*, *16*(4), 2347–2353. https://doi.org/10.1016/j.rser.2012.01.026

Sompech, K., Chisti, Y., & Srinophakun, T. (2012). Design of raceway ponds for producing microalgae. *Biofuels*, *3*(4), 387–397. https://doi.org/10.4155/bfs.12.39

Souliès, A. (2014). Contribution à l'étude hydrodynamique et à la modélisation des photobioréacteurs à haute productivité volumique. In *Thèse de Doctorat en génie procédées France*. Université de Nantes.

Spolaore, P., Joannis-Cassan, C., Duran, E., & Isambert, A. (2006). Commercial applications of microalgae. *Journal of Bioscience and Bioengineering*, *101*(2), 87–96. https://doi.org/10.1263/jbb.101.87

Stojkovic, D., Torzillo, G., Faraloni, C., & Valant, M. (2015). Hydrogen production by sulfur-deprived TiO2-encapsulated Chlamydomonas reinhardtii cells. *International Journal of Hydrogen Energy*, *40*(8), 3201–3206. https://doi.org/10.1016/j.ijhydene.2014.12.115

Sun, X., Wang, C., Tong, Y., Wang, W., & Wei, J. (2014). Microalgae filtration by UF membranes: Influence of three membrane materials. *Desalination and Water Treatment*, *52*(28–30), 5229–5236. https://doi.org/10.1080/19443994.2013.813103

Takache, H. (2010). *Caractérisation, modélisation de la croissance photosynthétique de Chlamydomonas reinhardtii en photoréacteur et mise en évidence du couplage à l'hydrodynamique*. Université de Nantes.

Takache, H., Pruvost, J., & Marec, H. (2015). Investigation of light/dark cycles effects on the photosynthetic growth of chlamydomonas reinhardtii in conditions representative of photobioreactor cultivation. *Algal Research*, *8*, 192–204. https://doi.org/10.1016/j.algal.2015.02.009

Tamburini, A., Cipollina, A., Micale, G., & Brucato, A. (2013). Particle distribution in dilute solid liquid unbaffled tanks via a novel laser sheet and image analysis based technique. *Chemical Engineering Science*, *87*, 341–358. https://doi.org/10.1016/j.ces.2012.11.005

Thakur, A., & Kumar, H. D. (1999). Use of natural polymers as immobilizing agents and effects on the growth of Dunaliella salina and its glycerol production. *Acta Biotechnologica*, *19*(1), 37–44. https://doi.org/10.1002/abio.370190107

Thombare, M. A., Chavan, P. V., Bankar, S. B., & Kalaga, D. V. (2019). Solid-liquid circulating fluidized bed: A way forward. *Reviews in Chemical Engineering*, *35*(1), 1–44. https://doi.org/10.1515/revce-2017-0017

Travieso, L., Benitez, F., & Dupeiron, R. (1992). Sewage treatment using immobilied microalgae. *Bioresource Technology*, *40*(2), 183–187. https://doi.org/10.1016/0960-8524(92)90207-E

Travieso, L., Hall, O., Rao, K. K., Benã Tez, F., Sã Anchez, E., & Borja, R. (2001). A helical tubular photobioreactor producing Spirulina in a semicontinuous mode. *International Biodeterioration & Biodegradation*, *47*, 151–155. https://doi.org/https://doi.org/10.1016/S0964-8305(01)00043-9

Tredici, M. R., & Zittelli, G. C. (1998). Efficiency of Sunlight Utilization: Tubular Versus Flat Photobioreactors. *Biotechnology and Bioengineering*, *57*, 187–197. https://doi.org/10.1002/(SICI)1097-0290(19980120)57:2<187::AID-BIT7>3.0.CO;2-J

Tree of Life web project. (n.d.). Retrieved October 1, 2021, from http://tolweb.org/tree/

Tripathi, U., Ramachandra Rao, S., & Ravishankar, G. A. (2002). Biotransformation of phenylpropanoid compounds to vanilla flavor metabolites in cultures of Haematococcus pluvialis. *Process Biochemistry*, *38*(3), 419–426. https://doi.org/10.1016/S0032-9592(02)00135-8

Unadkat, H., Rielly, C. D., Hargrave, G. K., & Nagy, Z. K. (2009). Application of fluorescent PIV and digital image analysis to measure turbulence properties of solid-liquid stirred suspensions. *Chemical Engineering Research and Design*, *87*(4), 573–586. https://doi.org/10.1016/j.cherd.2008.11.011

Vandamme, D., Foubert, I., Fraeye, I., Meesschaert, B., & Muylaert, K. (2012). Flocculation of Chlorella vulgaris induced by high pH: Role of magnesium and calcium and practical implications. *Bioresource Technology*, *105*, 114–119. https://doi.org/10.1016/j.biortech.2011.11.105

Vargas, G., Donoso-Bravo, A., Vergara, C., & Ruiz-Filippi, G. (2016). Assessment of microalgae and nitrifiers activity in a consortium in a continuous operation and the effect of oxygen depletion. *Electronic Journal of Biotechnology*, *23*, 63–68. https://doi.org/10.1016/j.ejbt.2016.08.002

Varicon Aqua Solutions. (n.d.). *Varicon Aqua*. Retrieved October 1, 2021, from http://www.variconaqua.com/products-services/phyco-flow/

Vasilieva, S. G., Lobakova, E. S., Lukyanov, A. A., & Solovchenko, A. E. (2016). Immobilized microalgae in biotechnology. *Moscow University Biological Sciences Bulletin*, *71*(3), 170–176. https://doi.org/10.3103/S0096392516030135

Védrine, C., Leclerc, J.-C., Durrieu, C., & Tran-Minh, C. (2003). Optical whole-cell biosensor using Chlorella vulgaris designed for monitoring herbicides. *Biosensors and Bioelectronics*, *18*, 457–463. https://doi.org/10.1016/s0956-5663(02)00157-4

Vílchez, C., Galván, F., & Vega, J. M. (1991). Glycolate photoproduction by free and alginate-entrapped cells of Chlamydomonas reinhardtii. *Applied Microbiology and Biotechnology*, *35*(6), 716–719. https://doi.org/10.1007/BF00169883

Vílchez, C., Garbayo, I., Lobato, M. v., & Vega, J. M. (1997). Microalgae-mediated chemicals production and wastes removal. *Enzyme and Microbial Technology*, *20*(8), 562–572. https://doi.org/10.1016/S0141-0229(96)00208-6

Virdung, T., & Rasmuson, A. (2007). Hydrodynamic properties of a turbulent confined solid-liquid jet evaluated using PIV and CFD. *Chemical Engineering Science*, *62*(21), 5963–5978. https://doi.org/10.1016/j.ces.2007.06.017

Wang, S., Guo, S., Gao, J., Lan, X., Dong, Q., & Li, X. (2012). Simulation of flow behavior of liquid and particles in a liquid-solid fluidized bed. *Powder Technology*, *224*, 365–373. https://doi.org/10.1016/j.powtec.2012.03.022

Wang, S., Li, X., Wu, Y., Li, X., Dong, Q., & Yao, C. (2010). Simulation of flow behavior of particles in a liquid-solid fluidized bed. *Industrial and Engineering Chemistry Research*, *49*(20), 10116–10124. https://doi.org/10.1021/ie101139h

Wang, S., Sun, J., Yang, Q., Zhao, Y., Gao, J., & Liu, Y. (2014). Numerical simulation of flow behavior of particles in an inverse liquid-solid fluidized bed. *Powder Technology*, *261*, 14–21. https://doi.org/10.1016/j.powtec.2014.04.017

Weber, B., von Campenhausen, M., Maßmann, T., Bednarz, A., & Jupke, A. (2019). CFD based compartment-model for a multiphase loop-reactor. *Chemical Engineering Science: X*, *2*. https://doi.org/10.1016/j.cesx.2019.100010

Wen, C. Y., & Yu, Y. H. (1966). A Generalized Method for Predicting the Minimum Fluidization Velocity. *AIChE Journal*, *12*(3), 610–612. https://doi.org/https://doi.org/10.1002/aic.690120343

Whitton, R., Ometto, F., Villa, R., Pidou, M., & Jefferson, B. (2019). Influence of light regime on the performance of an immobilised microalgae reactor for wastewater nutrient removal. *Algal Research*, *44*(January). https://doi.org/10.1016/j.algal.2019.101648

Wiley, P. E. (2013). *Microalgae Cultivation using Offshore Membrane Enclosures for Growing Algae*.

Williamson, C. J., Cameron, K. A., Cook, J. M., Zarsky, J. D., Stibal, M., & Edwards, A. (2019). Glacier algae: A dark past and a darker future. *Frontiers in Microbiology*, *10*. https://doi.org/10.3389/fmicb.2019.00524

Wu, X., & Merchuk, J. C. (2001). A model integrating fluid dynamics in photosynthesis and photoinhibition processes. *Chemical Engineering Science*, *56*, 3527–3538. https://doi.org/https://doi.org/10.1016/S0009-2509(01)00048-3

Xie, X., Le Men, C., Dietrich, N., Schmitz, P., & Fillaudeau, L. (2018). Local hydrodynamic investigation by PIV and CFD within a Dynamic filtration unit under laminar flow. *Separation and Purification Technology*, *198*, 38–51. https://doi.org/10.1016/j.seppur.2017.04.009

Yigitoglu, M., & Temoçin, Z. (2010). Immobilization of Candida rugosa lipase on glutaraldehyde-activated polyester fiber and its application for hydrolysis of some vegetable oils. *Journal of Molecular Catalysis B: Enzymatic*, *66*(1–2), 130–135. https://doi.org/10.1016/j.molcatb.2010.04.007

Yuan, F., & Isaac, K. M. (2017). A study of MHD-based chaotic advection to enhance mixing in microfluidics using transient three dimensional CFD simulations. *Sensors and Actuators, B: Chemical*, *238*, 226–238. https://doi.org/10.1016/j.snb.2016.07.063

Zalc, J. M., Szalai, E. S., Alvarez, M. M., & Muzzio, F. J. (2002). Using CFD to understand chaotic mixing in laminar stirred tanks. *AIChE Journal*, *48*(10), 2124–2134. https://doi.org/10.1002/aic.690481004

Zamani, N., Noshadi, M., Amin, S., Niazi, A., & Ghasemi, Y. (2012). Effect of alginate structure and microalgae immobilization method on orthophosphate removal from wastewater. *Journal of Applied Phycology*, *24*(4), 649–656. https://doi.org/10.1007/s10811-011-9682-3

Zbib, H., Ebrahimi, M., Ein-Mozaffari, F., & Lohi, A. (2018). Comprehensive analysis of fluid-particle and particle-particle interactions in a liquid-solid fluidized bed via CFD-DEM coupling and tomography. *Powder Technology*, *340*, 116–130. https://doi.org/10.1016/j.powtec.2018.09.009

Zheng, Y., & Zhu, J. X. (2000). Microstructural aspects of the flow behaviour in a liquid-solids circulating fluidized bed. *Canadian Journal of Chemical Engineering*, *78*(1), 75–81. https://doi.org/10.1002/cjce.5450780112

Zhou, L., Li, G., An, T., & Li, Y. (2010). Synthesis and characterization of novel magnetic Fe3O 4/polyurethane foam composite applied to the carrier of immobilized microorganisms for wastewater treatment. *Research on Chemical Intermediates*, *36*(3), 277–288. https://doi.org/10.1007/s11164-010-0134-5

Zhou, W., Lu, Q., Han, P., & Li, J. (2020). Microalgae cultivation and photobioreactor design. In *Microalgae Cultivation for Biofuels Production* (pp. 31–50). Elsevier. https://doi.org/10.1016/B978-0-12-817536-1.00003-5

List of Figures

List of Tables

List of Abbreviations and Symbols

Symbols

x	[mm]	reactor width
y	[mm]	reactor depth
z	[mm]	reactor height
y_t	[mm]	flipped reactor depth
y_{max}	[mm]	maximum reactor depth
I	[$\mu E.m^{-2}.s^{-1}$]	light intensity / irradiance
I_0	[$\mu E.m^{-2}.s^{-1}$]	light intensity at the reactor surface
C_x	[$g.L^{-1}$]	dry weight
D_a	[-]	Damköhler number
K_1	[$\mu E.m^{-2}.s^{-1}$]	half-saturation constant
K_H	[$\mu E.m^{-2}.s^{-1}$]	inhibition constant
x_1	[-]	fraction of biomass in the inactive/resting state
x_2	[-]	fraction of biomass in the active state
x_3	[-]	fraction of biomass in the inhibited state
k	[-]	Photosynthetic Factory model parameter
M_e	[h^{-1}]	Photosynthetic Factory model parameter
R^2	[-]	coefficient of determination in linear regression
t	[day]	culture time
A_s	[m^2]	cross section area of the reactor
D_h	[m]	hydraulic diameter
P_s	[m]	perimeter of the cross section area of the reactor

Re	[-]	Reynolds number
Re_p	[-]	particle Reynolds number
Re_ω	[-]	vorticity Reynolds number
u_L	[m.s^{-1}]	fluid velocity
u_S	[m.s^{-1}]	solid velocity
$u_{T,0}$	[m.s^{-1}]	settling solid velocity of a single bead
u_b	[m.s^{-1}]	hindered settling velocity of the bead bed
d_p	[mm]	particle diameter
C_D	[-]	drag coefficient
C_l	[-]	lift coefficient
g	[m.s^{-2}]	gravitational acceleration (set equals to 9.81)
e	[-]	elongation
f	[-]	fatness
K_{SL}	[kg.m^{-3}.s^{-1}]	fluid-solid exchange coefficient
p	[kg.m^{-1}s^{-2}]	pressure
p_s	[kg.m^{-1}s^{-2}]	solid pressure
e_{ss}	[-]	coefficient of restitution for particle collisions
T_S	[m^2. s^{-2}]	granular temperature energy
$g_{0,ss}$	[-]	radial distribution function
F_{lift}	[N.m^{-3}]	lift force
F_{vm}	[N.m^{-3}]	virtual mass force
A	[-]	pixel gray level values in the fluidized bed reactor
A_0	[-]	pixel gray level values in the blank image
k_a	[-]	absorption coefficient in light attenuation method

V_T	[m^3]	total volume of the reactor
V_h	[m^3]	volume of the reactor above a height of 350 mm
V_2	[m^3]	volume of the reactor between a height of 310 and 350 mm
V_p	[m^3]	volume of the reactor between a height of 55 and 310 mm
V_1	[m^3]	volume of the reactor between a height of 40 and 55 mm
V_b	[m^3]	volume of the reactor below a height of 40 mm
V_J	[m^3]	volume of the compartment J
n	[-]	empirical coefficient
St	[-]	Stokes number
$f^M_{\alpha\beta}$	[$m^3.s^{-1}$]	mean flow rate between α and β cells
$f'_{\alpha\beta}$	[$m^3.s^{-1}$]	fluctuant flow rate between α and β cells
$A_{\alpha\beta}$	[m^2]	exchange surface between α and β cells
$F_{JK}^{M,in}$	[$m^3.s^{-1}$]	mean inflow rate between J and K compartments
$F_{JK}^{M,out}$	[$m^3.s^{-1}$]	mean outflow rate between J and K compartments
$F_{JK}^{',in}$	[$m^3.s^{-1}$]	fluctuant inflow rate between J and K compartments
$F_{JK}^{',out}$	[$m^3.s^{-1}$]	fluctuant outflow rate between J and K compartments
Q_C	[$m^3.s^{-1}$]	transition matrix
Q_{J-K}	[$m^3.s^{-1}$]	outflow rate from a compartment J to a compartment K
Q_{J-J}	[$m^3.s^{-1}$]	total inflow rate in a compartment J
S_J	[-]	residence time distribution of a bead in the compartment J
p_{J-K}	[-]	probability of bead movement from compartment J to compartment K
e_{p1}	[m]	thickness of the reactor walls
e_{p2}	[m]	thickness of the internal panel
e_{L1}	[m]	depth of zone 1

e_{L2}	[m]	depth of zone 2
f_{ti}	[m]	normalized solid fraction
N_y	[-]	total number of compartments along the depth
N_{yi}	[-]	number of compartments in depth between the light source and a given compartment

Greek letters

μ	[day^{-1}]	growth rate
μ_{max}	[day^{-1}]	maximum growth rate
$\propto$	[($\mu E.m^{-2}$)$^{-1}$]	Photosynthetic Factory model parameter
β	[($\mu E.m^{-2}$)$^{-1}$]	Photosynthetic Factory model parameter
γ	**[s^{-1}]**	Photosynthetic Factory model parameter
δ	**[s^{-1}]**	Photosynthetic Factory model parameter
λ	[m]	wavelength
ρ_l	[$kg.m^{-3}$]	fluid density
ρ_s	[$kg.m^{-3}$]	solid density
η_l	[Pa.s]	liquid dynamic viscosity
η_s	[Pa.s]	solid dynamic viscosity
ν_l	[$m^2.s^{-1}$]	liquid cinematic viscosity
$\propto_S$	[-]	solid volume fraction
$\propto_L$	[-]	liquid volume fraction
ε_b	[$L.g^{-1}.m^{-1}$]	absorption coefficient of the biomass
ε_w	[m^{-1}]	absorption coefficient of the water
ε_p	[m^{-1}]	absorption coefficient of the Plexiglas
τ_{bio}	[s]	characteristic time of biological response
τ_I	[s]	characteristic time of light fluctuations

τ_S	[s]	particle relaxation time
$\langle \propto_S \rangle$	[-]	volume solid fraction over the reactor depth
$\overline{\langle \propto_S \rangle_T}$	[-]	solid fraction over the reactor depth in V_T
$\overline{\langle \propto_S \rangle_h}$	[-]	solid fraction over the reactor depth in V_h
$\overline{\langle \propto_S \rangle_2}$	[-]	solid fraction over the reactor depth in V_2
$\overline{\langle \propto_S \rangle_p}$	[-]	solid fraction over the reactor depth in V_p
$\overline{\langle \propto_S \rangle_1}$	[-]	solid fraction over the reactor depth in V_1
$\overline{\langle \propto_S \rangle_b}$	[-]	solid fraction over the reactor depth in V_b
$\overline{\langle \propto_S \rangle_{bed}}$	[-]	solid fraction in the bead bed
$\propto_{Sj}$	[-]	solid fraction in the compartment
$\propto_{J\text{-}K}$	[$m^3.s^{-1}$]	random fluctuant flow rate

Abbreviations

PAR	Photosynthetically Active Radiation
PFD	Photon Flux Density
L/D cycles	Light/Dark cycles
PSF	PhotoSynthetic Factory
PDADMAC	Poly(diallyldimethylammonium chloride
TMP	Tris-Minimal-Phosphate culture medium
TAP	Tris-Acetate-Phosphate culture medium
TMP 2x	Tris-Minimal-Phosphate concentrated 2 times
TMP 4x	Tris-Minimal-Phosphate concentrated 4 times
TRIS	Tris(hydroxymethyl)aminomethane
UV	UltraViolet
DW	Dry Weight

OD	Optical Density
RLU	Relative Luminescence Unit
3D	3 Dimensions
CFD	Computational Fluid Dynamics
PIV	Particle Image Velocity
rms	Root Mean Square
CTMC	Continuous-Time Markov Chain

a)

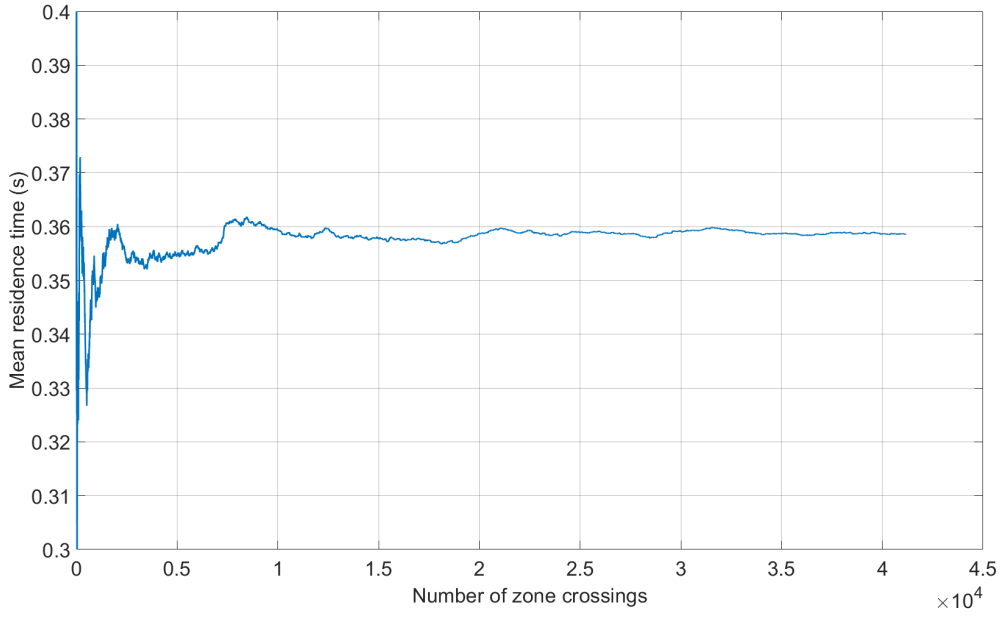
Mean residence time (s)
0.4
0.39
0.38
0.37
0.36
0.35
0.34
0.33
0.32
0.31
0.3
0
0.5
1
1.5
2
2.5
3
3.5
4
4.5
Number of zone crossings
×10^4

b)

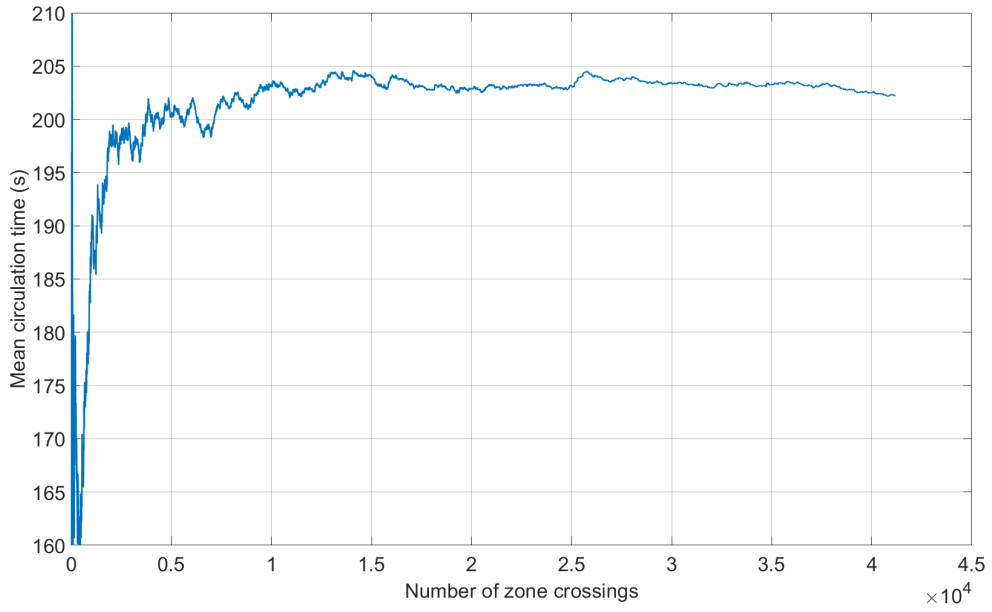
Mean circulation time (s)
210
205
200
195
190
185
180
175
170
165
160
0
0.5
1
1.5
2
2.5
3
3.5
4
4.5
Number of zone crossings
×10^4

c)

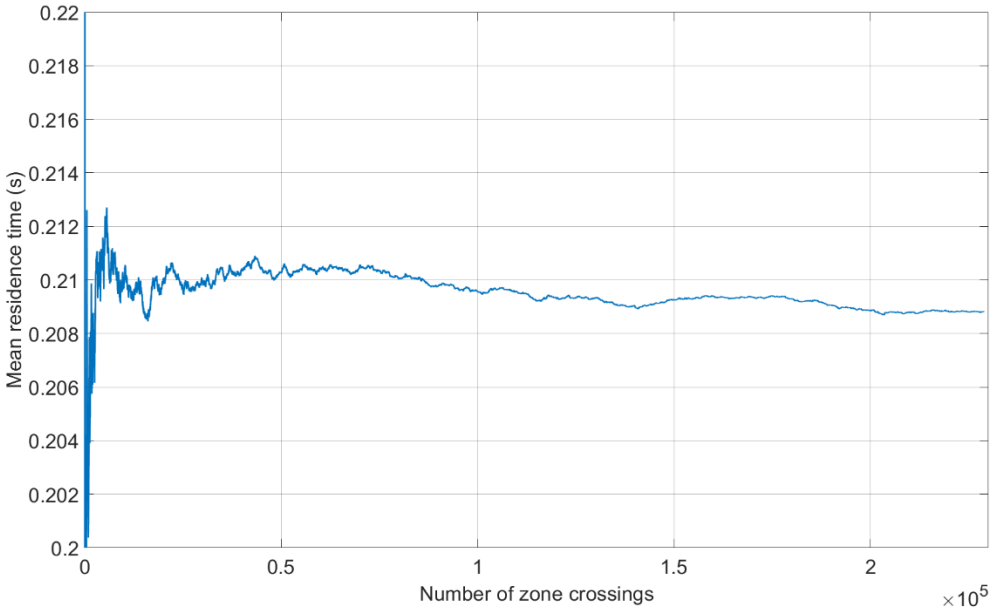

d)

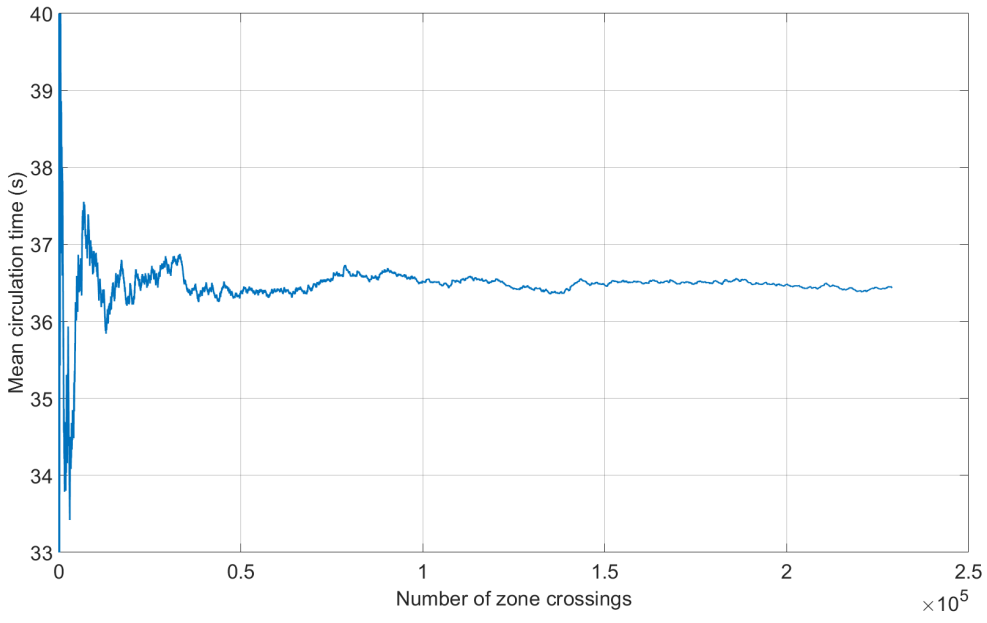

Figure 0.1- Mean residence time (a, c) and mean circulation time (b, d) obtained in zone s1 (a, b) and s3 (c, d) using the stochastic model. Zones are described in Figure 5.15. Mean on 40 particles. Calculations correspond to a total time of 58h in the reactor. 29h is considered satisfactory to characterize trajectories.